Étude du polymorphisme de VO pour des applications en microélectronique et radiofréquences

Laura Diebold

To cite this version:

Laura Diebold. Étude du polymorphisme de VO pour des applications en microélectronique et radiofréquences. Plasmas. Université Paris-Saclay, 2022. English. NNT : 2022UPAST128 . tel-04794669

HAL Id: tel-04794669
https://theses.hal.science/tel-04794669v1

Submitted on 21 Nov 2024

Study of VO_2 polymorphs for microelectronics and radiofrequency devices

Étude du polymorphisme de VO_2 pour des applications en microélectronique et radiofréquences

Thèse de doctorat de l'université Paris-Saclay

École doctorale n°575 Electrical, Optical, Bio-Physics and Engineering (EOBE)
Spécialité de doctorat : Physique
Graduate School : Sciences de l'Ingénierie et des Systèmes
Référent : Faculté des Sciences d'Orsay

Thèse préparée au **Centre de Nanosciences et de Nanotechnologies** (CNRS/Université Paris-Saclay), sous la direction de **Pascal AUBERT**, Professeur, et le co-encadrement de **Thomas MAROUTIAN**, Chargé de recherche, et **Olga ISHCHENKO**, Responsable R&D (entreprise TE-OX)

Thèse soutenue à Paris-Saclay, le 21 Novembre 2022, par

Laura DIEBOLD

Composition du Jury

Membres du jury avec voix délibérative

Aline ROUGIER Directrice de recherche, Institut de Chimie de la Matière Condensée de Bordeaux	Présidente
Corinne CHAMPEAUX Professeure, Université de Limoges (IRCER)	Rapportrice & Examinatrice
Mircea Gabriel MODREANU Professeur, University College Cork (Tyndall National Institute)	Rapporteur & Examinateur
Brahim DKHIL Maître de conférences, Université Paris-Saclay (CentraleSupélec)	Examinateur

THÈSE DE DOCTORAT

NNT : 2022UPAST128

Study of VO_2 polymorphs for microelectronics and radiofrequency devices

Étude du polymorphisme de VO_2 pour des applications en microélectronique et radiofréquences

Thèse de doctorat de l'université Paris-Saclay

École doctorale n°575 Electrical, Optical, Bio-Physics and Engineering (EOBE)
Spécialité de doctorat : Physique
Graduate School : Sciences de l'Ingénierie et des Systèmes
Référent : Faculté des Sciences d'Orsay

Thèse préparée au **Centre de Nanosciences et de Nanotechnologies** (CNRS/Université Paris-Saclay), sous la direction de **Pascal AUBERT**, Professeur, et le co-encadrement de **Thomas MAROUTIAN**, Chargé de recherche, et **Olga ISHCHENKO**, Responsable R&D (entreprise TE-OX)

Thèse soutenue à Paris-Saclay, le 21 Novembre 2022, par

Laura DIEBOLD

Composition du Jury

Membres du jury avec voix délibérative

Aline ROUGIER Directrice de recherche, Institut de Chimie de la Matière Condensée de Bordeaux	Présidente
Corinne CHAMPEAUX Professeure, Université de Limoges (IRCER)	Rapportrice & Examinatrice
Mircea Gabriel MODREANU Professeur, University College Cork (Tyndall National Institute)	Rapporteur & Examinateur
Brahim DKHIL Maître de conférences, Université Paris-Saclay (CentraleSupélec)	Examinateur

THÈSE DE DOCTORAT

NNT : 2022UPAST128

“If your dreams do not scare you, they
are not big enough.”

Ellen Johnson Sirleaf

université PARIS-SACLAY

DOCTORAL SCHOOL
Electrical, Optical, Bio:
Physics and Engineering
(EOBE)

Titre : Étude du polymorphisme de VO_2 pour des applications en microélectronique et radiofréquences.

Mots clés : Dioxyde de Vanadium, Épitaxie, Transition métal-isolant, Pulvérisation cathodique, Synthèse hydrothermale, Commutateurs radiofréquences.

Résumé : Dans l'industrie des communications, des efforts permanents sont déployés afin d'améliorer les performances des dispositifs et d'augmenter la vitesse d'échange de données. Historiquement, les composants utilisés en télécommunication reposent sur les matériaux semiconducteurs. En complément, les matériaux à changement de phase offrent des propriétés attrayantes pour de nouveaux dispositifs électroniques. La société TE-OX® a concentré son activité dans le domaine des radiofréquences (RF) sur le dioxyde de vanadium (VO_2) qui a démontré un comportement prometteur pour la fabrication de composants ultrarapides et fiables. Il s'agit en particulier d'exploiter la transition métal-isolant du VO_2 qui a lieu proche de la température ambiante. Bien que le VO_2 soit un simple oxyde binaire, son appartenance à un diagramme de phase complexe où coexistent de nombreuses phases à stœchiométrie mixte rend difficile la fabrication de ce matériau. L'obtention de VO_2 de haute qualité nécessite à la fois une maîtrise de la méthode de croissance et une bonne compréhension des mécanismes conduisant à la formation et à la stabilisation de cet oxyde.

Dans ce travail, la pulvérisation cathodique radiofréquence à effet magnétron et la synthèse hydrothermale ont été utilisées pour explorer les phases polymorphes de VO_2, en particulier les phases monocliniques M1 et B. Les analyses structurales réalisées principalement par diffraction des rayons X ont mis en évidence que les déformations dans le VO_2 développées lors de sa croissance étaient un élément clé de la stabilisation des polymorphes, et qu'elles pouvaient affecter la transition entre les phases M1 et rutile (R). En modifiant l'orientation et la nature du substrat (saphir Al_2O_3, titanate de strontium $SrTiO_3$) pour la croissance de films minces par épitaxie, nous mettons en évidence que la phase stabilisée est différente et que le mode de croissance des oxydes est modifié. Dans le cas de la croissance sur substrats d'Al_2O_3-c et -r, le fort désaccord de maille entraîne la croissance de VO_2(M1) avec relaxation des contraintes induites par l'épitaxie et formation de multiples variants cristallographiques. Les études des transitions structurale, électrique et optique ont montré que la déformation de compression suivant l'axe $c_{VO2(R)}$ (= $a_{VO2(M1)}$) conduit à une diminution de la température de la transition métal-isolant. Afin d'approfondir nos recherches sur les effets des contraintes lors de l'élaboration des couches minces, nous avons étudié la croissance des films de VO_2 sur substrat $SrTiO_3$. Les caractérisations physico-chimiques réalisées montrent que les phases B et M1 peuvent coexister au sein d'une même couche sur ce substrat. Les travaux menés par synthèse hydrothermale sur le VO_2(B) mettent en évidence la faible stabilité des nanopoudres sous atmosphère contrôlée. Le dépôt en film mince sur substrat de $SrTiO_3$ stabilise donc ce polymorphe et limite sa réoxydation.

La société TE-OX vise à exploiter l'expertise sur les couches minces de VO_2 acquise lors de cette thèse afin de développer des commutateurs RF activés optiquement. Des dispositifs de test ont ainsi été élaborés et caractérisés dans le cadre de la thèse, afin démontrer leurs commutations de comparer leurs performances RF aux technologies déjà existantes sur le marché. Les caractéristiques RF mesurées démontrent la faisabilité des commutateurs à base de VO_2 avec des paramètres fonctionnels très performants. Les tests d'activation optique ont démontré que le faisceau devait être suffisamment focalisé et intense pour faire transiter le VO_2. L'activation en moins de 10 ps mesurée avec un laser femtoseconde reste toutefois encourageante pour les prochaines générations de commutateur RF.

universite
PARIS-SACLAY

DOCTORAL SCHOOL
Electrical, Optical, Bio:
Physics and Engineering
(EOBE)

Title : Study of VO_2 polymorphs for microelectronics and radiofrequency devices.

Keywords : Vanadium dioxide, Epitaxy, Metal-insulator transition, Magnetron sputtering, Hydrothermal synthesis, Radiofrequency switches.

Abstract : In the communications industry, continuous efforts are made to improve device performance and increase the speed of data exchange. Historically, the components used in telecommunications have been based on semi-conductor materials. Phase change materials offer complementary and attractive properties for new electronic devices. The TE-OX® company has focused its radiofrequency (RF) activity on vanadium dioxide (VO_2), which has shown promising behavior for the manufacture of ultrafast and reliable components. The goal is to exploit the metal-insulator transition of VO_2, which takes place close to room temperature. Although VO_2 is a simple binary oxide, its belonging to a complex phase diagram where many phases with mixed stoichiometry coexist makes the obtention of this material difficult. Obtaining high quality VO_2 requires both a mastery of the growth method and a good understanding of the mechanisms leading to the formation and stabilization of this oxide.

In this work, magnetron radiofrequency sputtering and hydrothermal synthesis were used to explore the polymorphic phases of VO_2, in particular the monoclinic M1 and B phases. Structural analyses carried out mainly by X-ray diffraction (XRD) revealed that the strains in VO_2 developed during its growth were a key element in the stabilization of polymorphs, and that they could affect the transition between the M1 and rutile (R) phases. By changing the orientation and the nature of the substrate (sapphire Al_2O_3, strontium titanate $SrTiO_3$) for the growth of thin films by epitaxy, we highlight that the stabilized phase is different, and that the growth mode of the oxides is modified. In the case of growth on c-cut and r-cut sapphire substrates, the strong lattice mismatch leads to the growth of VO_2(M1) with relaxation of the epitaxy-induced stress and formation of multiple crystallographic variants. Structural, electrical, and optical transition studies have shown that the compressive strain along the $c_{VO2(R)}$-axis (= $a_{VO2(M1)}$) leads to a decrease in the temperature of the metal-insulator transition. In order to further investigate the effects of stress during the elaboration of thin layers, we studied the growth of VO_2 films on $SrTiO_3$ substrate. The physico-chemical characterizations show that the B and M1 phases can coexist within the same layer on this substrate. The work carried out by hydrothermal synthesis on VO_2(B) highlights the low stability of this phase under controlled atmosphere. The thin film deposition on $SrTiO_3$ substrate stabilizes this polymorph and limits its reoxidation.

TE-OX company aims to exploit the expertise on VO_2 thin films acquired during this thesis to develop optically activated RF switches. Test devices have been developed and characterized as part of the thesis, in order to evaluate their switching speed and to compare their RF performances to existing technologies. The measured RF characteristics demonstrate the feasibility of VO_2-based switches with very good functional parameters. Optical activation tests have demonstrated that the beam had to be sufficiently focused and intense to make VO_2 transit. The activation in less than 10 ps measured with a femtosecond laser remains encouraging for the next generations of RF switches.

Acknowledgments

This research work resulted from a partnership between the Centre for Nanoscience and Nanotechnology (C2N) and TE-OX company. I would like to express my gratefulness to the TE-OX CEO, Guy Garry, and to my thesis director, Pascal Aubert, for supporting this research work. Thank you for providing me with the opportunity and the resources to thrive during these four years.

I would like to convey my sincere gratitude towards my co-supervisors Olga Ishchenko and Thomas Maroutian. The quality of this work would not be what it is without the crucial role you both played.

Olga, I suspect that being your first PhD student has not always been easy, but I would like to thank you for your extraordinary coaching. You trusted and believed in me at all times, even in my doubtful moments. Your encouragement helped me to give my best.

Thomas, I was so fortunate to have you as my supervisor, and I would like to express my heartfelt appreciation for your encouragement, patience, and unwavering support. You're a well of knowledge and it is an enjoyment to converse with you whenever and wherever feasible. These four years have not always been easy, the blob being the proof, but you always found the right words for encouraging me. Thank you for managing to relax the atmosphere, even when the stress was felt, and especially during the writing process.

I also want to express my gratitude to all the members of the PhD jury, referees Corinne Champeaux and Mircea Gabriel Modreanu, together with examinators Aline Rougier and Brahim Dkhil, for accepting to evaluate my work. I am very thankful to them for their insightful comments and questions on my research.

I express my most sincere acknowledgment to the scientific experts of C2N who have accompanied me, advised me, often corrected me, and with whom it has always been a pleasure to work. In particular, Philippe Lecoeur, for your expertise and experience in many research domains. I will never forget that with a screwdriver, aluminum, and a bit of adhesive tape, it is possible to activate a plasma. Ludovic Largeau, for your knowledge in the reciprocal space and in XRD, which allowed me to understand the monoclinic system better. Alain Bosseboeuf, for four-probe temperature measurements. Adel Bousseksou for the FTIR formation. Thanks to you, I have successfully checked that my samples transited in temperature for the first time. Abdelkarim Ouerghi and Julien Chaste from the Mat2D team for the XPS Synchrotron and Raman measurements. Thank you for regularly checking in on me and ensuring everything went well during these thesis years.

The initial objectives of my thesis have been broadened thanks to the numerous collaborations we have carried out. For this, I thank Nicolas Guiblin and Maxime Vallet from the SPMS of CentraleSupélec, for the XRD temperature measurements and TEM preparation and analysis. Vincent Juvé from the Le Mans University for the help he gave us in the optical characterization of our layers by pump-probe experiments. Liam Floyd of Tyndall for RF measurements and Jocelyne Leroy of CEA Saclay for XPS analysis. My samples have not always been the easiest to analyze, and I hope you will not have too bad memories of VO_2.

I would also like to thank the OXIDE team members: Sylvia Matzen, Guillaume Agnus, and François

Pesty, who accompanied me during my PhD. Thank you all for the good insightful discussions and the good time during picnic group moments. I would like to give special thanks to all the doctoral students and engineers with whom I shared these thesis years. Thanks to Guillaume Chau for welcoming me into his office during the first part of the thesis. Know that our tea collection will remain engraved between the walls of the C101 office for a long time. Thanks to Florian Disdier for being an unwavering technical support during the sputtering assembly and for giving me his office after he left the team. We miss you very much. Added to this, Komalika Rani, Sopheasith Hem, Cléophanie Brochard, Stéphane Gable, Subhajit Roy, Hassan Melhem, Amine Mamouni, and Ali El Boutaybi for discussions, debates, and always entertaining meals. I also thank Romain Bude, with whom I worked with great pleasure, always in joy and good humor. Thank you for the discussions and mood, especially during the writing period. Thank you for supporting me during this second part of the thesis and especially for agreeing to fabricate my precious VO_2 switches.

Bien sûr, je n’oublie pas les membres de ma famille qui m’ont le plus soutenu depuis le début de mes études. Aucun mot ne pourrait pleinement exprimer la gratitude que j’éprouve envers vous et l’amour que je vous porte. Chaque instant, chacune de mes larmes, chaque moment de joie, mais aussi de travail vous appartiennent. Maman, Papa, merci à vous deux pour tous les efforts et les sacrifices que vous avez faits pour moi. Chaque ligne, mot et lettre expriment la reconnaissance, le respect et l’estime que je ressens pour vous.
Le dernier, mais non le moindre, Pierre, toi qui as su me soutenir et m’encourager au quotidien. Merci de m’avoir fait rire et surtout sourire dans notre petit studio. Je sais que les temps de l’écriture étaient difficiles, mais tu as toujours été mon rayon de soleil quand le ciel était gris.

Before I finish, I just want to say thank you again to everyone (even if I missed anyone unintentionally, I apologize). Today marks the end of an adventure, signaling the start of a new chapter in my life.

In memory of Thérèse Diebold and Albert Kieffer,

Contents

List of Abbreviations

VO_2	Vanadium dioxide
Al_2O_3	Aluminum oxide/Sapphire: (0001) and $(1\bar{1}02)$ correspond to c- and r-cut respectively
STO/$SrTiO_3$	Strontium Titanate oxide
OA	Oxalic acid

a, b, c and β	Lattice parameters
d_{hkl}	Interplanar distance
θ_{hkl}	Diffraction angle
FWHM	Full width at half maximum
T_{MIT}	Metal-insulator transition temperature ($T_{MIT}(VO_2) \sim 68°C$)
ΔH	Hysteresis width
E_F	Fermi level
ρ	VO_2 film resistivity
t	Film thickness
ε	Permittivity

AFM	Atomic Force Microscopy
FTIR	Fourier Transform InfraRed spectroscopy
HT	Hydrothermal
MIT	Metal-Insulator Transition
PCM	Phase change material
RF	Radiofrequency
RFMS	Radiofrequency Magnetron Sputtering
RT	Room temperature
sccm	Standard Cubic Centimeters per Minute
SEM	Scanning Electron Microscopy
TEM	Transmission Electron Microscopy
XPS	X-ray Photoelectron Spectroscopy
XRD	X-ray Diffraction

Pressure units: 10^{-2} mbar = 1 Pa = 7.5 mtorr

$$d_{hkl}(monoclinic) = \frac{1}{\sqrt{\left(\frac{h^2}{a^2} + \frac{l^2}{c^2} - \frac{2hl}{ac}\cos\beta\right)\frac{1}{\sin^2\beta} + \frac{k^2}{b^2}}}$$

Introduction

Radiofrequency (RF) switches are fundamental components for signal transport and control, commonly used in communications. These base elements must meet technological requirements such as power handling and low losses [WAI21]. Continuously increasing demand on the volume and speed of the information exchange pushes the RF industry to find new solutions to improve device performance and reduce their costs. Development of reliable, miniaturized, and low-cost technologies is the challenge for new generations of communication systems. Several technologies have been proposed over the last decades, but unfortunately, none could meet all requirements. Currently, a large part of RF devices is based on electromechanical switches (MEMS), offering sufficient performance (number of switching cycles = 10^{11}-10^{12}) [GOL95]. Unfortunately, their switching time limited to the microsecond, their complex and expensive integration, and their brittleness (membrane sticking) push the scientific community to move toward new technologies. The research on phase change materials (PCM) shows that they can be a promising solution for electronic components offering ultrafast and reliable operation [DUM07][GIV08][BOU10].

Among pioneers at European level, TE-OX® company focused its RF activities on vanadium dioxide (VO_2) which possesses a reversible metal-insulator transition (MIT) at a temperature T_{MIT}~68°C. This MIT is related to a monoclinic/rutile (M1/R) structural phase transition accompanied by a significant resistivity change by 4 to 5 orders of magnitude and optical properties modifications [MOR59]. In addition, the way for triggering the phase transition (thermal, optical, or through mechanical strain) impacts the transition rate, which opens the door to improved RF components. Beyond these attractive properties, the VO_2 belongs to a complex phase diagram with several oxides and coexistence domains, making difficult the material fabrication. A small variation of the vanadium oxidation state can conduct to the stabilization of vanadium oxides such as V_2O_3 or V_2O_5. Overall, no less than 52 stable and metastable phases have been identified, including at least 10 belonging to the VO_2 family [KAT03][YAN11]. Although many studies in the literature exist on VO_2, the numerous polymorphs (M1/R, A, B, D, etc.) hinder the understanding of growth mechanisms that would improve the quality of the obtained materials.

The industrial activities of TE-OX require to be independent in the supply of the VO_2 films that was subcontracted until now with partners in Russian Federation. Therefore, the main objective of this thesis is the establishment of an industrially scalable deposition process of high quality VO_2(M1) thin films. Such development cannot go alone without a good understanding of the material stabilization mechanisms in which the roles of the oxygen ordering and of the underlying substrate are still not fully understood. Only a tiny variation in oxygen is suspected to lead to the formation of another VO_2 polymorph. Thus, the second objective of this work is to gain a better understanding on the formation and growth of selected polymorphic phases. It is also in the scope of our research activity to open and shed light on some ways that were in the dark such as the VO_2(B) phase which presents a growing interest for energy storage applications and further development of self-powered RF components. To meet these objectives, the radiofrequency magnetron sputtering (RFMS) technique was selected for the thin film growth and the hydrothermal (HT) synthesis was used to start the investigation of VO_2(B) phase, leaning on the already established TE-OX expertise.

To step forward on an already widely studied but not fully understood material, it is fundamental to understand crystal structures and their transformations between vanadium oxides. The **First Chapter** presents the state of the art of the VO_2 family, focusing on mechanisms driving the MIT. A specific interest will be given to the substrate influence that significantly affects the phase stabilization and the material quality and is a key element of the crystalline growth. The technical development of the deposition process by RFMS is described in the **Second Chapter**, with a focus on the most significant experimental conditions and on the advanced characterization methods. The **Third Chapter** is fully dedicated to the VO_2(M1) film development on different sapphire substrates. This chapter highlights the influence of the crystallographic orientation of the sapphire on VO_2(M1) growth morphology, and on the MIT property. We carried out a detailed investigation based on X-ray diffraction (XRD) that established clearly for the first time all the epitaxial relationships between the film and the substrate.

The **Fourth Chapter** is devoted to the polymorphic VO_2(B) metastable phase. Leaning on existing expertise within TE-OX on HT synthesis, the study of this polymorph was started on nanostructures. However, this approach met limitations on the stability of this phase in nanostructure form that forced us to deviate towards the development of thin layers, with a subsequent detailed study of VO_2(B) thin film growth.

Finally, the **Fifth Chapter** gives a quality assessment of the developed materials which is directly translated in the performances of the developed and fabricated RF switches at TE-OX. The thermal activation as a well-known way to trigger the transition of the VO_2 switches was privileged. This activation mode allowed us to get the best performances in both “ON” and “OFF” states of the switches. Still, the limited activation speed of the thermal way does not exploit the full potential of the material, which presents an ultrafast transition down to femtosecond range when activated optically. To understand and develop this optical activation, exploratory pump-probe measurements were performed on the VO_2 thin films, in parallel with the optimization of test RF devices for optical activation.

Chapter 1: Oxygen ordering in Vanadium Oxides

Contents

Nowadays the telecommunication industry has emerged as one of the essentials in the modern society. Several of the most important society needs relay on the communication systems, starting from the general security and going to the everyday people information exchange without forgetting the growing demand of the Internet of Things (IOT) industry. Such continuously growing industry requires the permanent improvement of the communication systems by increasing the data exchange rate, the sustainability, and the market competitiveness. Historically, such devices rely on the semiconductor materials which are reaching their limits according to the Moor's law. The phase change materials (PCM) present an alternative to semiconductors, appealing by their ability to adapt their physico-chemical behavior in response to a stimulus. PCM emerge as a promising solution for ultrafast, reconfigurable and reliable electronic components [DUM07][GIV08][BOU10]. Among the existing PCM, vanadium oxides are distinguished from the others by their metal-insulator transition (MIT) dynamics, especially the VO_2, which has a transition temperature (T_{MIT}) close to the room temperature (RT). Unfortunately, the vanadium-oxygen (V-O) system has a wide range of oxides from oxidation states +II to +V (**Figure 1-1**), making it very difficult to obtain a given vanadium oxide as pure phase.

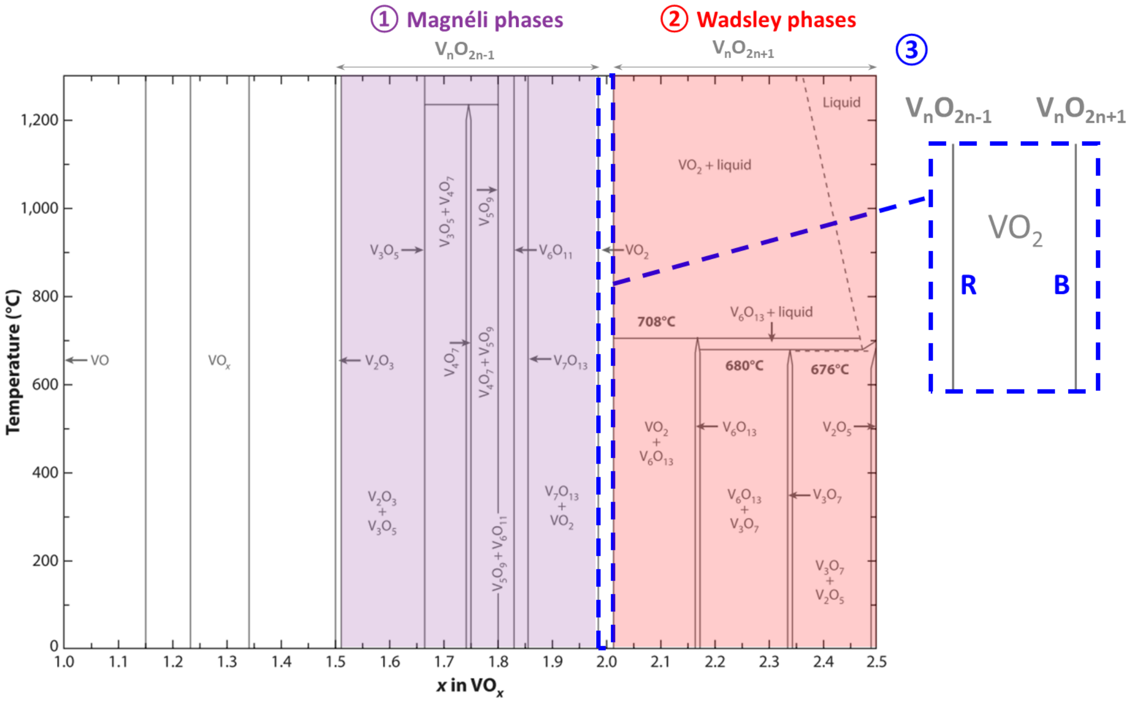

Figure 1-1: Phase diagram of VO_x system ($1.0 < x < 2.5$). Three areas are shown with vanadium oxidation states between +III and +V: ① the Magnéli phases, ② the Wadsley phases, and ③ the VO_2 [KAT03]. R and B letters stand for the rutile and B polymorphic phases of VO_2, respectively.

The phase diagram shown on **Figure 1-1** reflects the V-O system complexity, especially since each oxide may coexist with other oxides to create intermediate or mixed phases. No less than 52 stable and metastable oxides have been identified, including at least 10 belonging to the VO_2 [YAN11]. According to the vanadium oxidation state, the vanadium oxides form three distinct families. The first one is composed of Magnéli phases (V_nO_{2n-1}) with the vanadium oxidation state between +III and +IV. The second one comprises Wadsley phases (V_nO_{2n+1}) with an oxidation state between +IV and +V. Finally, in the middle zone, at the boundary between Magnéli and Wadsley phases, we find VO_2. Most of these vanadium oxides exhibit a MIT in the temperature range from -200 to 200°C (**Table 1-1**) [SCH04]. These metal-insulator transitions induce an important change in structural, electronic, and optical properties and offer a wide application potential such as optical and electronic switching devices, memory elements [LEE11], smart windows, and cathode materials for batteries [NI11].

Table 1-1: Transition temperature in vanadium oxides [SCH04].

Oxide	Transition temperature (°C)
VO_2(B)	-123
VO_2(R/M1)	68
V_6O_{11}	-103
V_4O_7	-23
V_3O_5	157
V_2O_3	-105

Mechanisms responsible for the transition in PCM are not fully understood despite the fact that they have been widely studied [BUR69][WAD63]. We believe that it is fundamental to understand crystal structures and involvement of the stoichiometry in the transformations existing between vanadium oxides to step forward on the material and device mastery. Consequently, this chapter firstly presents the state of the art of the $V_nO_{2n\pm1}$ families with a specific interest on the oxygen ordering. Then, the structures of the $VO_{2\pm\delta}$ family will be investigated with the objective to disclose the features explaining the phase transition. Finally, the last part of this chapter will be focused on the influence of the underlying substrate on the phase stabilization and its impact on the crystalline quality of the material.

1.1. Vanadium oxides: from Magnéli to Wadsley

The vanadium-oxygen system, consisting of Magnéli, VO_2, and Wadsley phases, has several coexistence domains, that originate from morphotropic transformations. These transformations are characterized by a structural change and occur between two neighboring homogeneous phases with different but close stoichiometries [KAT03]. We believe that key insights on the formation and stabilization of vanadium oxides, and especially of VO_2 polymorphs, can be gained by understanding the structural changes caused by different oxygen layouts in these oxides. Thus, this part is devoted to the exploring of Magnéli and Wadsley phases, whose symmetries are governed by a common structure [GEO56] [HOR76][MAR72].

1.1.1. The Magnéli phases

Magnéli phases encompass the vanadium oxides between V_2O_3 and VO_2, according to the vanadium-oxygen diagram (**Figure 1-1**). This area contains seven pure and five intermediate phases and can be described by the general formula (1.1) [SCH04]:

$$V_nO_{2n-1} = V_2O_3 + (n-2)VO_2 \text{ with } 3 \leq n \leq 9 \tag{1.1}$$

According to the literature [KAT03][SCH04][KAT03b][KAT03c], the Magnéli phases are related to the corundum-type structure of V_2O_3 (a_{V2O3}= b_{V2O3}, c_{V2O3}, γ=120°) and to the rutile-type structure of VO_2 ($a_{VO2(R)} = b_{VO2(R)}$, $c_{VO2(R)}$). To enable a direct comparison of structures, the tetragonal rutile unit cell of VO_2 is transformed into a supercell (SC) with $a_{SC} = 4c_{VO2(R)}$, $b_{SC} = a_{VO2(R)}$ and $c_{SC} = 3b_{VO2(R)}$, and the V_2O_3 into a supercell with $a_{SC} = 2a_{V2O3} + b_{V2O3}$, $b_{SC} = b_{V2O3}$ and $c_{SC} = c_{V2O3}$.

The transformation can be described with the help of these supercells represented in **Figure 1-2**. The oxygen atoms removed by the reduction process are illustrated in white in the VO_2 structure.

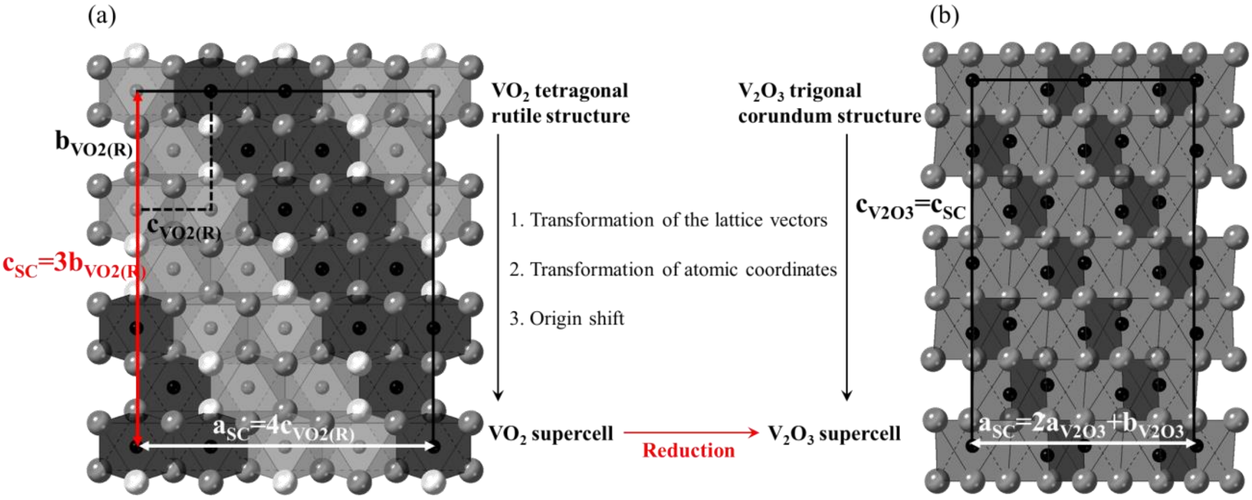

Figure 1-2: Transformation between the VO_2 rutile structure (left) and V_2O_3 corundum structure (right) projected along b_{sc}. Dashed lines show the tetragonal cell of $VO_2(R)$ and solid lines show both supercells. V atoms in black and O atoms in grey, O atoms removed by the reduction mechanism in white [KAT03c].

The reduction of VO_2 into V_2O_3 induces a rutile to corundum type transformation. It creates oxygen vacancies (O atoms removal by reduction from V^{+4} to V^{+3}), and further condensation of the structure occurs by crystallographic shear to eliminate the vacant sites and compensate for the oxygen deficiency. The crystallographic shear planes are parallel to (400) rutile supercell ($VO_2(R)/SC$) and the shear operation (400) [1/8 -1/2 0] can be described in the original rutile cell by respecting the transformations for (hkl) planes and [uvw] directions of eq.(1.2) [KAT03c].

$$\begin{aligned} (\mathrm{hkl})_{\mathrm{VO2(R)/SC}} * \begin{pmatrix} 0 & 0 & \frac{1}{4} \\ 1 & 0 & 0 \\ 0 & \frac{1}{3} & 0 \end{pmatrix} &= \left(\mathrm{k}\,\frac{\mathrm{l}}{3}\,\frac{\mathrm{h}}{4}\right)_{\mathrm{VO2(R)}} \\ \begin{bmatrix} \mathrm{u} \\ \mathrm{v} \\ \mathrm{w} \end{bmatrix}_{\mathrm{VO2(R)/SC}} * \begin{pmatrix} 0 & 1 & 0 \\ 0 & 0 & 3 \\ 4 & 0 & 0 \end{pmatrix} &= \begin{bmatrix} \mathrm{v} \\ 3\mathrm{w} \\ 4\mathrm{u} \end{bmatrix}_{\mathrm{VO2(R)}} \end{aligned} \qquad (1.2)$$

After transformation, the crystallographic shear operator becomes (001) $1/2[\bar{1}01]$ in the original rutile cell. Throughout this transformation, not only is the structure modified but a variation in stoichiometry appears. This change in stoichiometry is at the origin of the Magnéli phases between VO_2 and V_2O_3. To simplify, the Magnéli phases are represented as phases having a distortion of the rutile lattice due to an oxygen deficiency and are intermediate between the VO_2 and V_2O_3 structures of the V-O system. Therefore, the Magnéli phases have a triclinic crystal structure derived from the rutile structure of VO_2, the transformations of which can be obtained by the same steps as for the rutile/corundum transformation: transformation of native systems in supercells, then reduction, and finally crystallographic lattice matching. The general transformation of the lattice unit vectors is described by eq.(1.3), and eq.(1.4) gives the change of atomic coordinates.

$$(\mathbf{a_{Ma}}, \mathbf{b_{Ma}}, \mathbf{c_{Ma}}) = \left(\mathbf{a_{VO2(R)}}, \mathbf{b_{VO2(R)}}, \mathbf{c_{VO2(R)}}\right) * \mathrm{P}$$
$$(\mathbf{a_{Ma}}, \mathbf{b_{Ma}}, \mathbf{c_{Ma}}) = \left(\mathbf{a_{VO2(R)}}, \mathbf{b_{VO2(R)}}, \mathbf{c_{VO2(R)}}\right) * \begin{pmatrix} 1 & \bar{1} & 0 \\ 0 & 1 & \mathrm{n} \\ \bar{1} & \bar{1} & \bar{\mathrm{n}} \end{pmatrix} \tag{1.3}$$

Where *$(a_{VO2(R)}, b_{VO2(R)}, c_{VO2(R)})$* and *$(a_{Ma}, b_{Ma}, c_{Ma})$* are respectively the basis vectors of the original rutile cell and of the transformed triclinic cell (corresponding to the supercell described previously).

$$\begin{pmatrix} \mathrm{x_{Ma}} \\ \mathrm{y_{Ma}} \\ \mathrm{z_{Ma}} \end{pmatrix} = \mathrm{Q} * \begin{pmatrix} \mathrm{x} \\ \mathrm{y} \\ \mathrm{z} \end{pmatrix}_{VO2(R)}$$
$$\begin{pmatrix} \mathrm{x_{Ma}} \\ \mathrm{y_{Ma}} \\ \mathrm{z_{Ma}} \end{pmatrix} = \begin{pmatrix} 0 & \bar{1} & \bar{1} \\ \bar{1} & \bar{1} & \bar{1} \\ \frac{1}{\mathrm{n}} & \frac{2}{\mathrm{n}} & \frac{1}{\mathrm{n}} \end{pmatrix} * \begin{pmatrix} \mathrm{x} \\ \mathrm{y} \\ \mathrm{z} \end{pmatrix}_{VO2(R)} \tag{1.4}$$

Where *$(x, y, z)_{VO2(R)}$* and *(x_{Ma}, y_{Ma}, z_{Ma})* are atomic coordinates in the rutile cell and in the triclinic cell, respectively. From eq.(1.3) and (1.4), the structures of Magnéli phases can be compared with the structure of VO_2, and a general structural relationship can be written as:

$$\begin{aligned} \mathrm{a_{Ma}} &= \mathrm{a_{VO2(R)}} - c_{\mathrm{VO2(R)}} \\ \mathrm{b_{Ma}} &= -\mathrm{a_{VO2(R)}} + \mathrm{b_{VO2(R)}} - \mathrm{c_{VO2(R)}} \\ \mathrm{c_{Ma}} &= \frac{1}{2}(2\mathrm{n} - 1)(\mathrm{b_{VO2(R)}} - \mathrm{c_{VO2(R)}}) \end{aligned} \tag{1.5}$$

From eq.(1.5), it is possible to describe all V_nO_{2n-1} structures with $4 \leq n \leq 9$ starting from the rutile structure of VO_2 except V_3O_5. For the latter phase, a_{Ma} in eq.(1.5) is twice as large, as to get V_3O_5 by chemical reduction of VO_2, 4 oxygen atoms per VO_2 cell must be removed. **Table 1-2** summarizes all the Magnéli phase structures.

Table 1-2: Triclinic structure of the Magnéli phases obtained from the transformation of the rutile structure [KAT03]. VO_2(R) and Magnéli structures are related by their supercell transformation.

Oxide	Basis vectors	Unit cell volume
VO_2(R)	$\mathbf{a_{VO2(R)}} \equiv \mathbf{a_R}$, $\mathbf{b_{VO2(R)}} \equiv \mathbf{b_R}$, $\mathbf{c_{VO2(R)}} \equiv \mathbf{c_R}$	V_R
V_9O_{17}	$a_{Ma}=\mathbf{a_R}-\mathbf{c_R}$, $b_{Ma}=\mathbf{b_R}-\mathbf{a_R}-\mathbf{c_R}$, $c_{Ma}=\frac{17}{2}(\mathbf{b_R}-\mathbf{c_R})$	$\frac{17}{2}V_R$
V_8O_{15}	$a_{Ma}=\mathbf{a_R}-\mathbf{c_R}$, $b_{Ma}=\mathbf{b_R}-\mathbf{a_R}-\mathbf{c_R}$, $c_{Ma}=\frac{15}{2}(\mathbf{b_R}-\mathbf{c_R})$	$\frac{15}{2}V_R$
V_7O_{13}	$a_{Ma}=\mathbf{a_R}-\mathbf{c_R}$, $b_{Ma}=\mathbf{b_R}-\mathbf{a_R}-\mathbf{c_R}$, $c_{Ma}=\frac{13}{2}(\mathbf{b_R}-\mathbf{c_R})$	$\frac{13}{2}V_R$
V_6O_{11}	$a_{Ma}=\mathbf{a_R}-\mathbf{c_R}$, $b_{Ma}=\mathbf{b_R}-\mathbf{a_R}-\mathbf{c_R}$, $c_{Ma}=\frac{11}{2}(\mathbf{b_R}-\mathbf{c_R})$	$\frac{11}{2}V_R$
V_5O_9	$a_{Ma}=\mathbf{a_R}-\mathbf{c_R}$, $b_{Ma}=\mathbf{b_R}-\mathbf{a_R}-\mathbf{c_R}$, $c_{Ma}=\frac{9}{2}(\mathbf{b_R}-\mathbf{c_R})$	$\frac{9}{2}V_R$
V_4O_7	$a_{Ma}=\mathbf{a_R}-\mathbf{c_R}$, $b_{Ma}=\mathbf{b_R}-\mathbf{a_R}-\mathbf{c_R}$, $c_{Ma}=\frac{7}{2}(\mathbf{b_R}-\mathbf{c_R})$	$\frac{7}{2}V_R$

V_3O_5	$a_{Ma}=2(\mathbf{a_R}-\mathbf{c_R})$, $b_{Ma}=\mathbf{b_R}-\mathbf{a_R}-\mathbf{c_R}$, $c_{Ma}=\frac{5}{2}(\mathbf{b_R}-\mathbf{c_R})$	$5V_R$

From the **Table 1-2**, we see that the unit-cell volume of all the oxides can be expressed as function of the rutile phase volume V_R by $[(2n-1)/2]V_R$ for $4 \leq n \leq 9$ and $(2n-1)V_R$ for $n = 3$. Consequently, the VO_2(R) can be interpreted as the parent structure of Magnéli phases by successive transitions. A similar description was given by Hirotsu *et al.* of Magnéli phases [HIR78], which can be considered as a periodic modulation of VO_2 where one oxygen layer is removed every n^{th} V layer in the direction perpendicular to the $(211)_{VO2(R)}$ plane.

1.1.2. The Wadsley phases

In the V-O system, VO_x oxides where $2 \leq x \leq 2.5$ are known as Wadsley phases and can be defined by V_nO_{2n+1} with n=2, 3, and 6. Contrary to the Magnéli phases, the Wadsley phases have an excess of oxygen compared to VO_2 and the V oxidation state is between +IV and +V. The crystal structures of V_2O_5 [ENJ86], V_3O_7 [WAL74], V_6O_{13} [BER03], and VO_2(B) [THE76] which belong to the Wadsley phases can all be described as a face-centered cubic (fcc) structure with oxygen excess, based on the fcc structure of VO_x ($x \approx 1$). **Table 1-3** summarizes the crystallographic structures of Wadsley phases.

Table 1-3: Crystallographic structure of the Wadsley phases expressed with respect to the VO_x ($x \approx 1$) unit cell ($\mathbf{a}_x$, $\mathbf{b}_x$, $\mathbf{c}_x$) [KAT03].

Oxide	**Basis vectors**	**Unit cell volume**
VO_x	$\mathbf{a}_x$, $\mathbf{b}_x$, $\mathbf{c}_x$	V_x
V_2O_5	$3\mathbf{a}_x$, $\mathbf{b}_x$, $\mathbf{c}_x$	$3V_x$
V_3O_7	$6\mathbf{a}_x$, $\mathbf{b}_x$, $5\mathbf{c}_x$	$30V_x$
V_6O_{13}	$3\mathbf{a}_x$, $\mathbf{b}_x$, $3\mathbf{c}_x$	$9V_x$
VO_2(B)	$3\mathbf{a}_x$, $\mathbf{b}_x$, $2\mathbf{c}_x$	$6V_x$

As for Magnéli phases, Wadsley phases are fcc structures with oxygen vacancy layers. This can be seen as a closed packed stacking (ABC) of hexagonal layers. Each V_nO_{2n+1} structure has a specific oxygen vacancy concentration $(1-x_O) = \frac{1}{6}(V_2O_5), \frac{5}{18}(V_6O_{13}), 0.3(V_3O_7)$ and $\frac{1}{3}(VO_2(B))$, where x_O is the concentration of oxygen (**Figure 1-3**). These oxygen vacancy layers link Wadsley phases with one another and separate them from their VO_x parent structure [PAU90].

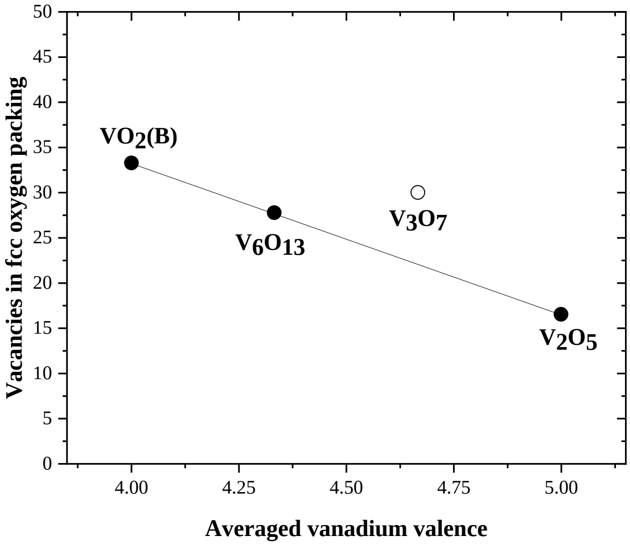

Figure 1-3: Oxygen vacancies (at%) in function of the average vanadium valence [KAT03].

During the transition from V_2O_5 to V_3O_7, V_6O_{13}, and finally VO_2(B), a crystallographic shear appears along the $\vec{c}$-axis and removes empty oxygen layers. This conducts to a deformation of the initial V_2O_5 structure. The V_6O_{13} is deduced from V_2O_5 by deleting one plane out of three in the (001) family which contains only oxygen atoms. Then the stacking of the layers tends to compact by deleting one out of two planes of V_6O_{13} to end up with VO_2(B) which presents itself as the boundary structure of the Wadsley phases. Below this in oxygen concentration, the Magnéli phases begin.

1.1.3. From Magnéli to Wadsley: The VO_2

We saw that in the range of vanadium oxides from Magnéli to Wadsley the intermediate link is the VO_2, with the VO_2(R) and VO_2(M1) polymorphs related to Magnéli phases and VO_2(B) to Wadsley phases. These polymorphs have similar stoichiometry (VO_2) but different crystalline structures. Based on an oxygen body-centered cubic lattice, the VO_2 polymorphic phases always have a vanadium atom in an octahedral site (VO_6). Depending on the structure, the oxygen octahedra can be aligned either along two perpendicular directions, such as in VO_2(R), or along only one direction as in VO_2(B) [LER98]. **Figure 1-4** shows the crystallographic structures of VO_2(R) and VO_2(B). In VO_2(B), the structure is formed by two identical layers of atoms along the $\vec{b}_{VO2(B)}$-axis so that the second layer is shifted by $(\frac{1}{2}, \frac{1}{2}, 0)$ with respect to the first one, making this structure look like the one of V_6O_{13}. This contributes to make VO_2(B) have a less stable structure than VO_2(R). Although no relationship has been found between different domains of the vanadium-oxygen system, the works of Théobald [THE76] and Leroux *et al.* [LER98] have demonstrated, under specific conditions (low pressure and heating), that VO_2(B) can transform into VO_2(R), with appearance of oxygen vacancies. A link between the Magnéli and Wadsley phases is thus highlighted. To better understand the different domains of the vanadium-oxygen system, it is necessary to focus on the ordering of oxygen in V oxides.

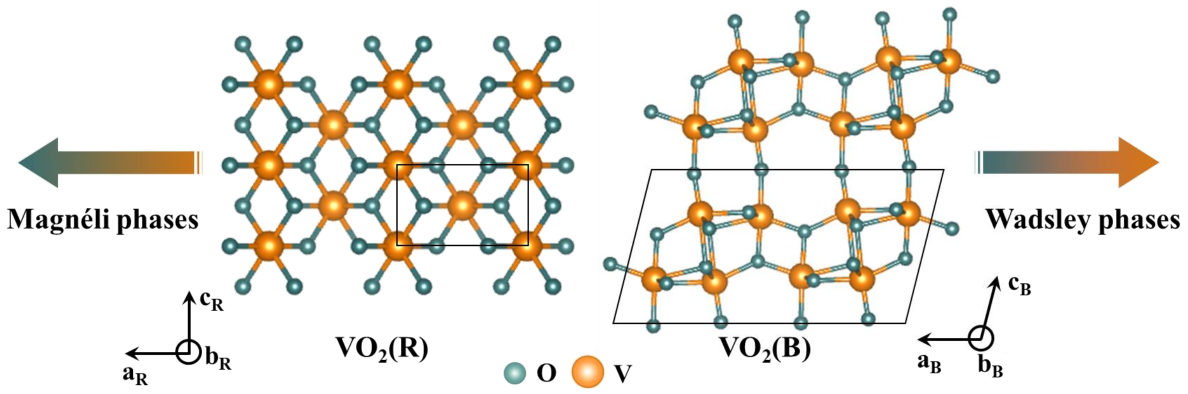

Figure 1-4: Crystal structures of $VO_2(R)$ and $VO_2(B)$ which are the limiting phases of the Magnéli and Wadsley phases, respectively.

1.2. Vanadium dioxide: polymorphism study

The VO_2 is known as the limiting oxide between the Magnéli and Wadsley phases and it is one of the most studied vanadium oxides due to its polymorphism. The polymorphism is the ability of a material to crystallize in different structures while retaining the same chemical composition. Each one of the crystalline structures has its properties and may be of interest for totally different applications. In the case of VO_2, there are no less than 10 polymorphs listed to date [YAN11]. This wide range of structures with different properties makes this oxide attractive to research and to development of new applications. In this part, we focus mainly on the R, M1, B, and A polymorphs of VO_2 that possess a structural transition when applying a stimulus. The other phases of VO_2 will just be brushed upon.

1.2.1. $VO_2(R)$: Magnéli limiting structure

Among the VO_2 polymorphs, the R phase has the highest symmetry structure. It belongs to space group $P4_2/mnm$ (136) with tetragonal parameters $a_{VO2(R)} = b_{VO2(R)} = 4.554$ Å and $c_{VO2(R)} = 2.85$ Å [WHA74]. In this phase, each vanadium atom has 6 equidistant bonds with 6 oxygen atoms and forms an octahedron with VO_6 coordination. The interatomic distances between vanadium and oxygen atoms being equal, strong electrostatic interactions between ions and electrons located in the *d*-orbital make the $VO_2(R)$ a highly correlated electron system. Known as the parent structure of the Magnéli phases, the $VO_2(R)$ has been of interest for many years due to its reversible MIT transition close to ambient conditions T_{MIT}~68 °C.

When $T<T_{MIT}$, the vanadium atoms come together to form V-V metal bonds. This dimerization of vanadium atoms along the $\vec{c}_{VO2(R)}$-axis forms a zig-zag lattice chain with long (3.16 Å) and short (2.61 Å) V-V distances [SCH04][MAR72][EYE02]. This lattice distortion leads to a lowering of the $VO_2(R)$ symmetry towards a monoclinic structure. The $VO_2(M1)$ is the most common VO_2 phase. It belongs to the space group $P2_1/c$ (14) with monoclinic parameters $a_{VO2(M1)} = 5.752$ Å, $b_{VO2(M1)} = 4.526$ Å, $c_{VO2(M1)} = 5.382$ Å, and $\beta_{VO2(M1)} = 122.602°$. **Figure 1-5** gives a schematic representation of $VO_2(R)$ and $VO_2(M1)$ crystallographic structures.

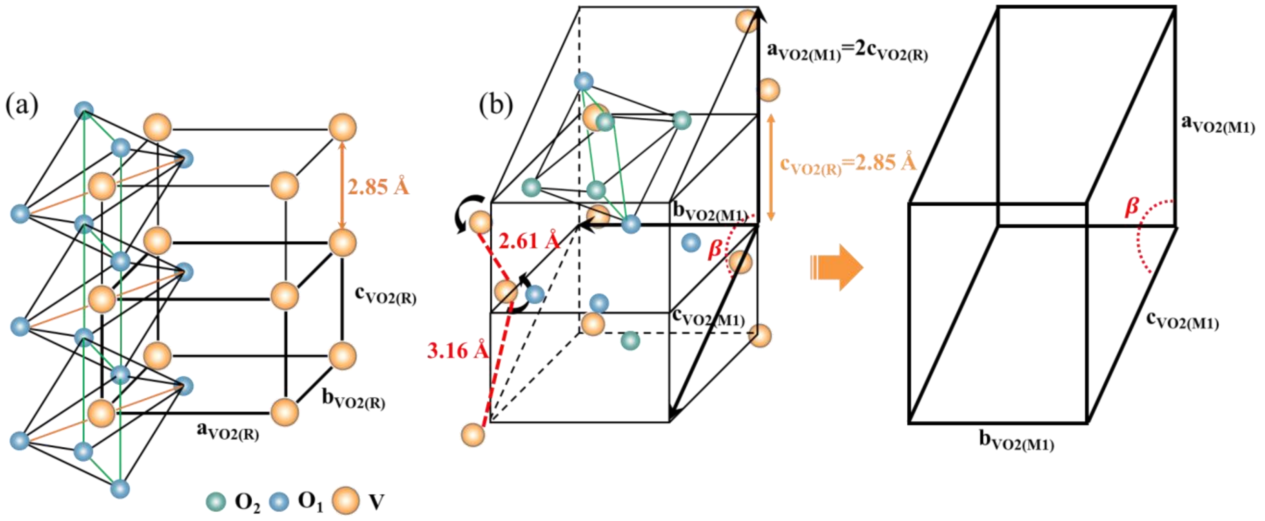

Figure 1-5: (a) VO_2(R) lattice structure above T_{MIT} and (b) relation between VO_2(R) and VO_2(M1) unit cells, with the VO_2(M1) monoclinic structure below T_{MIT} given on the right.

To better understand the relationship between M1 and R structures of VO_2, it is possible to describe the R structure in the framework of M1 using the following equation [LER98][LIU15]:

$$\begin{pmatrix} a \\ b \\ c \end{pmatrix}_{VO2(R)M1} = \begin{pmatrix} 0 & 0 & 2 \\ 1 & 0 & 0 \\ 0 & 1 & -1 \end{pmatrix} * \begin{pmatrix} a \\ b \\ c \end{pmatrix}_{VO2(R)}$$

$$\begin{cases} a_{R(M1)} = 5.70\ \text{Å} \\ b_{R(M1)} = 4.554\ \text{Å} \\ c_{R(M1)} = 5.37\ \text{Å} \\ \beta_{R(M1)} = 122.04° \end{cases} \tag{1.6}$$

The slight difference between these calculated parameters of the R phase in the M1 unit cell and those of the M1 phase given above comes from the fact that the reference samples for their respective JCPDS datasheets were not the same ones. According to eq.(1.6), the relationships between R and M1 lattice parameters are $\boldsymbol{a_{VO2(M1)} = 2c_{VO2(R)}}$, $\boldsymbol{b_{VO2(M1)} = a_{VO2(R)}}$, and $\boldsymbol{c_{VO2(M1)} = b_{VO2(R)} - c_{VO2(R)}}$.

Due to the modification of crystallographic structure of R to M1 (or reversely), the MIT of VO_2 in response to various stimuli such as optical [WEG15], thermal [MOR59], electrical or stress [CHE17] excitation is accompanied by a radical change in physical properties (electrical resistance, optical transmission, and thermal conductivity). The transition time scale varies according to the stimulus applied, in case of thermal activation it is from milliseconds to microseconds, while for the optical one it can be down to 100 femtoseconds. The optical activation makes VO_2 even more attractive for new-generation electronic and optical devices. In the following, the evolution of the electrical and optical properties of VO_2 will be described as a function of temperature.

As we can see on **Figure 1-6**, resistivity curves during heating (red curve) and cooling (blue curve) do not overlap and create a hysteresis cycle. In physics, a hysteresis cycle is defined as a shift or delay in the evolution of one physical phenomenon with respect to another. For this hysteresis, various characteristics can be determined such as transition temperature given by eq.(1.7) and hysteresis width (ΔH) given by eq.(1.8).

$$\mathrm{T_{MIT}} = \frac{\mathrm{T_{down}} + \mathrm{T_{up}}}{2} \tag{1.7}$$

Where T_{down} and T_{up} are the maxima of the first derivative of resistivity, and for VO_2 T_{MIT}~68°C.

$$\Delta\mathrm{H} = \mathrm{T_{up}} - \mathrm{T_{down}} \tag{1.8}$$

Finally, the hysteresis is also characterized by its amplitude (A), which corresponds to the resistivity ratio between the insulating state (ρ_{up}) and the metallic state (ρ_{down}) of VO_2.

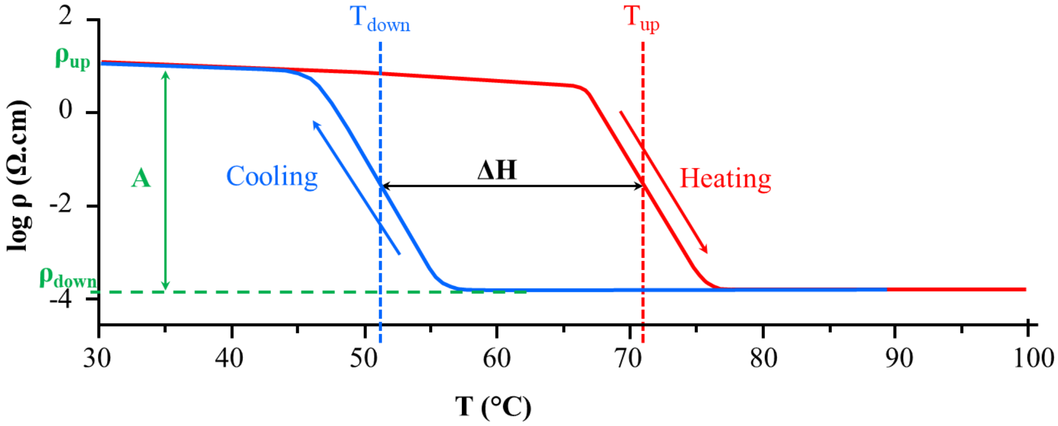

Figure 1-6: Schematic hysteresis of VO_2 electrical resistivity evolution with temperature.

Besides the resistivity change upon the electrical transition, the optical extinction coefficient k undergoes also a drastic change. In its insulating state, VO_2 is transparent in the infrared (IR) range, and it becomes opaque and reflective in its metallic state. By measuring reflectivity or transmittance in the IR domain as function of temperature, it is possible to observe the hysteresis cycle characteristic of VO_2 [VIC21][BUT18][PET16]. Whether optically or electrically, the MIT of VO_2 is characterized by its hysteresis cycle. The hysteresis width is a key parameter of the thin film quality, narrower is the width and higher is the film quality up to the single-crystal properties [DUC72][MOR59].

1.2.2. VO_2(B): Wadsley limiting structure

First reported in 1976 by Théobald *et al.* [THE76], VO_2(B) is one of the metastable VO_2 polymorphs, obtained by a reduction (hydrothermal treatment) of V_2O_5. This oxide belongs to space group C*2/m* (12) with monoclinic parameters $a_{VO2(B)} = 12.03$ Å, $b_{VO2(B)} = 3.693$ Å, $c_{VO2(B)} = 6.42$ Å, and $\beta_{VO2(B)} = 106.6°$. Its structure can be considered as formed by two identical layers of atoms along the $\vec{b}_{VO2(B)}$-axis, whose second layer is shifted with respect to the first one by a translation vector $(\frac{1}{2}, \frac{1}{2}, 0)$. **Figure 1-7** shows the arrangement of octahedra in the $(010)_{VO2(B)}$ plane. Due to the off-centering of V ions and their two available sites V(1) and V(2), VO_6 octahedra are deformed. In (110) plane, the bonds between V(1) and V(2) ions form long and short zig-zag chains with an offset of $(\frac{1}{2}, \frac{1}{2}, 0)$. The connections of the octahedra with the neighboring layers having this offset, channels are created with weaker bonds along the $\vec{c}_{VO2(B)}$-axis, that offer a possibility to intercalate atoms.

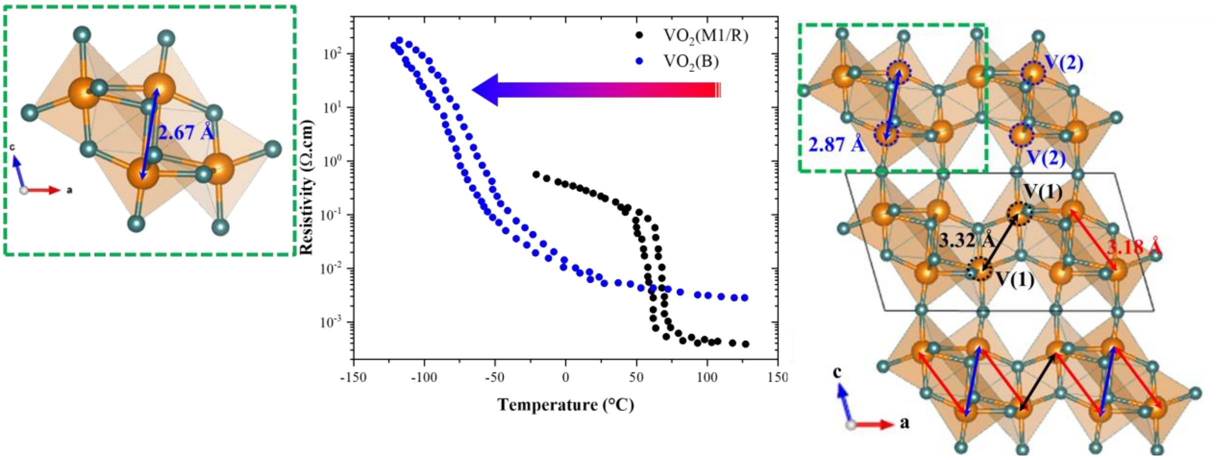

Figure 1-7: Structural transition of VO$_2$(B) between RT phase (right) and low temperature phase (left). Vanadium atoms in orange, and oxygen in green. The transition is accompanied by a resistivity change (middle panel), here compared to the one of the VO$_2$(M1) phase [QU11].

Similar to other vanadium oxides, VO$_2$(B) undergoes a structural transition at low temperature and accompanied by a modification of its properties. At RT, VO$_2$(B) presents the high temperature phase (HTP). During cooling (from RT to -123°C), half of the V ions move in the ac-plane, causing a shortening of V(2)-V(2) distance. The $\vec{c}_{VO2(B)}$-axis contraction conducts to an expansion of the $\vec{a}_{VO2(B)}$- and $\vec{b}_{VO2(B)}$-axes and increases the monoclinic angle. The low temperature monoclinic form (LTP) appears [OKA93]. This crystallographic transition is accompanied by a change in physical properties like for VO$_2$(R), as shown in **Figure 1-7** for the electrical resistivity. VO$_2$(B) is considered as a semi-metal at RT and exhibits a 4 orders of magnitude change in resistivity during cooling. Around -150°C, it is considered to be in an insulator state.

Although VO$_2$(B) has been known since the 70s, the interest for this oxide gained momentum with the growing demand in energy storage technologies (batteries, supercapacitors, etc.) [LEE17]. There is thus a need to develop more efficient energy storage materials, that offer bigger capacity and longer cycling endurance, as viable alternatives to current technologies. For the next-generation devices, miniaturization without losing electrochemical performance is challenging. Numerous efforts were undergone to maximize the specific surface area, in particular by using nanostructures. The Wadsley phases of vanadium oxides (e.g., VO$_2$(B), V$_6$O$_{13}$ or V$_2$O$_5$) are considered to have high potential as electrode for Li ion batteries (LIB) due to their crystalline structure. VO$_2$(B) presents one out of 3 vacant fcc layers along $\vec{c}_{VO2}$-axis, the so-called channels, expected to give both high capacity and rapid Li-ion diffusion. The work of Li *et al.* [LI94] has suggested for the first time, a high potential for VO$_2$(B) electrodes, with theoretical capacity and energy density (323 mAh/g) higher than those of state-of-the-art LIB electrodes, such as V$_2$O$_5$ (294 mAh/g) and LiFePO$_4$ (165 mAh/g) [LEE17] [LIU17][ZHA20]. However, despite many attempts with various nanostructures such as nanobelts, nanowires, or nanorods, there was no successful experimental confirmation of these properties. A rapid and irreversible loss of capacitance was observed in VO$_2$(B) electrodes. VO$_2$(B) being a metastable phase easily forms a mixed phase with other VO$_2$ polymorphs and/or other vanadium oxides with oxidation states other than V^{4+}. It is thus possible that its poor performance as LIB electrode could be attributed to extrinsic factors, such as structural defects, amorphous phases, and mixed orientations for example. To increase the stability of the B phase, one of the solutions considered is to grow it as a thin layer. The idea is to freeze the phase in its metastable structure by substrate lattice-induced stress. However, in thin film form, the specific surface of the material being reduced should lower the materials performance. The work conducted in 2017 by the Oak Ridge National Laboratory opened the door to possible battery application of VO_2(B) films that can hold up to 200 charge/discharge cycles [LEE17]. This cycling performance is the best reported in the literature for VO_2(B) electrodes, to our knowledge, and is very promising for energy storage.

1.2.3. VO_2(A): An intermediate phase?

The VO_2(A) is another VO_2 polymorph phase that was described by Théobald [THE77]. It crystallizes in tetragonal symmetry with cell parameters $a_{VO2(A)} = b_{VO2(A)} = 8.45$ Å, $c_{VO2(A)} = 7.686$ Å, space group *P4₂/ncc* (130), and appears as one possible intermediate phase in the transition from VO_2(B) to VO_2(R). In the same way as these two phases, VO_2(A) possesses a crystallographic structure comprised of a framework of edge-sharing VO_6 octahedra along the $\vec{c}_{VO2(A)}$-axis with alternating lateral offsets in the *ab* plane [POP14]. **Figure 1-8**(a) shows the octahedra arrangement in $(001)_{VO2(A)}$ plane. In the $(110)_{VO2(A)}$ plane, the bonds between V^{4+}-V^{4+} ions form long and short zig-zag chains along $\vec{c}_{VO2(A)}$-axis. Combined to the off centering of V ion, VO_6 octahedra are deformed. However, VO_2(A) remains more symmetrical than VO_2(B).

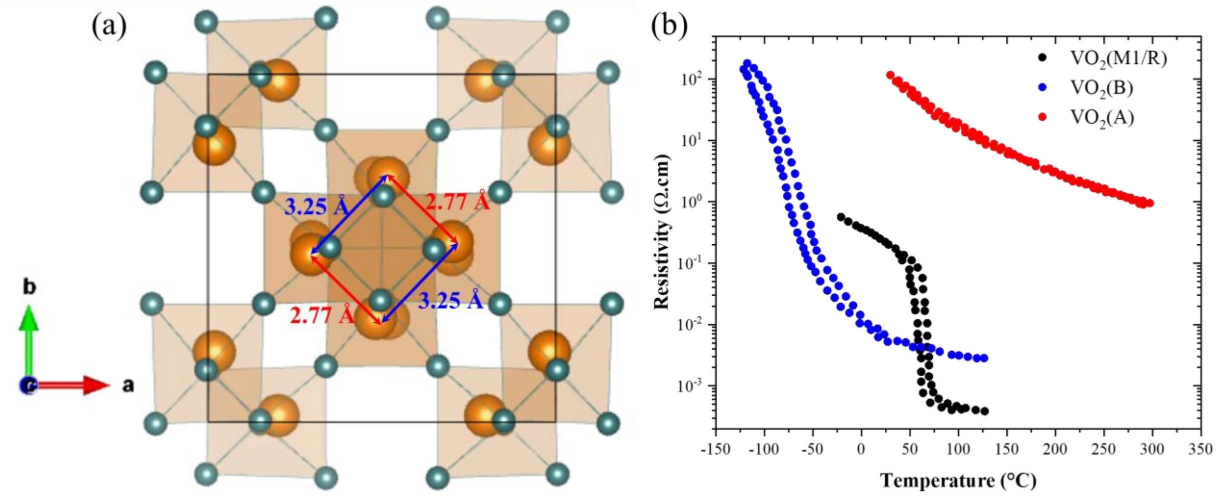

Figure 1-8: (a) VO_2(A) structure, with vanadium atoms in orange and oxygen ones in green, and (b) its electrical properties compared to other VO_2 polymorphic phases [QU11].

Since its discovery in 1977, few studies have focused on understanding the growth mechanism of this polymorph. Oka *et al.* in 1998 [OKA98] evidenced a metal-insulator phase transition at high temperature (T_{MIT}=162°C). At RT, VO_2(A) is in its so-called low-temperature form (LTP) with zig-zag chains along $\vec{c}_{VO2(A)}$-axis like **Figure 1-8**(a). During heating (from RT to 162°C), the V-atoms are rearranging to from a straight line with an equal distance between neighboring V^{4+} of 3.08 Å, thus forming the high-temperature phase (HTP) [POP14]. The lattice parameter $a_{VO2(A)}$ slightly increases from LTP to HTP phase while $c_{VO2(A)}$ lattice parameter is nearly halved (eq.(1.9)).

$$\begin{gathered} a_{VO2(A)HTP} \approx a_{VO2(A)LTP} \\ c_{VO2(A)HTP} \approx \frac{1}{2} c_{VO2(A)LTP} \end{gathered} \tag{1.9}$$

With $(a_{VO2(A)LTP}, c_{VO2(A)LTP})$ and $(a_{VO2(A)HTP}, c_{VO2(A)HTP})$ being the lattice parameters of LTP and HTP, respectively.

At 200°C, $VO_2(A)$ crystallizes in the *I4/m* (87) space group with cell parameters $a_{VO2(A)} = b_{VO2(A)} = 8.476$ Å, $c_{VO2(A)} = 3.824$ Å. The transition between LTP to HTP leads not only to a structural change of $VO_2(A)$ but also to a change in electrical properties. However, the electrical properties reported by Srivastava *et al*. in 2015 [SRI15] did not show such spectacular resistivity change as for $VO_2(M1/R)$. The $VO_2(A)$ always keeps an insulating behavior with a resistivity change of 2 orders of magnitude between LTP and HTP (**Figure 1-8**(b)). However, a lack of information on this polymorph limits its understanding.

1.2.4. Other phases of VO_2

As we have seen throughout this section, VO_2 exhibits several structures with various connectivities of the octahedral-site vanadium ions and different atomic arrangements. Obtaining and stabilizing these phases being difficult, the understanding of growth and of the transformation mechanisms were hindered for many years. Many efforts have been focused since the 2010s on the understanding of existing transformations by using soft chemistry synthesis and especially by hydrothermal synthesis [QU11][LIU12][SON16]. This method allows to easily obtain metastable phases with the possibility to adjust their morphology by various experimental conditions. **Table 1-4** lists the most known VO_2 polymorphs and the associated crystallography data.

Table 1-4: Crystallographic data of VO_2 polymorphs.

Polymorphs	Space Group	Unit cell volume				Reference (JCPDS data)
		a (Å)	b (Å)	c (Å)	α, β, γ	
$VO_2(R)$	*P 4₂/mnm*	4.554	4.554	2.85	α=β=γ=90°	00-044-0253,
$VO_2(M1)$	*P 2₁/c*	5.752	4.526	5.382	β=122.6°	01-082-0661
$VO_2(M2)$	*C 2/m*	9.083	5.763	4.532	β=91.3°	00-033-1441
$VO_2(A)$	*P 4₂/nmc*	8.450	8.450	7.686	α=β=γ=90°	00-042-0876
$VO_2(B)$	*C 2/m*	12.03	3.693	6.42	β=106.6°	00-031-1438
$VO_2(D)$	*P 2/c*	4.597	5.684	4.913	β=89.39°	[QU11]
$VO_2(P)$	*Pbnm*	4.890	9.390	2.930	β=90°	[LIU12]

The R, M1, and B phases have the most studied crystal structures among these polymorphs, in which one vanadium atom is surrounded by six oxygen atoms forming a VO_6 octahedron. For the other VO_2 polymorphs, the shape of the VO_6 octahedra and the connections between them are different. This conducts to differences in atomic coordinates and special symmetry groups. The M2 phase is typically in this case. It can be obtained by doping $VO_2(M1)$ with +3 valence ions [EYE02] or by applying strain (**Figure 1-9**). On contrary to the M1 phase (seen in section 1.2.1) in which V atoms form V-V zig-zag chains along $\vec{c}_{VO2(R)}$-axis (or $\vec{a}_{VO2(M1)}$-axis), the V atom chains in the M2 phase have two arrangements along the $\vec{c}_{VO2(R)}$-axis: Half of them are paired but not inclined relative to the $\vec{c}_{VO2}$-axis, and the second half forms a chain of equidistant V atoms. The M2 is considered to be an intermediate phase that can easily transit to R when the temperature is above 68°C (see section 1.4.1). **Figure 1-9** illustrates the transformations existing between VO_2 polymorphs and how to trigger them.

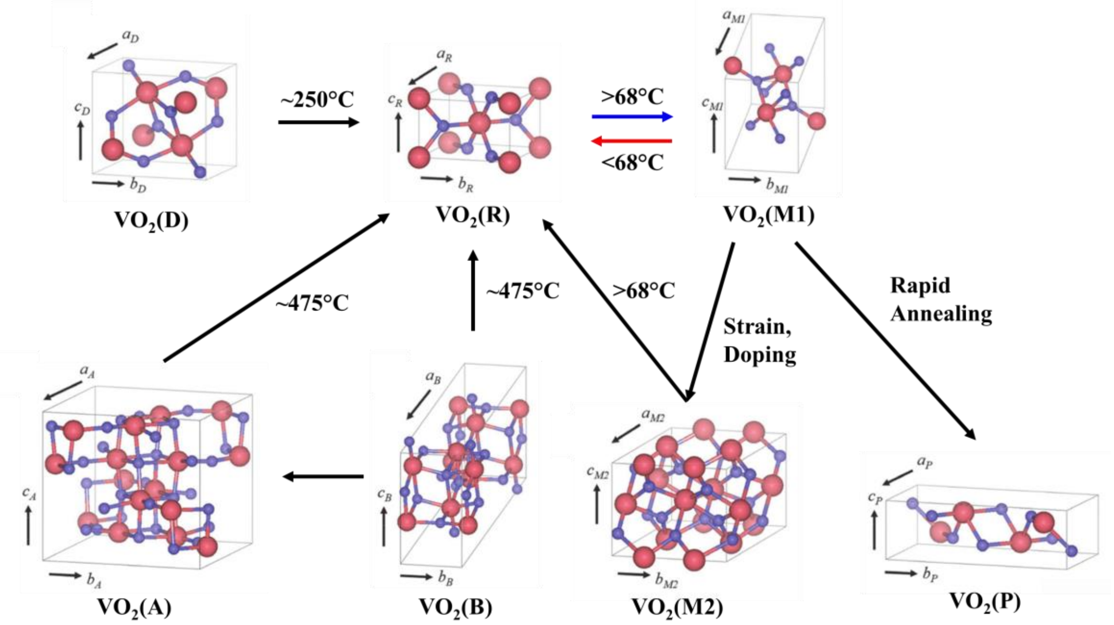

Figure 1-9: Crystal structures and phase transformations between VO_2 polymorphs [STE00].

Although, it could appear that VO_2 is simple to elaborate, considering that only 2 elements enter in its composition (V, O), the complexity of the V-O phase diagram and the interconnections between the different structures make it challenging to understand the formation and stabilization of VO_2 phases. By exploring the Magnéli (V_nO_{2n-1}) and Wadsley (V_nO_{2n+1}) structures, we observe the interconnections between these oxides resulting from the transformation of a parent structure. During these transformations, oxygen vacancies are created by reduction from V^{+5} to V^{+4} and V^{+4} to V^{+3}, and further condensation of the structure occurs to compensate for the oxygen deficiency. Even if Magnéli and Wadsley structures are strictly different, their transformation mechanisms are similar and related to oxides of the same stoichiometry: the VO_2. With technological development and the desire to promote the multi-functionality of materials, research on VO_2 has intensified in recent years. While 10 VO_2 polymorphs have been discovered, still a lot is lacking, especially about the mechanisms of formation and transformation within the phases. While the phase transition mechanism between M1 and R phases are the most studied, there is still not a clear consensus on it in the scientific community. Therefore, in the next section we remind the basis of existing theories on the metal to insulator transition which are mandatory to study VO_2 phase stabilization.

1.3. Metal to insulator phase transition theories

As we discussed in previous part, numerous vanadium oxides and especially VO_2 polymorphs R, B and A exhibit phase transition. The transition from a metallic state to an insulating state is one of the most spectacular phenomena in solid-state physics. Depending on the stimulus applied, thermal or electrical [STE00], stress [QU11][LIU12], or optical excitation [SON16][ZHA21], the behavior of charged carriers in a solid can change radically. Various approaches were already proposed in the literature to explain the phase transition phenomenon depending on the interaction between electrons and/or phonons. The Peierls mechanism based on electron-phonon interactions is one of them [PEI55] (**Figure 1-10**). At high temperature, the material is considered as a one-dimensional system whose atoms are equidistant. The thermal energy is sufficient to allow the transfer of electrons from one atom to another: The material behaves as a metal. By lowering the temperature, a deformation of the structure is observed. The distance between atoms is modified and they undergo a dimerization. The thermal energy is becoming too low to delocalize electrons, a gap opens, and an insulating state appears.

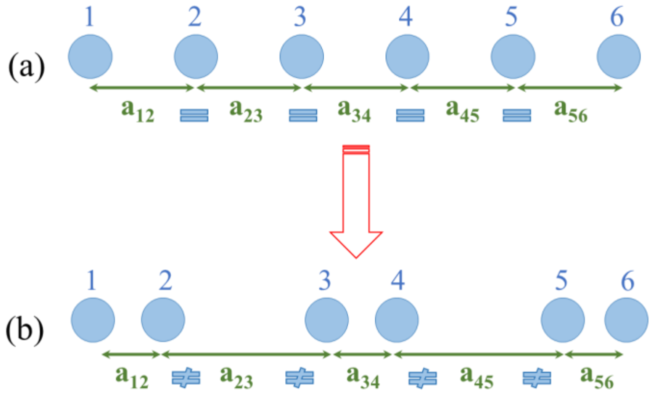

Figure 1-10: Representation of a one-dimensional system (a) before and (b) after Peierls transition.

In 1949, Mott described the MIT by considering mainly the electron-electron interactions [MOT49]. The insulating state of Mott appears when the repulsive electronic interaction leads to a localization of electrons. This phase is very different from a band insulator, in which the electrons fill the deepest energy bands and whose Fermi level is in the band gap (**Figure 1-11**(a)).

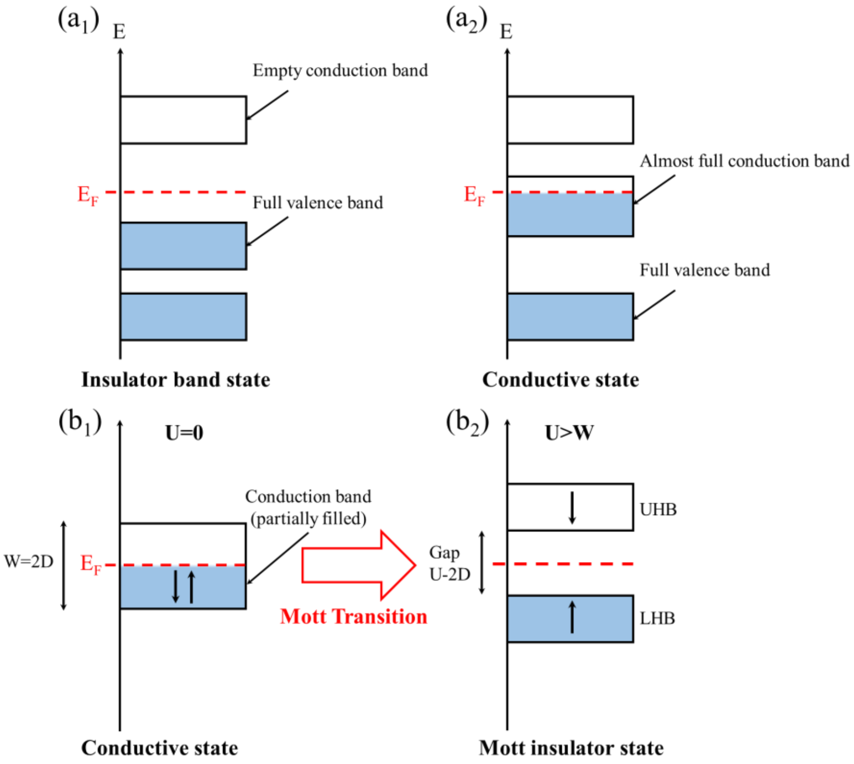

Figure 1-11: (a) Representation of the band structure of an insulating (a_1) and metallic state (a_2). The conduction band is empty for an insulator, and almost full for a metal. (b) Representation of the band structure of a partially filled system without correlations (b_1) and with electronic correlations (b_2). W is the band width, U the on-site Coulomb repulsion. For U>W, a Mott gap opens between the Hubbard bands LHB and UHB, giving a Mott insulator state.

To illustrate the electron-electron localization, we can consider a square lattice of identical one-electron atoms with one orbital per site [MOT68]. In the absence of Coulomb repulsion, the system has a half-filled conduction band (**Figure 1-11**(b)) [WEG15][OTT19]. The width W of the conduction band allows the jump of electrons from site to site, it is a metallic state. When the Coulomb repulsion is stronger than the width W, the conduction band splits into two Hubbard bands of width $D=W/2$.

Above E_F, we find the empty Upper Hubbard Band (UHB), and below E_F, we have the filled Lower Hubbard Band (LHB). A gap appears between UHB and LHB of $E_g=U-2D$ with D the half-bandwidth and U the on-site Coulomb interaction energy. This separation has the effect of constraining electrons on sites, and of stabilizing the system in the insulating phase of Mott.

In Mott picture, the insulating or metallic state of a system with strong electronic correlations is thus described by the U/W ratio. When U/W increases, the transition between the metallic state and the insulating Mott state appears. This evolution can be explained by the Hubbard model [WEG15] [PEI55]:

$$H = \underbrace{\sum_{ij,\sigma} t_{ij} c_{i\sigma}^{\dagger} c_{j\sigma}}_{\text{kinetic energy}} + \underbrace{U \sum_{i} n_{i\downarrow} n_{i\uparrow}}_{\text{local Coulomb energy}} \tag{1.10}$$

The Hubbard model is composed of a kinetic term t_{ij}, and a local coulomb energy U. The kinetic term describes the hopping of electrons between sites i and j, with creation and annihilation operators $c_{i\sigma}^{\dagger}$ and $c_{j\sigma}$. U is the on-site Coulomb repulsive term between two electrons localized on the same site i, with n_i the density of electrons at site i (for up and down spins). The kinetic term t being related to the bandwidth W by $W=zt$, z being the number of first neighbor sites, its value and that of W depend on the size of atomic orbitals, and on the interatomic distances. The electronic correlations are also influenced by the size of atomic orbitals, and by their electronic filling. When two electrons occupy the same atomic orbital, the Coulomb repulsion is more significant as the volume is restricted. Thus, the system tends to be strongly correlated when atomic orbitals are small (e.g., d and f orbitals) [IMA98]. Typically, transition metals have d orbitals near E_F.

1.3.1. MIT in vanadium dioxide M1 phase

During the transition from metallic to insulating state, the structural transition in VO_2 with lowering of the symmetry is accompanied by a modification of the electronic structure. This change close to Fermi level (E_F) results from the octahedral environment and hybridization of O *2p* orbitals with V *3d* orbitals (p-d hybridization). The hybridized *3d* electron level of vanadium (V^{4+}) and *2p* electron level of oxygen ion are divided into low and high energy states named t_{2g} $(d_{//}, \pi, \pi^*)$ and e_g (σ, σ^*), respectively [EYE02][GOO71][SUG90]. Under the effect of dimerization of V atoms along the [001] direction and change of V-O distance, $d_{//}$ band is divided into two bands:

i. a low energy bonding band ($d_{//}$)
ii. a high-energy empty antibonding band ($d^*_{//}$).

In addition, due to the change in V-O hybridization, the antibonding band π^* is pushed towards the higher energies and rises above E_F, as depicted in **Figure 1-12**. These changes lead to the formation of a gap $E_g\approx0.7$eV [GOO71][ILI12], between the bonding and antibonding bands. The material thus behaves like a semiconductor (VO_2(M1) phase).

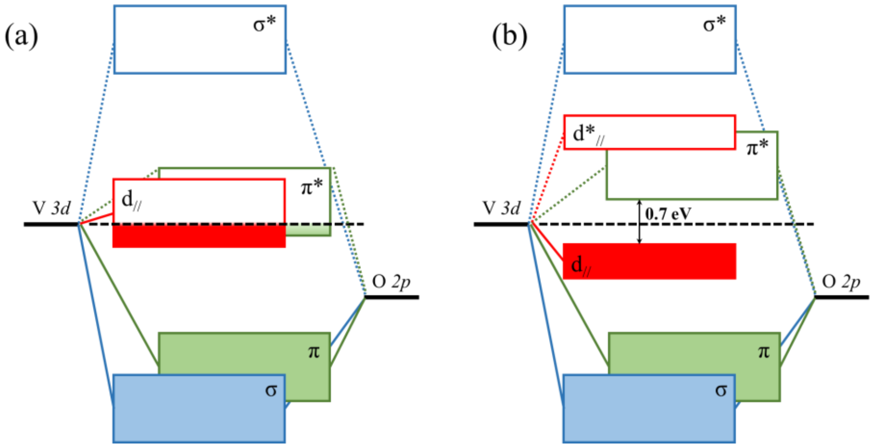

Figure 1-12: VO_2 band structure in the (a) metallic (R phase) and (b) insulating (M1 phase) states.

As we have seen, the 3*d* band plays an important role in the band structure during the metal-insulator transition. The knowledge of the position of the orbitals is therefore essential to understand the effect of strain applied on the material. **Figure 1-13** illustrates electronic orbitals of *3d* level of vanadium atom placed at the center of oxygen octahedra for the rutile configuration of VO_2(R).

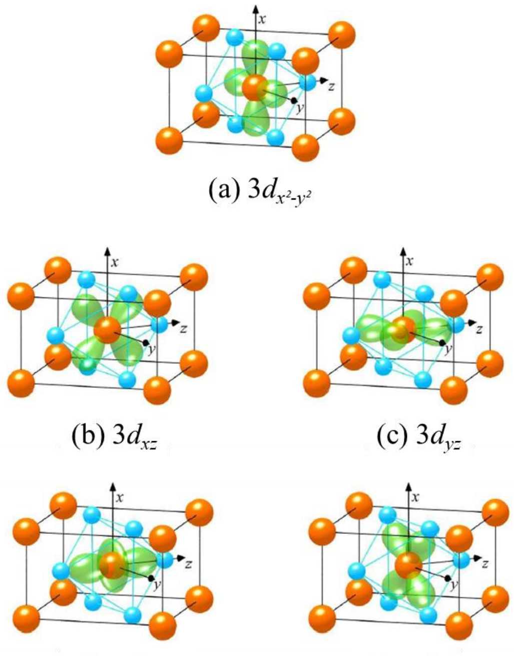

(a) $3d_{x^2-y^2}$

(b) $3d_{xz}$

(c) $3d_{yz}$

(d) $3d_{3z^2-r^2}$

(e) $3d_{xy}$

Figure 1-13: 3d orbitals of t_{2g} level (a, b, c) and e_g level (d, e) of V atom in VO_2(R) [EYE02].

Despite hybridization of O *2p* orbitals with V *3d* orbitals, only $3d_{3z^2-r^2}$ *and* $3d_{xy}$ orbitals are oriented in the direction of oxygen atoms . The remaining three *3d* orbitals ($3d_{x^2-y^2}$, $3d_{yz}$, and $3d_{xz}$) are nonbonding to oxygen atoms. However, it is $3d_{xy}$ and $3d_{yz}$ orbitals which will form vanadium-oxygen ionic bonds with the $2p_x$, $2p_y$, and $2p_z$ orbitals of the *2p* energy level of the oxygen atom (**Figure 1-14**), after degeneracy lifting of the *2p* level because these orbitals have the same symmetry [EYE02].

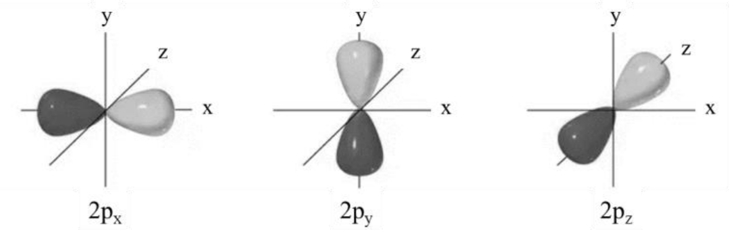

Figure 1-14: 2p orbitals of oxygen atom aligned along x, y, and z directions.

1.3.2. When Mott meets Peierls

During the last decades, numerous studies seeking to elucidate the mechanism(s) at the origin of phase transition in VO_2 have been reported in the literature. Some opt for a Mott mechanism [ZYL75], others for a Peierls-type transition [GOO71][HAV05], or for a combination of both mechanisms. This long-standing debate has continued to be animated by the complex interaction between orbital, electronic degrees of freedom, and lattice parameters, which modify the MIT temperature and hysteresis width. Despite the growing interest for VO_2 polymorphs, the understanding of the phase transition nature is still one of the most challenging topics in condensed matter physics.

One of the significant works about the phase transition mechanisms was performed by Ilinskiy *et al*. [ILI12], who proposed a relatively complex and innovative concept concerning the MIT mechanism in VO_2. They suggested that the Mott transition and the Peierls transition play the role of distinct components in the whole mechanism and occur at different stages of the transition. To understand the transition present in VO_2(M1/R), it is necessary to consider the strong correlation between electrons responsible for the energy positions of the bands. When the temperature increases, the correlation interaction between electrons first gradually reduces the energy gap until the bottom of the π^* band and the top of the $3d_{//}$ sub-band touch the Fermi level (**Figure 1-15**).

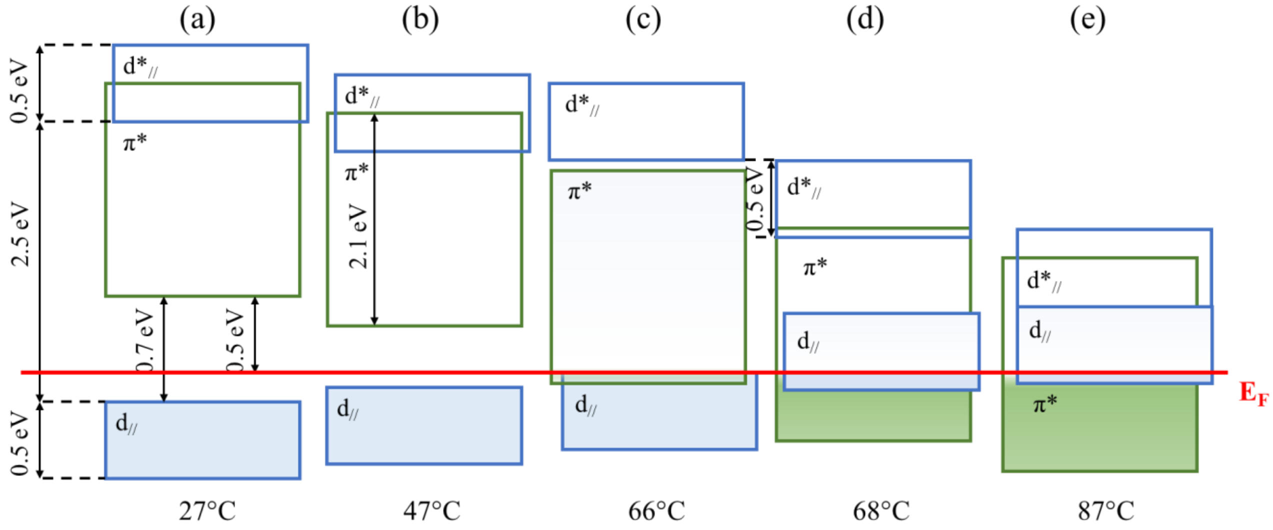

Figure 1-15: Step by step evolution of the electronic band diagram of VO_2 depending on temperature: (a, b) monoclinic insulator phase at low temperature; (c) monoclinic phase near the structural transition (66°C); (d) rutile metallic phase after the structural transition (68°C); and (e) rutile metallic phase at high temperature [ILI12].

According to Ilinskiy and coworkers, when the sample is heated, the electronic correlation decreases π^* band position with respect to the Fermi level. As a result, transitions of electrons from $d_{//}$ to π^* band are intensified, and the disruption of dimers can start. For the structural transition to occur, it is necessary that the great majority of $d_{//}$ (bonding) band electrons that form dimers pass into the π^* (antibonding) band. And this is only possible if the number of levels in the $d_{//}$ band is lower than the π^* band. As a critical concentration of broken dimers is attained, the structural phase transition to the rutile phase occurs. It should be noted that only when this critical concentration of broken dimers at the temperature $T = T_{MIT} + \Delta T$ is attained, a nucleus of the R phase located within the M1 phase will have extended over the whole VO_2 film, with ΔT the temperature spread of the transition [ILI12] [ALI06]. Thus, it is only at $T = T_{MIT} + \Delta T$ on the temperature scale, that the VO_2 structural phase transition is achieved (**Figure 1-15**(d)). Step by step, the new rutile metallic phase appears under the influence of forces produced by the σ bonds of the oxygen octahedra and vanadium ions that realign to the centers of these octahedra. Once the structural transition is activated, the $d^*_{//}$ sub-band also moves down by 0.5 eV due to the disappearance of the 1D zig-zag chain (Peierls interaction). Due to the increase in electronic correlations induced by the narrowing of $d_{//}$ band gap, bringing the $d^*_{//}$ and $d_{//}$ sub-bands together, Peierls interactions are in turn able to stimulate Mott insulator-metal electronic transition within the $d_{//}$ band. To summarize, the stepwise lowering of the upper $d^*_{//}$ sub-band decreases its energy gap with the upper $d_{//}$ from 2 to 0 eV, making VO_2 fully metallic.

During the transition, electronic correlation and structural phase transition both occur in VO_2 but at different stages. This model was confirmed by D'Elia *et al.* [DEL21] in his study of VO_2 films and nanowires by X-ray Absorption Near Edge Spectroscopy (XANES) and resonant Photoemission spectroscopy. The interest in comparing two structures comes from the fact that, contrary to thin films, nanowires are free of substrate-induced strains. The lattice mismatch of VO_2 grown on different substrates modify the V-O distance. For instance, in the case of VO_2 grown on TiO_2(001), the V-O distance increases, reducing the overlap between oxygen and vanadium orbitals, and thus, the *3d-2p* hybridization [AET13]. In turn, this decrease in V-O hybridization reduces the bonding-antibonding energy separation; hence the π^* orbital is shifted to lower energy. On the contrary, the $d^*_{//}$ shifts upwards since the strain reduces the inter-pair distance, increasing the orbital superposition within the 1D zig-zag chains (V-V). To summarize, changing the interatomic distances in a controlled way by applying an epitaxial strain, e.g., affects the orbital overlap and electron correlation and, consequently, the electronic structure of VO_2. In the case of nanowires, the description of the electronic structure can be more complicated due to the presence of multiple coexisting phases or of structural defects. Whether for thin films or nanowires, it has been demonstrated and confirmed that electron correlation and structural phase transition are the key parameters behind the MIT in VO_2. The structural phase transition always appears as a tool to complete the MIT and to make VO_2 fully metallic.

1.3.3. Phase transition activation mode of VO_2

It should be noted that the major part of the works about the phase transition in VO_2 or phase change materials is dealing with temperature. Therefore, it is natural to ask the questions: "What would happen to the transition, if the activation mode is changed? Could not the structural phase transition be activated in the first place, which would lead to electronic effects and thus, to a modification of the band structure?". To answer these questions, several different MIT activation modes such as pressure and optical excitations will be presented in this part.

Pressure

To understand the highly electronically correlated systems, strain stimuli have been used. The volume compression usually has the effect of both symmetrizing the crystal structure and reducing or completely removing local or extended lattice distortions [SAC06]. Coupled with Raman spectroscopy and IR measurements at RT, Marini *et al.* [MAR10] work on the determination of the Grüneisen parameter helped to identify the role of lattice-charge coupling in the physical properties of VO_2. The Grüneisen parameter (γ_i) describes the relationship between a variation in the frequency of the vibrational mode of a crystalline structure and a variation in volume (eq.(1.11)).

$$\gamma_{\mathrm{i}} = -\frac{\partial \ln(\mathrm{w_i})}{\partial \ln(\mathrm{V})} = -\frac{\mathrm{V}}{\mathrm{w_i}}\frac{\mathrm{dw_i/dP}}{\mathrm{dV/dP}} \tag{1.11}$$

According to the experimental data (**Figure 1-16**(a)), when pressure is applied on the VO_2 structure at RT, a new configuration of the V-V chain, directly related to the Peierls distortion, appears above a critical pressure (~10 GPa) and leads to a structural modification together with the observation of an increasingly metallic character. As the monoclinic symmetry is the indication of Peierls distortion, the strong increase of metallicity within the M1 phase hints at a major role of electronic correlations.

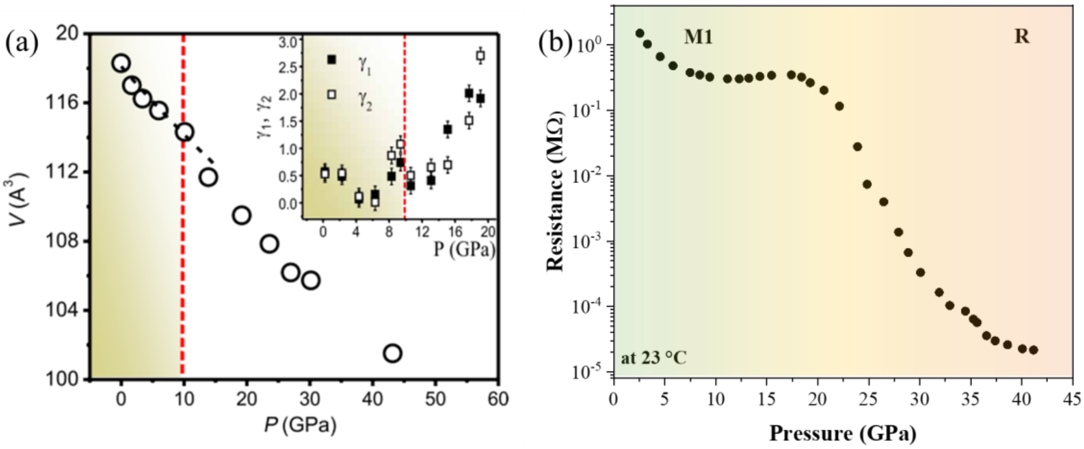

Figure 1-16: Evolution of (a) the volume of the VO_2 unit cell and (b) the resistance as function of pressure at RT [CHE17]. Inset: Grüneisen parameter as function of pressure. γ_1 and γ_2 values were associated with V(1)-V(1) and V(2)-V(2) chain motions in the VO_2(M1) structure [MAR10].

More recently, Chen *et al*. reported similar findings on VO_2 activated by high pressure [CHE17]. As pressure increases, the 1D zig-zag chain disappears and V atoms align. The unit cell is restructured due to the disappearance of dimers, and consequently its symmetry increases. Due to this structural transformation, the Mott-Hubbard transition is achieved and the band gap disappears by overlapping of the bands and VO_2 becomes metallic (**Figure 1-16**(b)).

Optical excitation

With the advent of ultrafast lasers at the end of the last century, photoexcitation provided another path to initiate the MIT. Roach and Balberg were the first to show that after 20 ns, photoexcited VO_2 exhibits a metal-like optical response [ROA71]. Since this discovery, many time-resolved experiments from terahertz to ultraviolet (UV) aimed to uncover the connection in VO_2 between the photoinduced MIT and the changes in lattice structure [WEG15][OTT19]. In 2014, Morrison *et al.*

[MOR14] combined ultrafast electron diffraction (UED) and mid-infrared spectroscopy to show that there is two distinct photo-induced MIT in VO_2(M1) (**Figure 1-17**):

i. The first, at high pump fluence, is associated with the lattice structural transition between M1 and R phases.
ii. The second, at lower pump fluence, produces a metastable, monoclinic metallic phase (mM) that retains the crystallographic symmetry of the M1 monoclinic phase.

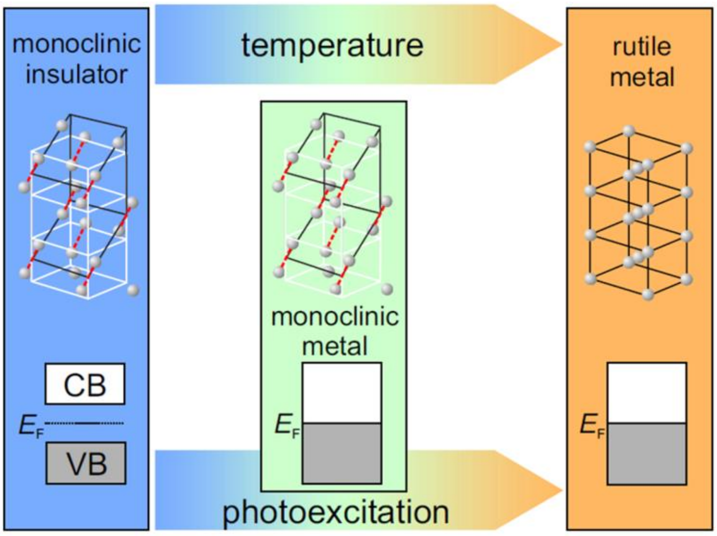

Figure 1-17: Structural and electronic VO_2 transitions during photoexcitation: (Bottom) At low fluence photoexcitation produces a metallic monoclinic metastable phase; (Top) A high fluence excitation directly drives the M1 phase to transit to R by the thermal effect (laser-induced heating) [WEG15].

Differently from pressure activation, the photoinduced phase transition requires more attention to the time scale. If sufficiently photoexcited (high pump fluence), VO_2 becomes metallic in <1 ps after the pulse absorption [WEG15]. Experiments at lower pump fluence have been carried out to understand if the transition occurs faster or simultaneously with the onset of the structural phase transition. During the photoexcitation of the insulating M1 phase below a critical fluence, a change in the population of electronic states occurs. This significantly changes the Coulomb interaction through the depopulation of top valence band (VB) states, as the electrons from the top of the valence band pass into the conduction band (CB). This results in a collapse of the insulating band gap, making VO_2 metallic. The non-thermal MIT has occurred. At the same time, the depopulation of V-V bonding orbitals modifies the forces that act on the ions. The monoclinic symmetry is modified and triggers a structural phase transition: the monoclinic metallic phase appears. This transient phase is characterized by a metallic band structure and a monoclinic atomic arrangement, different from the one of the M1 phase. At this stage, the VO_2 is in a non-equilibrium state that will evolve to the rutile structure. 200 to 300 fs after the emergence of mM phase, electronic and lattice relaxations occur, respectively. Thus, the 1D zig-zag chain disappears, destroying the periodic lattice distortion along the $\vec{c}_{VO2}$-axis, and increasing the symmetry of the unit cell. The excess energy of electrons and holes after photoexcitation is transferred to the lattice and the crystal structure changes towards the rutile arrangement to reach an equilibrium state.

We have seen in this part that a reversible MIT can be obtained using different stimulations: thermal, by applying a pressure or stress, or by optical excitation. The transition time varies according to the applied stimulus. It is generally slower for thermal activation (in the millisecond or microsecond range) than optically (reaching a hundred femtoseconds), which opens the door to many applications [YAN11][VIC21][CUI18][ISH19]. However, despite numerous theoretical studies and experimental works, the exact origin of the phase transition remains unclear. Progress made in the last 20 years has shown the close relationship between the Peierls and Mott-Hubbard mechanisms, while the activation mode leaves this question open.

1.4. VO_2 growth and MIT control for applications

To develop new devices based on VO_2 transition, many studies have been carried out in order to synthesize nanowires, nanoparticles, and thin films with perfect stoichiometry and high MIT performance. Indeed, the VO_2 electrical and optical properties are closely related to its composition, morphology, and crystalline quality. **Figure 1-18** shows that single crystals and thin films of VO_2 do not have the same properties, as seen from the resistivity hysteresis cycle [DUC72]. Unlike the single crystal, which has a sharp resistivity change at T_{MIT}~68°C, the thin film has deteriorated electrical properties. The resistivity change is lower with a hysteresis width of ~5°C in best cases. Therefore, we are interested in the phenomena that can explain this difference and the parameters that can improve the MIT of VO_2.

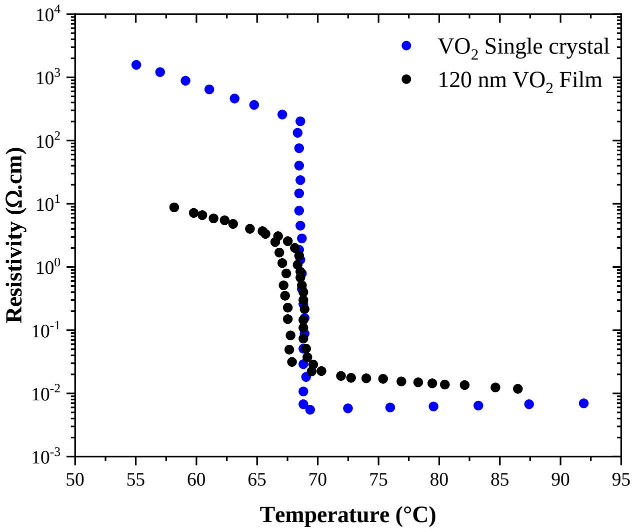

Figure 1-18: Resistivity evolution as function of temperature for a VO_2 thin film compared to a VO_2 single crystal [DUC72].

1.4.1. Influence of the substrate

Single crystals are difficult to integrate in an industrial process flow. Therefore, the development of thin films with the best possible crystalline quality is required for the successful integration of VO_2 into industrial applications. Unfortunately, thin films can have a reduced crystalline quality due to defects in the layer, mixed phases, grain size and grain boundaries, or substrate-induced stress. This quality can vary significantly, ranging from amorphous to epitaxial thin films. Amorphous films have their atoms without long-range order, thus no crystalline arrangement exists. Contrary to an epitaxial thin film, which refers to a crystalline layer grown with its lattice parameters close to the ones of the substrate. For most technological applications, epitaxial thin films are preferred since their properties are closer to those of a single crystal. To obtain epitaxy of a layer on a substrate, two ways are possible:

i. Homostructural epitaxy: Thin film growth on a substrate that is structurally similar to the film.

The substrate material is selected based on lattice matching.

ii. Heterostructural epitaxy: Thin film growth on substrate of different crystallographic structure than the film. In this case, any chemical system can be considered. The epitaxial relationships between film and substrate are determined through a set of criteria such as crystallographic properties, interfacial chemistry, and the minimal lattice mismatch. The misfit strain is defined by eq.(1.12):

$$\mathrm{m_x} = \frac{\mathrm{x_{RT}^{s}} - \mathrm{x_{RT}^{bulk}}}{\mathrm{x_{RT}^{bulk}}} \tag{1.12}$$

Where x_{RT}^{s} and x_{RT}^{bulk} are the lattice parameters of the substrate and of the thin film material in bulk form, respectively, to obtain the misfit strain m_x for the appropriate x-axis of the unit cell. Note that the misfit strain can also be calculated at the growth temperature, taking into account the linear coefficients of expansion of the materials. The experimental lattice parameters of the film (x_{RT}^{film}) allow to calculate the effective epitaxial strain from eq.(1.13). If $x_{RT}^{film} = x_{RT}^{s}$ for in-plane lattice parameters, that is for a so-called pseudomorphic growth, then epitaxial strain corresponds to the misfit strain. Typically, epitaxial growth requires a misfit strain between substrate and film below 5% for in-plane lattice parameters [CHE96].

$$\varepsilon = \frac{\mathrm{x_{RT}^{film}} - \mathrm{x_{RT}^{bulk}}}{\mathrm{x_{RT}^{bulk}}} \tag{1.13}$$

For VO_2, studies conducted by Lee *et al.* [LEE16] and Ding *et al.* [DIN16] with Density Functional Theory (DFT) calculations revealed that to get homostructural epitaxy, only TiO_2(R) matches with the metallic VO_2 phase (**Table 1-5**). In the case of TiO_2(R) as substrate, the in-plane misfit strain of epitaxial VO_2(R) is $m_a = m_b = (4.594 - 4.554)/4.554 = 0.8\%$. This stretching of the $\vec{a}$- and $\vec{b}$-axes results in a contraction of the $\vec{c}$-axis. This was confirmed experimentally by Paez *et al.* [PAE20] [PAE20b] but did not allow versatility for VO_2 thin film growth. Thus, further works were mainly oriented towards heterostructural epitaxial growth.

Table 1-5: Structures of TiO_2 polymorphs compared to VO_2(R, M1, B and A).

Structure	Space group	a (Å)	b (Å)	c (Å)
TiO_2(R) [SAS]	*P4₂/mnm*	4.594	4.594	2.958
Brookite	*Pbca*	9.184	5.447	5.145
Columbite [PAE20]	*Pbcn*	4.59	4.94	5.58
TiO_2(A) [SAS]	*I4₁/amd*	3.785	3.785	9.514
VO_2(R) [WHA74]	*P4₂/mnm*	4.554	4.554	2.85
VO_2(M1)	*P2₁/c*	5.752	4.526	5.382
VO_2(B) [THE76]	*C2/m*	12.03	3.693	6.42

VO_2(A) [THE76]	*$P4_2/ncc$*	8.45	8.45	7.686

When the substrate and film do not have the same lattice parameters, a lattice mismatch appears, at the origin of substrate-induced stress or so-called epitaxial stress. The growth can then proceed in two different ways as shown in **Figure 1-19**, depending on the misfit strain and on the film thickness.

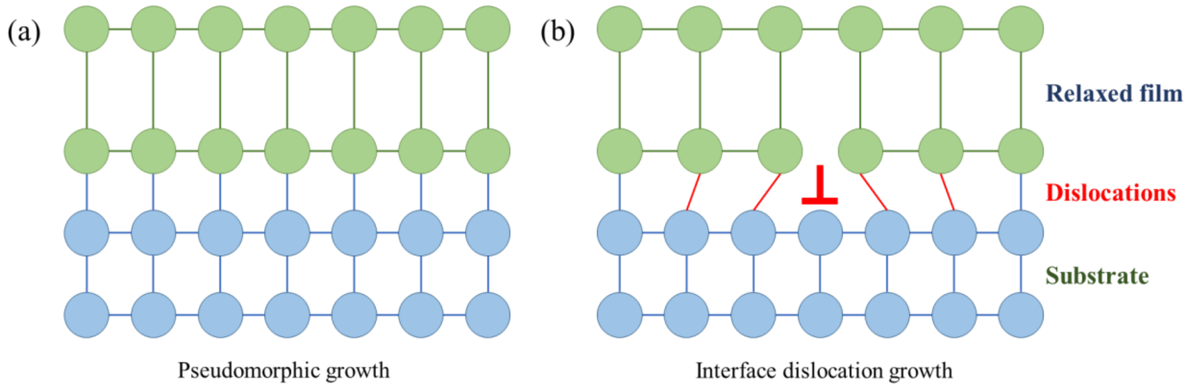

Figure 1-19: Schemes of heterostructural epitaxy by (a) pseudomorphic growth and (b) relaxed growth with interface dislocations.

When misfit strain (m_x) is low, a pseudomorphic growth can take place. In this case, the film is initially constrained such that the epitaxial material adopts the lattice parameters of the substrate in the growth plane. This gives rise to an elastic deformation of the lattice (**Figure 1-19**(a)), to which is associated elastic energy given by eq.(1.14) [MAR96]:

$$E = \frac{2G(1+\nu)}{1-\nu} t * m_x^2 \tag{1.14}$$

Where *G* is the shear modulus and *ν* is the Poisson ratio of the epitaxial material. Thus, elastic energy is proportional to the strained film volume and increases with the film thickness (*t*). When m_x or t are high, matching between the film and the substrate by elastic deformation is no longer possible. Thus, dislocations appear and either stay at the interface from the nucleation of the first layer (m_x too high, misfit dislocations), or appear during growth (*t* too high) and migrate towards the interface (threading dislocations). Textured or polycrystalline layers are also often encountered in heterostructural growth systems, as alternative or complementary stress relaxation mechanisms.

Stabilization of VO_2 polymorphic phases

Research on stabilizing VO_2 polymorphic phases in thin films has shown that no substrate perfectly matches the M1 phase. Theoretical calculations offered an approach based on the minimization of the coincidence area between the substrate and the film from superlattices (*m* unit cells of substrate for *n* unit cells of film) [ZUR84]. To accommodate a lattice mismatch, the film is considered to be strained within the epitaxial plane. For maximizing epitaxial lattice matching, different substrate orientations were considered. **Figure 1-20** shows the results of Ding *et al*. [DIN16] with a maximum 3% misfit strain for three known VO_2 polymorphs (M1, A, and B phases) on the following common substrates: $SrTiO_3$, MgO, $LaAlO_3$, and Al_2O_3. Interestingly, the model predicts that (001)Al_2O_3 substrate (c-cut sapphire) should be the best choice to grow the VO_2(A) phase, whereas in fact M1 is frequently found experimentally [FAN13][ZHA12]. Conversely, these calculations show that the B phase should be favored on (100)$SrTiO_3$, as was indeed confirmed experimentally [SRI15][CHE14]. In summary, the calculation of misfit strain and elastic energy can be used as preliminary guide for substrate selection, in order to tune this choice to a particular VO_2 polymorph. Then, in practice many other parameters must be taken into account, such as the deposition technique, the substrate preparation, or the growth parameters that all significantly influence the phase stabilization and growth morphology of the films, as well as the material performances.

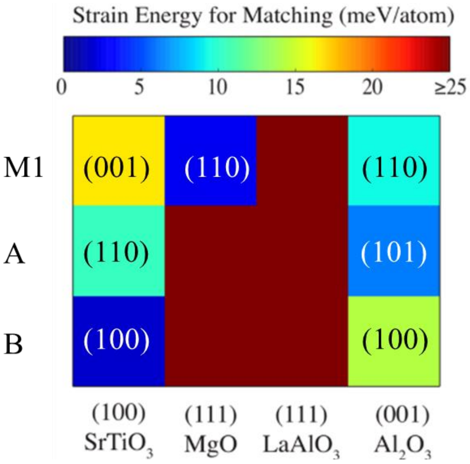

Figure 1-20: Calculated VO_2 film misfit strain energy for several different polymorphs and substrates. The orientation of the film on a given substrate is labeled with Miller indices [DIN16].

As we have seen so far, the substrate nature and orientation can strongly affect the VO_2 phases, the crystalline quality, and the layer morphologies that lead to modifying the MIT characteristics. The presence of differently oriented grains, point defects, dislocations, or impurities can increase the hysteresis width and affect the transition temperature. In this way, some research has been undertaken to try to control the strains to understand the mechanisms behind the formation and stabilization of one phase over another. The final goal is to improve VO_2(M1) performance for industrial applications. Pouget's team was the first to demonstrate that the deformation at the origin of the appearance of a new phase was uniaxial in the $[110]_R$ direction (or [011] in the M1 phase) [POU75]. Under strain effect, the monoclinic symmetry of M1 phase is broken and leads to its reduction until the formation of another phase (e.g., T, M2). Guo *et al*. work in 2011 [GUO11] investigated nanowires without substrate-induced stress and showed that a deformation in the $\vec{c}_{VO2(R)}$-axis (or $\vec{a}_{VO2(M1)}$-axis) of the material can lead to the appearance of a new phase. That is also in agreement with Pouget's study.

Impact on phase transition characteristics

We have previously shown that the substrate impacts the epitaxial growth and can conduct to textured or polycrystalline layers. A polycrystalline layer is composed of crystallites with or without a preferential growth orientation. Then, a textured crystalline layer does have a preferential crystalline orientation, resulting in a superior crystalline arrangement. Depending on the crystallinity of the layers, thus depending on the substrate, the characteristics of the VO_2(R/M1) MIT can be modified. The percolation theory gives some insights into this phenomenon. This theory is based on statistical considerations to characterize the behavior of a set of incompletely connected objects. In such a system, long-distance communication is possible or not, depending on the number of objects and of contacts between them [CEL95][CHR02][BEA16]. Considering the heterostructural VO_2 layers, they tend to present grain boundaries and defects induced by the substrate. When a stimulus is applied, e.g., temperature, nanocrystals of the insulating phase will transit to the metallic phase. In percolation theory picture, these first sites are called clusters, and their number and size will increase when the temperature rises. The metal filling factor (f_i), defined as the metallic phase volume fraction, will also increase until a critical point called the percolation threshold. At this point, the clusters start to merge and form a connected network. Above the transition temperature, the filling factor is higher than the percolation threshold, and the clusters form a metallic domain across the whole film. **Figure 1-21** shows the evolution of VO_2(R) phase from the metallic phase nucleation sites in a VO_2 thin film.

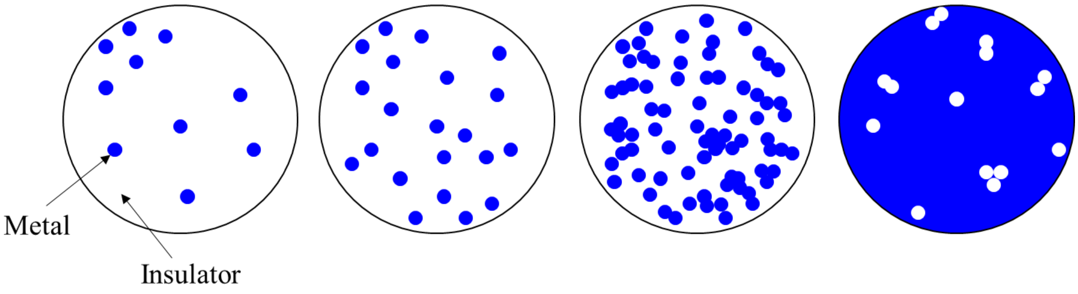

Figure 1-21: Percolation theory applied to a VO_2 polycrystalline thin film during the MIT.

1.4.2. Phase transition control through oxygen stoichiometry

The crystalline quality of a VO_2 layer has an important impact on its properties. It depends on several parameters such as epitaxial strain, roughness, or lattice defects. In the same way as (voluntary) doping, defects also often modify the physical properties of a material, and in some cases can be used to improve its performances. Among these defects, such as point defects, line defects (dislocations), planar and volume defects, oxygen vacancies are the most encountered in oxides [HUM05]. **Figure 1-22** shows the three most common types of point lattice defects in a crystal.

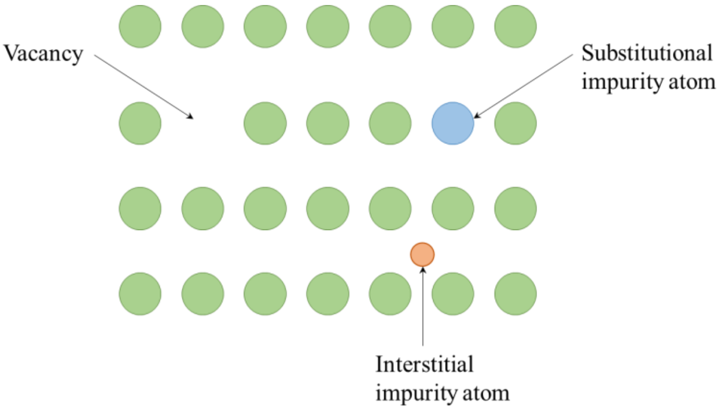

Figure 1-22: Representation of various point defects in crystals [HUM05].

The VO_2 polymorphs are known to be very sensitive to the oxygen, therefore we will focus on oxygen vacancies. This particular defect in VO_2 crystalline films ($VO_{2-\delta}$) was found to be responsible for the modulation of the MIT behavior with a decrease of the critical transition temperature. Fan [FAN18] performed ellipsometric studies to determine n and k values for VO_2 and $VO_{2-\delta}$ films. The refractive n index is the real part of the complex optical index, whereas k is the imaginary part. Based on these indices, the optical conductivity (σ) can be obtained according to the eq.(1.15):

$$\sigma = \frac{\varepsilon''\omega}{4\pi} \qquad (1.15)$$
$$\varepsilon'' = 2nk\varepsilon_0$$

Where ε'' describes the imaginary part of the dielectric constant, and ω the photon frequency, as the optical conductivity is wavelength-dependent.

From the optical conductivity, it was possible to follow the VO_2 transformation in temperature (**Figure 1-23**). An isosbestic point[1] has been observed for VO_2 and $VO_{2-\delta}$, related to electron-electron correlations. For $VO_{2-\delta}$, the isosbestic point shifts towards a low wavenumber. It is suggested that the oxygen vacancies in the VO_2 lattice weaken the interaction between V and O ions, and it decreases the electron-electron correlations. This phenomenon could be traced by the conductivity curves of **Figure 1-23**, through the shifting of the A, E and C peaks towards lower energy at A*, E* and C* if oxygen vacancies are present. According to DFT calculations, this results in a change of the electron orbital occupancy and of the band structure, leading to a decrease of the critical temperature [FAN18] [QAZ08].

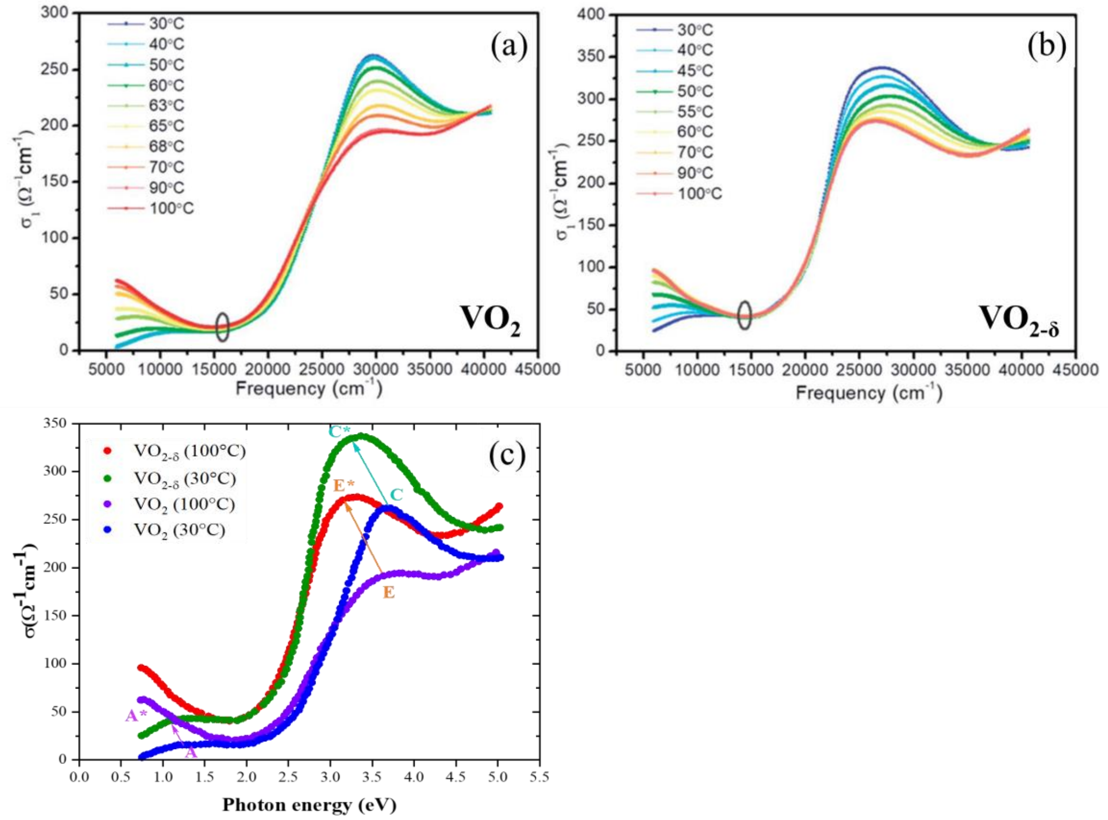

Figure 1-23: Optical conductivity curves of VO_2 and $VO_{2-\delta}$ layers at different temperatures around T_{MIT}. The isosbestic point in (a) and (b) is highlighted by the dark circle. (c) Comparison of the optical conductivity at 30°C and 100°C [FAN18].

In addition, recent studies reported that oxygen deficiencies impact MIT dynamics. In particular, the

---

[1] Isosbestic point: In VO_2 case, it is the wavelength or frequency at which the absorbance remains constant during the metal-insulator transition.

work conducted by the Oak Ridge National laboratory (United States) [LU20] looked at the oxygen vacancy migration from TiO_2 to VO_2. Three TiO_2 films were grown at different oxygen pressures (low (LP), medium (MP), and high (HP)) on VO_2 films previously deposited on (001)TiO_2 substrate. Compared to the highly crystalline VO_2 films on (001)TiO_2, a $\vec{c}_{VO2}$-axis expansion was observed after TiO_2 layer growth, more pronounced at lower oxygen pressure. Oxygen diffuses from VO_2 into the oxygen-deficient TiO_2 layer through the interface, creating more oxygen vacancies in the VO_2 layer and thus increasing the lattice parameter along the $\vec{c}_{VO2}$-axis. When oxygen vacancy concentration increased, a deterioration of electrical properties was observed. **Figure 1-24** shows the electrical resistivity evolution during cooling and heating for LP, MP, and HP samples.

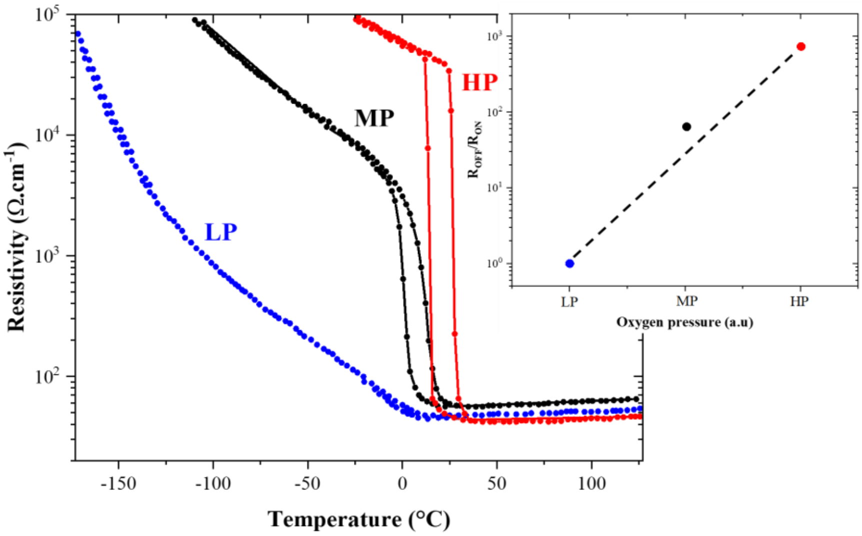

Figure 1-24: Electrical resistivity evolution of VO_2 as function of temperature for 3 different oxygen pressures during the growth of oxygen-deficient TiO_2 on top of VO_2. Insert shows the ratio of resistivity measured during cooling and heating for low (LP), medium (MP), and high pressure (HP) samples [LU20].

The TiO_2 film synthesized at HP gives the lowest oxygen vacancy concentration in VO_2, for which a well-defined and sharp change of resistivity is measured at a low transition temperature (T_{MIT}~27°C), significantly lower than for VO_2(M1) single crystal (T_{MIT}~68°C). The increase of the oxygen vacancy concentration in VO_2 increases this shift even more, until the complete suppression of MIT (**Figure 1-24**, LP sample). The accurate control of the oxygen vacancies appears as a potential way to tune the MIT, and provides a novel route to control electronic properties.

1.4.3. Doping effect on the MIT

Despite the advantages of thin films through their compatibility with electronic and optical devices, the deteriorated performance of VO_2 layers is detrimental to their full exploitation. The doping of VO_2 allows to purposely modify the characteristics of the MIT and its temperature (T_{MIT}). Indeed, various applications can require different transition temperatures. For instance, for RF applications operating in critical environmental conditions, an active material with switching temperature above 100°C is required. The doping with germanium (Ge) has made it possible to raise T_{MIT} up to ~94°C [KRA17] [MUL20]. The Ge has been selected because acceptor-like elements of low oxidation state and smaller ionic radii such as Al^{3+}, Cr^{3+} or Fe^{3+}, increase T_{MIT}. In contrast, donor-like dopants with large ionic radii such as W^{6+}, Mo^{6+}, and Nb^{5+}, decrease it. Until now, tungsten (W) has been considered the most efficient dopant to reduce T_{MIT} by 49-55°C/at.% [PAO15]. The chemical substitution of a V^{4+} ion by a W^{6+} ion provides two electrons to the VO_2 system. Taking into account charge neutralization, these electrons cause an increase in the electron density and change the band structure. The latter is characterized by a decrease in the energy levels of the $d^*_{//}$ and π^* orbitals and, consequently, results in a reduction of the activation energy of VO_2 (**Figure 1-25**). This facilitates the system transition from the insulating state to the metallic state [TAN85][HE15]. In addition, with increasing W dopant concentration, the decrease of $d_{//}$ orbitals cause V-V dimers to break and leads to the formation of W^{6+}-V^{4+} and V^{4+}-V^{3+} bonds. This drives the destabilization of the monoclinic structure and facilitates the phase transition. While the case of W doping is well-studied, the interpretation of the effect of doping remains complex. It is worth also to note that the doping of VO_2 has often a detrimental effect on the transition dynamics, by increasing the hysteresis width and decreasing the resistivity ratio between metallic and insulator states.

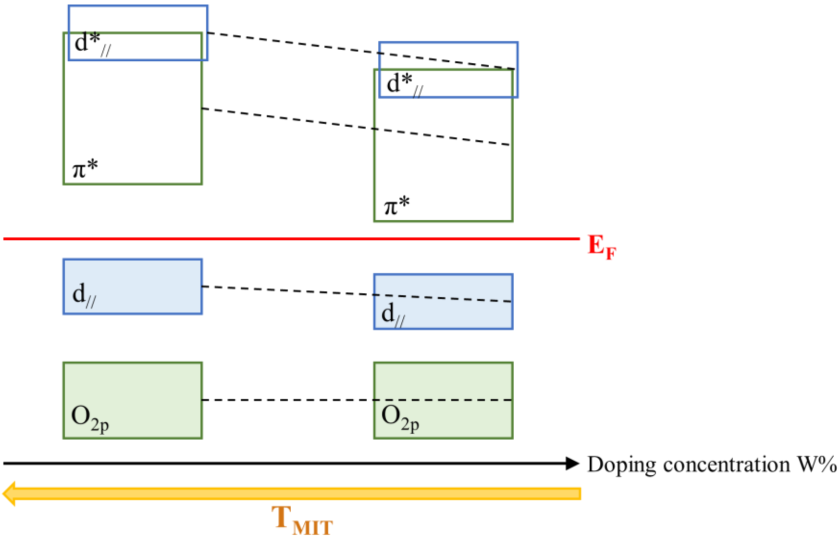

Figure 1-25: Orbital structure evolution of VO_2 as function of W doping [HE15].

While the main purpose of doping is usually to alter the transition temperature, it was also observed that the insertion or substitution of elements could lead to the formation of other VO_2 phases. Marezio *et al.* [MAR72] work on chromium (Cr) doping has, e.g., evidenced the M2 and M3 phases of VO_2 layers at RT (**Figure 1-26**). The M3 phase, also called T [EYE02], is described as an intermediate phase existing when Cr concentration is below 1.5% (at RT). In this one, the V-V pairs along the $\vec{c}_{VO2(R)}$-axis present in the M2 phase, gradually start to tilt. In addition, the zig-zag chains in the M2 phase start to dimerize until distortions in both chains are identical, and eventually, the M1 phase is reached. The appearance of these new phases by Cr, Al, Fe, and Ti doping has opened the door to many questions. Indeed, they had already been observed after (undoped) VO_2 growth on difference substrates. As we have seen in the 1.4.1 section, uniaxial stress along the $\vec{c}_{VO2}$-axis induced by the lattice mismatch can suppress the zig-zag-type displacement on V-V chains, and as a result, the pairing on the other chains will be also reduced. Today, stabilizing M2 and M3 (or T) phases in two different ways, allows emerging new studies. They contribute to the research on understanding the VO_2 polymorphs, especially on stabilizing the M1 and R phases, which are still challenging to obtain with excellent characteristics.

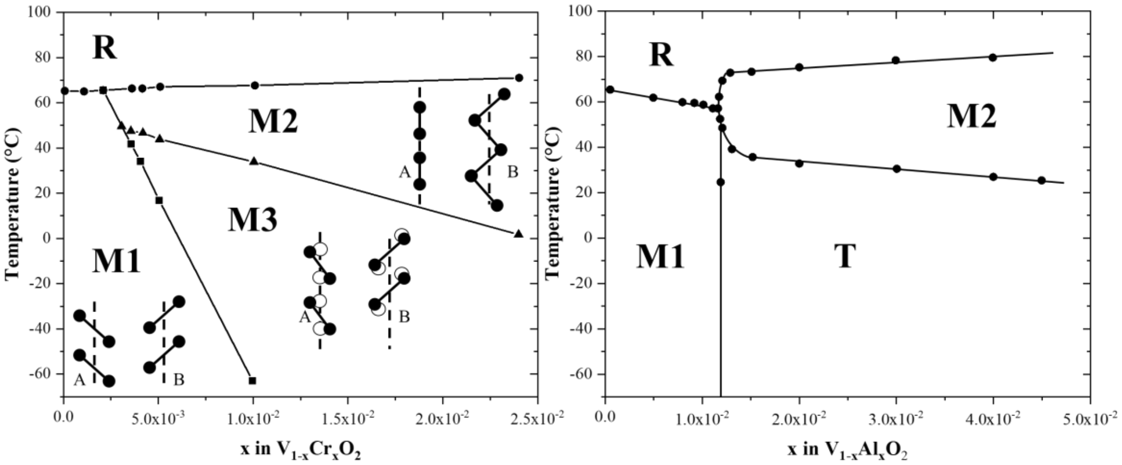

Figure 1-26: Phase diagrams of $V_{1-x}Cr_xO_2$ (left) and $V_{1-x}Al_xO_2$ (right) [MAR72][EYE02].

1.5. Summary and research project

Although vanadium oxides are already widely studied, the mechanisms responsible for their phase transitions are not fully understood. Most often, PCM belong to rich and complex phase diagrams, where the stabilization of a pure phase requires precise control on the synthesis parameters and a perfect knowledge of the crystallographic structures. The works on VO_2 have shown the complexity of the V-O system, especially since each oxide can coexist with other oxides and create mixed or intermediate phases. Depending on the oxidation state of vanadium, the vanadium oxides form three distinct families, where the VO_2 appears at the limit between Magnéli (V_nO_{2n-1}) and Wadsley (V_nO_{2n+1}) phases. Basically, it is possible to describe the stoichiometric phases through a phenomenological approach where interconnections between oxides are based on transformations from the same parent structure. During such transformations, oxygen vacancies are created by reduction from V^{+5} to V^{+4} and V^{+4} to V^{+3} and following condensation of the structures crystallographic shear occurs. Thus, the structures of the $V_nO_{2n\pm1}$ families can be interpreted as a succession of crystallographic planes where oxygen reduction leads to the stabilization of the different oxides of the V-O system.

Even if their stoichiometries are different, the existence of similar transformation mechanisms in the $V_nO_{2n\pm1}$ structures (crystallographic shear) raises new questions and offers technological perspectives favoring the multi-functionality of materials. The VO_2 being delimited by the R and B phases, the study of their structures has shown that a crystallographic distortion along the $\vec{c}$-axis leads to forming the Magnéli and Wadsley phases, respectively. Furthermore, we know that VO_2(R) structurally transits to VO_2(M1) upon external stimulus application. The equidistant V atoms dimerize along the $\vec{c}_{VO2(R)}$-axis, resulting in lattice distortion and symmetry lowering to form the M1 structure. By analogy, if a contraction of the $\vec{c}_{VO2(B)}$-axis occurs, eliminating the intercalation channels present in the VO_2(B) could lead to a distortion of the lattice and allow the phase to transit towards higher symmetry structures such as M1 or R phases. Thus, the $\vec{c}$-axis in the VO_2 structures seems to be a key element to understand vanadium oxides formation and stabilization, and the transition mechanisms between phases.

The final goal of this work is the development of VO_2-based radiofrequency (RF) switches. In order to meet this objective, the VO_2 must be present in thin film form and possess high crystalline quality. As we have seen throughout this Chapter, the substrate is an important element to be considered during the fabrication of the device, because it can impact phase stabilization and transition performances. At the same time, the substrate must be compatible with RF applications, with low losses to maintain good RF performances. The targeted high crystalline quality of the VO_2 film and compatibility with the RF applications reduce significantly the potential candidates for the film deposition, and present a technological challenge. According to the state-of-the-art presented above, TiO_2(R) has a good lattice parameter matching with VO_2 but has high losses in the RF domain. On the contrary, high resistivity silicon (Si-HR) and lanthanum aluminate ($LaAlO_3$ or LAO) are both excellent candidates for our applications. However, the Si-HR cost and the difficulty in obtaining LAO on large surfaces exclude their use in this work. Consequently, the best compromise to obtain high-quality VO_2 films for RF applications was found with sapphire (Al_2O_3) substrates.

In parallel, the $SrTiO_3$ (STO) substrates were also used during this thesis to explore the growth of the VO_2(B) polymorph. The work developed in this thesis mainly aims to understand the origin of the phase stabilization and the consequences of the strain induced in VO_2 films on the MIT.

Chapter 2: Synthesis and characterization of VO_2 layers

Contents

There are many thin-film deposition techniques classified into two main categories: physical methods such as evaporation, sputtering, or pulsed laser deposition, and chemical processes in the vapor or liquid phase (chemical vapor deposition CVD, metalorganic MOCVD, atomic layer deposition ALD, etc.). The choice of one method rather than another is mainly based on the material chemical nature (metallic, organic, or composite), its morphology (thin film, nanowires, nanoparticles), its application and scalability for industrial processes. In order to achieve the thesis objectives, which lean on the high-quality films and later, the industrial ones at TE-OX, the radiofrequency magnetron sputtering (RFMS) technique was selected. Under optimized conditions, this method allows epitaxial growth and can be upscaled for industrial needs.

This chapter presents the description of our experimental RFMS setup, followed by a discussion about the influence of process parameters on the growth and stabilization of VO_2 oxide films. Then, the characterization tools involved in the physicochemical investigation of the deposited material will be described. Among the characterization techniques we will focus on X-ray diffraction (XRD), which allowed us to carry out a major part of our structural analysis. Raman spectroscopy allows a submicron local crystallographic characterization. A brief description of this technique will also be given. Finally, the last part of this chapter will be devoted to the characterization of electrical and optical properties of the material.

2.1. Radiofrequency Magnetron Sputtering (RFMS)

The sputtering is a well-established technique in the worlds of industry and research. It can synthesize metastable phases in specific thermodynamic conditions on large surfaces. This method is based on the ejection of atoms from the surface of a solid material (the target) by interacting with an ion flow. The resulting vapor condenses on a substrate and creates a continuous layer. This process of atom extraction by the kinetic energy transfer of incident ions from the plasma is known as sputtering. A mechanical mechanism of momentum transfer occurs when ion kinetic energy (E_i) is in the range of 10-1000 eV. At lower E_i, the ions are neutralized in contact with the target and are reflected as neutral particles. In opposite, at higher E_i, ionic implantation will occur (**Figure 2-1**).

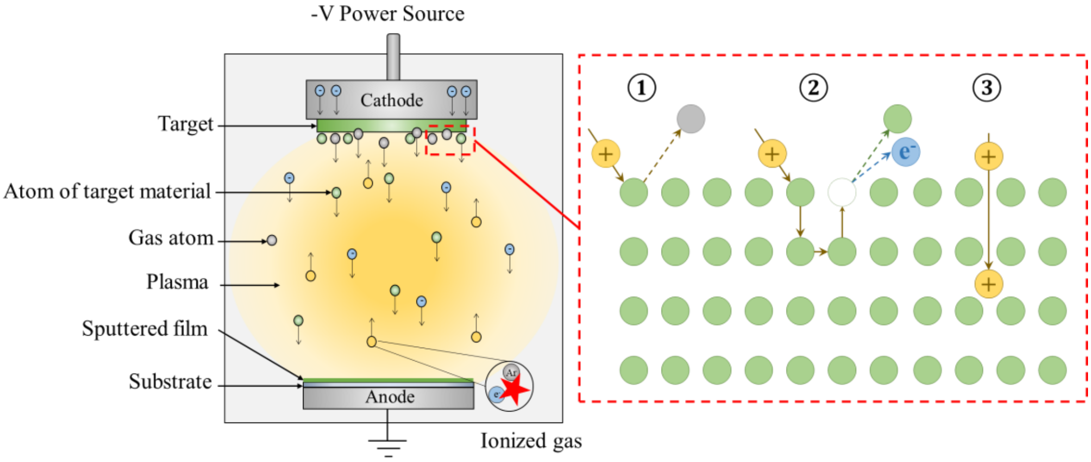

Figure 2-1: Principle of sputtering deposition technique and physical mechanisms during the ion-target interactions: ① The low energy ion reflects as a neutral particle, ② the sputtering mechanism, and ③ the high energy ion implants itself in the target.

The ion kinetic energy and its mass govern the number of atoms ejected from the target per incident ion. The average number of particles emitted from the target per incident ion is called the sputtering yield ($Y(E_i)$) (**Figure 2-2**).

$$\boxed{Y(E_i) \sim \frac{3}{4\pi^2}\frac{\alpha}{U}\frac{4M_T M_I}{(M_T+M_I)^2}E_i}$$

$$\alpha = 0.15 + 0.13\frac{M_T}{M_I}$$

M_I: Masses of incident ion (M_T~39.94 g/mol)
M_T: Masses of the sputtered atom (M_V~50.94 g/mol)
U: sublimation energy of target material
(Vanadium: 9283.2 J/g)

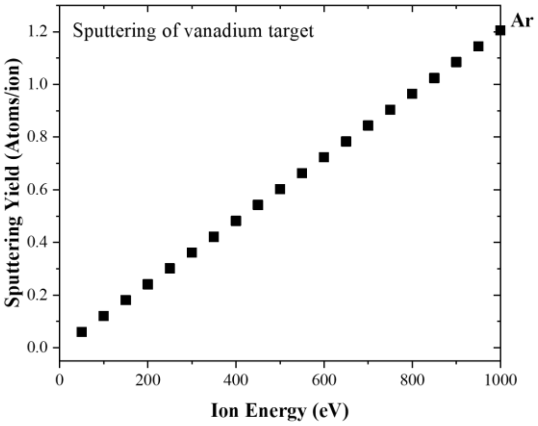

Figure 2-2: Sputtering yield of Vanadium target calculated as a function of the energy of incident ions for a range of 0-1000 eV.

The nature of the gas used significantly influences the sputtering yield. The higher the gas atomic mass (e.g., Krypton or Xenon), the higher is the sputtering yield. During the sputtering, secondary electron emission from the target is also observed. It can result from different phenomena such as thermionic emission, field emission, or bombardment by the particle flow. Although the study of these phenomena is complex, it is indisputable that the emission of secondary electrons participates in the ionization of the gas and contributes to the self-maintenance of plasma. To maximize these collisions, it is necessary to work at pressures higher than 10^{-2} mbar. Unfortunately, this pressure range leads to low deposition rates and high thermalization of the sputtered atoms resulting in the synthesis of porous coatings. To overcome such trouble, the so-called magnetron configuration is used to increase ion production by increasing the collisions between electrons (primary and secondary) and the gas in the vicinity of the target. The combined effects of the electric field ($\vec{E}$) created by the potential gradient around the cathode and the magnetic field ($\vec{B}$) from permanent magnets impact the trajectories of electrons hitherto rectilinear (eq.(2.1)). The electrons wrap around the magnetic field lines and are confined closest to the cathode. This phenomenon is also known as the magnetron effect.

$$\vec{\mathrm{F}} = \mathrm{q}\left(\vec{\mathrm{E}} + \vec{\mathrm{v}} \wedge \vec{\mathrm{B}}\right) \tag{2.1}$$

Where $\vec{\mathrm{F}}$ is the Lorentz force, q the electric charge, and $\vec{v}$ the instantaneous velocity of the particle.

The magnetron effect increases the distance traveled by the electrons and raises the probability of collision and, consequently, the ionization of gas atoms. The increase of the number of electrons leads to more important ion bombardment of the target, which increases the amount of sputtered material. Higher deposition rates are achieved (> 10 nm.min^{-1}) together with a stabilized discharge at lower pressures (10^{-3} mbar). Although the numerous advantages of the magnetron device, the confinement of the electrons results in a non-uniform erosion of the target (**Figure 2-3**). In addition, the increased ion bombardment induces higher heating of the target, requiring an efficient cooling circuit.

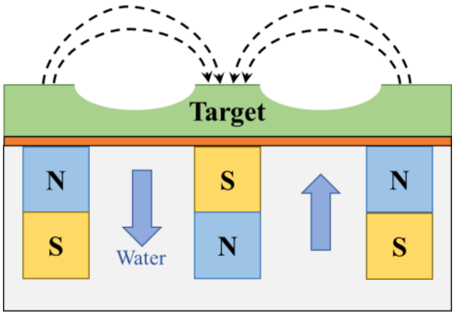

Figure 2-3: Magnetron source with a non-uniform target erosion profile. Central magnet has its poles (north N and south S) inverted with respect to edge magnets, to obtain field lines as displayed (dashed).

2.1.1. Experimental setup

The development of VO_2 layers was performed using a 1-inch vanadium metal target (99.9% purity) and a gas mixture of argon (Ar) and oxygen (O_2)[1]. The stoichiometry of the deposited layers being very sensitive to the injected O_2 flow rate, the O_2 massflow used can change the amount introduced from 1 to 5 sccm with a precision of 1%. The 1-inch diameter and 3 mm thick target was mounted on a 1.33-inch MEIVAC® cathode, placed at a distance (d_{st}) from the substrate that can be varied. The substrate is placed in front of the cathode (face-to-face sputtering) and fixed with silver paste on the sample holder. Substrate heating during the deposition is performed by an electric resistance placed inside a heating rod. The substrate holder was screwed on the heating rod in order to ensure good thermal contact between the rod and the sample holder. All pieces that undergo high temperature conditions (sample holder, heating rod, and screws) are made of Inconel® 600 in order to resist in the oxidizing atmosphere. The temperature is controlled by a TDK Lambda® Genesys 600 V- 2.8 A power supply allowing for a temperature range from 20°C to 700°C. The difference between temperatures measured on the sample surface and on the heating rod is reported in Appendix 1. The deposition chamber is connected to a pumping system and the limit vacuum of 10^{-7} mbar is achieved by a Pfeiffer® HiPace turbomolecular pump linked to an Edwards® primary pump. The pressure inside the chamber is controlled by a cold cathode vacuum gauge (Pfeiffer®) and has a knife gate valve to adjust it. **Figure 2-4** shows an overview of the experimental setup.

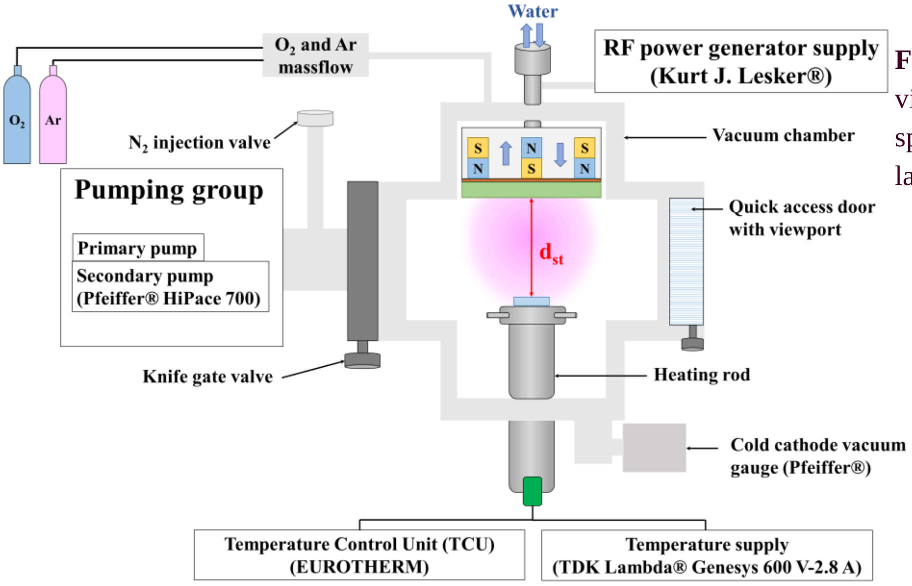

Figure 2-4: Schematic view of the RF magnetron sputtering system at C2N laboratory (OXIDE team).

---

[1] For simplicity of writing, we will use the abbreviation sccm (standard cubic centimeter per minute) to describe gas volume flow. The O_2/Ar ratio is defined as the ratio of their respective volume flows.

To initiate and maintain an active plasma, we have seen previously that it is necessary to bring thermal or electromagnetic energy. Electrons subjected to a magnetic field and an electric field for magnetron sputtering acquire sufficient kinetic energy to ionize the gas and maintain the discharge. In our study, the alternating mode discharge was used to initiate the discharge more easily and to grow insulating materials such as VO_2. The working frequency is set at 13.56 MHz, at which only electrons respond to the electric field. Ions are subjected to a time-averaged potential because of their strong inertia. This difference in mobility conducts the RF electrode self-bias to a negative potential during the voltage alternation. Since no charge can flow through an insulating target, the surface potential of the electrode adjusts to equalize the positive and negative charge flows. In this way, the average current on the electrode is zero. The major drawback encountered when using a RF power supply is the low spraying efficiency due to the alternating voltage, that lowers the deposition rate compared to a continuous or pulsed power supply.

2.1.2. VO_2 growth parameters

In the RFMS technique, many parameters are interconnected and can influence the growth. The target-substrate distance (d_{st}) impacts particle kinetics and the power injected at the cathode. The temperature and/or the pressure influence the diffusion kinetics of the particles on the substrate surface, but also the microstructure and crystallinity of the deposited film. In our work, we have focused on the parameters that can impact the stabilization of the VO_2 polymorphic phases. In the rest of this section, we will first discuss the phenomena that occur at the target, then the interaction of sputtered atoms with the plasma, and finally, the kinetics of incident particles at the sample surface (**Figure 2-5**).

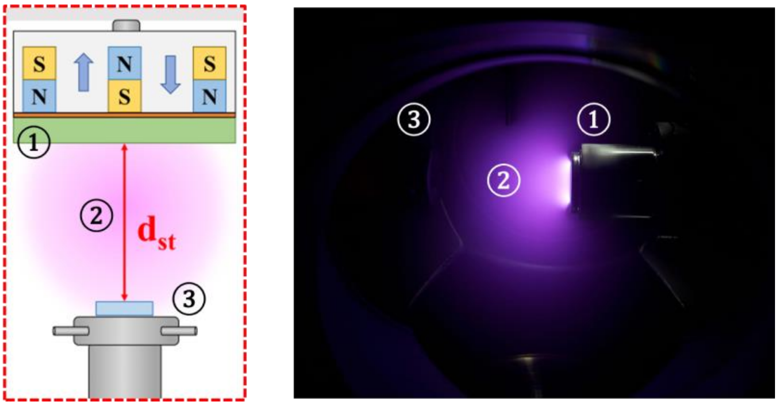

Figure 2-5: Scheme and picture of ① the cathode, ② the plasma, and ③ the sample holder placed in front of the cathode at distance d_{st} (tunable).

Influence of oxygen flow

When oxygen is introduced into the reactor during the sputter deposition, some of the gas will interact with the various elements such as the target or the reactor walls (including the substrate). The RFMS technique confines the plasma as close as possible to the target by magnetron effect, the reactivity is higher near the target. Depending on the experimental conditions (oxygen amount, RF power, etc.), two physical phenomena can occur on the Vanadium target: the oxidation and the sputtering. The dynamic equilibrium between these two states is characterized by a hysteresis cycle which affects the state of the metallic target, the reactor walls and finally the film stoichiometry. The introduction of oxygen leads to oxidation of all reactive surfaces into the reactor (cathode, film deposited on chamber walls, etc.). Once the plasma discharge is activated, argon ions interact with the target with kinetic energy between 10 and 1000 eV, and tear off neutral species such as metallic atoms, metallic oxides, but also oxygen atoms. Thus, the sputtering depends on the introduced gas flows and on the kinetic energy of argon ions that interact with the target. There is a continuous competition between these oxidation and sputtering phenomena on the target surface.

The growth of stoichiometric oxide layers is generally impacted by the nature of the incident species, that makes essential the control of the flow of introduced oxygen. If the oxygen flow is high, the oxidation phenomenon overcomes the sputtering. In other words, each atom ejected from the target is immediately replaced by an O-atom. An oxide layer will progressively form on the target until its entire surface is oxidized. This phenomenon is known as “target poisoning”. The sputtering rate of the oxide being much lower than that of the metal, it will strongly decrease the deposition rate. On the contrary, if the oxygen flow is low, the erosion rate is higher than the oxidation rate. On the surface of the target, its metallic atoms appear. Change of the physicochemical state of the cathode due to O_2 introduction modifies the plasma impedance and results in a hysteresis cycle, which is defined as two stable states (oxidized and metallic) with rapid transitions between them. This hysteresis can be observed through the variation of the electrical parameters of the discharge that can be experimentally monitored. **Figure 2-6** shows the evolution of the self-bias voltage (V_{DC}) during O_2 injection in our RFMS system. The argon flow was kept constant while the oxygen flow was varied to change the O_2/Ar ratio. The total pressure was kept constant at $2.5*10^{-2}$ mbar with the knife gate valve.

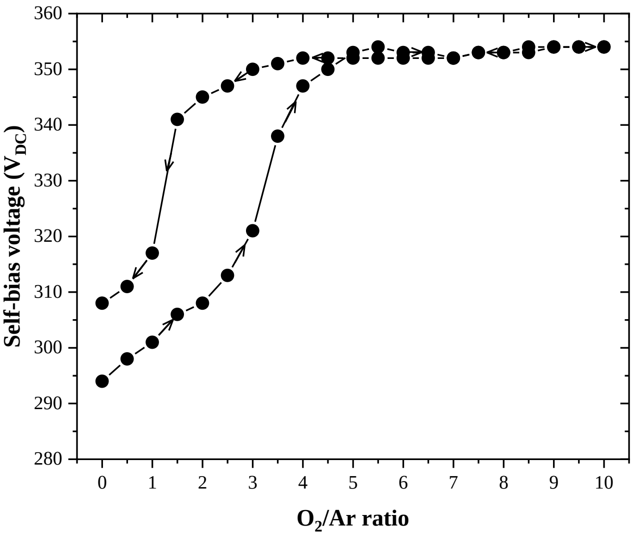

Figure 2-6: Experimental measurement of the self-bias voltage (V_{DC}) as a function of the O_2/Ar ratio. The O_2 flow was swept as indicated by the arrows, while the total pressure was kept constant at $2.5*10^{-2}$ mbar.

When low O_2 flow rates are introduced in the deposition chamber, the amount of reactive gas adsorbed on the target is insufficient to form a continuous dielectric oxide layer on the target surface. The target remains in its metallic state. When the quantity of introduced oxygen becomes important (beyond $O_2/Ar \geq 5$), the oxide created on the surface of the target modifies the plasma impedance, decreases the sputtering yield ($Y(E_i)$), and consequently, the particle flow coming from the target. Between the metallic and oxidized states, the cathode is in an unstable state where the history of the deposition chamber and target operating parameters can have an impact. As we will see in the following section, the formation of “stoichiometric” VO_2 occurs in a restricted range of O_2/Ar ratio around the center of the hysteresis. This hysteresis phenomenon makes it even more challenging to control and obtain perfectly stoichiometric VO_2 by sputtering.

Influence of RF power

Since the 1980s [THO77], the cathode hysteresis phenomenon has been recognized as a difficult-to-control parameter that impacts film properties. Still, many oxides are obtained at the limit of the metal/oxide transition of the target. At this point, the dynamic balance between sputtering and oxidation phenomena is sensitive. A slight change in the experimental conditions can result in under or over oxidized films. Since the parameters and growth kinetics are specific to each reactor, power tests were performed to optimize the stoichiometric VO_2 growth. **Figure 2-7** shows the influence of RF power on the oxidation state of Vanadium for different oxygen flow rates. The sputtering rate of metallic species being more important than that of oxidized species, it is essential to pay attention to the erosion rate according to the O_2 flow introduced. If the erosion rate is higher than the oxidation rate, a higher O_2 flow rate will be necessary. In the opposite case, a low erosion rate can lead to a predominance of the oxidation phenomenon. This results in a decrease of the sputtering yield and an overoxidation of the V-atoms.

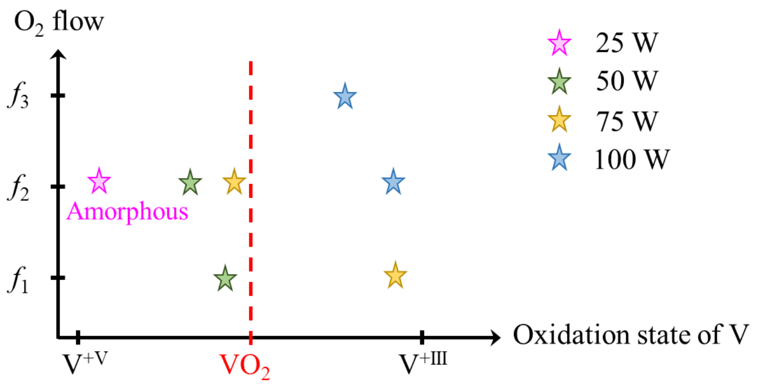

Figure 2-7: Influence of RF power on the oxidation state of vanadium atoms for different O_2 flow ($f_1 < f_2 < f_3$). From experimental data, the obtained vanadium oxides are identified by XRD after growth.

Influence of total pressure

Before reaching the substrate, the particles ejected from the target will interact with the plasma composed essentially of neutral argon atoms. Depending on the distance traveled by the particles and the gas pressure, these will undergo collisions that can modify their kinetic energy and direction. This generally results in a thermalization of the sputtered atoms simultaneously with an increase of the average temperature of the gas. The probability of collision is expressed from the mean free path of a particle. The latter is defined as the average distance traveled by a particle between two successive collisions (eq.(2.2)).

$$\lambda = \frac{k_B T_{RT}}{P(\pi\sqrt{2}(r_{Ar} + r_V)^2} \tag{2.2}$$

Where k_B is the Boltzmann constant, T_{RT} the room temperature (300 K), r_{Ar} and r_V are the atomic radii of argon and vanadium, and P is the pressure in Pa. **Figure 2-8** shows the calculation result for vanadium and oxygen atoms.

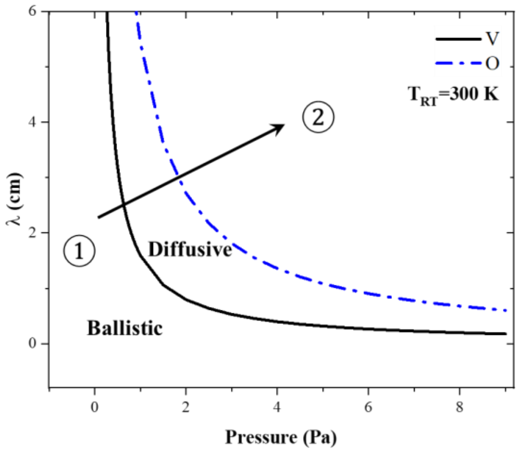

Figure 2-8: The mean free path in function of the total pressure for vanadium and oxygen atoms.

When the substrate-target distance (d_{st}) is smaller than the mean free path, the particles do not undergo any collision on average. In this case, their transport within the plasma is done according to a ballistic regime. When the particle ejected from the target undergoes collisions (such as argon), it loses kinetic energy and "relaxes". Beyond a certain number of collisions, this particle thermalizes, i.e., its energy becomes comparable to the thermal energy of the gas atoms, i.e., 0.04 eV at RT (300 K). Under these conditions, the particles lose their initial direction, and their transport is done according to a diffusive regime. The reactor used for VO_2 layer growth has a variable target distance allowing, in theory, to scan a wide range of pressure-distance values. This would theoretically enable us to reach different zones from the purely ballistic ① regime to the thermalized ② one (**Figure 2-8**). In our experimental setup, we work at a substrate-target distance of 7 cm and a total pressure of $2.5*10^{-2}$ mbar = 2.5 Pa. Consequently, we can be supposed that particles ejected from the target can be in the thermalized regime.

Influence of the substrate temperature

When the particles (metal atoms, metal oxides, oxygen atoms) leave the target (after interactions in plasma), they collide with the substrate surface with different kinetic energies. Their adsorptions with the substrate surface form adsorbates (or adatoms). Depending on the interactions between adatoms with the substrate, the adsorption can be classified into two families: physisorption and chemisorption. In the case of physisorption, the adatoms form weak Van der Waals bonds with the substrate. There is no electronic transfer between the adatom and the surface. For chemisorption, stronger chemical bonds are formed, such as covalent, ionic, or metallic bonds.

After adsorption of adatoms, the diffusion mechanisms appear due to the thermal energy brought by the heater sample-holder. Depending on the provided thermal energy, the growth mode and the structure of the layers can be significantly affected. They are able to influence many properties of films in electrical devices, for example. Thus, it is important to understand firstly these growth mechanisms.

a) Temperature impact on growth mechanism

Diffusion plays a significant role during the epitaxial growth of the layers. Depending on the technique used, the nature, and the surface of the substrate, different types of growth can be obtained. **Figure 2-9** shows the elementary processes occurring on the surface of the substrate during thin film growth.

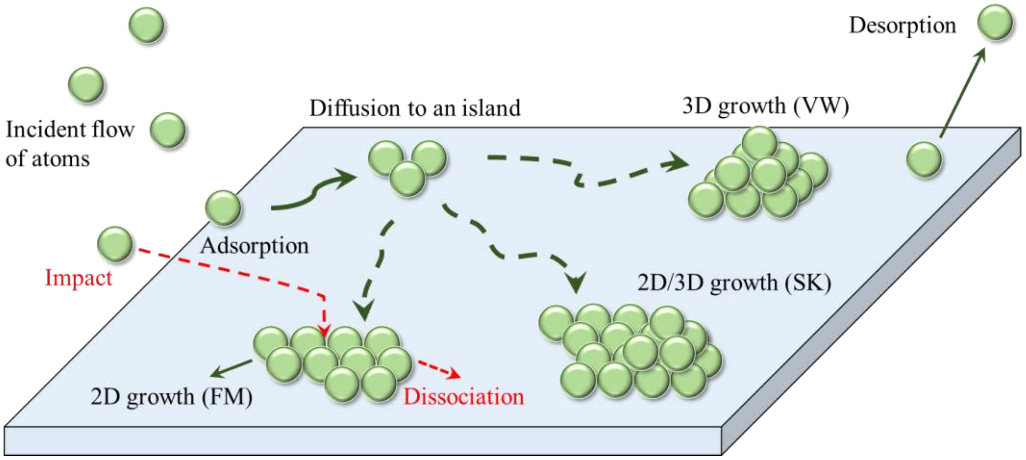

Figure 2-9: Elementary processes during thin film growth. The incident atoms adsorb, diffuse, and gather into islands on the substrate surface. The islands grow in two or three dimensions depending on the surface energy balance between film and substrate.

After adsorption of incident atoms on the substrate, adatoms diffuse on the surface and interact to form islands. Islands can be defined as stable or unstable depending on their size: if they are smaller than a critical size, they are considered unstable. In this case, their atoms diffuse towards the stable islands of larger size, for which the growth process can start. Depending on the surface energies of the substrate (γ_s), the growing film (γ_f) and the interface energy between the two (γ_i), different growth modes are established [MAR96][LUT10].

i. Frank van der Merve growth: When $\gamma_f + \gamma_i < \gamma_s$, the minimization of surface energy favors a layer-by-layer growth. It results in a two-dimensional (2D) growth where the whole substrate is covered with a flat and low roughness film.
ii. Volmer-Weber growth: When $\gamma_f + \gamma_i > \gamma_s$, the growth proceeds through the formation of three-dimensional (3D) islands. The Wulff theorem allows one to understand the facet geometry of the islands and can explain in part the roughness of the films [MAR96][PON18].
iii. Stranski-Krastanov mode is an intermediate case: After forming one or several 2D monolayers, 3D island formation occurs. Many factors can explain this mixed growth mode, such as lattice mismatch between substrate and film. The elastic energy stored by the layer increases with the thickness (t) until reaching a critical thickness (t_c). When $t > t_c$, the stress relaxes by the formation of 3D islands.

In parallel to the different growth modes, the incident particles coming from the target continue to arrive on the substrate surface at different energies. Thus, the islands can also be dissociated under the impact of an incident particle with high kinetic energy. Also, adatoms can desorb from the surface if their thermal energy (substrate temperature) is high enough.

b) Temperature impact on microstructure

The substrate temperature provides energy to the system during thin film growth. It powers the diffusion of adatoms on the surface and can modify the film microstructure. Based on experimental results and Thornton model [THO77], Grovenor *et al*. proposed a new model in 1984 explaining the link between temperature and microstructure [GRO84]. **Figure 2-10** shows this substrate temperature effect on the film microstructure as of function of the melting temperature of the deposited material.

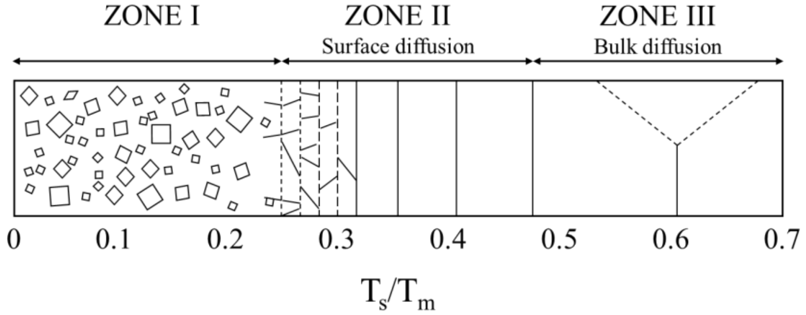

Figure 2-10: Effect of the substrate temperature (T_s) on the film microstructure as a function of the melting temperature (T_m) of the deposited material. The ideal temperature is in the range $0.3 < T_s/T_m < 0.5$ [GRO84].

Zone I ($T_s/T_m < 0.2$) consists of tiny crystals (5-20 nm) separated by voided boundaries. The thermal energy brought to the system is low, leading to a strongly reduced adatom mobility. The resulting films are generally rough and have a high dislocation density. With the increase of T_s/T_m up to $T_s/T_m < 0.3$, the diameter of crystallites increases. When a higher temperature is applied (Zone III, $T_s/T_m > 0.5$), bulk diffusion becomes the predominant phenomenon. It favors the growth of large crystallized grains, but also the interdiffusion of atoms between the substrate and the layer. Generally, substrate temperatures allowing the surface diffusion of adatoms while avoiding interdiffusion are between $0.3 < T_s/T_m < 0.5$ (Zone II). In this zone, the films appear smooth with low roughness, and dislocations are primarily in boundary regions. Grain size increases with T_s/T_m and may extend through the whole film thickness at high T_s/T_m.

Like the Thornton or Movchan-Demchishin model, the Grovenor model remains a qualitative representation of the link between morphology and deposition conditions. In practice, the zones can vary according to the deposition technique, the type of power source, or the material deposited. For VO_2, the optimal substrate temperature (T_s) range calculated from its melting point (1967°C=2240 K) is given by eq.(2.3):

$$\begin{gathered}(0.3 * 2240) < \mathrm{T_s} < (0.5 * 2240) \\ 672 < \mathrm{T_s} < 1120\ \mathrm{K} \Longrightarrow 400 < \mathrm{T_s} < 850\ ^{\circ}\mathrm{C}\end{gathered} \tag{2.3}$$

c) Temperature stabilization of VO_2 polymorph phase

As we have seen above, many parameters can influence layer growth. Depending on oxygen flow, the target surface can be modified, changing the plasma impedance and consequently, modifying the sputtering yield. The particle flow from the target combined with the partial pressure of oxygen introduced in the chamber may influence the capacity of stabilizing one oxide rather than another. The VO_2 being particularly sensitive to its oxidizing environment and belonging to a rich phase diagram, two parameters, substrate temperature and O_2/Ar flow ratio, had to be carefully controlled. The phase diagram presented in **Figure 2-11** shows the conditions specific to our experimental setup allowing to obtain different phases of vanadium oxides. The pressure was kept at $2.5*10^{-2}$ mbar and the RF power was constant at 100 W.

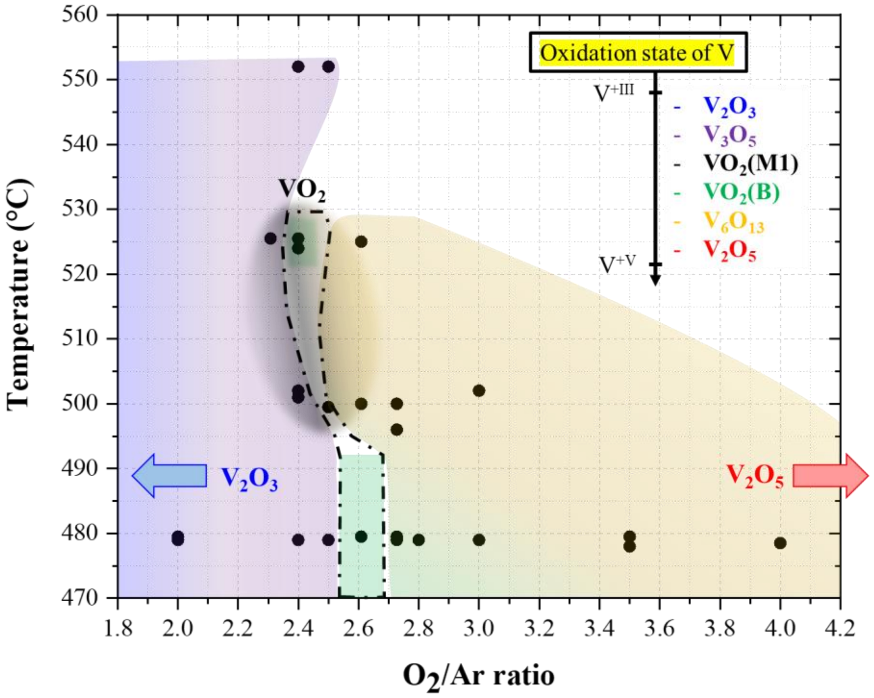

Figure 2-11: Experimental phase diagram for vanadium oxide thin films obtained by RFMS.

Although theoretical optimal substrate temperature was previously calculated between 400 to 850°C, our experimental investigation shows that in order to stabilize VO_2 (M1 or B) phase, we must work in the $450 < T_s < 550$°C temperature range under a O_2/Ar flow ratio between 2.4% and 2.8%. Below 450°C, the thermal energy brought to the system is insufficient to obtain a crystalline epitaxial layer. Furthermore, growth below 2.4% resulted in the stabilization of oxides with lower oxidation states (between +III and +IV), such as V_2O_3 or V_3O_5. While, over 2.8%, the oxidation phenomenon was accentuated, and oxides such as V_6O_{13} or V_2O_5 were promoted.

2.1.3. Thickness effect on VO_2 deposited layers

The growth of VO_2 thin film by the RFMS technique relies on many parameters: distance, RF power, pressure, and temperature. All of them are significant, and a slight modification of one can lead to an oxide with a different Vanadium oxidation degree. For a good reproducibility each of these parameters requires to be well controlled. During this work a significant number of process optimization and setup maintenance steps were performed that also highlighted or revealed the importance of the target setup on the cathode.

As presented in section 2.1.1, VO_2 films were obtained from a 1-inch vanadium target mounted on a MEIVAC® cathode. For this type of cathode, two means of target attachment are possible. The first one is to screw the target with a keeper. The second method is to glue the target with silver paste on a copper plate, itself screwed to the keeper. In both cases, the assembly is fixed to the cathode by magnetic force. The second method was selected for this work, using a high-performance silver paste (Pelco®) compatible with high vacuum. For some technical reasons (maintenance), two series of deposition were performed, and the target was removed then glued again in between the two. When we compared the two series at similar experimental conditions, we found that the film thicknesses were not identical. At the same O_2 flow rate and temperature, we observed a deposition thickness twice as high as the value measured previously. The thickness was estimated by an etched step height measurement with a stylus profilometer (Veeco® Dektak08). Therefore, the determined film thickness allows estimating the growth rate (v_D) and indicates a change from 12.5 nm.min^{-1} to almost 25 nm.min^{-1}. The difference in films thickness between these two series is mainly due to how the target was glued to the copper plate. It is thus very important to pay attention to the target fixation. If open spaces remain at the interface between the two elements or if the silver paste overflows from the target (**Figure 2-12**(b)), a parasitic capacitance can appear (**Figure 2-12**(a)) that affects the RF discharge.

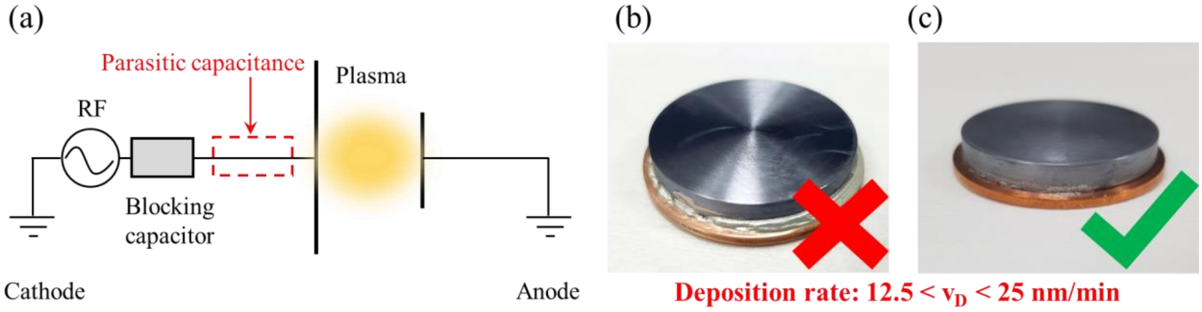

Figure 2-12: (a) Equivalent electrical diagram of a cathode fed by an RF generator. A possible bad contact between the target and the target keeper is represented by a parasitic capacitance. (b) and (c) Pictures of two glued vanadium target with silver paste.

When the target fixation was well established and substrate/target distance was selected at 7 cm, the thickness calibration has been performed. **Figure 2-13** shows experimental data for the evolution of film thickness as a function of deposition time that follows a quasi-linear behavior between 5 and 30 min.

For TE-OX industrial applications and process requirements, the VO_2 film thickness was targeted at 250 nm. This choice will be further justified in Chapter 5.

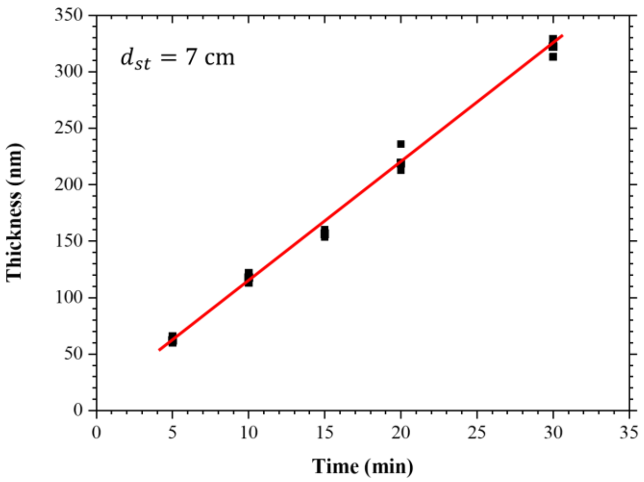

Figure 2-13: Evolution of the film thickness for a fixed substrate/target distance of 7 cm. The optimal time to obtain a 250 nm layer is 20 min.

In this section, we have seen an overview of our experimental sputtering setup and presented in details the impact of multiple parameters involved in the deposition process, individually and in interplay between them. The oxygen flow, total pressure and substrate temperature are here the most important parameters that influence vanadium oxide stabilization. The following section will introduce the main characterization techniques that were necessary for the optimization and understanding of VO_2 film growth as well as the characterization methods allowing to explore the grown film properties.

2.2. Structural and morphological characterizations of the layers

2.2.1. X-ray diffraction (XRD)

X-ray diffraction (XRD) is the ultimate characterization technique to gain information on the crystal structure of materials. Governed by Bragg law, this non-destructive probe allows determining the crystalline phase, the lattice parameters, and in some cases, the thickness of a layer. It also provides information about the preferential growth orientation, the lattice deformation state, and the size of crystallites. During this thesis, the deposited layers were systematically analyzed by XRD. The crystalline phase, orientation and epitaxial relations were determined using a PANalytical® X'Pert Pro diffractometer. Reciprocal space mappings were done with a Rigaku® Smartlab diffractometer. Finally, temperature-dependent XRD measurements of our VO_2 films have been performed on a custom-built diffractometer at CentraleSupélec.

X'Pert Pro diffractometer (**Figure 2-14**) is equipped with a Copper (Cu) source. A 1/2° slit is placed right after the X-ray source to limit the beam divergence. The incident beam is made parallel thanks to parabolic mirror (Göbel mirror). The $K_{\alpha 1}$ (λ=1.5406 Å) line of Cu is selected by a monochromator with four oriented germanium crystals (220) placed after the parabolic mirror. The size of the incident beam can be adjusted with the help of crossed slits placed behind the monochromator. Once diffracted on the sample, the beam first passes through a 1/4° slit before reaching the detector. This slit allows reducing the parallel beam-induced width of the diffraction peaks.

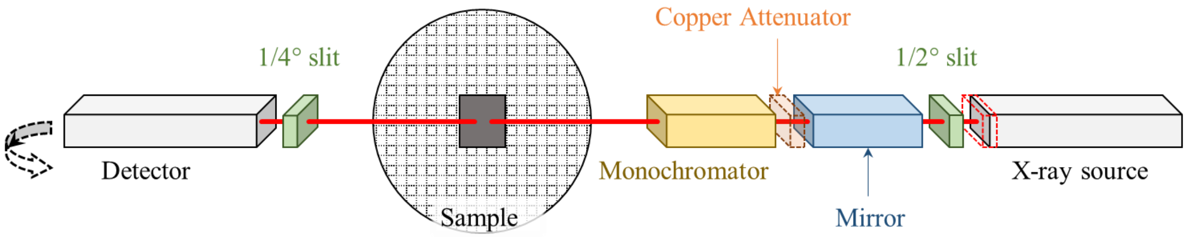

Figure 2-14: PANalytical® X'Pert Pro diffractometer configuration for θ-2θ diffractogram acquisition.

Samples are placed on a motorized sample holder that enables x, y, and z translations. The rotations ω, χ, and φ more precisely align the sample with the (*hkl*) planes in diffraction conditions by compensating for the angle offsets of the sample on its support. During a θ-2θ (also called ω-2θ) scan, the incident X-rays have an angle ω to the sample corresponding to an angle θ with the (*hkl*) planes (due to ω-offset). The detector collects the diffracted beam at an angle 2θ (**Figure 2-15**(a)) from the incident beam. When incident monochromatic X-rays interact with a sample, they are scattered in all directions by inelastic or elastic processes. Inelastic scattering occurs when the scattered length is greater than the incident wavelength. For elastic scattering, the incident length is equal to the scattered length. In this case, diffracted intensity direction follows Bragg law given by eq.(2.4):

$$n\lambda = 2d_{hkl}\sin(\theta) \tag{2.4}$$

Where *n* is the order of diffraction, d_{hkl} the inter-reticular distance between (*hkl*) planes, θ the angle between the incident beam and the diffracting planes, and λ the wavelength of X-rays. From the θ-2θ diffractogram, the peak position analysis allows identifying the crystalline phases, orientations, and to calculate the lattice parameters from the inter-reticular distances.

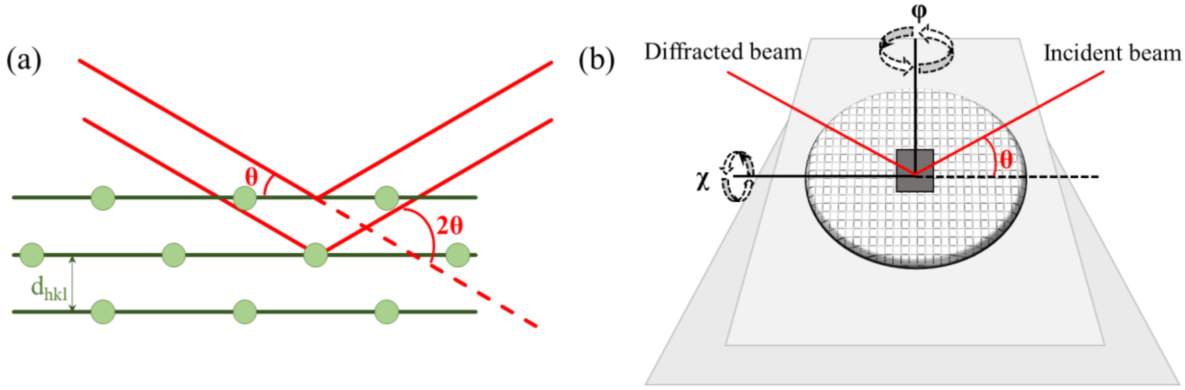

Figure 2-15: Schematic representation of (a) Bragg law, and (b) principle of φ-scan measurement in XRD.

The epitaxial relationships between film and substrate can also be determined with the X'Pert Pro diffractometer from φ-scan measurements in asymmetrical and symmetrical conditions. To perform them, sample (θ) and detector (2θ) angles were fixed to the values of the selected (*hkl*) plane (**Figure 2-15**(b)). The sample holder was then tilted by an angle χ (symmetrical case) or ω (asymmetrical case), corresponding to the crystallographic angle between the surface and the selected plane. This brings this plane in diffraction condition provided the azimuth (φ) allows it. The diffracted intensity is finally measured while the φ angle is scanned over 360°. Asymmetrical scans are usually preferred for a best angular resolution, but sometimes it is impossible to do that. Some planes in these conditions can have low diffusing power or are situated in the "blind" regions of reciprocal space. Symmetrical conditions are more easily attained but care must be taken in their interpretation. In our case, symmetrical conditions were appropriate to determine epitaxial relationships between VO_2 film and substrate. The measurements were made for several selected (*hkl*) planes from layer and substrate to determine in-plane epitaxial relationships.

During our work, triple-axis mode measurements were performed to help understand the relationships between VO_2 and substrate. Contrary to the dual-axis configuration, the triple-axis mode has a low angular acceptance at the detector, which allows for a quasi-total deconvolution of the $2\theta - \omega$ scans and more resolved diffraction peak profiles. We used this mode when diffraction peaks from two (*hkl*) planes were too close to be resolved in the classical dual-axis configuration.

Rigaku® Smartlab diffractometer (**Figure 2-16**) is equipped with a 9 kW rotating copper anode allowing 6 to 7 times more intensity than a traditional system. This equipment has been used to map the reciprocal space of VO_2 layers to help understand their epitaxial relationships with the substrate, and to measure the in-plane lattice parameters.

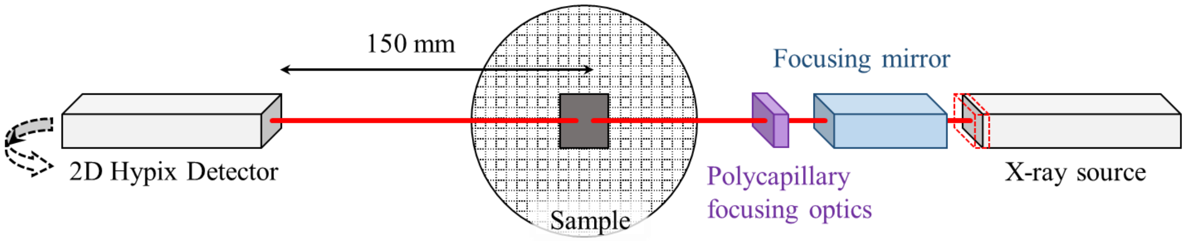

Figure 2-16: Rigaku® Smartlab diffractometer configuration for realization of reciprocal space mapping.

The instrumental configuration used to map large sections of the reciprocal space does not have a monochromator. The incident X-ray beam is first concentrated linearly by a focusing mirror. Then a point beam is defined by a converging polycapillary lens. We used a 5 mm mask and no collimating optics in reception. Finally, a 2D Hypix detector placed at 150 mm from the center of the goniometer is used to allow the largest possible field of observation. Reciprocal space mapping (RSM), by definition, corresponds to a set of $\theta - 2\theta$ scans taken over a range of ω offsets (sample inclination). They are generally represented in units of the reciprocal lattice using the Q_x and Q_z components of the diffusion vector **Q** defined by the following relationships:

$$\begin{aligned} Q_x &= K[\cos(\theta - \omega) - \cos(\theta + \omega)] \\ Q_z &= K[\sin(\theta - \omega) + \sin(\theta + \omega)] \end{aligned} \tag{2.5}$$

Where $K=2\pi/\lambda$ is the magnitude of the X-ray wave vector. From the indexed coordinates for each diffraction spot in the reciprocal space, it is possible to calculate the inter-reticular distance (eq.(2.6)) of the corresponding planes.

$$d_{hkl}[nm] = \frac{1}{\sqrt{Q_x^2 + Q_z^2}} \tag{2.6}$$

A custom-built diffractometer is used for X-ray diffraction in temperature. X-ray data collection was performed on a homemade goniometer (radius = 500 mm) [BER80] associated with a Rigaku RA-HF18 rotating anode generator (50 kV, 200 mA). The diffractometer was upgraded, adding a few sample stage movements from Newport and Huber in order to manage measurements on powders, bulk single crystals and thin films. There are seven movements: four rotations (2θ, ω, χ, φ) and three translations (x, y, z). The wavelength is Cu $K_{\alpha 1}$ obtained with a Göbel mirror and Ge monochromator. Two types of measurements were carried out on this equipment:

i. At high temperature (HT), each data set was recorded in 10-55° plus 75-88° 2θ ranges, with a step size of 0.02°, and a counting time of 2 seconds per step. The temperature was varied in a Rigaku furnace from room temperature to 727°C.
ii. At low temperature (LT), the measurements were performed in a liquid nitrogen cryofurnace from -173°C to 92°C. Each 2θ scan was taken with a step size of 0.02° and a counting time of 1 second per step.

2.2.2. Raman spectroscopy

Raman spectroscopy is an analytical technique where scattered light is used to measure the vibrational modes of the sample, or so-called Raman active phonon modes. This non-destructive optical analysis can provide both chemical and structural information. When a monochromatic laser light excites a material, a part of the incident light is transmitted, another is reflected, and a small portion is scattered. The latter is presented in two distinct forms, Rayleigh scattering and Raman scattering. Rayleigh scattering can be defined as the elastic scattering of light whose wavelength is equal to the wavelength of the incident radiation ($\lambda_{scatter} = \lambda_{laser}$). The Raman scattering has much less intensity and is an inelastic process. If the molecule gains energy from the photon during scattering, then the wavelength of the scattered photon increases and this is called Stokes Raman scattering ($\lambda_{scatter} > \lambda_{laser}$). Conversely, if the molecule loses energy by relaxing, the wavelength of the scattered photon decreases and this is called anti-Stokes Raman scattering ($\lambda_{scatter} < \lambda_{laser}$). The energy difference between the incident and scattered photons can take discrete values that are specific to the vibrational modes of the material. **Figure 2-17**(a) presents the characteristic Raman spectra of VO_2 polymorphs. The Raman spectra are not represented as a function of wavelength but as a function of Raman shift ($\bar{\nu}$) given by eq.(2.7).

$$\bar{\nu}\,[\mathrm{cm}^{-1}] = \frac{\Delta\nu}{c} = \Delta\left(\frac{1}{\lambda}\right) \tag{2.7}$$

Each VO_2 polymorph has a Raman signature specific to its crystal structure, despite the identical composition. The VO_2(M1) structure has 18 Raman-active vibrations ($9A_g + 9B_g$), the same number as for VO_2(B) ($12A_g + 6B_g$), e.g., but they do not correspond to the same phonon vibrations [SHV19]. The bands at 192 cm^{-1} and 225 cm^{-1} in VO_2(M1) correspond to the stretching motion of V-V dimers along the $\vec{c}_{VO2}$-axis and the peak at 614 cm^{-1} could be related to the stretching mode of V-O vibrations. For the B phase, the four bands observed at 185, 257, 400 and 464 cm^{-1} are assigned to the V-O-V bending and V-O-V stretching modes. These differences can help identify the VO_2 phase of the films.

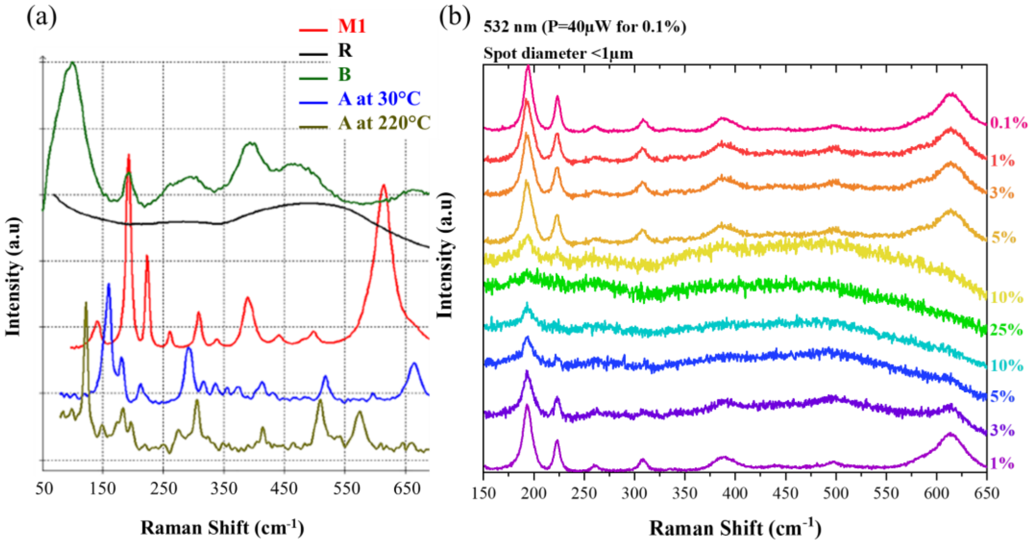

Figure 2-17: (a) Raman scattering of several VO_2 polymorphs [SHV19] and (b) evolution of experimental VO_2(M1) spectrum as a function of the laser power, at 532 nm excitation wavelength.

Additionally, depending on the penetration depth (z_p) of the incident beam, the substrate Raman signature can be visible together with the film spectrum. This characteristic absorption length can be determined by the Beer-Lambert law (eq.(2.8)).

$$\begin{gathered} I(z) = I(z=0)\exp(-\alpha . z) \\ z_p = \frac{1}{\alpha} = \frac{4\pi * k}{\lambda} \end{gathered} \tag{2.8}$$

Where α is the absorption coefficient and k the wavelength-dependent refractive index of the film, λ is the wavelength of the incident beam and z the depth taken from the film surface. At 532 nm, for our VO_2(M1) films $\tilde{n} = n + ik = 1.54 + i0.34$ (from ellipsometry measurements, see section 2.3.3), the calculated penetration depth is z_p~124 nm. z_p being less than half our VO_2 thickness, the substrate contribution to the Raman spectra is negligible, and indeed we never detected sapphire- or $SrTiO_3$-

related phonon peaks.

Raman spectroscopy measurements were performed on a HORIBA® LabRam HR evolution Raman spectroscope. The excitation source is a laser at 532 nm with a maximum power of 40 mW focused on the sample through a x100 magnification objective (Olympus®). The spot size is 1 µm in diameter. To reduce the laser beam energy, several attenuation filters can be used. Typically, our VO_2 layers were analyzed with 0.1 to 1% of the maximum laser power (**Figure 2-17**(b)). Above 3%, the laser beam tends to heat the layer and to make the VO_2 switch to its metallic phase: This laser heating-induced reversible M1 to R phase transition is clearly revealed by the Raman spectra. For temperature-dependent measurements, a Linkam® stage is used to control the sample temperature from -195°C to 200°C.

2.2.3. Other techniques

SEM (Scanning Electron Microscopy) **and AFM** (Atomic Force Microscopy) are non-destructive techniques used to investigate the topography and morphology of the films. Measurements were performed with a Hitachi® SU8000 SEM and a Bruker® Innova AFM, respectively. Processing of AFM images was performed with WsxM5.0 software developed by Nanotec Electrónica® [HOR07]. Topography and conductive AFM (c-AFM) measurements were also performed on a NX10 from Park Systems®. The contact cantilever for c-AFM is coated by B-doped diamond for electrical conductivity. The tip length is around 300 nm and has 10 nm radius (probe AD-2.8-AS). Thus, the root mean square roughness (R_{rms}) can be extracted for substrates and VO_2 thin films.

Energy-dispersive X-ray spectroscopy (EDX) was used after sputtering setup maintenance to analyze the sample elemental composition and detect a possible surface contamination. This powerful technique is based on the capacity of high-energy electrons to eject core-shell electrons from an atom, giving rise to radiative de-excitation with characteristic energy in the X-ray range. The detection of the resulting X-ray spectrum allows for a quantitative analysis of the sample composition, with about 1% (atomic) precision.

Transmission electron microscopy (TEM) was performed to follow temperature-assisted structural changes in the deposited VO_2 layers. The sample lamellas were previously prepared with focused ion beam (FIB) on the microscope Helios Nanolab 660 (FEI ThermoFischer®). The TEM measurements were performed with a Titan^3 G2 80-300 (FEI ThermoFischer®). Sample lamellas were placed on Protochips® (Fusion Select) for in situ electrothermal analysis, able to heat the sample up to 1200°C.

The understanding of VO_2 polymorph growth relies not only on physical characterizations, but also on the chemical aspects. We have seen in Chapter 1 that VO_2 is at the boundary between the Magnéli and Wadsley phases in the V-O system, where a slight variation of the vanadium oxidation may induce the formation of various polymorphs. Therefore, to characterize the vanadium oxidation state, **X- ray photoelectron spectroscopy (XPS)** was performed at room temperature. Further polymorph investigation by XPS probed the electronic structure (valence states) as a function of temperature. These measurements were made on the TEMPO beamline of SOLEIL synchrotron.

2.3. Electrical and optical characterizations

2.3.1. Electrical characterization: Resistivity measurement

Electrical characterization of the phase transition of the VO_2 layers was performed using resistivity versus temperature measurements. For this purpose, the four-point probe method was used. This one consists in putting four metallic probes spaced by 1 mm, in contact with the surface of the studied sample. **Figure 2-18** illustrates the four-probes (in line) method.

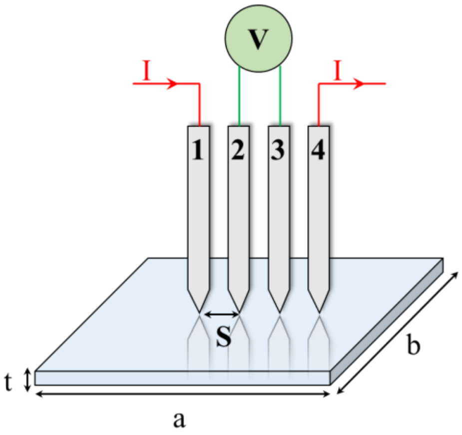

$$\boxed{\boldsymbol{\rho = \frac{\pi}{ln(2)} * t * R_s * F}}$$

$$R_S = \frac{\rho}{t} = \frac{\pi}{ln(2)} \frac{\Delta V}{I}$$

R_S: Sheet resistance (Ω.cm)
t: Thickness (cm)
F: Geometric correction factors
(10x10 mm: F≈0.93)

Figure 2-18: Resistivity measurement by the four-probe method. The current is injected through probes 1 and 4, and the voltage is measured by a voltmeter connected to probes 2 and 3.

The principle involves injecting a current between the external points (1 and 4) and measuring the voltage across the inner points (2 and 3). The sheet resistance (R_s) can then be calculated from the current-voltage measurements, and the resistivity (ρ) can be deduced. Although the equation for sheet resistance is independent of sample geometry, this only applies when the sample is both significantly larger and significantly thinner than the probe spacing. If this is not the case, the current paths between the probes are limited by the proximity to the edges of the sample, resulting in an overestimation of the sheet resistance. To account for this difference, a correction factor (F) based upon the geometry of the sample is required, as given by mathematical tables: For a 10x10 mm^2 square sample and 1 mm probe spacing, F is around 0.93 [SMI57]. Measurements have been performed on a home-built probe station under vacuum at 10^{-5} mbar, at temperatures ranging from room temperature to 100°C.

For the VO_2, the resistivity ratio between metallic and insulator states is one of the benchmarks for film quality. High film quality is observed for thicknesses well above 100 nm by sputtering with a MIT ratio of more than four orders of magnitude [BRA17]. Since film quality is a crucial element for developing photonic and electronic devices, it is essential to control the thickness of the synthesized sample.

2.3.2. Fourier-transform infrared spectroscopy (FTIR)

Alongside the electronic transition, VO_2 also exhibits an optical transition. To carry out these spectroscopic infrared (IR) measurements, the reflectance of VO_2 layers in the IR range was measured by Fourier transform infrared spectroscopy (FTIR). This non-destructive technique uses a Michelson interferometer to split the incident light into two beams using a semi-transparent KBr splitter. **Figure 2-19** shows a schematic representation of FTIR such as used at C2N.

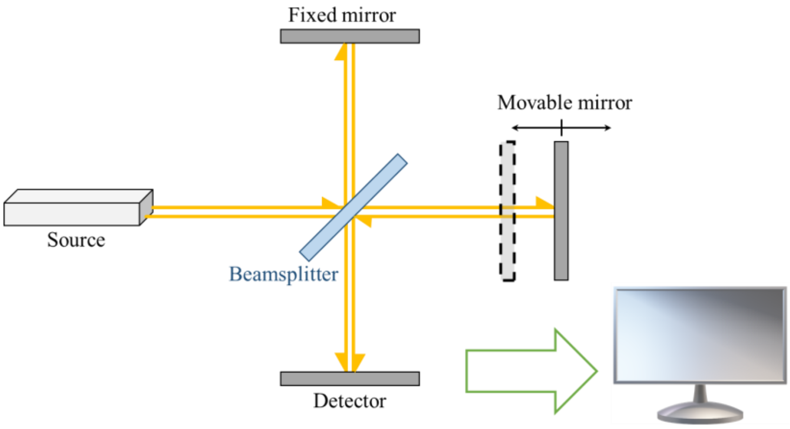

Figure 2-19: Schematic representation of the operation of a Michelson interferometer for FTIR.

When the incident light from the source arrives on the beam splitter, a part of the beam is reflected on a fixed mirror and the other one on a moving mirror whose displacement can delay the beam. During the recombination of the two beams, due to the phase shift an interference pattern is obtained. From the interferogram, the Fourier transform generates a FTIR spectrum that corresponds to the detector response as a function of the wavelength. The incident beam is focused with a collimator lens on the sample and then is detected with a MCT detector (Mercury Cadmium Tellurium) cooled with liquid nitrogen. During the measurements, the fast mode was used. The moving mirror is moved at a constant speed, and the detector signal is recorded as a function of mirror position. The measurement presents a background noise due to the low integration time, that was not found detrimental in our case. For characterization of the insulating-metal phase transition of VO_2 layers, measurements were made in reflectivity as a function of temperature using a Linkam® stage.

2.3.3. Spectroscopic ellipsometry

The thickness of the layers grown by RFMS was measured by ellipsometry, to avoid damaging the samples. Ellipsometry is a non-destructive optical technique that measures the change in polarization of an optical wave reflected by the surface of a sample. This technique has three main steps: instrument calibration, measurement, and data analysis. The measurements can be performed over a wide spectral range on complex structures such as multilayers or films with high roughness.

Considering a polarized monochromatic electromagnetic plane wave, a part of it is reflected by the surface, and the other is transmitted. The electric field of the reflected wave is described with two components resulting from the different reflections at each interface. These two components are the complex amplitudes of the electric field E_{rp} and E_{rs} , as depicted in **Figure 2-20**(a).

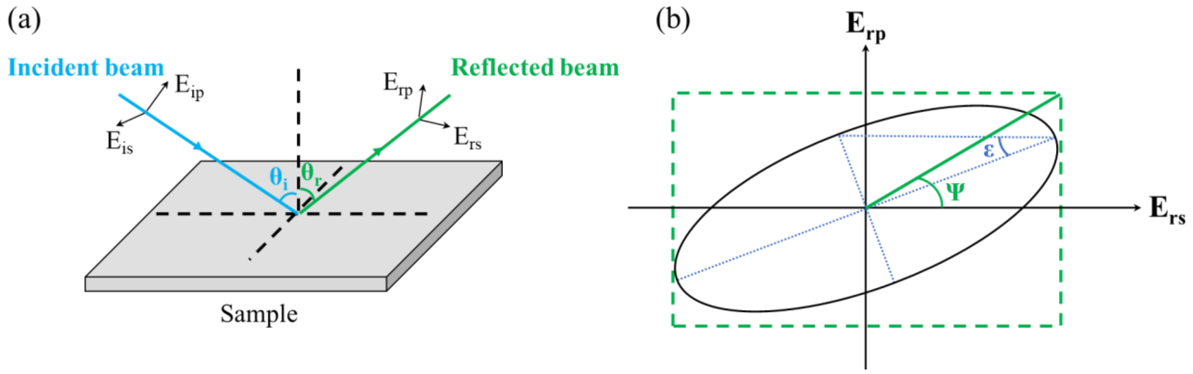

Figure 2-20: (a) Principle of ellipsometry measurement (E_{is}: the component perpendicular to the plane of incidence of the electric field of the incident wave, E_{ip}: the component parallel to the plane of incidence of the electric field of the incident wave, E_{rp}: the component parallel to the plane of incidence of the electric field of the reflected wave, E_{rs}: the component perpendicular to the plane of incidence of the electric field of the reflected wave). (b) Elliptical polarization of the reflected light, with Ψ and ε (ellipticity) angles.

After reflection on the sample, the light polarization modification is represented by two coefficients acting on each component of the field. Eq.(2.9) defines the reflection coefficients for a polarization parallel (r_p) and perpendicular (r_s) to the plane of incidence [BER15].

$$\begin{aligned} r_p &= \frac{E_{rp}}{E_{ip}} = |r_p|e^{j\delta_p} \\ r_s &= \frac{E_{rs}}{E_{is}} = |r_s|e^{j\delta_s} \end{aligned} \tag{2.9}$$

The coefficients r_p and r_s are complex numbers: Their modulus represents the change in the amplitude of the field components, their phase contains the delay induced by the reflection. The ellipsometer measures the ratio of these coefficients, which is expressed by eq.(2.10).

$$\begin{gathered} \frac{r_p}{r_s} = \tan\Psi\, e^{(j\Delta)} \\ \text{Where } \tan\Psi = \frac{|r_p|}{|r_s|} \text{ and } \Delta = \delta_p - \delta_s \end{gathered} \tag{2.10}$$

Ψ and Δ are called the ellipsometric angles, which are measured experimentally. They provide the optical properties of the reflecting system. Given the permittivity of all layers, it is possible to fit Ψ and Δ in order to obtain the thickness of the layers. The permittivity is related to the optical indices by the eq.(2.11).

$$\varepsilon = \varepsilon' + i\varepsilon'' = \tilde{n}^2 = (n + ik)^2 \tag{2.11}$$

With ε the complex dielectric function, ε′ its real part and ε″ its imaginary part, ñ the complex optical index, n the refractive index (real part), and k the extinction coefficient (imaginary part). Once the optical model is chosen, the layer parameters, thickness, and roughness are optimized to fit the experimental data. The simulations are performed using the CompleteEase® software provided with the equipment. The program minimizes the mean square error between the simulated and measured Ψ and Δ. We thus obtain both the optical indices and the thickness of the layer.

VO_2 layers were measured with a Woolam® M-2000 ellipsometer. The measurements were performed from 245 to 900 nm at four angles of incidence: 60°, 65°, 70° and 75°. **Figure 2-21** shows the ellipsometer used for thickness determination. A polarizer and a compensator combination circularly polarizes the incident wave. The first one linearly polarizes the wave emitted by the light source, and the second one circularly converts the linear polarization. The size of the samples is around 1 cm², and the beam is focused to a spot size in the 100 µm range. The wave is then reflected on the sample and transmitted to an analyzer and a detector. Temperature-dependent optical indices of VO_2 were obtained using the ellipsometer coupled to a Peltier module. The temperature was monitored using a K- type thermocouple positioned on the module surface, next to the sample.

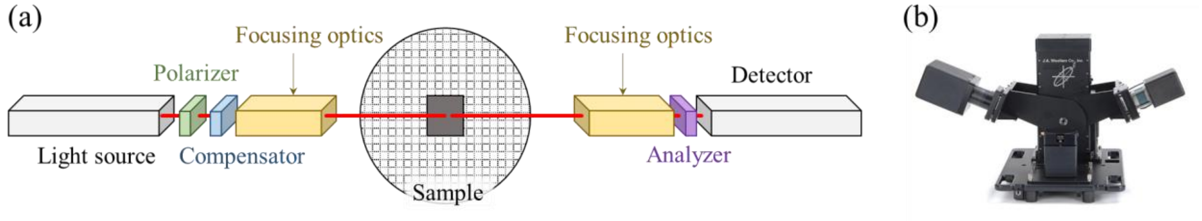

Figure 2-21: (a) Schematic and (b) picture of the Woolam® M-2000 ellipsometer used to determine VO_2 layer thicknesses.

To choose the optical model associated with our VO_2 films we based ourselves on the material specific characteristics and the literature data. The transparent, semiconducting, or opaque character and the insulating or conducting nature of the material also guide the choice of the model.

The sapphire substrate was simulated using a Cauchy model [COM07] (see insert of **Figure 2-22**). Where n and k are respectively the refractive index and the extinction coefficient of sapphire, k_{amp} is the amplitude of k, k_{exp} a constant and $E_{band\ edge}$ the energy value above which there is absorption. This model is generally employed to describe insulating and semiconducting materials in their optical transparency zone. To extend this model beyond the transparent zone, we use the Cauchy-Urbach model in which the extinction coefficient is described for energies above the bandgap.

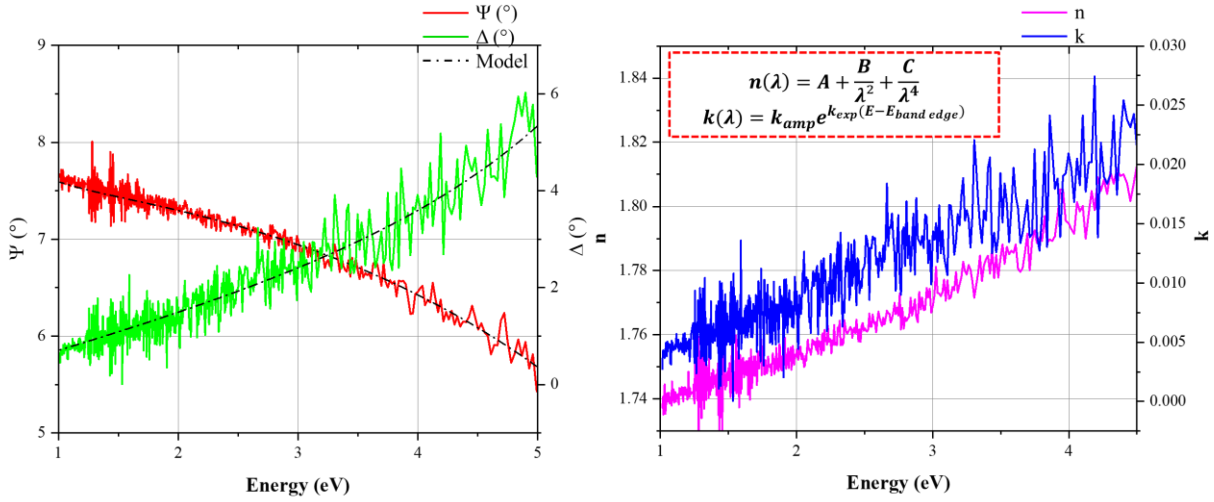

Figure 2-22: Ellipsometric angles Ψ (red) and Δ (green) and optical indices n (pink) and k (blue) of sapphire substrate as a function of energy. The Cauchy-Urbach model is shown as dotted lines.

For **the VO_2 layer**, a series of oscillators is used to describe both the absorption and transparency regions. Each oscillator describes a particular zone, and is characterized by the amplitude A, width

B_r, and energy E_n. Several types of oscillators are possible: Gaussian, Tauc-Lorentz, Drude, etc. Since the oscillators reflect the energy transitions between the different orbitals, namely *O 2p* and *V 3d* (t_{2g} and e_g) for VO_2, it is necessary to look at the behavior of VO_2 in its different states. In the insulating phase, the dielectric function can be described by the Tauc-Lorentz oscillator.

$$\varepsilon_2^{TL}(E) = \begin{cases} \dfrac{AE_0C(E-E_g)^2}{(E^2-E_0^2)^2+C^2E^2} * \dfrac{1}{E} & E > E_g \\ 0 & E \leq E_g \end{cases} \tag{2.12}$$

$$\varepsilon_1(E) = \varepsilon_1(\infty) + \frac{2}{\pi} P \int_{E_g}^{\infty} \frac{\xi \varepsilon_2(\xi)}{\xi^2 - E^2} d\xi \tag{2.13}$$

The imaginary part of the dielectric function ε_2 is given by eq.(2.12). A is the product of $A_T * A_L$ of the Tauc coefficient and the amplitude of the Lorentz oscillator. The latter is related to the carrier density and the effective mass of electrons. E_0 is the maximum transition energy, *C* an oscillator constant, *E* the photon energy, and E_g the bandgap. The real part of the dielectric function ε_1 is given by eq.(2.13), where *P(Integral)* expresses the principal part of the Cauchy integral and $\varepsilon_1(\infty)$ is the high-frequency dielectric constant.

As the temperature increases, the spectral behavior of Ψ and Δ changes significantly due to the appearance of metallic domains in the insulating phase. This phase coexistence calls for a description of the VO_2 as a composite material, for which the ellipsometric fitting was performed by including between 3 to 5 Lorentz oscillators. This combination has already been studied in the work of Huang *et al.* [HUA18], providing a basis for the realization of our model. At high temperature, the dielectric function comprises a Drude oscillator (eq.(2.14)) due to the optical properties of the metallic VO_2 below 1.5 µm [ASP14][RAM18].

$$\tilde{\varepsilon}(\omega) = 1 - \frac{Ne^2}{m\varepsilon_0} * \frac{1}{(\omega^2 - i\Gamma_d\omega)} = 1 - \frac{\omega_p}{-\omega^2 + i\Gamma_d\omega} \tag{2.14}$$

$$\omega_p = \sqrt{\frac{N * e^2}{m * \varepsilon_0}} \tag{2.15}$$

Where *N* is the carrier concentration, *e* the electric charge, ε_0 the vacuum dielectric constant, *m* the mass of the electron, Γ_d the collision frequency, and ω_p the plasma frequency. The plasma frequency corresponds to the photon energy at which the real part of the dielectric function is approximately zero.

To summarize, the model for VO_2 layers is composed of 1 Drude and 1 Tauc-Lorentz oscillator at energies between 1 to 2 eV, and 3 to 5 Lorentz oscillators at energies between 2 to 5 eV. The fitted spectra are shown in **Figure 2-23**. The addition of 5 Lorentz oscillators leads to an improvement in the accuracy in the 2 to 5 eV area. Moreover, the parameter E_g associated with the Tauc-Lorentz oscillator characterizing the bandgap of the VO_2 insulating state is closer to reality. With 3 oscillators, E_g is about 0.46 eV (with $E_0 \approx 1.95$ eV) against 0.75 eV with 5 oscillators (with $E_0 \approx 1.91$ eV). The obtained VO_2 thickness is also close to what was measured by profilometry on the etched sample: 242 nm (3 oscillators) and 260 nm (5 oscillators) by ellipsometry versus 263 nm by profilometry.

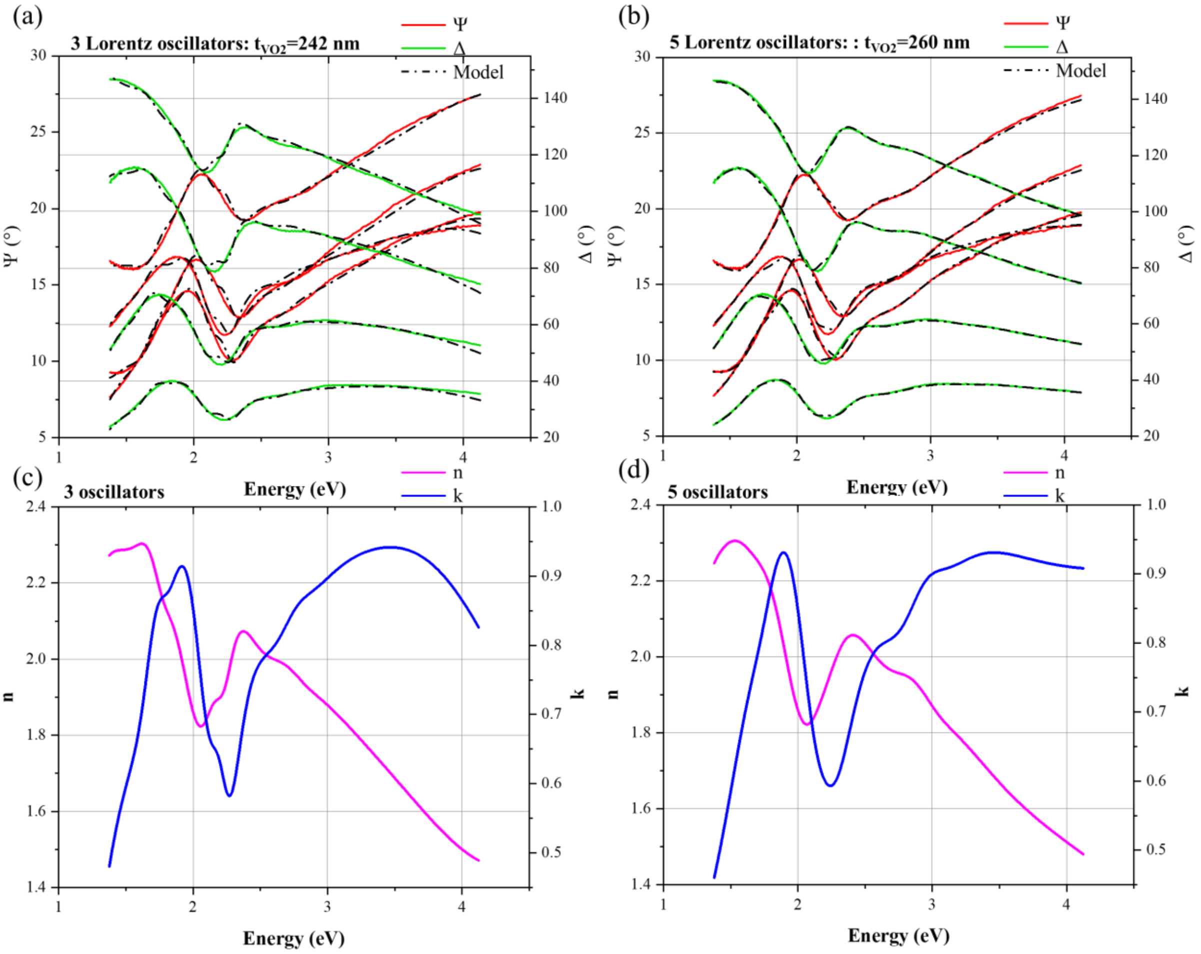

Figure 2-23: Ellipsometric angles Ψ (red) and Δ (green) and optical indices n (pink) and k (blue) as a function of incident light energy at 65° angle. The model comprised 3 (a), (c) or 5 (b), (d) Lorentz oscillators. Sample: VO_2(263 nm-thick)/Al_2O_3.

2.3. Substrate preparation

Sapphire **(Al_2O_3)** is an aluminum oxide commonly used in microelectronic fabrication because of its stability at high temperature, its transparency in the IR (λ < 6 µm) and terahertz wavelengths (λ > 45 µm), and its ease of cleaning. It crystallizes in the hexagonal/rhombohedral structure with the $R\bar{3}c$ (167) space group and lattice parameters $a_{Al2O3}=b_{Al2O3}=4.758$ Å and $c_{Al2O3}=12.992$ Å [PIS09]. Depending on the cutting direction of the single crystal, the Al_2O_3 substrates present different orientations. The most widespread are sapphire oriented along the c (0001), r $(1\bar{1}02)$, and a $(11\bar{2}0)$ planes. In this work, c- and r-cut sapphire were used (**Figure 2-24**).

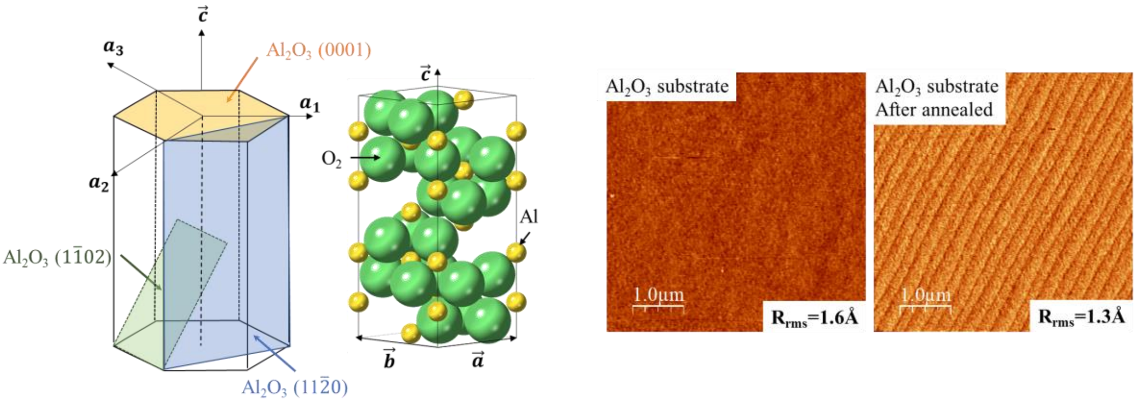

Figure 2-24: Crystallographic structure of Al_2O_3 and AFM topography of c-sapphire substrate before and after annealing at 1190°C under O_2 flow, revealing atomic steps of 2 Å height (1/6 of c parameter).

The c- and r-cut sapphire substrates were chemically and thermally treated in the same way to improve reproducibility between depositions. The substrates (10 mm x 10 mm x 0.5 mm) are polished on one side and were purchased from the Crystec GmbH® company. Samples were cleaned following a standard procedure by sequential ultrasonication for 5 min in acetone, ethanol and isopropanol and dried under N_2 flow. After this cleaning, they were annealed at 1190°C in a tubular furnace under an O_2 flow for 3 hours. It is essential to do chemical degreasing before the thermal treatment otherwise it could stabilize an eventual surface pollution at high temperature, which would be very difficult to remove. The substrate preparation conditions were based on the expertise of the C2N OXIDE team. The surface topography measured by AFM visible in **Figure 2-24** shows that the preparation reveals atomic steps with a height of 2 Å. This characteristic height corresponds to the distance between two oxygen planes in the crystal structure of sapphire.

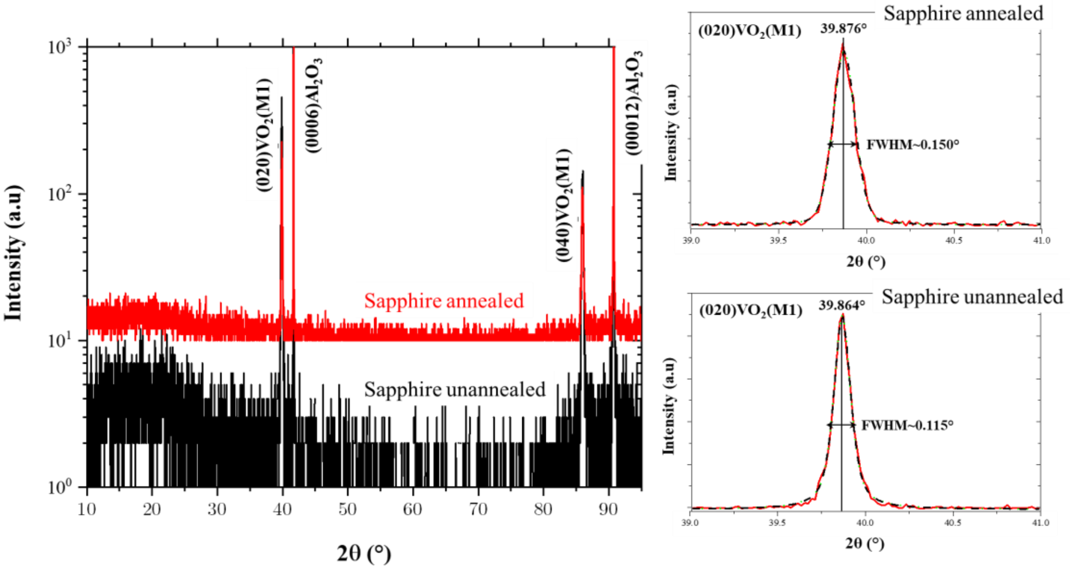

Figure 2-25: (a) Comparison of VO_2 films grown on unannealed (black) and annealed (red) c-cut sapphire substrate measured by XRD. (b) Rocking curves around the (020) peak of VO_2.

The influence of annealing the sapphire substrate was investigated by XRD. VO_2 films deposited on annealed and unannealed c-cut sapphire substrates show identical results (**Figure 2-25**). The slight change in full width at half maximum of the $(020)_{VO2(M1)}$ diffraction peak is probably not significative. However, to avoid an eventual contamination on the substrate that might disturb the growth of VO_2, the annealing step was systematically performed for all sapphire substrates in this work.

Strontium Titanate **($SrTiO_3$ or STO)** is an oxide which crystallizes in cubic structure under the $Pm\bar{3}m$ (221) space group with a_{STO}= 3.905 Å (**Figure 2-26**) [LON10]. In conforming with the state of the art substrate optimization for epitaxial growth of VO_2 metastable phases [DIN16], orientation (001) was selected to explore the stabilization of the B phase.

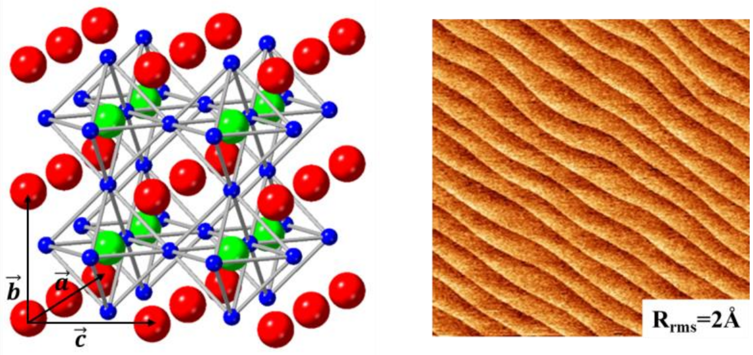

Figure 2-26: Crystallographic structure of $SrTiO_3$ and AFM topography (size 5x5 µm²) after chemical preparation and annealing at 950°C under O_2 flow. The characteristic atomic steps have 4 Å height (one unit cell height).

In order to insure a single TiO_2 termination of the (001)-oriented STO substrates, a dedicated chemical preparation is needed. The substrates (5 mm x 5 mm x 0.5 mm) were first rinsed in deionized water with ultrasonics. Then, an acid etch with hydrofluoric acid (HF) is performed for each sample before being rinsed, dried, and annealed at 950°C under O_2 flow. Then, the surface topography measured by AFM visible in **Figure 2-26** shows the typical atomic steps with a height of 4 Å. Having observed no difference on the stabilization of VO_2(B) with a simpler chemical cleaning, without the HF etch and annealing steps, it was agreed that all STO substrates will be cleaned only by acetone, ethanol, and isopropanol.

In the first part of this Chapter, we have seen how experimental sputtering conditions impact the stabilization of stoichiometric VO_2 and how complex is the sputtering approach due to the interplay of numerous parameters. The amount of introduced O_2, temperature and nature of the substrate and RF power applied at the cathode and target setup have been carefully controlled. Then in the second part, we developed a sample characterization methodology with the intention to obtain detailed insights into physicochemical properties of the deposited thin films.

Chapter 3: Study of VO_2 thin films deposited on sapphire substrates

Contents

The vanadium oxide layer development discussed in Chapter 2, allowed to see that many parameters influence the vanadium dioxide (VO_2) stabilization. Despite the numerous studies carried out [FAN13][WON13][YAN10][ZHA12], the formation of polymorphs is still under discussion. The goal of the thesis being to acquire expertise in film growth for the development of industrial activities on a larger scale, we sought to understand the influence of the substrate crystalline structure on VO_2 stabilization. To do that, VO_2 films were deposited on c-cut and r-cut sapphire (Al_2O_3) substrates. Based on a comprehensive X-ray diffraction (XRD) study, we highlighted the structural relationships between VO_2 and Al_2O_3 lattices that allowed us to gain a better understanding of the mechanisms at the origin of phase stabilization.

3.1. Deposition of VO_2(M1) phase

3.1.1. C-cut sapphire: Epitaxial relations and variants

The VO_2 thin film deposition by RFMS was first studied on a c-cut sapphire $(0001)Al_2O_3 \equiv (001)Al_2O_3$ substrate. The vanadium oxide and the out-of-plane orientation were characterized by Raman spectroscopy and by XRD in $\theta - 2\theta$ mode at RT, and further detailed studies were performed by φ-scans and reciprocal space mappings.

The Raman analysis in **Figure 3-1**(a) shows three main bands visible at 192, 223, and 614 cm^{-1}. The two first bands could be associated with the motion of vanadium along the $\vec{c}_{VO2}$-axis of the VO_2 crystal (stretching motion of V-V dimers), while the third could be related to the stretching mode of V-O vibrations. At 339 cm^{-1}, the tilting motion of V-V dimers is visible. The other bands were assigned to different bending modes of V-O vibrations [MAR08][ZAG15][SHV19], and the whole Raman spectrum highlights the VO_2(M1) phase [URE17][SHV19].

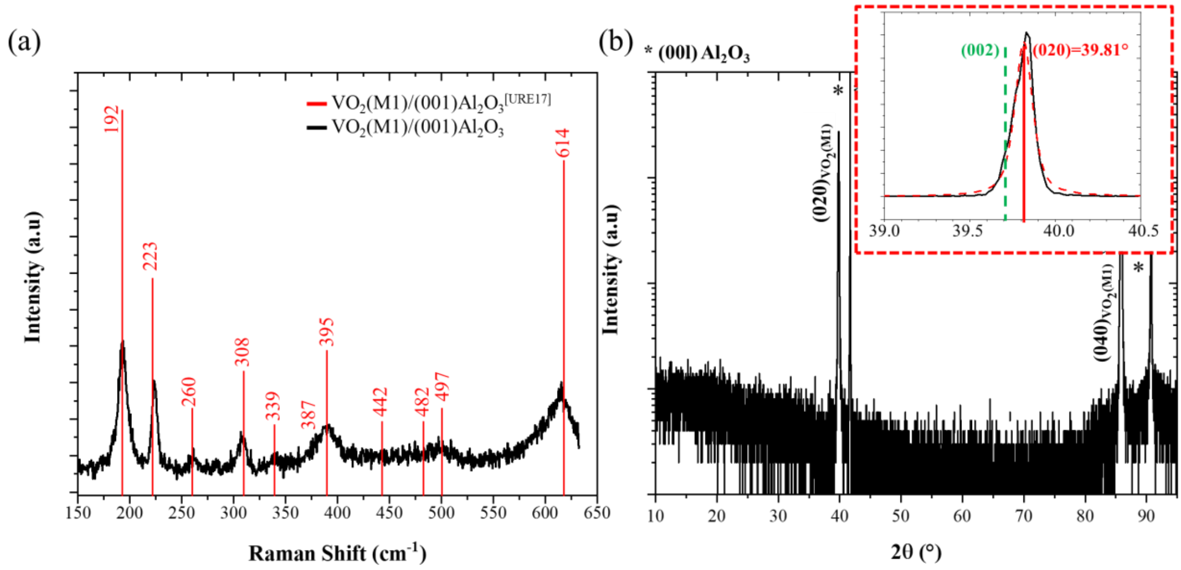

Figure 3-1: (a) Raman spectra and (b) θ-2θ scan at RT of a VO_2 layer deposited on c-cut sapphire substrate. The Raman spectrum is compared to the one of a 200 nm VO_2 film on $(001)Al_2O_3$ obtained by electron beam evaporation followed by a post-annealing under oxygen atmosphere (red) [URE17].

After that, structural characterizations were performed by XRD. The corresponding diffractogram in **Figure 3-1**(b) shows that the peaks at 39.81° and 85.83° are respectively attributed to the reflections from the $(020)_{VO2(M1)}$ and $(040)_{VO2(M1)}$ planes and confirms the VO_2(M1) phase. The peaks at 41.69° and 90.74° correspond to the reflections of $(00l)$ planes of the Al_2O_3, with $l = 6$ and 12, respectively. In the limit of the sensitivity of our X-ray detectors, no other peaks were observed even by powder

X-ray diffraction, which means that films are pure VO_2(M1) layers with $(0k0)$ preferential orientation. We deduce that the planes $(0k0)$ of the VO_2(M1) are parallel to the planes $(00l)$ of the Al_2O_3. It should be noted that some previous works [WON13][ZHO11] point out the ambiguity in determining between $(0k0)VO_2(M1)$ and $(00l)VO_2(M1)$, due to their close peak positions (inset of **Figure 3-1**(b)). In our work, we will present a detailed investigation by XRD analysis including φ-scans to confirm the film orientation as $(0k0)VO_2(M1)$.

Once the M1 phase was confirmed, the in-plane orientation of the VO_2 layer with respect to the substrate was determined by XRD from inclined planes in symmetric conditions. **Figure 3-2**(a) shows the φ-scans of the oblique planes $(104)_{Al2O3}$ and $(220)_{VO2(M1)}$. The $(220)_{VO2(M1)}$ plane was selected because its trace in the $(010)_{VO2(M1)}$ plane is parallel to the $\vec{c}_{VO2(M1)}$-axis of the VO_2.

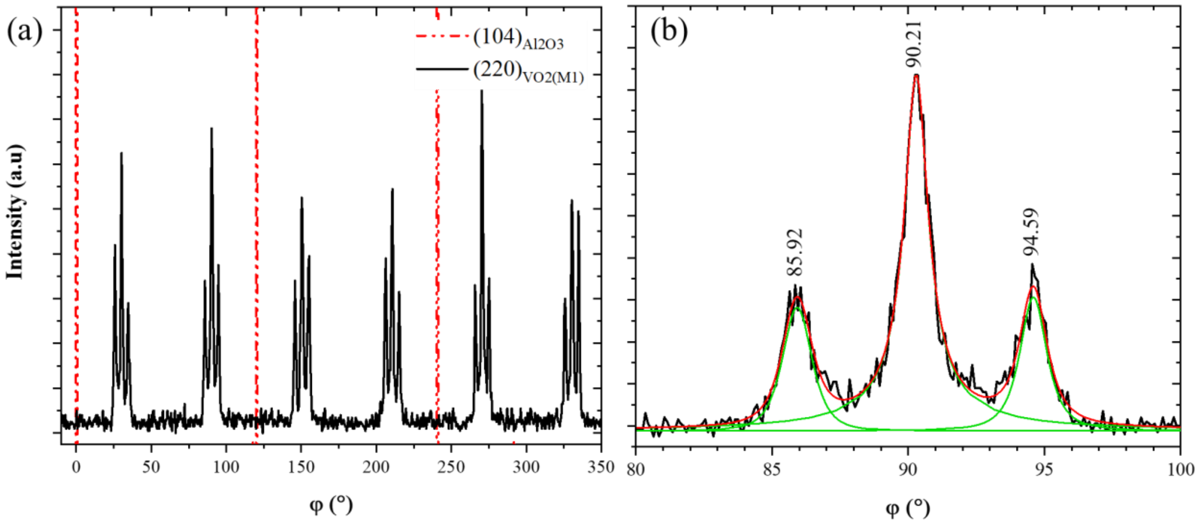

Figure 3-2: (a) φ-scan diagram of VO_2(M1)/(001)Al_2O_3 measured at RT. The $(220)_{VO2(M1)}$ plane is shown in black, and the red dashed lines indicate the positions of the $(104)_{Al2O3}$ planes. (b) Fit of one triple peak around φ=90.21°. In green the individual peak fits and in red their sum.

For φ angles between -10° and 350°, the diagram of the oblique plane $(104)_{Al2O3}$ reveals the threefold symmetry of the hexagonal structure of Al_2O_3 around the $\vec{c}_{Al2O3}$-axis visible by the three peaks spaced by 120° respectively. The φ-scan of $(220)_{VO2(M1)}$ planes reveals six triple peaks spaced by 60°. Combining the intrinsic two-fold symmetry of VO_2 around the $\vec{b}_{VO2(M1)}$-axis (space group #14 2_1 screw axis) with the threefold symmetry around the $\vec{c}_{Al2O3}$-axis gives the pseudo-six-fold symmetry revealed by these six triplets. The zoom on one triplet (**Figure 3-2**(b)) shows that it is comprised of one main peak between two smaller satellites spaced by ~4.3°.

One study that discuss these triplets in the literature attributes them to the zig-zag chain of V^{4+}-V^{4+} around $\vec{a}_{VO2(M1)}$-axis of the monoclinic structure [ZHA12]. Instead, we ascribe the triplets to two sets of planes of VO_2(M1). Indeed, working in symmetrical configuration of XRD with a 1/4° slit placed in front of the detector, it is possible to measure several (hkl) planes simultaneously if they are very close in 2θ and Ψ angles. To differentiate the satellite peaks from the main peak, scans in triple-axis mode were performed (cf. Chapter 2). **Figure 3-3** shows the $2\theta - \omega$ scans of the triplet near φ=90°.

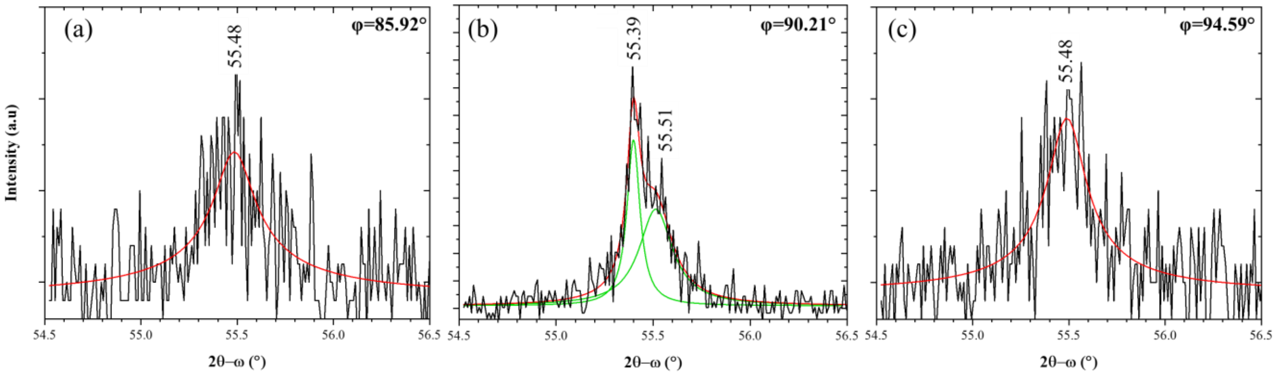

Figure 3-3: 2θ-ω scans of each peak of the $(220)_{VO2(M1)}$ triplet measured with the triple-axis configuration at (a) φ =85.92°; (b) φ =90.21 and (c) φ=94.59°. The solid black line corresponds to the experimental data and the red and green ones to the fit.

The fit of each peak was conducted using a Pearson type VII function and allowed us through the 2θ position to identify the corresponding plane. **Table 3-1** summarizes the experimental positions of the peaks located at φ= 85.92°, 90.21°, and 94.59° and compares them to the VO_2(M1) JCPDS datasheet.

Table 3-1: XRD experimental peaks of VO_2 planes compared to the JCPDS-01-082-0661 datasheet.

Planes	d_{hkl}	**2θ (°)**	**Ψ* (°)**
φ=85.92°	1.654	55.48	
φ=94.59°	1.654	55.49	
φ=90.21°	1.657	55.39	
	1.654	55.31	
(220) JCPDS	1.6539	55.514	42.9
$(\bar{2}22)$ JCPDS	1.6576	55.382	43.0

*Ψ is calculated by CaRIne 3.1 crystallography software from JCPDS VO_2(M1) unit cell parameters.

As seen from the JCPDS data in **Table 3-1**, the $(220)_{VO2(M1)}$ and $(\bar{2}22)_{VO2(M1)}$ planes are close on the VO_2 Ewald's sphere. This explain why they can both contribute to the central peak (at φ=90.21°), as evidenced by the $2\theta - \omega$ scan of **Figure 3-3**(b). Regarding the satellite peaks, they can be attributed to the $(220)_{VO2(M1)}$ plane alone. Therefore, each triplet is the signature of a doublet from $(220)_{VO2(M1)}$ planes added to a single peak from $(\bar{2}22)_{VO2(M1)}$ planes.

In the same way that for the $(220)_{VO2(M1)}$ plane, we measured the $(011)_{VO2(M1)}$ plane. This time, the trace of the $(011)_{VO2(M1)}$ plane in the $(010)_{VO2(M1)}$ plane is parallel to the $\vec{a}_{VO2(M1)}$-axis. **Figure 3-5** shows the φ-scan for angles between -10° and 350° and reveals six double peaks spaced by 60°.

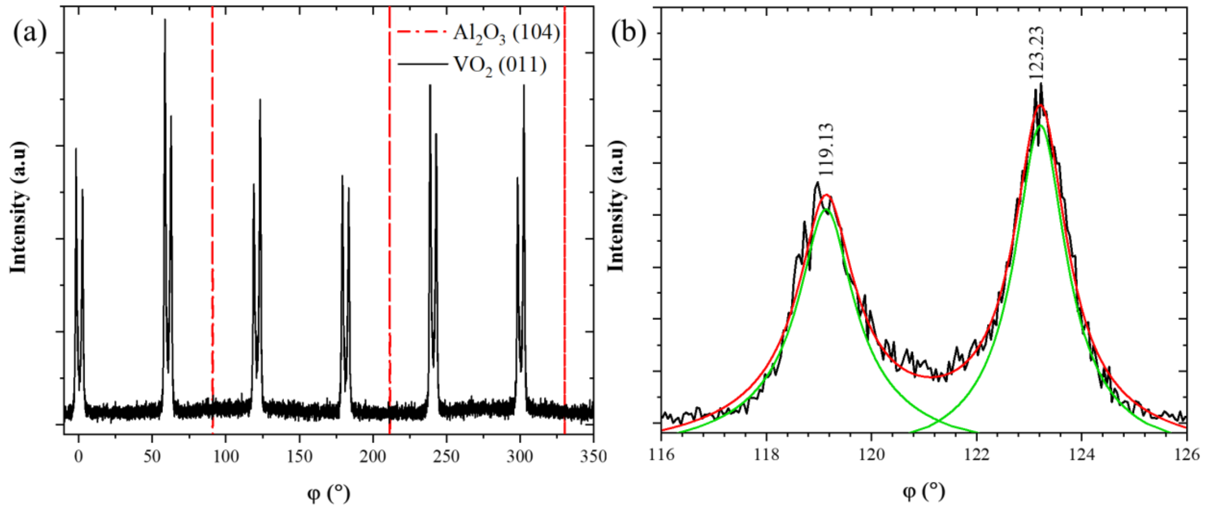

Figure 3-5: (a) φ-scan diagram of VO_2(M1)/(001)Al_2O_3 measured at RT. The $(011)_{VO2(M1)}$ plane is shown in black and the red dashed lines indicate the positions of the (104) sapphire planes. (b) Fit of one doublet around φ=121°. Individual fits are in green and their sum in red solid line, respectively.

The six doublets confirm the pseudo-six-fold symmetry existing between the VO_2(M1) and the Al_2O_3. Measurements were also performed in the symmetrical configuration without discriminating slit. The peaks of the doublet could again belong to two different planes. XRD scans in triple-axis mode were performed to try and differentiate these planes. **Figure 3-4** presents such scans for the doublet located near φ=121°. Each 2θ position identified from the fit is summarized in **Table 3-2** and compared to the VO_2(M1) JCPDS datasheet.

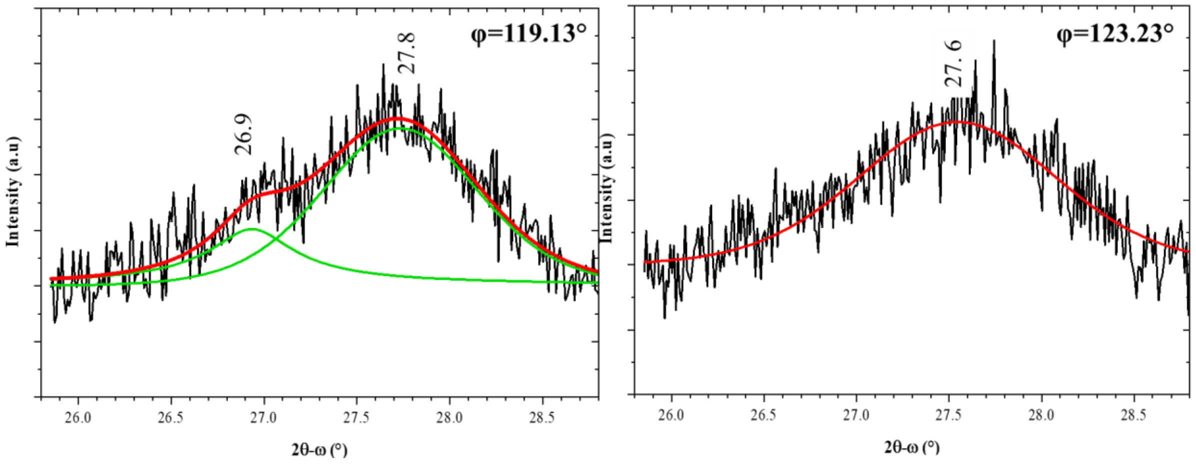

Figure 3-4: 2θ-ω scans of each peak of the $(011)_{VO2(M1)}$ doublet measured with triple-axis configuration at φ=119.13° and φ=123.23°. The solid black line corresponds to the experimental data and the red and green ones to the fit.

Table 3-2: XRD experimental measurement of VO_2 planes compare to the JCPDS-01-082-0661 datasheet.

Planes	d_{hkl}	**2θ (°)**	**Ψ* (°)**
φ=119.13°	3.31	26.9	
	3.21	27.8	
φ=123.23°	3.22	27.6	
(011) JCPDS	3.2034	27.827	44.8
$(\bar{1}11)$ JCPDS	3.3152	26.871	43.0

* Ψ is calculated by CaRIne 3.1 software from JCPDS VO_2(M1) unit cell parameters.

Regarding the peak at φ=119.13°, alongside the predominant $(011)_{VO2(M1)}$ plane a second contribution at 26.9° is needed to reproduce the overall peak shape, that can be attributed to the $(\bar{1}11)_{VO2(M1)}$ plane. Therefore, each doublet is the signature of the $(011)_{VO2(M1)}$ and $(\bar{1}11)_{VO2(M1)}$ planes, with the former on the "right side" (larger φ) and the latter on the "left side" (smaller φ), respectively. This is in agreement with the φ-scan of $(220)_{VO2(M1)}$ planes having contribution from the $(\bar{2}22)_{VO2(M1)}$ planes.

Having identified all the diffraction peaks of both φ-scans, we can now position the $\vec{a}_{VO2(M1)}$ and $\vec{c}_{VO2(M1)}$ axes with respect to the Al_2O_3 axes, and identify the number of crystallographic variants. As will be shown below, VO_2(M1) film on c-cut sapphire has a single (010) orientation and 12 different in-plane crystallographic variants.

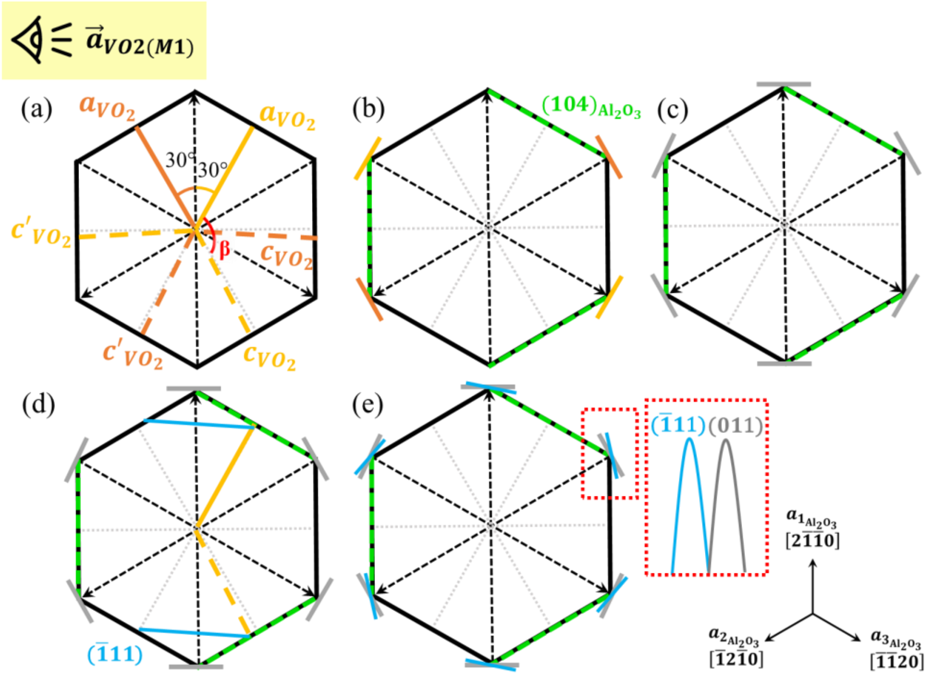

Figure 3-6: VO_2 variants in-plane orientation: $\vec{a}_{VO2(M1)}$-axes as inferred from $(011)_{VO2(M1)}$ φ-scan. (a) Two possible $\vec{a}_{VO2(M1)}$-axes represented as yellow and orange solid lines at ±30° from the azimuth $\vec{a}_{1_{Al2O3}}$, corresponding to four possible variants as shown by their respective $\vec{c}_{VO2(M1)}$ axes in dotted lines. (b) The resulting traces of $(011)_{VO2(M1)}$ planes in the $(001)_{Al2O3}$ plane as orange and yellow lines, together with the traces of $(104)_{Al2O3}$ planes in green dashed lines, respectively; (c) Repeating this pattern for all three Al_2O_3 azimuths, six $(011)_{VO2(M1)}$ traces are obtained (in grey). (d) Traces of the $(\bar{1}11)_{VO2(M1)}$ plane in blue for the variant in yellow, giving (e) six doublets as the one highlighted in red dotted line when combined with the other variants and the $(011)_{VO2(M1)}$ traces.

For a (010) oriented VO_2 film, the $\vec{b}_{VO2}$-axis is in the out-of-plane direction, while the $\vec{a}_{VO2(M1)}$- and $\vec{c}_{VO2(M1)}$-axes are both in the $(001)Al_2O_3$ substrate plane, with an angle of 122.6° between them (β angle). If we consider that the $\vec{a}_{VO2(M1)}$-axes are positioned at ±30° with respect to the three azimuths $\vec{a}_{1_{Al2O3}}$, $\vec{a}_{2_{Al2O3}}$, and $\vec{a}_{3_{Al2O3}}$ of Al_2O_3, six first peaks are obtained in the φ-scan of the $(011)_{VO2(M1)}$ planes (**Figure 3-6**(c)), as a signature of six VO_2 variants. Now, considering the traces of the $(\bar{1}11)_{VO2(M1)}$ planes that are detected together with the $(011)_{VO2(M1)}$ ones as explained previously, six peaks are added to form the six observed doublets, as shown in **Figure 3-6**(e). We note that alongside a configuration of VO_2(M1) unit cell with the $\vec{b}_{VO2(M1)}$-axis oriented "up" (towards the surface), there can also be one with the $\vec{b}_{VO2(M1)}$-axis oriented "down" (towards the substrate). These two variants have different in-plane orientations $c_{VO2}$and c'_{VO2} of their $\vec{c}_{VO2(M1)}$-axis, as depicted in **Figure 3-6**(a), but as they share the same $\vec{a}_{VO2(M1)}$-axis, this φ-scan of $(011)_{VO2(M1)}$ planes alone is not enough to discriminate between them.

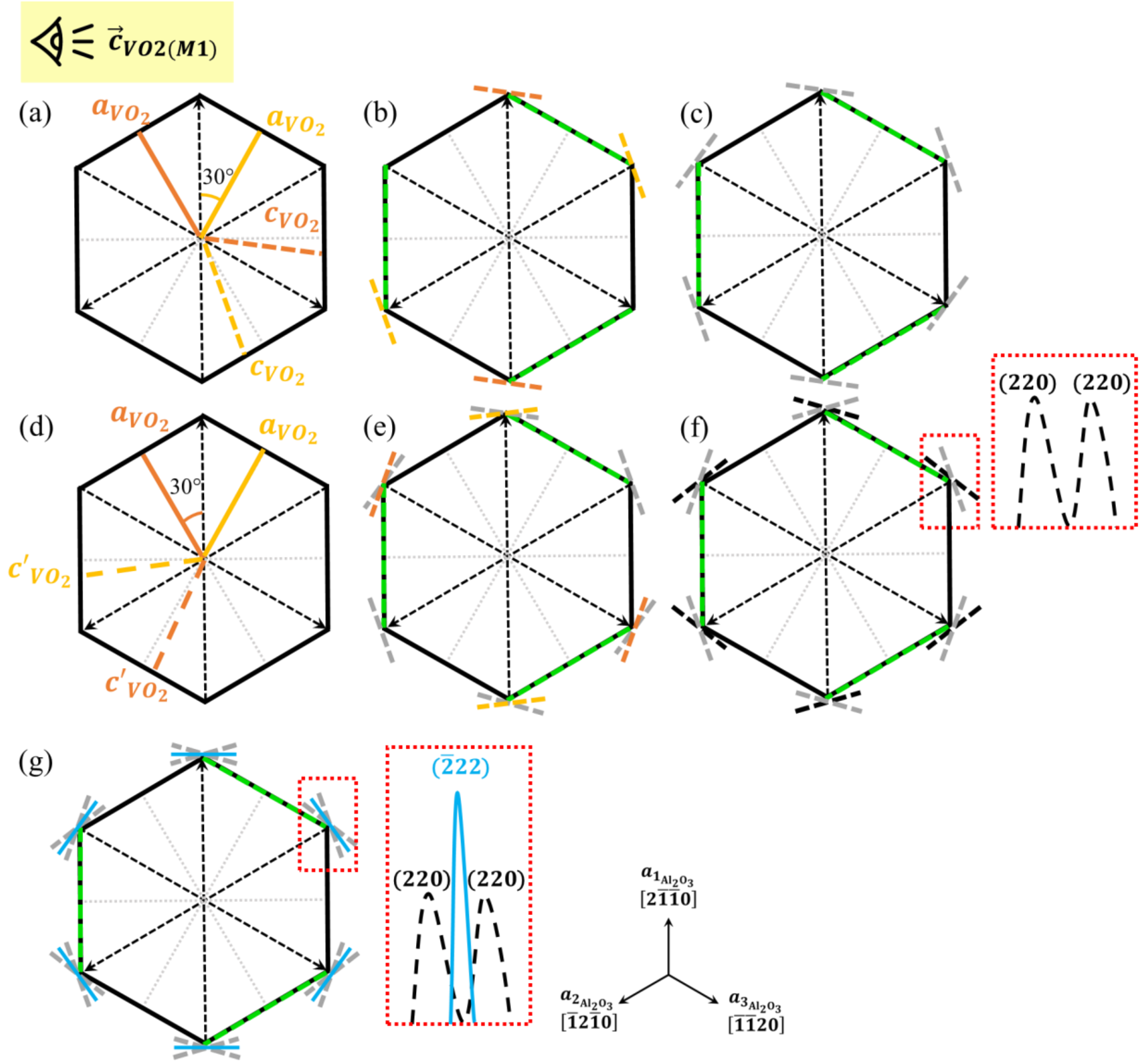

Figure 3-7: VO₂ variants in-plane orientation: $\vec{c}_{VO2(M1)}$-axes as inferred from $(220)_{VO2(M1)}$ φ-scan. (a) Two possible VO₂ variants in yellow and orange colors with their respective $\vec{a}_{VO2(M1)}$ (solid line) and $\vec{c}_{VO2(M1)}$ (dotted line) axes; (b) The corresponding traces of $(110)_{VO2(M1)}$ parallel to $\vec{c}_{VO2(M1)}$-axis in matching colors, together with the traces of the $(104)_{Al2O3}$ planes in green dashed lines; (c) Repeating this pattern for each Al_2O_3 azimuth ($\vec{a}_{1_{Al2O3}}$, $\vec{a}_{2_{Al2O3}}$, and $\vec{a}_{3_{Al2O3}}$), 6 traces (in grey) are obtained. (f) 6 other traces forming an angle ~5° with the former (one example framed in red dotted line) are obtained when considering the variants with their $\vec{b}_{VO2(M1)}$ axis towards the substrate, as depicted in (d) and (e); (g) Finally, adding the traces of the $(\bar{1}11)_{VO2(M1)}$ planes in blue (as presented in **Figure 3-6**(d)), 6 triplets as the one framed in red are obtained, in agreement with the measurement. The 12 satellite peaks are the signature of the 12 variants.

We now turn to the analysis of the $(220)_{VO2(M1)}$ φ-scan, that reveals the traces of both $(220)_{VO2(M1)}$ and $(\bar{2}22)_{VO2(M1)}$ planes. **Figure 3-7**(a) illustrates the two possible orientations of the $c_{VO2(M1)}$ axes around the $\vec{a}_{1_{Al2O3}}$ azimuth of Al_2O_3 for the first two VO₂ variants. As depicted in **Figure 3-7**(c), repeated for each Al_2O_3 azimuth this gives six traces in the $(001)_{Al2O3}$ plane, corresponding to six VO₂ variants. Again, as depicted in **Figure 3-7**(d) two additional variants are obtained by considering the $\vec{a}_{VO2(M1)}$-axes as in **Figure 3-7**(a) but with their $\vec{b}_{VO2(M1)}$-axis oriented "down", thus giving two orientations identified as c'_{VO2} for their respective $\vec{c}_{VO2(M1)}$-axes. Now, as the angle between $\vec{a}_{VO2(M1)}$- and $\vec{c}_{VO2(M1)}$-axes is 122.6°, the c_{VO2} and c'_{VO2} axes do not have the same traces, but have instead two different ones forming an angle of ~5° between them. As shown in **Figure 3-7**(f), this explains the two peaks on each side of the triplets (**Figure 3-7**(g)). In other words, this $(220)_{VO2(M1)}$ φ-scan reveals that there are not six but twelve different variants for the VO_2(M1) film on c-cut sapphire.

In summary, the performed φ-scans highlight the multiple growth of VO_2(M1) on c-cut sapphire substrate, giving 12 crystallographic variants. Considering the VO_2(M1) monoclinic structure and the heterostructural epitaxy with the sapphire substrate, interpreting experimental results can be difficult. A few articles in the literature address this subject but to our knowledge, none of them mention the number of variants [FAN13][ZHA12][HON17].

Reciprocal space mappings (RSM) were done to confirm the multiple growth variants of VO_2(M1) on c-cut sapphire and to calculate the film lattice constants. The RSM alignments were along the three azimuths of the substrate at φ=60°, φ=180°, and φ=300°, respectively. As expected from symmetry considerations and from the previous φ-scans, the obtained RSM at these φ positions were identical, therefore here we only discuss the measurement at φ=60°. **Figure 3-8**(a) shows the RSM at φ=60°, here aligned according to $\vec{a}_{3_{Al2O3}}$ of Al_2O_3 (for example).

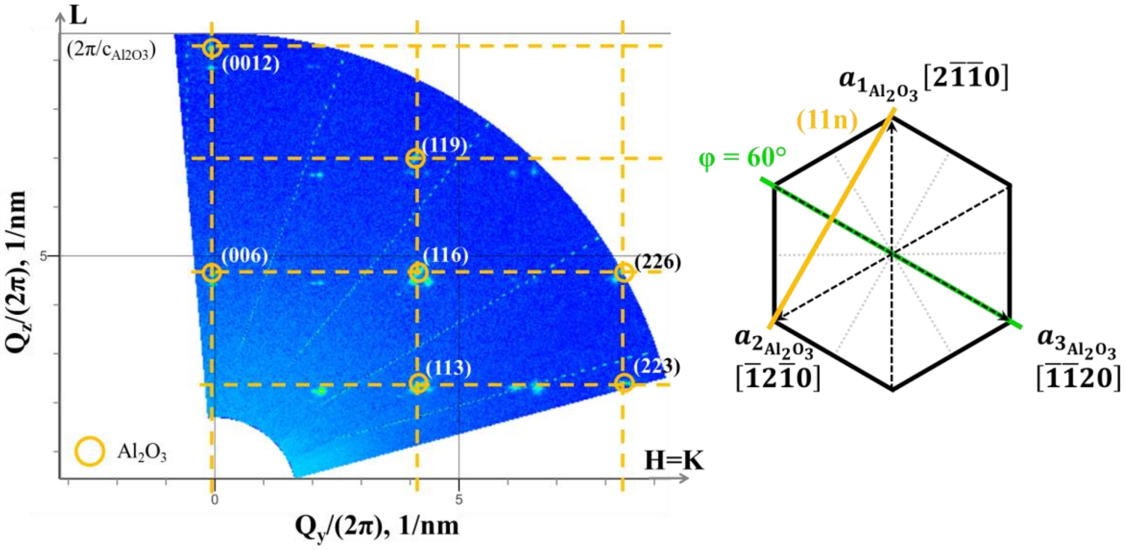

Figure 3-8: Reciprocal space mapping at φ=60° along one Al_2O_3 $\vec{a}$-axis as shown on the right (green line). The yellow grid is the reciprocal lattice of Al_2O_3, with the detected diffraction spots indexed and circled. (Q_y, Q_z) are the vertical and in-plane coordinates of the diffusion vector, corresponding to the L and H=K directions of Al_2O_3 reciprocal space in (HKL) notation, respectively.

First, we identified the diffraction spots of the substrate. Thanks to the theoretical a, b, and c lattice parameters of Al_2O_3, the unit vectors of reciprocal space can be determined. The latter is represented by the yellow grid on the map in **Figure 3-8**. The (006) and (0012) planes were indexed, knowing the c-cut orientation of the sapphire substrate. The other Al_2O_3 spots were then identified with the help of the reciprocal space grid, and expecting to find (hkl) planes for this azimuth, as shown in **Figure 3-8**. Second, a set of diffraction spots is used to find the reciprocal space grid for one variant of VO_2, as traced in red dashed lines in **Figure 3-9**. The in-plane unit vector for this grid is found to have a value of 2.20 nm^{-1}. This is identified as the $c^*_{VO2(M1)}$direction of reciprocal space, with a unit vector value L given by eq.(3.1):

$$\mathrm{L}\,[\mathrm{nm}^{-1}] = \frac{1}{c_{\mathrm{JCPDS}}\sin(\beta)} = \frac{1}{0.53825 * \sin(122.6)} = 2.20\ \mathrm{nm}^{-1} \tag{3.1}$$

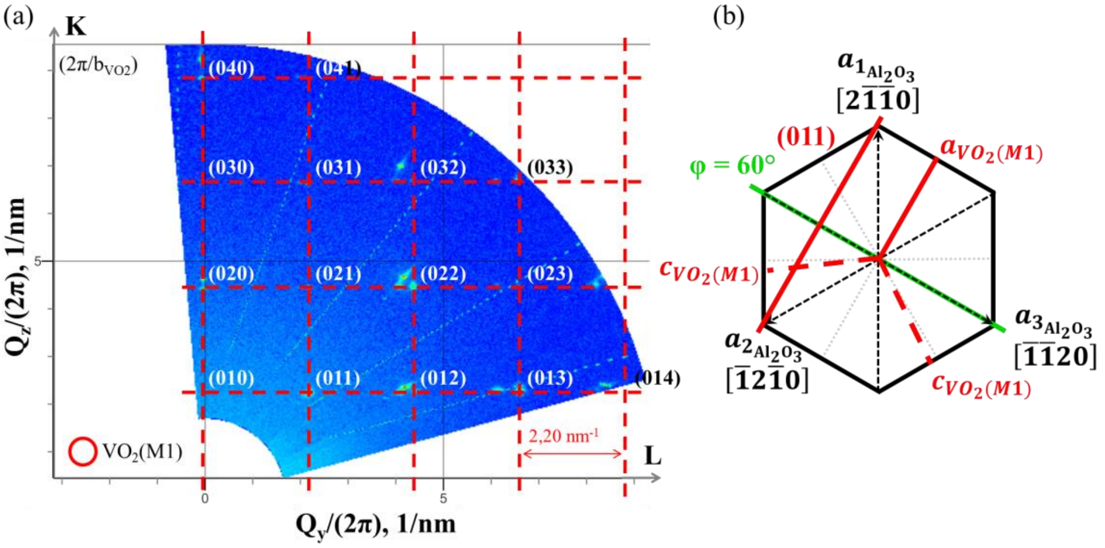

Figure 3-9: Reciprocal space mapping at φ=60° along one Al_2O_3 $\vec{a}$-axis as shown on the right (green line). The red grid is the reciprocal lattice of one VO_2(M1) variant, with the detected diffraction spots indexed and circled. (Q_y, Q_z) are the vertical and in-plane coordinates of the diffusion vector, corresponding to the K and L directions of this VO_2 variant reciprocal space in (HKL) notation, respectively. As depicted on the right, the planes with their traces parallel to $\vec{a}_{VO2(M1)}$-axis such as $(011)_{VO2(M1)}$ are probed in this RSM.

From the reciprocal space grid that is now oriented, all the diffraction spots of this particular VO_2 variant can be indexed. They are all belonging to the VO_2(M1) phase, as reported on the JCPDS 082-0661 datasheet. Only the spots corresponding to the $(021)_{VO2(M1)}$ and $(033)_{VO2(M1)}$ planes do not appear on this particular datasheet. We note that all the planes of this variant in this RSM have their trace in the $(001)_{Al2O3}$ plane parallel to that of the $(011)_{VO2(M1)}$ plane, as displayed in **Figure 3-9**. This confirms the orientation of the $\vec{a}_{VO2(M1)}$-axis of this variant, as given in the figure.

Now, the RSM along this φ=60° azimuth exhibits a second family of diffraction spots, belonging to a different VO_2 variant. The reciprocal space grid is traced again as red dotted lines in **Figure 3-10**, evidencing a different unit vector from the one of the previous variant. Following the same method, the in-plane unit vector is identified as $-a^*_{VO2(M1)} + c^*_{VO2(M1)}$ and all the diffraction spots are indexed accordingly. And again, only the spots for $(\bar{1}41)_{VO2(M1)}$ and $(\bar{4}24)_{VO2(M1)}$ are not confirmed by the JCPDS datasheet, due to their too low d_{hkl} value. This time, all the planes of this variant in this RSM have their trace in the $(001)_{Al2O3}$ plane parallel to that of the $(\bar{1}11)_{VO2(M1)}$ plane, as displayed in **Figure 3-10**. We note that these planes are sensitive to both the $\vec{a}_{VO2(M1)}$- and $\vec{c}_{VO2(M1)}$-axes, with an angle of 122.6° between these two axes, and their trace is thus not perfectly perpendicular to the Al_2O_3 azimuth. The RSM measurement does not have enough resolution along the φ angle direction to detect this offset, contrary to the φ-scans presented previously.

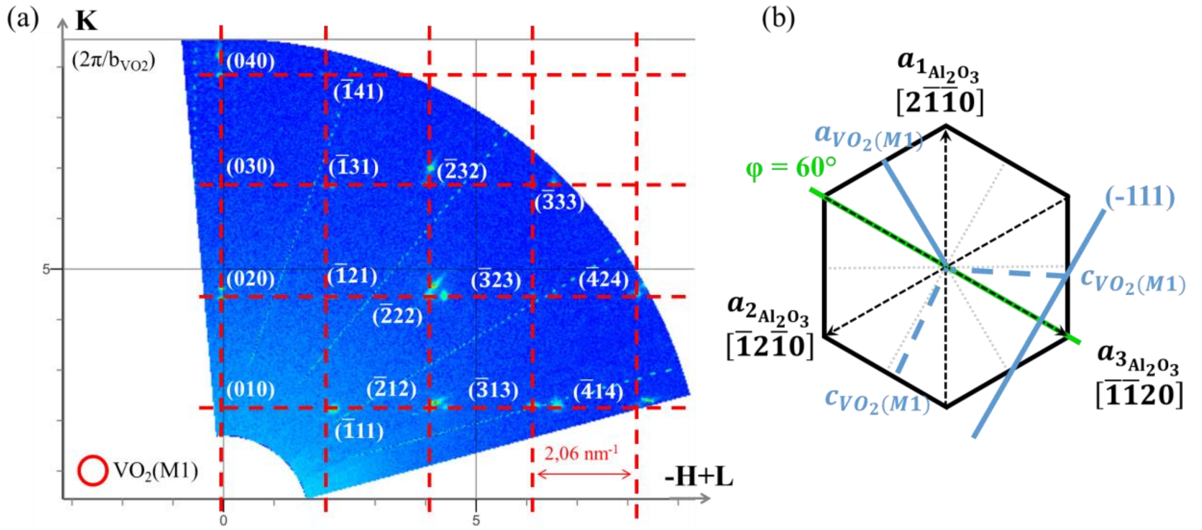

Figure 3-10: Reciprocal space mapping at φ=60° along one Al_2O_3 $\vec{a}$-axis as shown on the right (green line). The red grid is the reciprocal lattice of a second VO_2(M1) variant, with the detected diffraction spots indexed and circled. (Q_y, Q_z) are the vertical and in-plane coordinates of the diffusion vector, corresponding to the K and –H+L directions of this VO_2 variant reciprocal space in (HKL) notation, respectively. As depicted on the right, the planes having the same trace in the $(001)_{Al2O3}$ plane as the $(\bar{1}11)_{VO2(M1)}$ plane are probed in this RSM.

The identified variants from the (identical) RSM at all three azimuths φ=60°, φ=180° and φ=300° are reproduced in **Figure 3-11**. The three RSM revealed six variants, thus compared to the φ-scan data (**Figure 3-2** and **Figure 3-7**) the six other variants could not be detected, due to the angle resolution limitation discussed above. In the end, the combined RSM and φ-scan data are compatible with a total of 12 crystallographic variants in the VO_2(M1) film on c-cut sapphire.

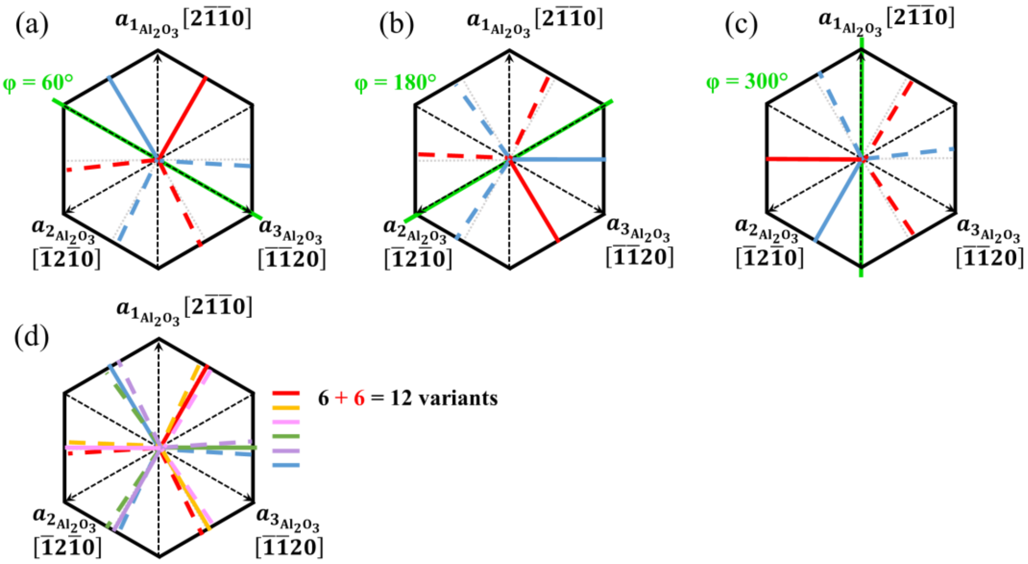

Figure 3-11: Orientations of the $\vec{a}_{VO2(M1)}$ (solid line) and $\vec{c}_{VO2(M1)}$ (dashed line) axes of the VO_2(M1) variants on (001)Al_2O_3 as inferred from the RSM taken at (a) φ=60°, (b) φ=180°, and (c) φ=300°. (d) From these three RSM, six VO_2 variants are detected, of the 12 that were evidenced by the φ-scan study.

We have done the same analysis for φ-scans at φ=90°, φ=210° and φ=330° and have found the same variants as described for the other azimuths. **Figure 3-12** shows an example of the reciprocal space mapping at φ=210°, 30° away from a Al_2O_3 azimuth, and thus aligned with one $\vec{a}_{VO2(M1)}$-axis.

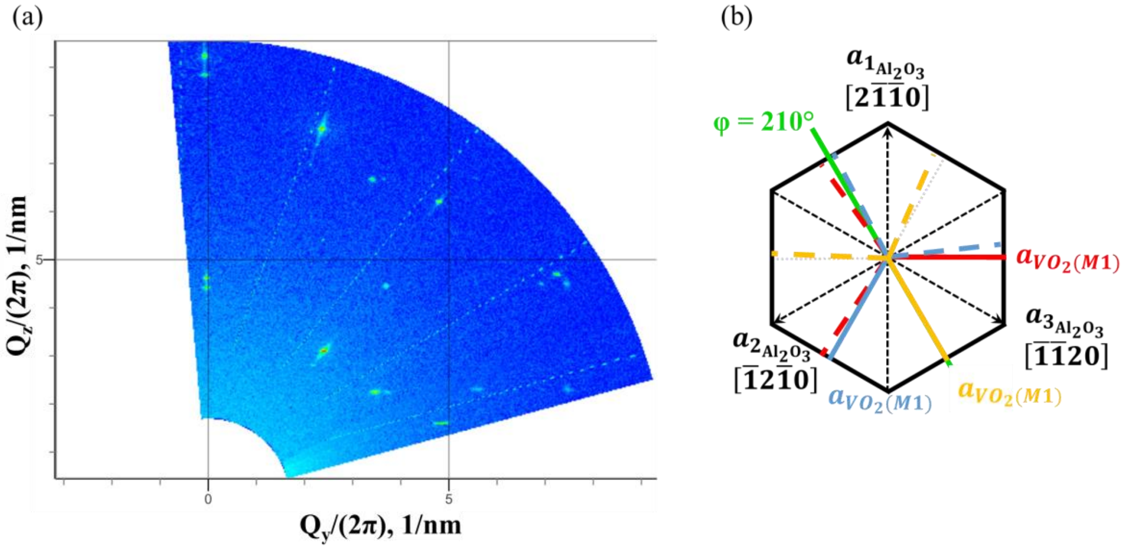

Figure 3-12: Reciprocal space mapping at φ=210° along one VO_2 $\vec{a}$-axis as shown on the right (green line). The VO_2 variants inferred from the diffraction spots are displayed in red, blue and yellow on the right (a_{VO2} solid line, c_{VO2} dashed line).

In conclusion, the φ-scan analysis has highlighted the crystallographic complexity of the VO_2 growth on c-cut sapphire and helped elucidate the epitaxial relationships (given by (3.2) for two particular variants). Coupled with $\theta - 2\theta$ scans to discriminate between several contributions, 12 variants on VO_2(M1) are evidenced. **Figure 3-13** summarizes their different positions with respect to the three azimuths of Al_2O_3.

$$[010]_{VO2}//[0001]_{Al2O3}$$
$$a_{Al2O3}\begin{cases} <100>_{VO2}//[<\bar{1}100>_{Al2O3} \\ <001>_{VO2}/<10\bar{1}0>_{Al2O3} \\ <001>_{VO2}/<1\bar{1}00>_{Al2O3} \end{cases} \qquad (3.2)$$

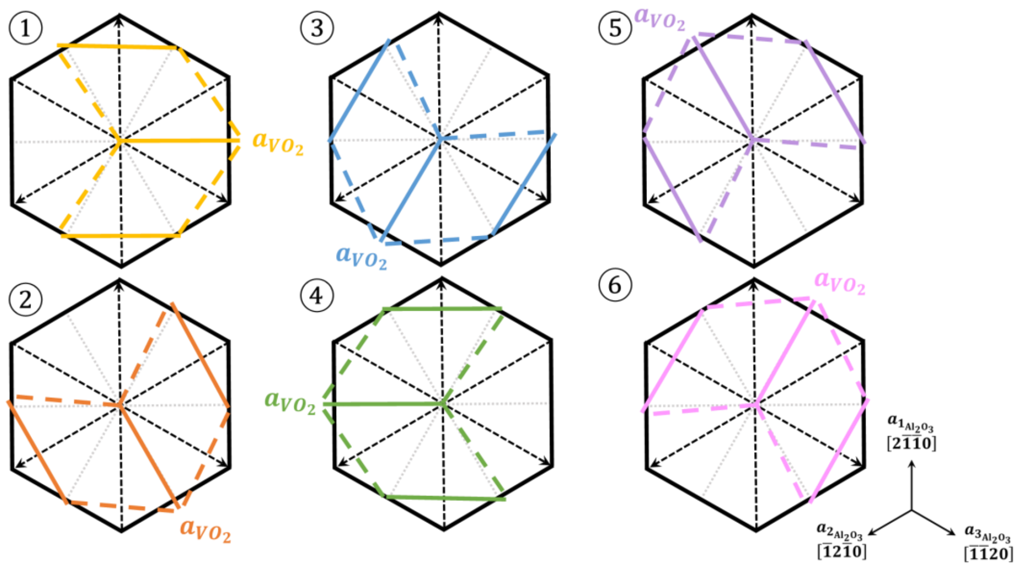

Figure 3-13: Schematic of the 12 VO_2(M1) variants in the (001)Al_2O_3 surface plane. ① and ② are the 4 with their $\vec{a}_{VO2(M1)}$-axis on each side of the azimuth $\vec{a}_{3_{Al2O3}}$, ③ and ④ of $\vec{a}_{2_{Al2O3}}$, and ⑤ and ⑥ of $\vec{a}_{1_{Al2O3}}$.

3.1.2. Epitaxial strain on c-cut sapphire

The previous results give the VO_2(M1) unit cell positioning on c-cut sapphire substrates, our purpose in this part is to determine the epitaxial strain. To do that, we choose one VO_2(M1) variant with its $\vec{a}_{VO2(M1)}$-axis 30° away from $\vec{a}_{2_{Al2O3}}$(**Figure 3-14**).

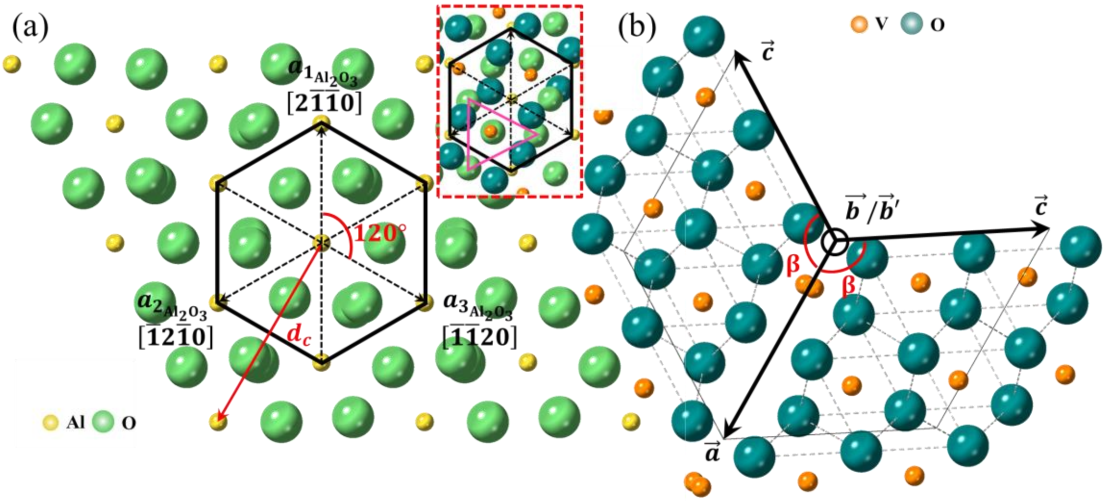

Figure 3-14: (a) Atomic arrangement of sapphire projected in the [0001]-direction. $\vec{a}_{1_{Al2O3}}$, $\vec{a}_{2_{Al2O3}}$, and $\vec{a}_{3_{Al2O3}}$ are <$11\bar{2}0$> translation vectors of the hexagonal Al_2O_3 unit cell for the basal plane. (b) Atomic arrangement in the (010) plane of VO_2 for the two variants with their a_{VO2} axis at 30° from $\vec{a}_{2_{Al_2O_3}}$ azimuth.

By superimposing the two structures, we observe differences in dimension between VO_2(M1) and Al_2O_3, due to the lattice mismatch. The vanadium ion is placed in the center of a triangle of oxygen ions of the substrate and can form bonds with them (inset of **Figure 3-14**). The misfit strain between the VO_2(M1) bulk and the (001)Al_2O_3 was calculated for one variant by eq.(3.3) [WON13].

$$\mathrm{m}_{\mathrm{a(M1)}} = \frac{|\mathrm{d}_c| - \mathrm{a}_{\mathrm{RT}}^{\mathrm{bulk}}}{\mathrm{a}_{\mathrm{RT}}^{\mathrm{bulk}}} \tag{3.3}$$

Where $\mathrm{m}_{\mathrm{a(M1)}}$ is the misfit strain along the a_{VO2} axis of VO_2(M1), a_{RT}^{bulk} is the corresponding VO_2 bulk lattice parameter at RT (cf. **Table 3-4**), and d the vector of the $(001)_{Al2O3}$ plane depending on the crystal structure of the substrate and aligned with the $\vec{a}_{VO2(M1)}$-axis, that can be defined by $d_c = 2a_{2_{Al2O3}} + a_{3_{Al2O3}}$ (**Figure 3-15**).

During growth at high temperature, the rutile phase is formed first on the sapphire surface, with 6 different variants [MOA17], and transforms during cooling into the monoclinic phase with 12 variants that we experimentally measured (**Figure 3-15**). Recent work has shown that the M1 and R phases share their common $(111)_{VO2(R)}$ planes during the transition [ROD21]. Thus, misfit strain was also determined for the rutile phase along $\vec{c}_{VO2(R)}$-axis. **Table 3-3** summarizes the calculated misfit values along $a_{VO2(M1)}$ and $c_{VO2(R)}$.

Table 3-3: Misfit strain calculated for the VO_2(M1) on (001)Al_2O_3. JCPDS-46-1212 was used for Al_2O_3 lattice parameter and JCPDS-01-082-0661 for VO_2. Misfit for VO_2(R) is also given.

Substrate	**a(Å)**	**c(Å)**	**$\lvert d \rvert$ (Å)**	**$m_{a(M1)}$ (%)**	**$m_{c(R)}$ (%)**
Al_2O_3	4.7587	12.992	4.755	-17.3	-16.7

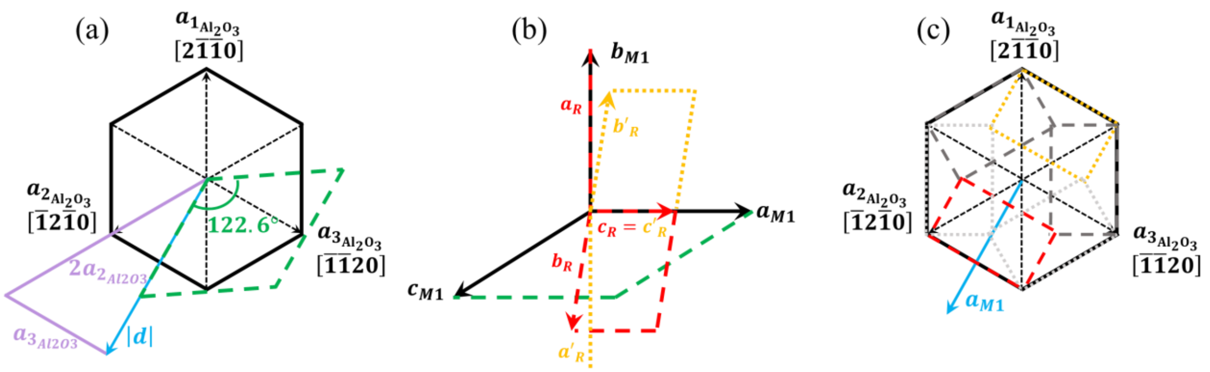

Figure 3-15: Schematic of (010)VO_2(M1) epitaxy on (001)Al_2O_3. (a) The $\vec{a}_{VO2(M1)}$-axis and (c) $\vec{c}_{VO2(R)}$-axis of VO_2 are aligned along the vector d of the (001)Al_2O_3 plane. The monoclinic cell is represented in green and the rutile cell in red (its opposite at 180° in yellow). (b) Relationship between lattice unit vectors of rutile and monoclinic structures given by $a_{M1} = 2c_R$, $b_{M1} = a_R$, and $c_{M1} = b_R - c_R$.

The direct matching results in -17.3% compressive misfit strain along the $\vec{a}_{VO2(M1)}$-axis or -16.7% compressive strain along the $\vec{c}_{VO2(R)}$-axis in rutile phase. In both cases, such large deformations prohibit any possibility of pseudomorphic epitaxial growth (cf. Chapter 1). This confirms that the epitaxy of VO_2 on Al_2O_3 is incommensurate, possibly through a domain matching epitaxy mechanism where n VO_2 unit cells fit m Al_2O_3 unit cells (with $n \neq m$) [NAR03]. Indeed, a compressive misfit strain along $a_{VO2(M1)}$of around -0.8% is obtained by matching 5 VO_2(M1) with 6 Al_2O_3 unit cells. Misfit dislocations are induced during nucleation of the first layer, and stay confined at the interface (**Figure 3-16**). This growth mechanism generally leads to textured or polycrystalline layers and is compatible with the multiple variants obtained.

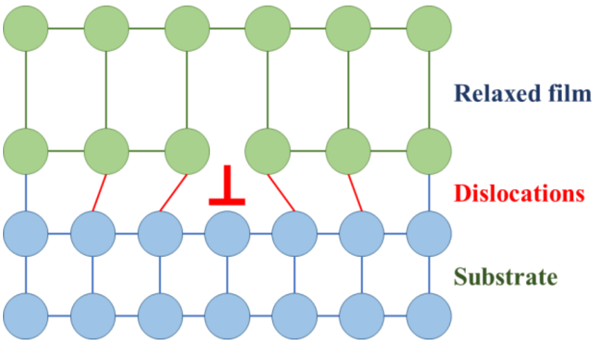

Figure 3-16: Schematic of an incommensurate epitaxy of a film on a substrate, such as in the domain matching epitaxy mechanism, with formation of misfit dislocations at the interface.

From the reciprocal space mappings that we have previously indexed, the experimental film lattice parameters can be determined following the eq.(3.4), and they are compared with the VO_2(M1) bulk parameters. The data summarized in **Table 3-4** allow us to calculate the effective epitaxial strain of the film with eq.(3.5).

$$d_{hkl} = \frac{1}{\sqrt{\left(\frac{h^2}{a^2} + \frac{l^2}{c^2} - \frac{2hl}{ac}\cos\beta\right)\frac{1}{\sin^2\beta} + \frac{k^2}{b^2}}} \tag{3.4}$$

Table 3-4: Lattice parameters calculated for VO_2(M1) film deposited on c-cut sapphire substrate and compared to the JCPDS 01-082-0661 sheet.

Phase	**a (Å)**	**b (Å)**	**c (Å)**	**β (°)**	**V (10^6 pm3)**
VO_2(M1) film	5.73	4.53	5.35	122.2	117.5
VO_2(M1) JCPDS 01-082-0661	**5.7529**	**4.5263**	**5.3825**	**122.602**	**118.07**
$\boldsymbol{\varepsilon}$ (%)	-0.39	+0.08	-0.60	-0.32	-0.48

*a,b,c and β are calculated from d_{hkl} values of (200), (020), (012), and (202) planes, V is calculated by $V = abc * sin\beta$

$$\varepsilon = \frac{x_{RT}^{film} - x_{RT}^{bulk}}{x_{RT}^{bulk}} \tag{3.5}$$

Where x_{RT}^{bulk} (x = a, b or c) is the theoretical lattice parameter at RT of VO_2(M1), and x_{RT}^{film} is the experimental lattice parameter of VO_2(M1) film calculated from the reciprocal space mappings.

Comparing with the bulk lattice constants, the out-of-plane strain seems relaxed, and the film only presents a rather small deformation (+0.08%). Moreover, larger in-plane compressive deformations are found along the $\vec{a}_{VO2(M1)}$-axis (-0.39%) and $\vec{c}_{VO2(M1)}$-axis (-0.60%), respectively, and are responsible for the volume compression of the VO_2 unit cell. This is in agreement with the expected epitaxial strain, although a contribution from the thermal expansion mismatch between the VO_2 thin film and the sapphire substrate upon cooling down from growth temperature might also be considered [THE16][LIU22]. As biaxial tensile strain is known to affect the MIT temperature, we performed temperature-dependent structural characterizations to try and detect a possible effect of strain evolution on MIT characteristics (section 3.3.1).

3.1.3. R-cut sapphire: Epitaxial relations and variants

The VO_2 deposition on r-cut sapphire substrate was performed with similar growth conditions as reported above for c-cut sapphire. The vanadium oxide phase and the crystalline quality of thin film were confirmed by Raman spectroscopy and XRD. As shown on **Figure 3-17**(a), similar to the case on c-cut sapphire, Raman spectra show three bands at 192, 223 and 614 cm^{-1} that are the signature of the VO_2(M1) phase. The intensity and narrowness (FWHM) of Raman peaks, particularly at low frequency (around 190 cm^{-1}), confirm the high crystalline quality. Additionally, we see an intensity variation of the bands at 308, 339 and 442 cm^{-1} compared to the film on c-cut sapphire (**Figure 3-1**(a)). According to the literature, this could be due to the different VO_2 crystal orientations [SHV19]. In this work, we will further investigate the structural characterization with a focus on the substrate influence.

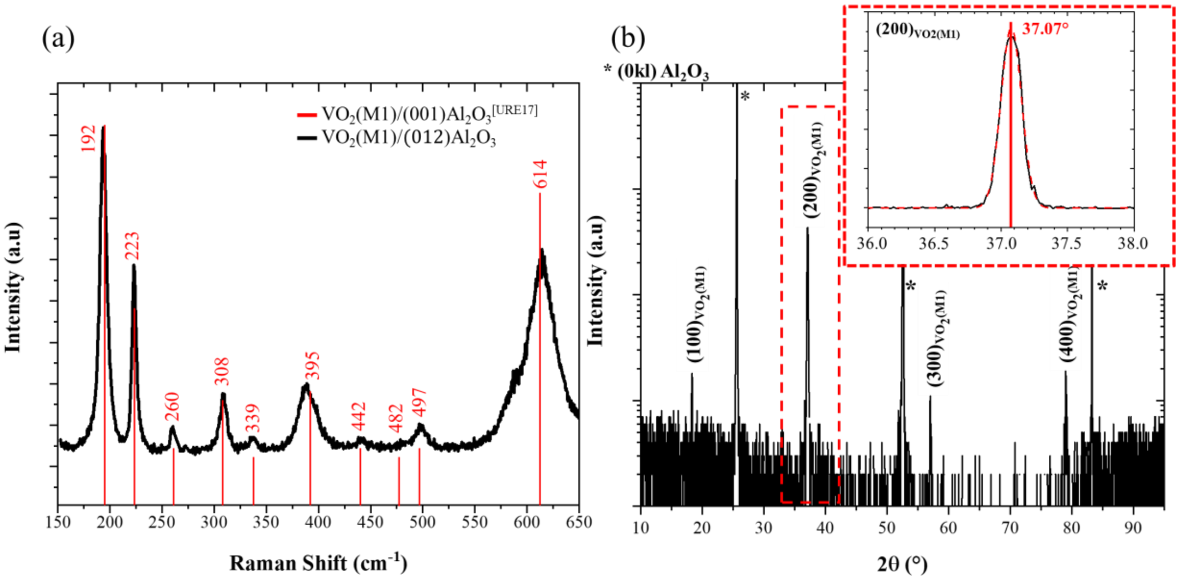

Figure 3-17: (a) Raman spectra and (b) θ-2θ scan at RT of a VO_2 layer deposited on r-cut sapphire substrate. The Raman spectrum is compared to the one of a 200 nm VO_2 film on (001)Al_2O_3 obtained by electron beam evaporation followed by a post-annealing under oxygen atmosphere (red) [URE17].

The XRD characterization performed at RT in $\theta - 2\theta$ mode is shown on **Figure 3-17**(b) and confirms the deposition of VO_2 layer on a r-cut sapphire substrate. The recorded 2θ peaks at 18.29°, 37.07°, 57.03° and 79.01° reveal that the deposition on $(1\bar{1}02)Al_2O_3$ ($\equiv(012)Al_2O_3$) induces the growth of a $(h00)$-oriented VO_2(M1) phase. Other peaks at 25.59°, 52.57° and 83.25° are attributed to $(0kl)$ planes of the substrate, with k=1, 2, 3, and l=2, 4, 6. We deduce that the $(h00)$ planes of the VO_2(M1) are parallel to the $(0kl)$ planes of the substrate.

Then, we proceed with the determination of the in-plane epitaxial relationships between the film and the substrate. **Figure 3-18**(a) shows the φ-scans of the oblique planes $(006)_{Al2O3}$ and $(220)_{VO2(M1)}$. The results indicate that the trace of $(220)_{VO2(M1)}$ is in the r-cut sapphire plane, ±90° away from the $(006)_{Al2O3}$ trace. The $c_{VO2(M1)}$ is thus aligned with the $[1\bar{1}01]$ direction of the $(012)_{Al2O3}$ plane. Since the $\vec{b}_{VO2(M1)}$ unit vector is in the same $(100)_{VO2(M1)}$ plane as $\vec{c}_{VO2(M1)}$ with an angle of 90° between them, it follows that $b_{VO2(M1)}$ is aligned along the $[11\bar{2}0]$ direction of Al_2O_3.

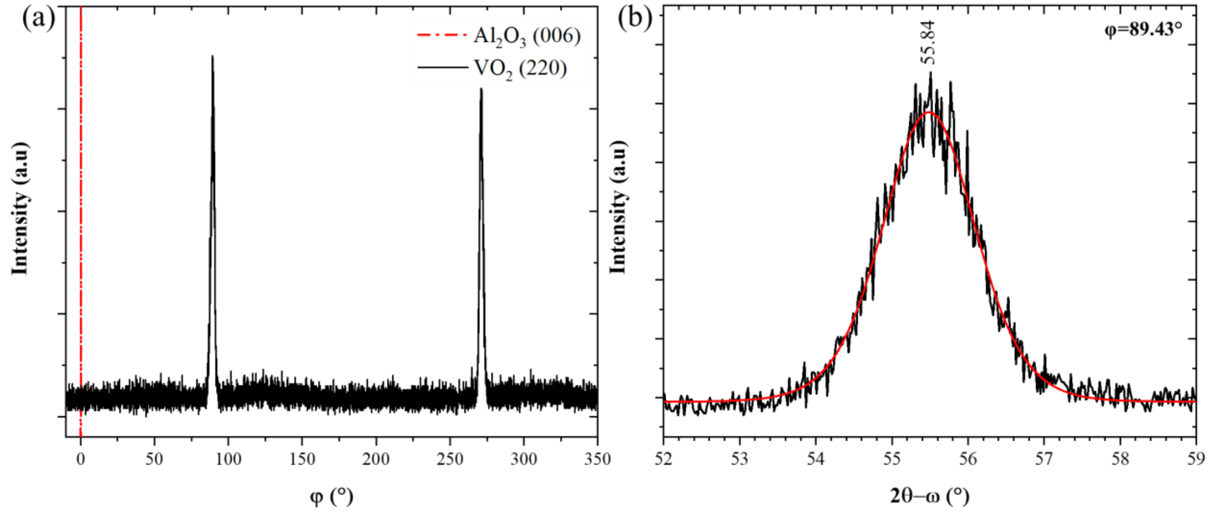

Figure 3-18: (a) φ-scan diagram of VO_2(M1)/(012)Al_2O_3 measured at RT. The $(220)_{VO2(M1)}$ plane is shown in black and the red dashed line indicates the position of the $(006)_{Al2O3}$ plane. (b) 2θ-ω scan at φ =89.43°of the oblique $(220)_{VO2(M1)}$ plane. The solid black line corresponds to the experimental points and the red line to the fit.

The $(012)_{Al2O3}$ plane has a rectangular unit cell, with its shorter side aligned along the azimuth $\vec{a}_{3_{Al2O3}}$ (the 2 others giving equivalent planes) of the Al_2O_3 (**Figure 3-19**(a)). The trace of the $(006)_{Al2O3}$ plane in the $(012)_{Al2O3}$ plane is aligned along the short side of the rectangle, corresponding to the $[11\bar{2}0]$ direction.

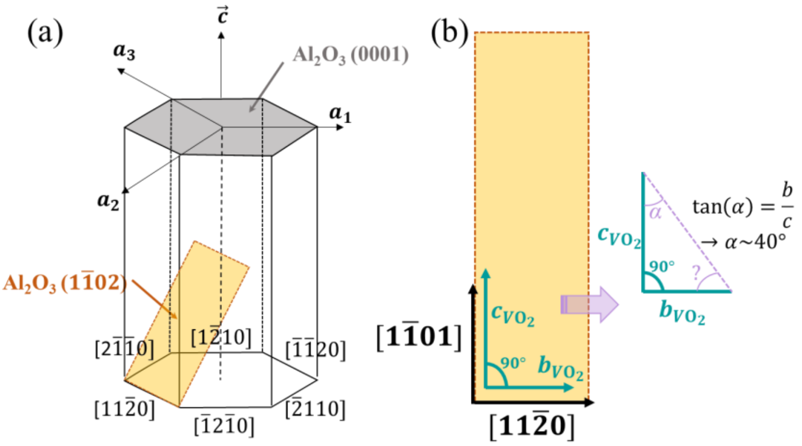

Figure 3-19: (a) Schematic representation of the hexagonal unit cell of Al_2O_3. The r-plane is in orange, aligned parallel to the azimuth a_3 of Al_2O_3. The $(001)_{Al2O3}$ plane is represented in grey. (b) Alignment of the VO_2 unit cell directions according to the $[11\bar{2}0]_{Al2O3}$ and $[1\bar{1}01]_{Al2O3}$ ones in the $(012)_{Al2O3}$ plane.

The φ-scans of the oblique planes $(006)_{Al2O3}$ and $(011)_{VO2(M1)}$ are visible in **Figure 3-20**. As depicted in **Figure 3-19**(b), the trace of $(011)_{VO2(M1)}$ forms an angle $\alpha = \tan^{-1}(b/c) \approx 40°$ with the $c_{VO2(M1)}$ direction, and an angle ~50° with the $b_{VO2(M1)}$ direction. Therefore, as the $(006)_{Al2O3}$ trace is parallel to $b_{VO2(M1)}$, the two $(011)_{VO2(M1)}$ traces are on each side and 50° away from the $(006)_{Al2O3}$ trace.

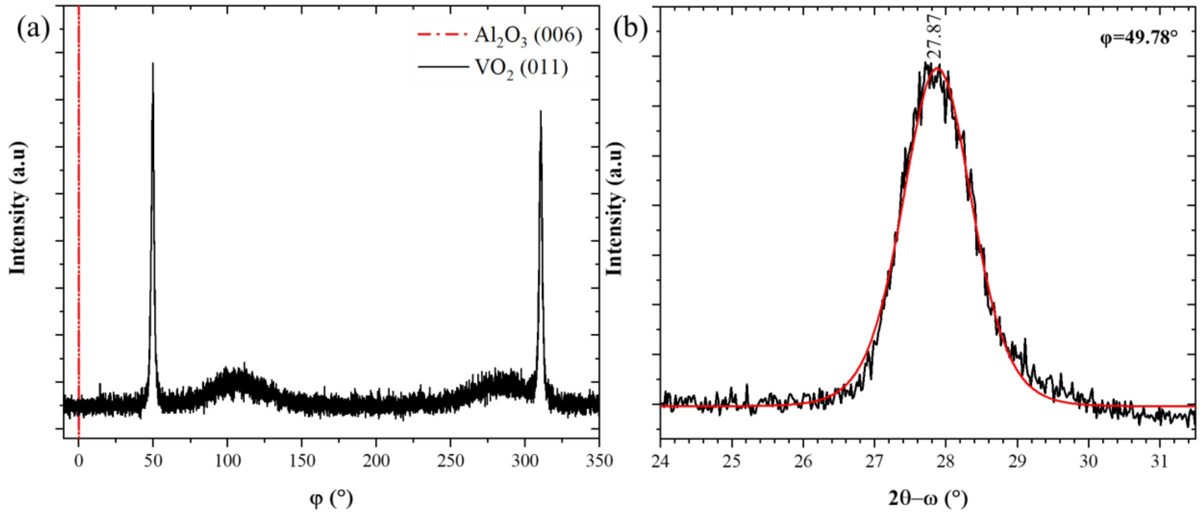

Figure 3-20: (a) φ-scan diagram of a $VO_2(M1)/(012)Al_2O_3$ measured at RT. The $(011)_{VO2(M1)}$ plane is in black and the red dashed line indicates the position of the $(006)_{Al2O3}$ plane. (b) 2θ-ω scans at φ =49.78°of the oblique $(011)_{VO2(M1)}$ plane. The solid black line corresponds to the experimental points and the red to the fit.

We note that given the $VO_2(M1)$ crystallographic structure, the measured φ-scans on r-cut sapphire would be exactly the same for VO_2 variants with their $\vec{b}_{VO2(M1)}$ unit vector at 180° from the one shown in **Figure 3-19**(b). Thus, two possible variants of $VO_2(M1)$ on r-cut sapphire must be considered, with $b_{VO2(M1)}$ and $b'_{VO2(M1)}$ directions (**Figure 3-21** ① and ②). Two additional variants (③ and ④) are obtained if $\vec{c}_{VO2(M1)}$ is reversed along with $\vec{b}_{VO2(M1)}$. **Figure 3-21** summarizes these four possibilities of $VO_2(M1)$ growth on r-cut sapphire substrate.

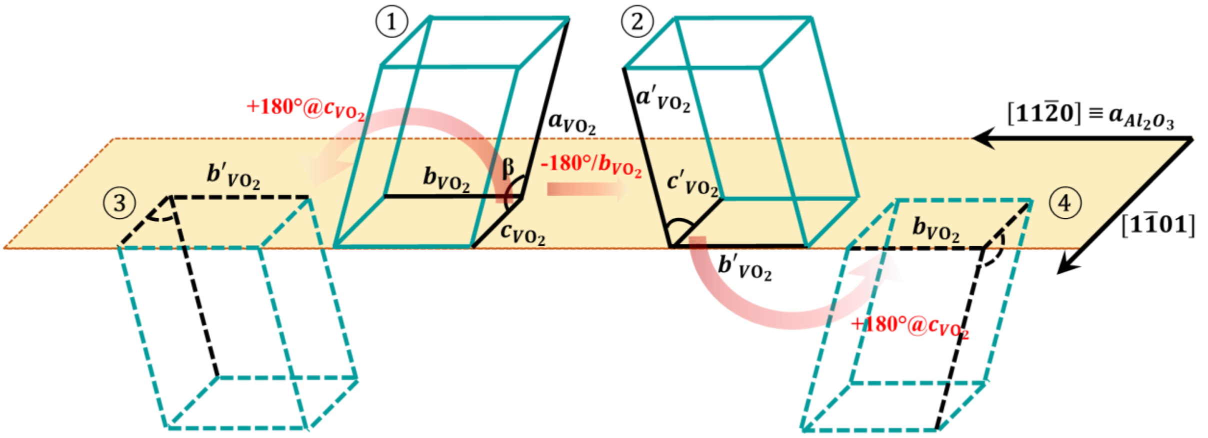

Figure 3-21: Schematic showing the 2 and 4 variants possibilities of $VO_2(M1)$ deposited on r-cut sapphire, considering the 180° rotation in plane of $b_{VO2(M1)}$ and out-of-plane around $c_{VO2(M1)}$.

Although it looks like 4 variants are possible, we see in **Figure 3-21** that ① and ④ unit cells are equivalent given a rotation of 180° around the $\vec{b}_{VO2(M1)}$-axis, corresponding to an inversion of the directions of both the $\vec{a}_{VO2(M1)}$ and $\vec{c}_{VO2(M1)}$ unit vectors. This operation is shown in **Figure 3-22**(a). In this picture, a (hkl) plane in unit cell ① corresponds to a $(-hk-l)$ plane in unit cell ④. Now, given the symmetries of the $VO_2(M1)$ structure (space group #14 $P2_1/c$), these planes have in fact the very same interreticular distance (eq.(3.4)) and atomic arrangement as illustrated in **Figure 3-22**(b).

The same observation can be made for the variants ② and ③, so that finally ① = ④ and ② = ③, and only 2 different variants are found. In conclusion, the VO_2(M1) growth on the r-cut sapphire substrate is done according to 2 variants. To confirm these, and measure the film lattice constants, reciprocal space mappings were performed and are presented below.

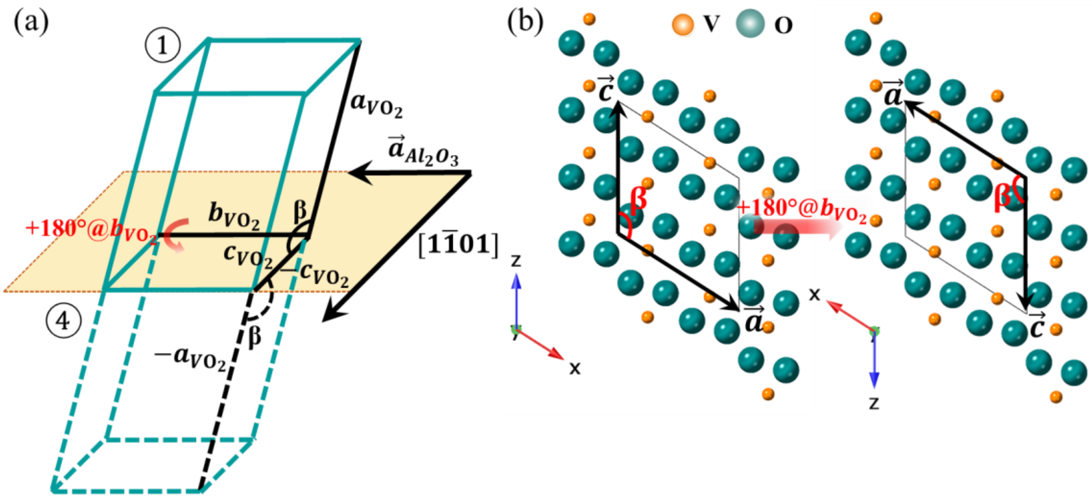

Figure 3-22: (a) Schematic representation of the variants ① and ④. By rotation of ① around $\vec{b}_{VO2(M1)}$-axis by 180°, $a_{VO2(M1)}$ becomes -$a_{VO2(M1)}$ in ④, and $c_{VO2(M1)}$ becomes -$c_{VO2(M1)}$. (b) Atomic arrangement in the $(100)_{VO2(M1)}$ plane as seen from the ① and ④ variants.

The mappings were aligned according to the $(1\bar{1}02)_{Al2O3}$ plane at φ=0°, φ=90°, φ=180° and φ=270° as shown in **Figure 3-23**.

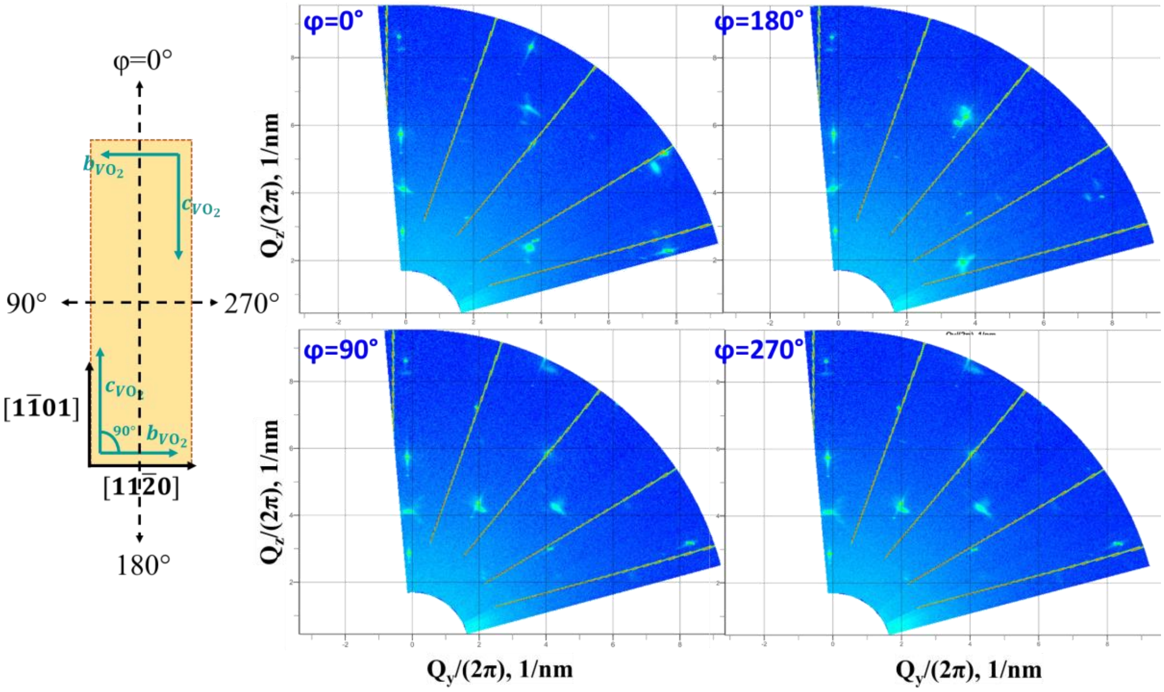

Figure 3-23: Reciprocal space mappings at φ=0°, 90°, 180° and 270°. On the left are schematized the two possible in-plane variants with $b_{VO2(M1)}$ and $c_{VO2(M1)}$ in the (012) sapphire surface plane (in orange) and $a_{VO2(M1)}$ oriented out-of-plane at 122.6° from $c_{VO2(M1)}$. (Q_y, Q_z) are the vertical and in-plane coordinates of the diffusion vector, respectively. The yellow lines are measurement artefacts due to the 2D detector.

As expected, the RSM at φ=0° and φ=180° differ, while they are equivalent at φ=90° and φ=270°. Indeed, $b_{VO2(M1)}$ and $c_{VO2(M1)}$ are in the (012) sapphire surface plane while $a_{VO2(M1)}$ is positioned out-of-plane at 122.6° from $c_{VO2(M1)}$. A RSM along the φ=0°/180° azimuths will thus be parallel to the $\vec{a}_{VO2(M1)}$-axis and will be sensitive to the direction of the latter with respect to the surface plane. In particular, it should differentiate between the variants ① and ②, as depicted in **Figure 3-21**. Two different RSM are experimentally obtained, for which the Al_2O_3 (**Figure 3-24**) and VO_2(M1) (**Figure 3-25**) spots could be indexed. Regarding the φ=90°/270° azimuths, the RSM show the same information as they are perpendicular to the $\vec{a}_{VO2(M1)}$-axis.

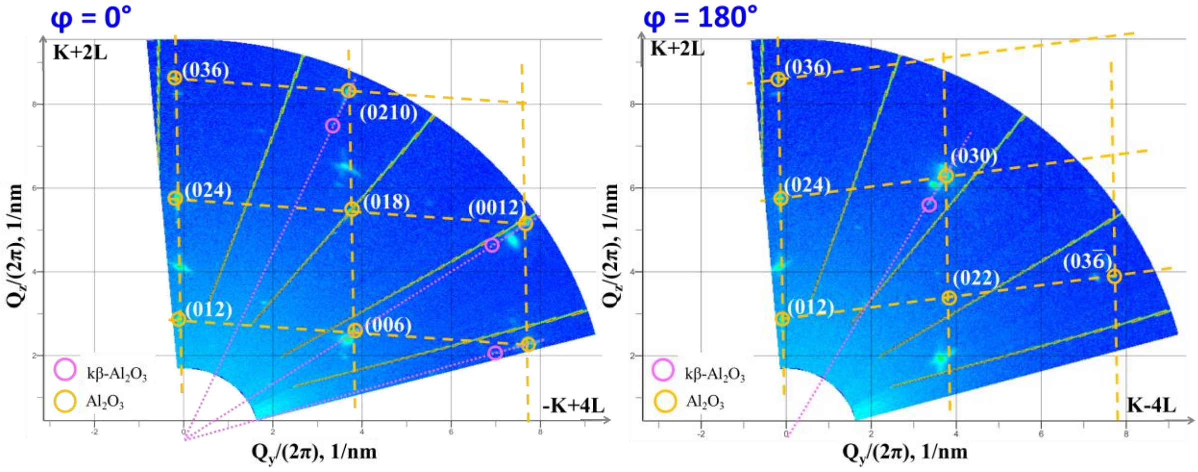

Figure 3-24: Reciprocal space mappings at φ=0° and φ=180°. Al_2O_3 reciprocal lattice and spots are in yellow and kβ-Al_2O_3 spots in pink. (Q_y, Q_z) are the vertical and in-plane coordinates of the diffusion vector, corresponding to K+2L and –K+4L directions of Al_2O_3 reciprocal space in (HKL) notation, respectively.

Let us first discuss the mappings at φ=0° and φ=180°. Having identified the spots of the substrate in **Figure 3-24**, the unit vectors of reciprocal space were determined and the Al_2O_3 reciprocal lattice materialized by a yellow grid. Note that the "horizontal" reciprocal direction appears inclined for Al_2O_3 as the $\vec{a}_{VO2(M1)}$-axis is not perpendicular to the surface plane, thus the $c^*_{VO2(M1)}$ reciprocal vector is not in the surface plane. Out-of-plane vector is $b^*_{Al2O3} + 2c^*_{Al2O3}$ for the two mappings, while the in-plane ones are of opposite signs between φ=0°/180° and along the $-b^*_{Al2O3} + 4c^*_{Al2O3}$ direction. The indexing of all the sapphire diffraction spots confirms the r-cut orientation of the substrate. Aligned with the $(012)_{Al2O3}$ surface plane, the $(200)_{VO2(M1)}$ and $(400)_{VO2(M1)}$ planes confirm the preferential orientation of the growth: $(100)_{VO2(M1)} // (012)_{Al2O3}$. **Figure 3-25** shows all the VO_2(M1) spots on the RSM at φ=0° and φ=180° indexed according to the JCPDS 082-0661 datasheet. Two variants are detected, with an in-plane angle of 180° between them as depicted in **Figure 3-21** (① and ②). We note that the variant ① with its $\vec{c}_{VO2(M1)}$-axis oriented in the $[1\bar{1}01]$ direction has diffraction spots of higher intensity than the variant ② with opposite direction of its $\vec{c}_{VO2(M1)}$-axis. This might indicate a higher proportion of one variant with respect to the other, but determining the origin of this unbalance is out of the scope of this work.

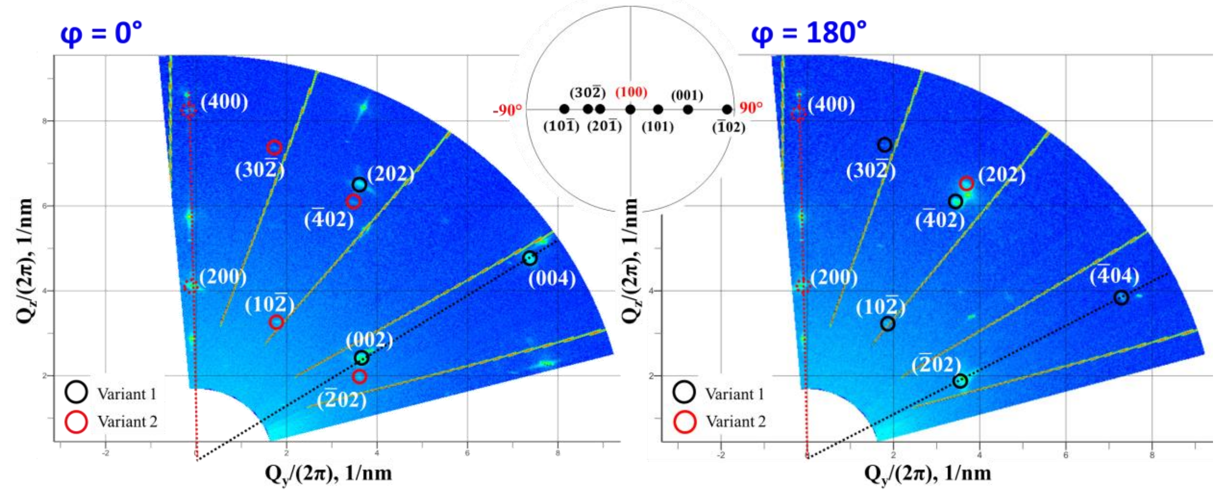

Figure 3-25: Reciprocal space mappings at φ=0° and φ=180°. The diffraction spots of the two VO_2(M1) variants are circled in black and red. (Q_y, Q_z) are the vertical and in-plane coordinates of the diffusion vector, the origin at (0,0) being at the intersection of the red and black dotted lines. The stereographic projection evidences that the VO_2 spots belong to two variants at 180° with respect to one another.

We have done the same study for φ-scans at φ=90°/270° as shown in **Figure 3-23**. The obtained results at these φ angles being similar, here we discuss the measurement at φ=90° displayed in **Figure 3-26**.

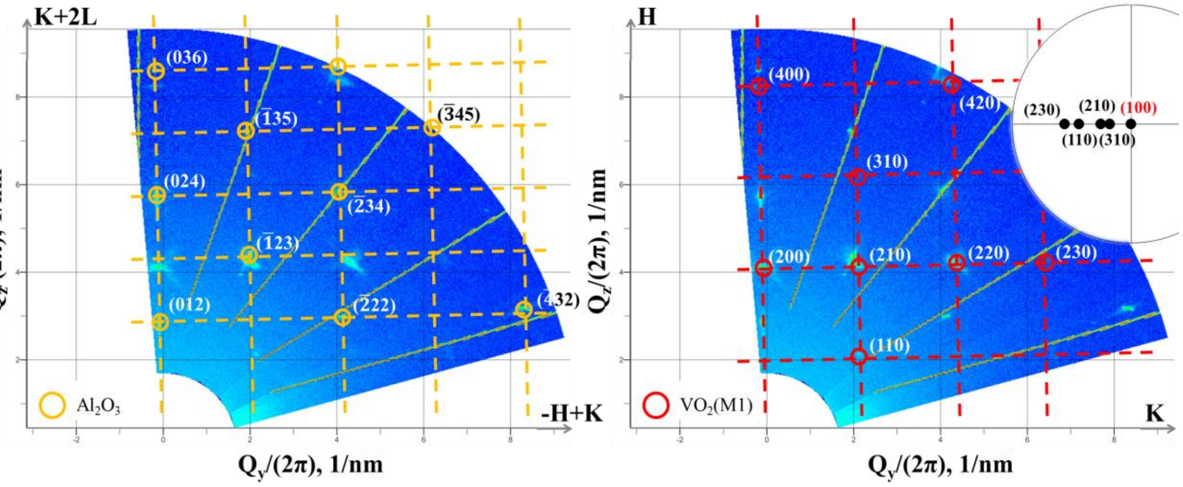

Figure 3-26: Reciprocal space mappings at φ=90°. Al_2O_3 is indexed in yellow and VO_2(M1) in red. (Q_y, Q_z) are the vertical and in-plane coordinates of the diffusion vector, corresponding to the K+2L (Al_2O_3) = H (VO_2) and –H+K (Al_2O_3) = K (VO_2) directions of reciprocal space in (HKL) notation, respectively. The stereographic projection on the right evidences that the VO_2 spots cannot be distinguished among the two variants, as all the planes have their normal along the same azimuth on the projection.

As for preceding mappings, the substrate reciprocal lattice is represented (in yellow) and all the spots corresponding to VO_2(M1) are identified (in red) and belong to the $(hk0)_{VO2(M1)}$ family. As discussed above, the RSM taken along the φ=90°/270° azimuths cannot distinguish the two crystallographic variants as they cannot differentiate between $(hk0)_{VO2(M1)}$ and $(-hk0)_{VO2(M1)}$ planes.

In conclusion, both the φ-scan and RSM measurements have evidenced two variants for VO_2(M1) on r-cut sapphire. Finally, the epitaxial relationships are given by eq.(3.6):

$$\begin{array}{ll} \underline{\text{Variant 1}}: & (100)_{\mathrm{VO2}}//(1\bar{1}02)_{\mathrm{Al2O3}} \\ & [010]_{\mathrm{VO2}}//[11\bar{2}0]_{\mathrm{Al2O3}} \\ & [001]_{\mathrm{VO2}}//[1\bar{1}01]_{\mathrm{Al2O3}} \\ \underline{\text{Variant 2}}: & (100)_{\mathrm{VO2}}//(1\bar{1}02)_{\mathrm{Al2O3}} \\ & [010]_{\mathrm{VO2}}//[\bar{1}\bar{1}20]_{\mathrm{Al2O3}} \\ & [001]_{\mathrm{VO2}}//[\bar{1}101]_{\mathrm{Al2O3}} \end{array} \tag{3.6}$$

3.1.4. Epitaxial strain on r-cut sapphire

From the combination of φ-scan and reciprocal mapping methods, we saw that the VO_2 grows on r-cut sapphire substrate following 2 possibilities, much less than the 12 possibilities determined for c-cut sapphire. Based on these results, we purpose to determine the misfit strain expected in our layer. To do that, VO_2(M1) bulk structure was aligned with the $(200)_{VO2(M1)}$ plane parallel to the $(012)_{Al2O3}$ plane (**Figure 3-27**). The misfit between VO_2(M1) and Al_2O_3 was calculated for one variant of VO_2 following eq.(3.7).

$$\mathrm{m}_{\mathrm{x(M1)}} = \frac{|\mathrm{d_r}| - x_{\mathrm{RT}}^{\mathrm{bulk}}}{x_{\mathrm{RT}}^{\mathrm{bulk}}} \tag{3.7}$$

Where x_{RT}^{bulk} in the formula correspond to the $b_{VO2(M1)}$ and $c_{VO2(M1)}$ lattice parameters, and d_r the corresponding distance in the substrate surface plane equal to 5.127 Å along $[1\bar{1}01]_{Al_2O_3}$ and 4.755 Å (a_{Al2O3} parameter) along $[11\bar{2}0]_{Al_2O_3}$ (**Figure 3-27**(b)). The pseudomorphic matching of the lattices would result in 5.1% tensile strain along the $\vec{b}_{VO2(M1)}$-axis and -4.7% compressive strain along the $\vec{c}_{VO2(M1)}$-axis. Similar to the case on c-cut sapphire substrate, these significant misfit strains call for a growth mechanism such as domain matching epitaxy, where 22 VO_2(M1) unit cells would fit with 23 Al_2O_3 unit cells, for a resulting tensile misfit strain reduced to about 0.4% according to $\vec{b}_{VO2(M1)}$-axis. As for c-cut sapphire, the VO_2(M1) film lattice parameters on r-cut sapphire have been determined from reciprocal space mappings and the experimental results are summarized in **Table 3-5**.

Table 3-5: Lattice parameters calculated for VO_2(M1) film deposited on r-cut sapphire and compared to the JCPDS 01-082-0661 datasheet to obtain the misfit strain ε.

Phase	**a (Å)**	**b (Å)**	**c (Å)**	**β (°)**	**V (10^6 pm3)**
VO_2(M1) film	5.71	4.55	5.37	121.9	118.4
VO_2(M1) JCPDS 01-082-0661	**5.7529**	**4.5263**	**5.3825**	**122.602**	**118.07**
ε (%)	-0.74	+0.52	-0.23	-0.57	+0.27

*a,b,c and β are calculated from d_{hkl} values of (002), (210), (220), and $(\bar{2}04)$ planes, V is calculated by $V = abc * sin\beta$

Overall, the VO_2 lattice parameters at room temperature are close to the bulk and slightly smaller than those developed on the c-cut sapphire substrate. In the plane of the substrate, the film presents an anisotropic strain, tensile along b_{VO2} and compressive along c_{VO2}, giving a high compressive strain out-of-plane (-0.74% along a_{VO2}). Interestingly, we note that the film grown on r-cut sapphire substrate have more compressive strain along $\vec{a}_{VO2(M1)}$ than on c-cut sapphire substrate. It is reported in literature that strain affects the MIT performance [LIU22][ABR12], and especially the MIT temperature when applied in the $\vec{c}_{VO2(R)}$-axis = $\vec{a}_{VO2(M1)}$-axis direction. Then, the rest of this chapter will be mainly dedicated to the analysis of the properties of the layers and how the substrates impact the transition dynamics of the VO_2 epitaxial films.

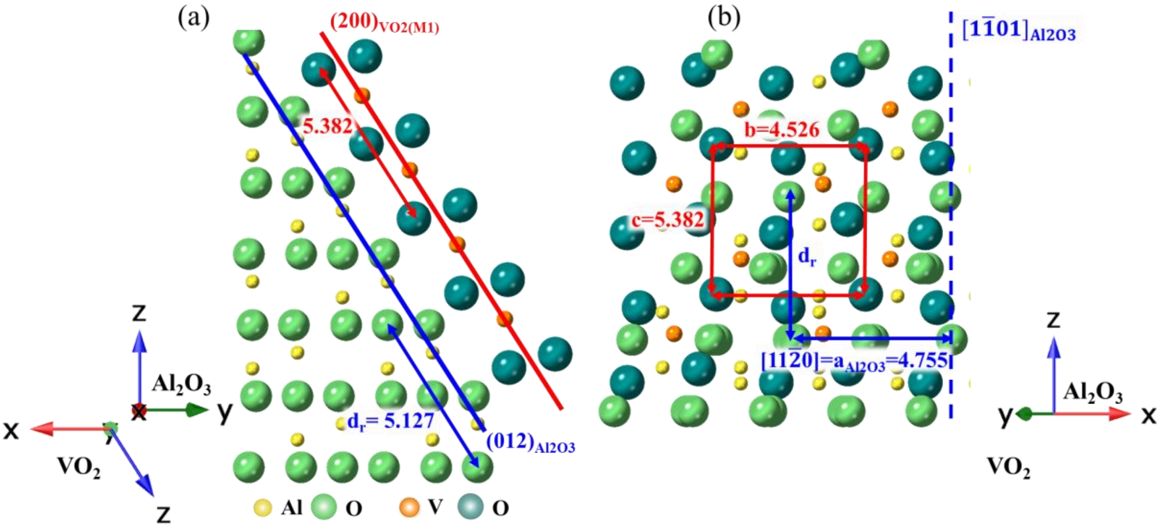

Figure 3-27: Structural representation of VO_2(M1) aligned with Al_2O_3. (a) $(200)_{VO2(M1)}$ plane in red is parallel to the $(012)_{Al2O3}$ plane in blue. (b) We put the $b_{VO2(M1)}$ and $c_{VO2(M1)}$ vectors in the plane of a_{Al2O3} and $[1\bar{1}01]_{Al_2O_3}$. Misfit between VO_2(M1) and Al_2O_3 can be determined.

3.2. Influence of the substrate orientation on morphology

We previously saw that VO_2 has multiple possibilities to grow on sapphire substrates. We evidenced 12 different variants for (001)Al_2O_3 against 2 on (012)Al_2O_3. Further investigation of the films was focused on morphological insights. The SEM and AFM measurements on the layers deposited on (012)Al_2O_3 (**Figure 3-28**(b) and (d)) show that grains appear preferentially oriented in one direction thus forming a continuous film with root mean square roughness (R_{rms}) of ~20 nm.

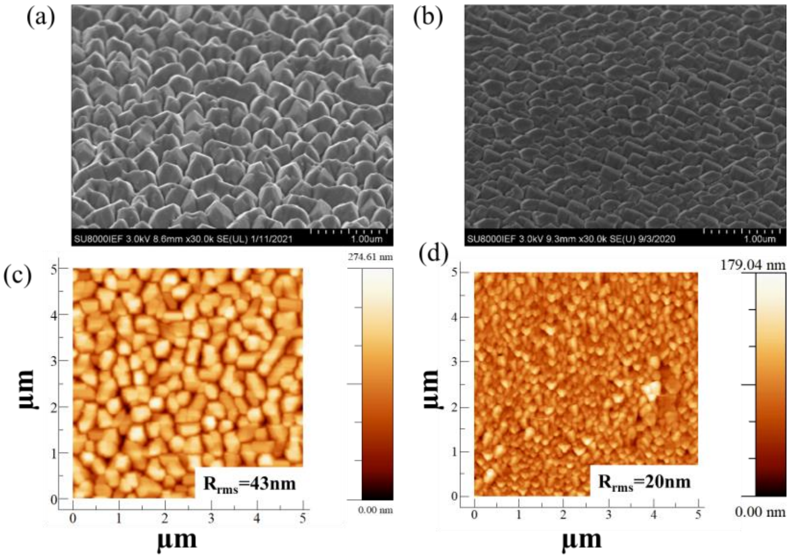

Figure 3-28: SEM images of VO_2(M1) films deposited on (a) c-cut and (b) r-cut sapphire (tilted at 45°). Surface topography measured by AFM of (c) VO_2(M1)/(001)Al_2O_3 and (d) VO_2(M1)/(012)Al_2O_3.

The film deposited on $(001)Al_2O_3$ is much rougher (R_{rms} ~40 nm) with large grains that show no obvious preferential in-plane orientation. The width of the MIT hysteresis generally depends on the crystalline quality of the material, i.e., on the size of the crystalline domains (or crystallites) [THE16][MOL14] and on the defect density. Low material quality generally leads to higher hysteresis width and slower transition dynamics that result in worse performances of devices.

3.3. The metal-insulator transition of VO_2 films

In our study of the substrate influence on the epitaxy of VO_2(M1) phase, we previously demonstrated the considerable difference of the material growth in terms of preferential orientation and morphology, between c- and r-cut sapphire substrates. Now, we focus on the functional properties of VO_2(M1) thin films and in particular on the metal-insulator transition dynamics. The structural transition of VO_2 was firstly investigated by temperature-assisted XRD. Subsequently, film resistivity was measured by 4-point probe method between 30°C and 100°C, and the optical reflectivity was characterized in the same temperature range by Fourier-transform infrared spectroscopy (FTIR).

3.3.1. Structural transition by XRD

The diffractograms were acquired between 27°C to 92°C with a temperature step of 5°C from 27°C to 62°C and from 72°C to 92°C, while the step was reduced to 1°C in the transition temperature range from 62°C and 72°C. In the case of the samples grown on c-cut sapphire substrate, the temperature-dependent XRD was tracking the evolution of the $(020)_{VO2(M1)}$ diffraction peak during the heating and the cooling. **Figure 3-29** and **Figure 3-30** show the θ-2θ scans obtained on a c-cut sapphire substrate.

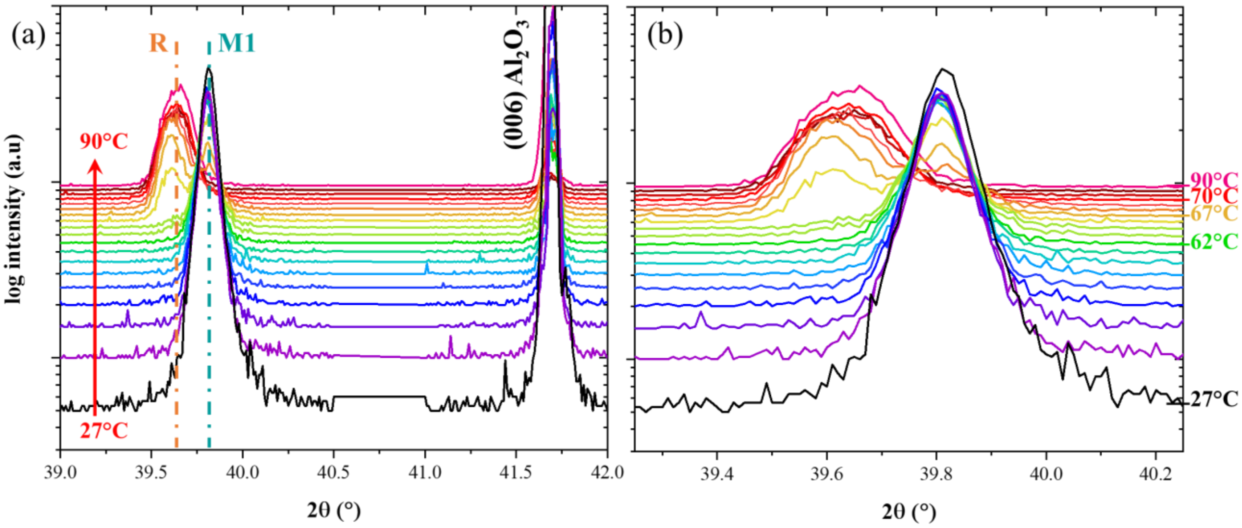

Figure 3-29: (a) Temperature-dependent XRD θ-2θ scans of $VO_2(M1)/(001)Al_2O_3$. (b) Evolution of $(020)_{VO2(M1)}$ peak **during heating** between 27°C and 90°C.

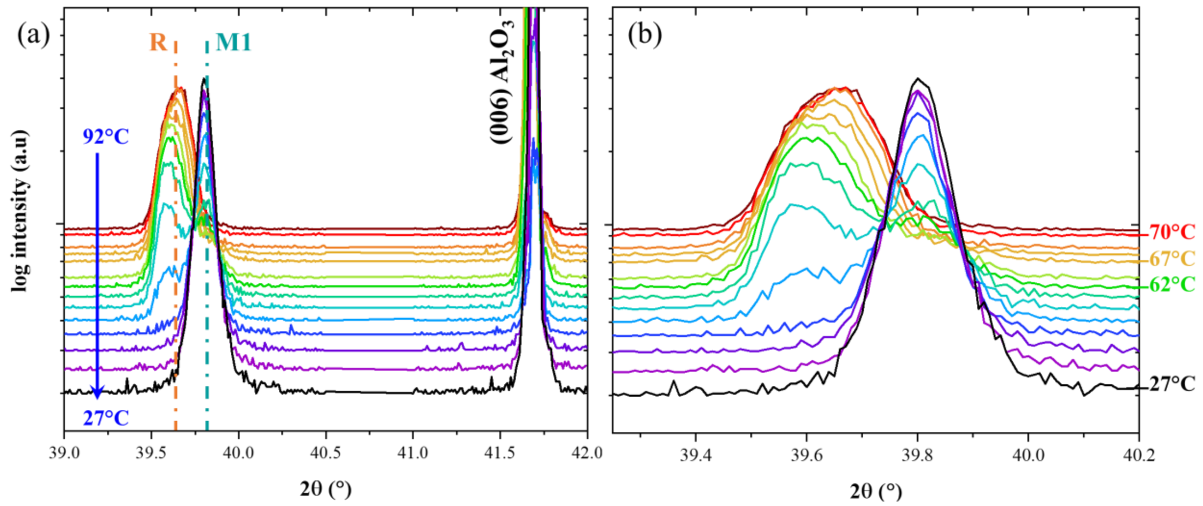

Figure 3-30: (a) Temperature-dependent XRD θ-2θ scans of VO_2(M1)/(001)Al_2O_3. (b) Evolution of $(020)_{VO2(M1)}$ peak **during cooling** between 27°C and 92°C.

The 2θ range was restricted between 39° and 42°. The diffraction peak located around 41.7° is the one of the $(006)_{Al2O3}$ plane, and its position does not vary with temperature. No visible shift of this peak in the investigated temperature range was detected, so the thermal expansion of the substrate is not considered as affecting the VO_2 transition in these measurements. The temperature rise induces notable changes on the VO_2 diffraction peaks, with the intensity of the $(020)_{VO2(M1)}$ peak decreasing while a peak corresponding to the $(020)_{VO2(R)}$ appears. This change is indicative of the structural evolution of VO_2 between the monoclinic phase M1 at low temperature, and the rutile phase R at high temperature. We can detect the simultaneous presence of both the M1 and R peaks over a range of 3° (67°C-70°C). The same phenomenon is observed during the cooling, highlighting the coexistence of the M1 and R phases during the structural transition over a range of 8°C (62°C-70°C).

For the film grown on r-cut sapphire substrate, the temperature-dependent XRD analyses were focused on the $(200)_{VO2(M1)}$ diffraction peak between 36.5° and 37.5°. **Figure 3-31** and **Figure 3-32** present the evolution of the θ-2θ scans during the heating and the cooling. When the temperature increases, the intensity of the $(200)_{VO2(M1)}$ peak drops and at 64°C, the (011) peak of the metallic phase appears and starts increasing.

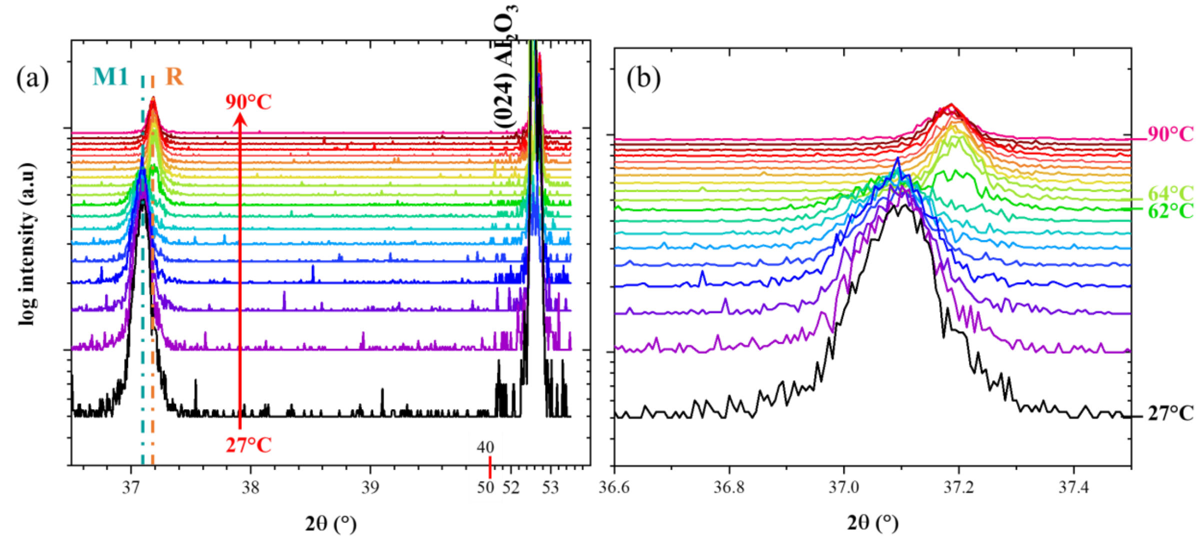

Figure 3-31: (a) Temperature-dependent XRD θ-2θ scans of VO_2(M1)/(012)Al_2O_3. (b) Evolution of $(200)_{VO2(M1)}$ peak **during heating** between 27°C and 90°C.

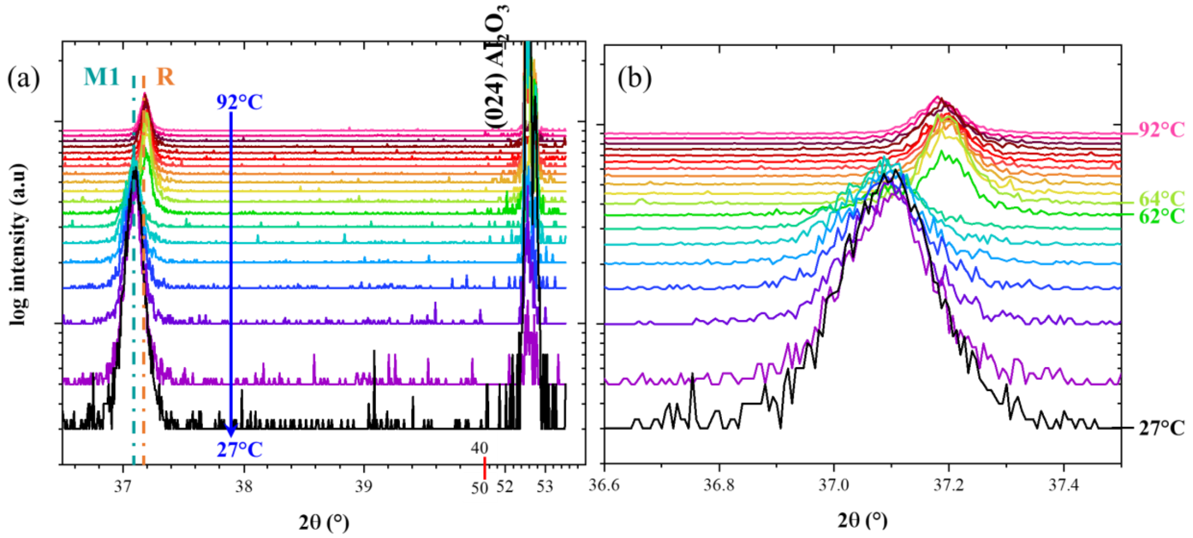

Figure 3-32: (a) Temperature-dependent XRD θ-2θ scans of $VO_2(M1)/(012)Al_2O_3$. (b) Evolution of $(200)_{VO2(M1)}$ peak **<u>during cooling</u>** between 27°C and 92°C.

To follow more accurately the evolution of each phase during the transition, the position and (areal) intensity of $(020)_{VO2(M1)}$ and $(200)_{VO2(M1)}$ peaks were determined by a fit with pseudo-Voigt functions. **Figure 3-33** shows the evolution of the VO_2 peak position as a function of temperature.

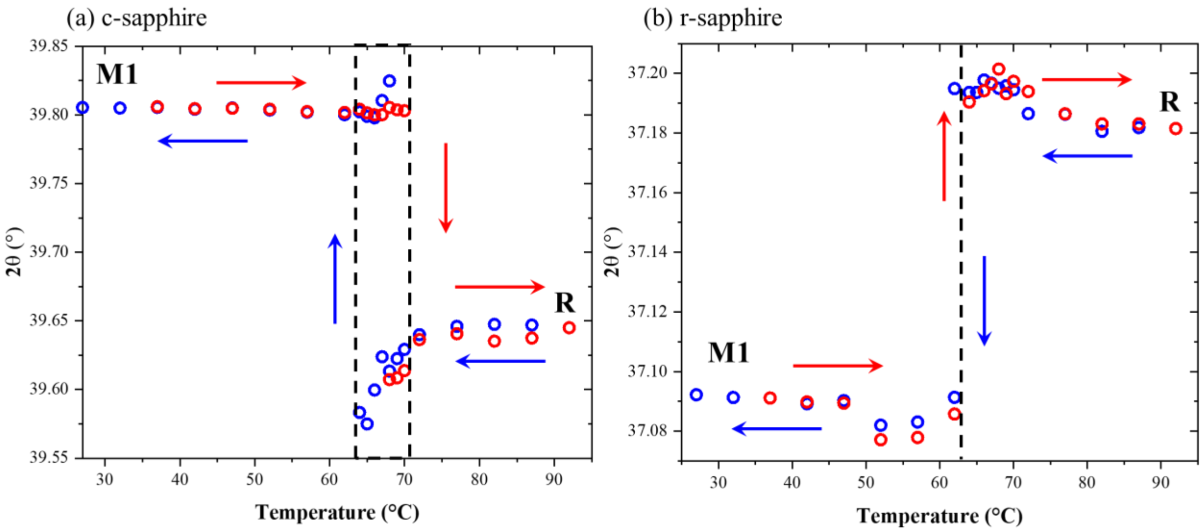

Figure 3-33: Evolution of the VO_2(M1) peak position as function of temperature (heating in red and cooling in blue). The films are deposited on (a) c-cut and (b) r-cut sapphire substrates. The area framed in black dotted line corresponds to the coexistence of the M1 and R phases.

For the film deposited on c-cut sapphire substrate, the graph exhibits three distinct zones. When the temperature is between the ambient and 60°C, the position of the $(020)_{VO2(M1)}$ peak remains stable. Starting from 62°C, the peak position shifts slightly towards higher 2θ values. This phenomenon is accentuated when the second diffraction peak appears. Between 64°C and 70°C, the coexistence of the two peaks is observed. Considering the epitaxy of the VO_2 deposited on c-cut sapphire (section 3.1.1), the VO_2 layer presents grain boundaries and defects due to the 12 variants. When the thermal stimulus is applied, crystallites of the insulating phase will transit to the metallic phase. As the temperature increases, the number and size of affected clusters will increase. The formation of the R phase, which has higher density than the M1 phase, can induce a local strain on the crystallites and explain the slight shift in 2θ of the peak (higher 2θ corresponds to higher out-of-plane parameter). Finally, when the temperature is higher than 75°C, the second peak stabilizes around the value of 2θ = 39.64°, corresponding to the (020) plane of the rutile phase. In the case of the VO_2 film deposited on r-cut sapphire, the evolution of the VO_2 diffraction peaks in the $2\theta = 36.5° - 37.5°$ range (**Figure 3-33**(b)) also confirms the phase transition but without the phase coexistence region. Up to 62°C, the 2θ position of the peak is relatively stable. Further heating shifts abruptly the peak position to higher 2θ angles and stabilizes it around a value of $2\theta = 37.19°$, corresponding to the rutile phase of VO_2. Contrary to previous works that reported an intermediate M2 phase during the transition in temperature [ROD21][THE16], our epitaxial VO_2 films transit from M1 to R without intermediate phase as shown in **Figure 3-34**.

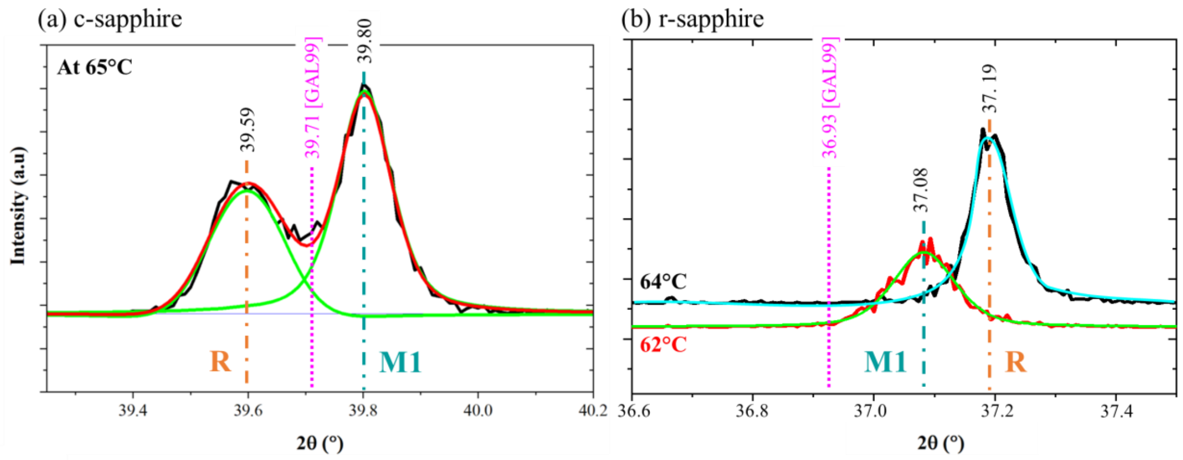

Figure 3-34: θ-2θ scans of VO_2(M1) on (a) c-sapphire at 65°C and (b) r-sapphire at 62°C and 64°C. The theoretical peak position of $(200)_{VO2(M2)}$ at 39.71° and $(021)_{VO2(M2)}$ at 36.93° are represented in pink [GAL99].

In Chapter 1, we showed that strain within films could strongly affect the MIT characteristic of the VO_2. According to the literature [ROD21][POU75][GUO11], a tensile strain along the $\vec{c}_{VO2(R)}$-axis (or $\vec{a}_{VO2(M1)}$) leads to the stabilization of a new phase (M2), whereas a compressive strain conducts to the single M1/R transition (**Figure 3-35**). For our films, we measured a compressive strain along $\vec{a}_{VO2(M1)}$-axis on both c-cut and r-cut sapphire. The sign and magnitude of strain in VO_2 films can be dependent on the deposition technique used, that can for example affect the energy of the formed species [THE16]. That could explain the M2 phase observed for a film grown by electron-beam (E-beam) evaporation with tensile strain, while in our case the film directly transits between M1 and R without an intermediate M2 phase.

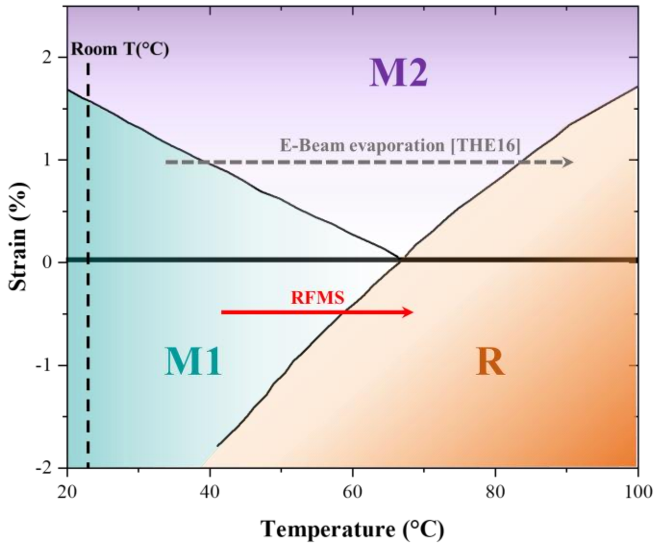

Figure 3-35: Representation of the VO₂ phase diagram as a function of temperature and material strain [POU75]. The VO₂(M1) films obtained by RFMS in this work are compared to a VO₂(M1) film deposited on c-sapphire substrate by electron-beam evaporation [THE16].

We will now try to evaluate the amplitude of the M1 and R phases proportion as a function of temperature of both substrates through the determination of the ratios of the diffracted intensities of the phases M1 and R. First, from the fitting of the VO₂ diffraction peaks, the peak (areal) intensity ratio (x_i where i=R or M1) of M1 and R could be determined by the eq.(3.8) [THE16]:

$$\begin{aligned} x_{M1}(T) &= \frac{I_{M1}(T)}{I_{M1,max}} \\ x_{R}(T) &= \frac{I_{R}(T)}{I_{R,max}} \end{aligned} \tag{3.8}$$

Where $I_{M1,max}$ and $I_{R,max}$ are the maximum integrated intensities of the diffraction peaks of M1 and R phases calculated at 60°C and 80°C, respectively (**Figure 3-36**). Temperature evolution for VO₂ deposited on both c-cut and r-cut sapphire substrates shows a hysteresis cycle.

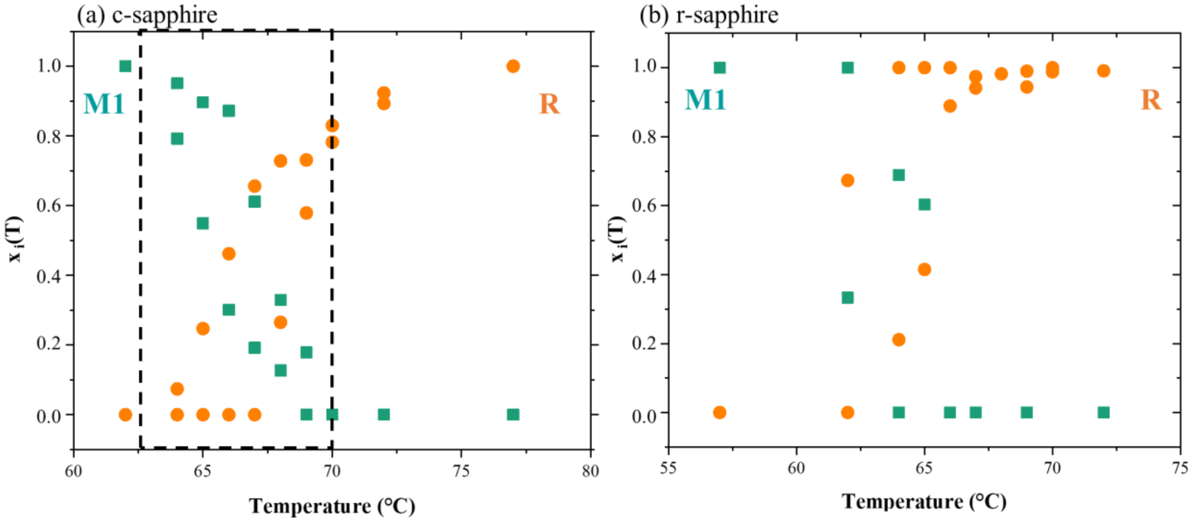

Figure 3-36: (a) Evolution of the position of the VO₂ diffraction peak as a function of temperature. (b) Temperature evolution of the peak intensity ratio of the M1 (blue) and R (orange) phases for a temperature range between 55°C and 75°C. Data obtained for a VO₂(M1) layer deposited on r-sapphire substrate.

Then, the structural phase transition temperature (T_{SPT}) was calculated from eq.(3.9). To do that, the first derivative of **Figure 3-37** was calculated for M1 and R phases during the heating and the cooling, as shown in **Figure 3-38**. Then, T_{up} and T_{down} were determined, and their average gives the structural transition temperature :

$$T_{SPT} = \frac{T_{up} - T_{down}}{2} \tag{3.9}$$

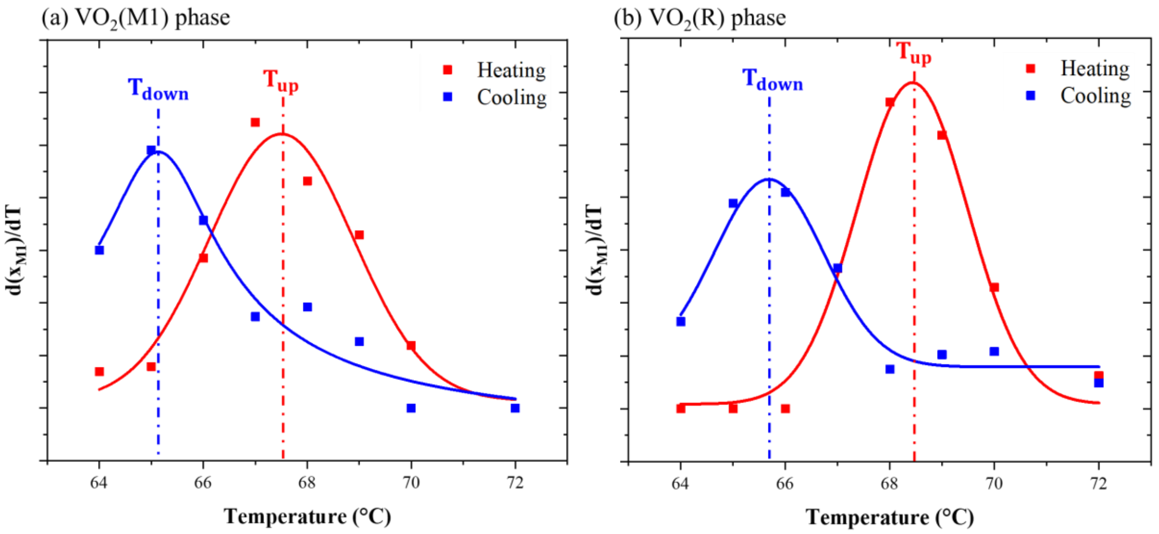

Figure 3-37: Evolution of the first derivative of the peak intensity ratio for (a) monoclinic and (r) rutile phase with temperature. Calculations were performed for a VO$_2$(M1) layer deposited on **c-cut sapphire substrate.**

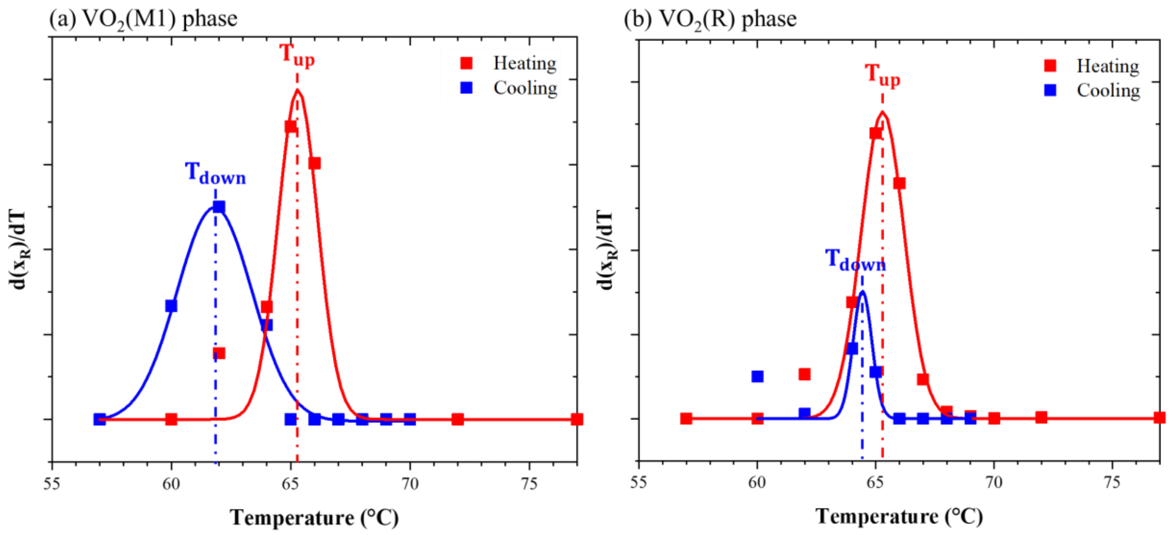

Figure 3-38: Evolution of the first derivative of the peak intensity ratio for (a) monoclinic and (r) rutile phase with temperature. Calculations were performed for a VO$_2$(M1) layer deposited on a **r-cut sapphire substrate.**

The structural transition temperatures were found at 67°C for VO$_2$(M1) grown on (001)Al$_2$O$_3$ and at 65°C for VO$_2$(M1) grown on (012)Al$_2$O$_3$. Compared to the bulk transition temperature of 68°C, both layers exhibit slightly lower transition temperatures. The presence of misfit strain at the interface of the films leading to the growth of multiple VO_2 crystallites may explain this change in the transition temperature. The epitaxial strain experimentally determined previously (section 3.1) along the $\vec{c}_{VO2(R)}$-axis (or $\vec{a}_{VO2(M1)}$) could impact the electronic structure of VO_2(M1) [POU75][ABR12] and modify the transition temperature.

3.3.2. Electrical transition by resistivity measurement

The temperature induced structural transition gave an overview of the MIT character on both studied sapphire substrates. Further study focuses on the resistivity change upon the thermally induced MIT, which is often used as an indirect indicator of the material quality and of device performances. **Figure 3-39** shows the evolution of the electrical resistivity as a function of temperature for 293 nm and 263 nm-thick VO_2 films deposited on c-cut and r-cut sapphire, respectively.

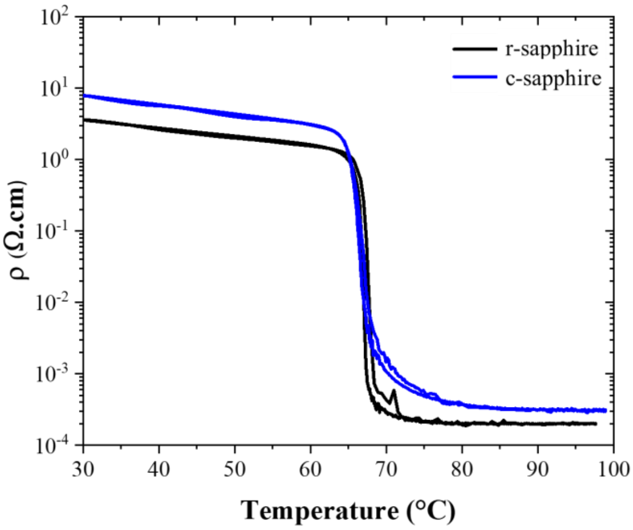

Figure 3-39: Evolution of the resistivity as function of the temperature for VO_2(M1) films deposited on c-cut (blue curve) and r-cut (black curve) sapphire substrates

At around 67°C, the electrical properties of both layers undergo significant resistivity drop, which is characteristic of the metal-insulator transition of VO_2. These two samples both demonstrate abrupt resistivity changes over 4 orders of magnitude. In **Table 3-6**, the VO_2 MIT characteristics including the resistivity change ratio ($\frac{\rho_{max}}{\rho_{min}}$), the critical transition temperature (T_{MIT}), and the hysteresis width (ΔH) are summarized.

Table 3-6: Comparison of electrical and MIT properties of VO_2(M1) deposited on c-cut and r-cut sapphire.

Sample	**Thickness (nm)**	**ρ (Ω.cm) at 25°C**	**ρ (Ω.cm) at 90°C**	$\frac{\rho_{max}}{\rho_{min}}$ **(10^4)**	**T_{MIT}* (°C)**	**ΔH* (°C)**
$VO_2(M1)/(001)Al_2O_3$	293	17	$5*10^{-4}$	3	~67	< 1
$VO_2(M1)/(012)Al_2O_3$	263	4	$2*10^{-4}$	2	~67	< 1

*T_{MIT} is calculated from $(T_{down}+T_{up})/2$ from **Figure 3-40**.

*ΔH is calculated from T_{up}-T_{down} (cf. Chapter 1).

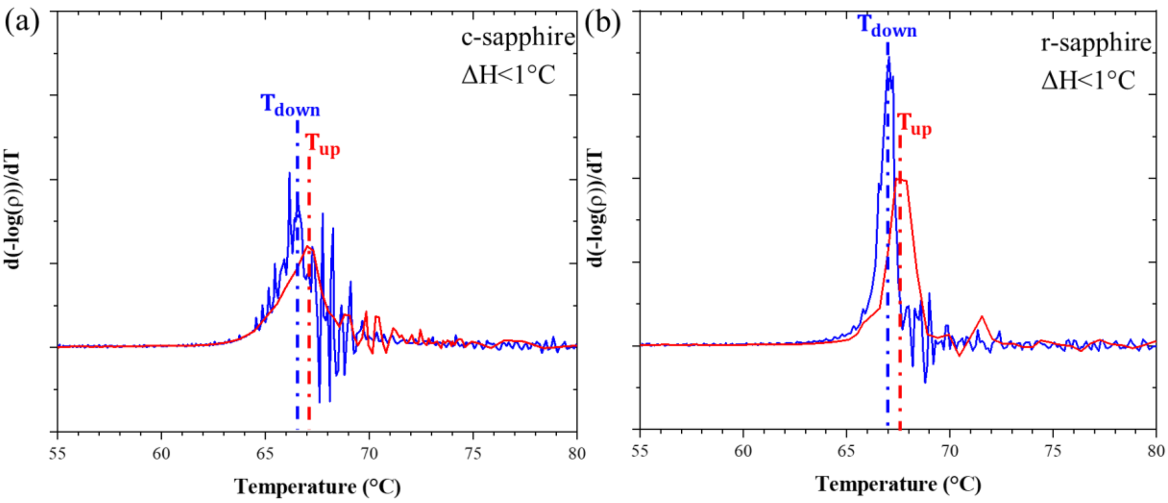

Figure 3-40: First-order derivative of -log(ρ) as a function of temperature for VO_2 thin films. From curves (b) and (c), the hysteresis width ΔH can be determine.

The 4-point probe resistivity measurements on the VO_2(M1) films reveal that the dynamics of thermally induced metal to insulator transition for the samples on both substrates are identical, independent of the substrate orientation. This is at variance with the behavior of the structural transition followed by XRD.

3.3.3. Optical properties by FTIR

Besides the electrical properties change, VO_2 also presents a modification of optical properties during the phase transition. The study was performed on the same samples as for electrical measurements, to verify how the growth conditions and the morphology may impact the VO_2 optical properties (293 nm of VO_2(M1)/(001)Al_2O_3 and 263 nm of VO_2(M1)/(012)Al_2O_3). The temperature-dependent infrared (IR) reflectivity evolution of these samples is presented on **Figure 3-41**. The reflectivity measurement was performed on VO_2 film and on Au reference, between 30 to 90°C with 1°C step.

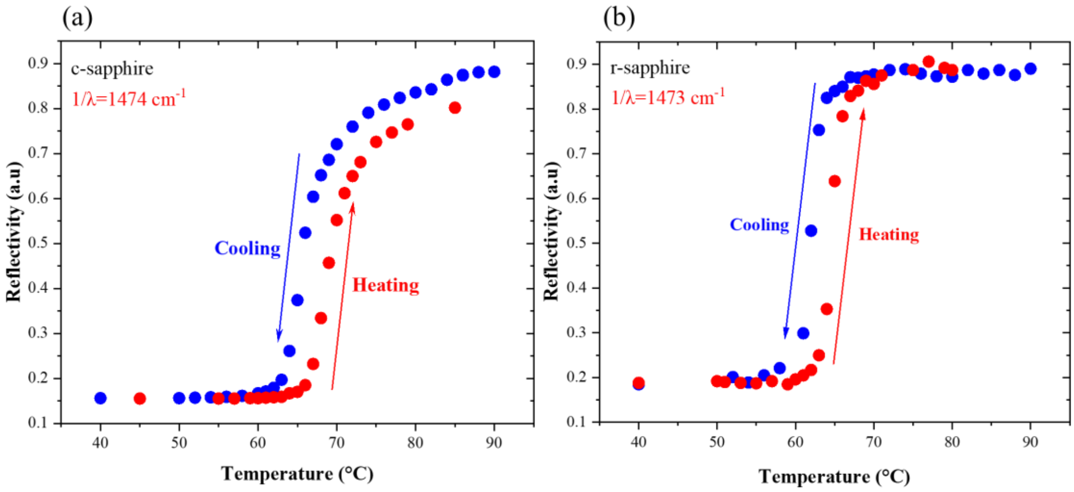

Figure 3-41: IR reflectivity of VO_2 thin films deposited on (a) c-cut and (b) r-cut sapphire substrates. First, samples were cooled down (in blue) to ambient temperature, then heated up (in red) to 90°C.

Both VO_2 samples show a characteristic metal-insulator transition in their reflectivity curves. At low temperature ($T < T_{MIT}$), VO_2 is in its insulating form, and the presence of the optical gap induces a high transmittance in the IR range, an so very low reflectivity. When the temperature increases, the transmittance of the layer decreases and leads to an increase in reflectivity. At $T > T_{MIT}$, the material becomes metallic, and the samples reflect almost all the IR signal. Although the optical properties are very close on both sapphire substrates, we find that the film deposited on $(001)Al_2O_3$ has a larger hysteresis width (ΔT=3°C) than the $VO_2(M1)/(012)Al_2O_3$ (ΔT=1°C). Furthermore, we note that the hysteresis cycle does not "close" at high temperature for the film on c-cut sapphire, as the reflectivity does not go back to its initial high temperature value. The multiple growth of VO_2 identified in the first part of this chapter (section 3.1) may explain these differences. 12 crystallographic variants (VO_2 on c-cut sapphire) may well lead to a larger hysteresis width compared to 2 variants (VO_2 on r-cut sapphire).

3.3.4. Summary and discussions

In this part, the transition dynamics of VO_2 films deposited on c-cut and r-cut sapphire substrates was structurally, electrically, and optically studied, and the results are summarized on **Figure 3-42**.

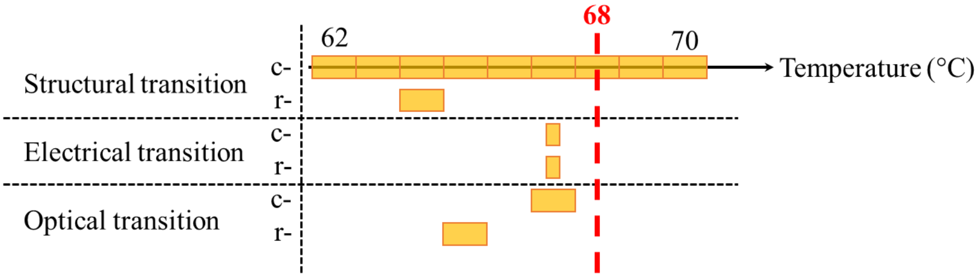

Figure 3-42: Structural, electrical, and optical transition dynamics of $VO_2(M1)$ films deposited by RFMS on c-cut and r-cut sapphire substrate during thermal activation.

Although the samples analyzed have similar transition dynamics, a much less abrupt structural transition for the VO_2 on c-cut sapphire is reported. The 12 variants (section 3.2) induce grain boundaries and defects that could impact the transition dynamics and explain the higher hysteresis width observed in optical properties. When a thermal stimulus is applied, some VO_2 clusters start to transit and can be measured by XRD. Further temperature increase extends the number and size of the transited clusters. Above the transition temperature, the number of clusters in the metallic domain allows the percolation of these clusters and gives a first path for the electrical current. The resistance exhibits a rapid fall. These paths lower a bit more the resistance of the layer. This could also explain the higher hysteresis width observed in optical properties, that also means higher defect density.

Furthermore, in both c-cut and r-cut sapphire, the T_{MIT} previously determined is slightly lower than established for the VO_2 bulk (~68°C). If we observe the films grown by RFMS, the compressive strain experimentally measured along the $\vec{c}_{VO2(R)}$-axis (or $\vec{a}_{VO2(M1)}$-axis) could impact the transition temperature. Indeed, in the literature [ABR12][POU75], it has been shown that a tensile deformation along the $\vec{c}_{VO2(R)}$-axis leads to a shift of the anti-bonding band π^* towards higher energies. Although the binding energy d approaches the Fermi level, the displacement of the π^* band is more important than that of the $d_{//}$ band, which increases the width of the bandgap (> 0.7 eV). In our case, we relate the multiple growths of VO_2 with a compression of the $\vec{c}_{VO2(R)}$-axis. This deformation displaces the anti-bonding band π^* towards lower energies (**Figure 3-43**) and may conduct to a narrowing of the band. The transition becomes easier to the metallic phase when the temperature increases and the MIT temperature decreases. The phenomenon could then be accentuated for films grown on r-cut sapphire for which the measured compressive strain is higher.

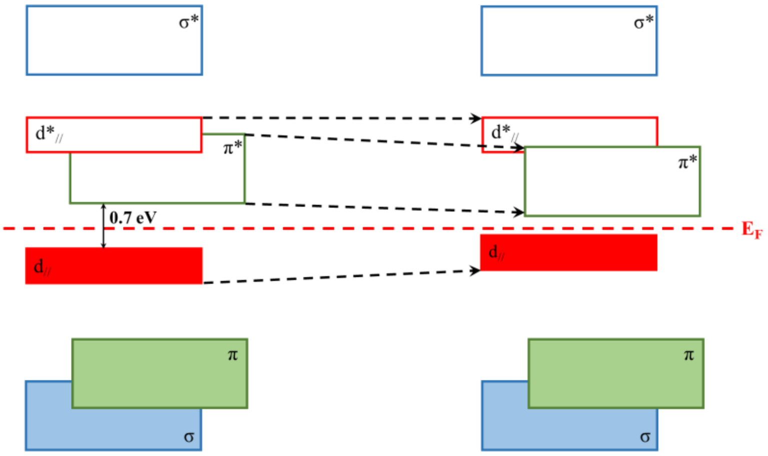

Without deformation **With structural deformation**

Figure 3-43: Schematic representation of the evolution of the band diagram of a deformation-free VO_2 (left) and a constrained VO_2 (right).

3.4. Conclusions

The results reported in this chapter highlighted the complexity of the VO_2 epitaxy, calling for a careful analysis of all XRD measurements in order to find the proper number of variants and epitaxial relations. We have proposed a new explanation of the epitaxial relationships which uncovers the interplay between intrinsic strains and phase stability in VO_2 films deposited on c-cut and r-cut sapphire. Our study emphasize that the choice of the substrate is a determining element for the growth of high-quality VO_2 films. It impacts the growth mode that induces a compressive or tensile strain in the films, which in turn is responsible for the functional MIT properties. For instance, the compressive strain lowers the MIT temperature. Moreover, we showed that the substrate has also an influence on the film morphology. In the case of the growth on c-cut sapphire, the high number of crystallographic domains induces a higher film roughness that could hinder the material’s performance. Therefore, the r-cut sapphire substrate leads to much better defined structural, electrical, and optical transitions for RF applications related to our thesis work.

Chapter 4: VO_2 polymorphic phases as thin films and nanopowders

Contents

The investigation of VO_2 polymorphic phases relies on the stabilization of metastable phase(s) among the very complex and rich vanadium oxide system, that makes this objective a challenging one. Currently, in literature, there is an intensive research activity focused on the VO_2(B) phase grown as nanopowder by hydrothermal (HT) synthesis. Indeed, this particular phase appears as an emerging and very promising material for Li-ion batteries and supercapacitors. Moreover, study of metastable VO_2 polymorphs should bring new insights into their link with the VO_2(M1) phase for which some properties are still misunderstood. In particular, it would help to figure out what are the leading forces that promote the growth a one polymorph instead of another.

Our strategy for this work implied in the beginning to investigate VO_2(B) nanowires grown by the hydrothermal method (cf. Appendix 2), based on already well-established expertise at TE-OX®, and then to move forward by developing new growth conditions of VO_2(B) thin films by sputtering. These two different approaches allowed us to compare how morphology of VO_2(B) may impact its functional properties and stability.

In this chapter, we aim to benefit from our experience to stabilize the VO_2 on an appropriate substrate (Chapter 3) and thus improve our understanding of this material. To study the VO_2(B) stabilization it is necessary to overcome certain difficulties: First, VO_2(B) is a so-called metastable phase that has been less investigated than the M1 and R phases. The second constraint is that the VO_2(B) can easily oxidize into a vanadium oxide of a higher oxidation state such as V_6O_{13} or V_2O_5. We have taken advantage of TE-OX experience in hydrothermal synthesis and our RFMS experience to overcome these obstacles.

4.1. Growth of VO_2(B) nanopowders and their structural investigation

VO_2(B) is one of the metastable phases of VO_2, that has mainly been obtained by chemical means. It is known that the key parameters responsible for the growth and stabilization of the polymorphic phases of VO_2 lie in the arrangement of the oxygen octahedra, thus we will focus on structural studies of the B phase.

We followed the hydrothermal approach for VO_2(B) nanowires synthesis. This method is largely investigated in the literature [POP13][GAN12][ZOU17] and allows the VO_2(B) synthesis in relatively gentle conditions. HT synthesis is a chemical elaboration technique that has been proven in many fields of application for its simple setup and the high-quality of the resulting materials. Widely used to prepare vanadium oxide nanostructures, this technique is based on heterogeneous reactions in a closed system in the presence of an equilibrium between liquid and vapor phases under pressure and temperature conditions above 100°C and 1 bar, respectively. Able to get high quality crystalline material with a possibility to control the morphology, the HT method remains complex as all involved parameters are interconnected (such as temperature, filling ratio, precursor concentration, etc.) and finally impact the results.

Generally, the HT synthesis of VO_2(B) is carried out from V_2O_5 and an aqueous solution of the oxalic acid (OA) $H_2C_2O_4$ as precursors. The idea is to reduce the most stable oxidation state of V_2O_5 (V^{+5}) to V^{+4}.

$$V_2O_5 + H_2C_2O_4 \xrightarrow{T,P} 2VO_2 + H_2O + 2CO_2 \qquad (4.1)$$

In the reaction between V_2O_5 and oxalic acid (eq.(4.1)), vanadate (VO_4^{3-}) reacts with the acidic medium to form octahedral bis(oxalate). As the medium becomes rich in oxalate, the vanadium V(v) becomes a strong oxidant ($E^{O}(VO_2(O_x)^-/VO(O_x)) = 1.13$ V and $E^{O}(VO_2(O_x)_2^{3-}/VO_2(O_x)_2^{2-} = 1.22$ V, with E^0 standard redox potential) that oxidizes the $HC_2O_4^-$ into [$CO_2^{\bullet-}$] radicals. These radicals being strong reductants, reduce V^{+5} to V^{+4} and potentially to V^{+3} [BRU01][LIV10]. Assuming that VO_2 Wadsley polymorphs have the mixed valence V^{+4}/V^{+5}, a change in growth conditions could affect the formation of polymorphic phases. To verify this hypothesis, we performed experiments at different molar ratios (V^{+5}/OA) and synthesis times. According to internal TE-OX experience, the temperature suitable for the VO_2(B) synthesis was set at 160°C.

4.1.1. Effect of the synthesis conditions

The HT synthesis is known to be sensitive to the experimental conditions and the interplay between all parameters makes it a complex approach. The autoclave filling ratio and temperature will impact on the generated pressure, the concentration of precursors and the synthesis time are used to influence the crystal growth. Moreover, in our case the precursor concentration may also impact on the pressure as gaseous by-products are generated by the chemical reaction (eq.(4.1)). However, our experimental setup did not allow to measure the pressure during synthesis of VO_2(B) phase, as it is below 5 bar (pressure sensor limit).

In this work, we mainly focused on the influence of precursor concentration and synthesis time on the VO_2(B) stabilization. Three molar ratios of V^{+5}/OA were chosen at 1.0, 1.1 and 1.2, and two reaction times at 24h and 48h. The obtained powders were characterized by X-ray diffraction (XRD) and measured θ-2θ scans are shown in **Figure 4-1**.

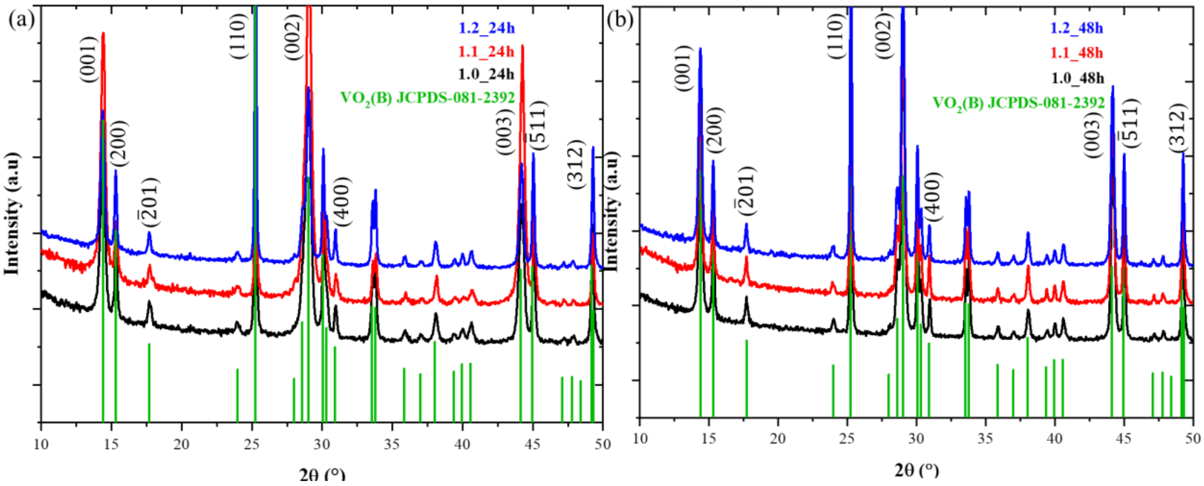

Figure 4-1: XRD θ–2θ scans of VO_2 nanopowder synthesized at 160°C during (a) 24h and (b) 48h for three different molar ratios in black, red and blue, respectively. Only the VO_2(B) phase is formed, as seen with the JCPDS-01-081-2392 reference (in green).

The XRD scans were performed in the 2θ range between 10° and 50°. All diffraction peaks correspond to the reflections of the VO_2(B) phase (JCPDS datasheet N° 01-081-2392). Any trace of other VO_2 polymorphic phases or additional vanadium oxides was not detected in these diffractograms, which highlight the purity of the nanopowders. Comparing our XRD patterns with the literature, we observe that three peaks corresponding to the $(001)_{VO2(B)}$, $(002)_{VO2(B)}$, and $(003)_{VO2(B)}$ planes are wider than reported previously. According to the work of Théobald [THE76], these reflections corresponding to the $(00l)$ planes parallel to the $(\vec{a}_{VO2(B)}, \vec{b}_{VO2(B)})$ base plane are more sensitive to the crystallinity of the $VO_2(B)$ structure. Authors also noticed that the $VO_2(B)$ structure exhibits weaker bonds related to the oxygen lattice along the $\vec{c}_{VO2(B)}$-axis [THE76]. It was found to be in agreement with the shear planes of Wadsley phases parallel to $(00l)$, which favor the transformation of V_2O_5 to V_6O_{13} and $VO_2(B)$ [KAT03]. A noticeable increase of $(002)_{VO2(B)}$ peak width shown in **Figure 4-2** follows the modification of the synthesis conditions (duration and OA concentration).

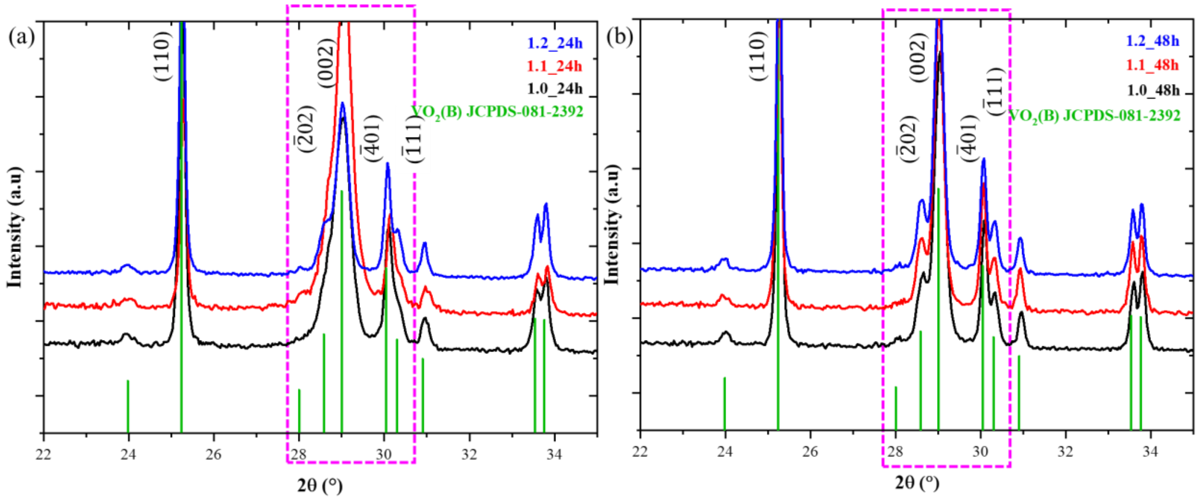

Figure 4-2: Enlargement between 22° to 35° of the $VO_2(B)$ XRD scans for (a) 24h and (b) 48h HT synthesizes.

The deconvolution of the $(002)_{VO2(B)}$ peak presented in **Figure 4-4** gives two contributions, $(\bar{2}02)_{VO2(B)}$ and $(002)_{VO2(B)}$, and shows a decrease of the FWHM of $(002)_{VO2(B)}$ peak with the increase of synthesis time. For example, a FWHM of 0.4° is measured for molar ratio 1.0 at 24h against 0.3° at 48h. This indicates that the crystallinity of nanopowders increases with the synthesis time. Increasing OA concentration is another way to improve the crystallinity, as also seen in **Figure 4-3** with the decrease of the FWHM of $(002)_{VO2(B)}$ peak with OA ratio.

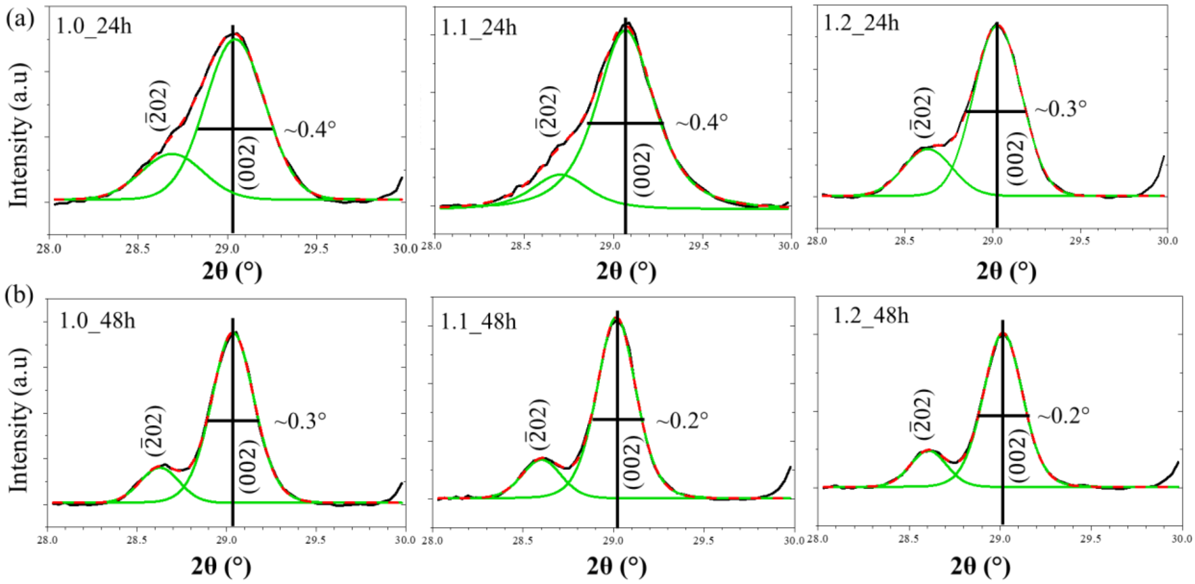

Figure 4-3: Evolution of the $(002)_{VO2(B)}$ peak in function of the oxalic acid concentration for (a) 24h and (b) 48h HT synthesis. The FWHM of the $(002)_{VO2(B)}$ peak is indicated next to it.

We note from the fits displayed in **Figure 4-3** that the peaks are slightly shifted depending on synthesis conditions. In XRD, a peak shift may be associated with the presence of strain such as compression or tension. This strain can come from impurities or oxygen vacancies. To analyze it, we focused our attention on the structural parameters of our VO_2(B) nanowires. The lattice parameters including β-angle were determined from eq.(4.2).

$$d_{hkl} = \frac{1}{\sqrt{\left(\frac{h^2}{a^2} + \frac{l^2}{c^2} - \frac{2hl}{ac}\cos\beta\right)\frac{1}{\sin^2\beta} + \frac{k^2}{b^2}}} \tag{4.2}$$

From the lattice parameters, we can calculate the volume of VO_2(B) unit cell by $V = abc * sin\,\beta$. **Table 4-1** summarizes the results calculated from the experimental data. Although all samples present high crystallinity, VO_2(B) structure was impacted by both synthesis time and OA concentration. Focusing on samples synthesized at molar ratio of 1.2 (24h) and 1.0 (48h), respectively, we can see that $a_{VO2(B)}$, $b_{VO2(B)}$, $c_{VO2(B)}$, and $\beta_{VO2(B)}$ parameters are the same for a unit cell volume of $274.6*10^6$ pm^3, allowing us to identify these OA ratio/synthesis time combinations as conducting to similar structures. Increasing the synthesis time at a lower molar ratio or decreasing time at a higher OA concentration lead to a similar product. An example of the morphology after HT synthesis is shown in **Figure 4-4** for 1.2 (24h) and 1.0 (48h).

Table 4-1: Lattice parameters calculated for VO_2(B) nanopowders as a function of V^{+5}/OA ratio and synthesis time. The results are compared to the JCPDS 01-081-2392 for VO_2(B) nanopowders synthesized by HT method [OKA93].

Molar ratio	Time (h)	a (Å)	b (Å)	c (Å)	β (°)	V (10^6 pm3)
1.0	24	12.08	3.70	6.42	107.0	274.4
1.1		12.09	3.69	6.43	106.9	274.5
1.2		12.07	3.70	6.43	107.0	274.6
1.2	48	12.06	3.69	6.42	107.0	273.2
1.1		12.09	3.70	6.43	107.0	275.1
1.0		12.07	3.70	6.43	107.0	274.6
$VO_2(B)_{JCPDS\ 01\text{-}81\text{-}2392}$	**-**	**12.0930**	**3.7021**	**6.4330**	**106.97**	**274.46**

*a, b, c and β are calculated from d_{hkl} values of (200), (020), (001), and (201) planes, V is calculated by $V = abc * sin\,\beta$

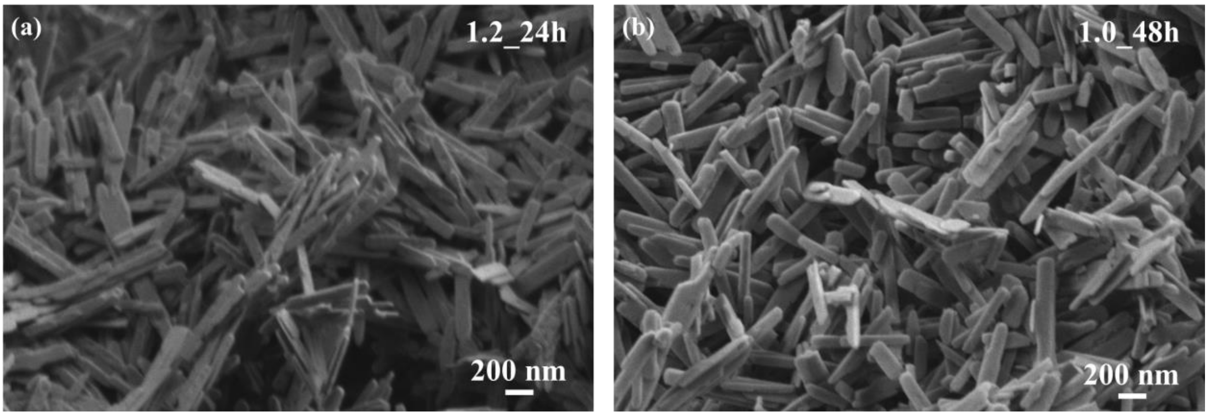

Figure 4-4: SEM images showing the nanopowder morphology after HT synthesis from V_2O_5 and OA at 160°C during (a) 24h at 1.2 molar ratio of V^{+5}/OA and (b) 48h at 1.0 molar ratio of V^{+5}/OA.

The SEM observations confirm the similar morphology of synthesized nanostructures (nanoplatelets), which grow according to a preferential orientation. By comparing this platelet-like morphology of VO_2(B) at different OA concentrations and synthesis times, we observed that their size was slightly different. To estimate the size from XRD data, three methods could be considered [CHA03][COS03]:

i. The study of the variance of the intensity distribution.
ii. The deconvolution of the line profile into a Fourier series.
iii. The method of integral width introduced by Scherrer.

The most accurate methods are the variance study and the profile deconvolution into a Fourier series, as they do not require any approximation [CHA03]. Unfortunately, these methods are also tricky to use for diffractograms with overlapping peaks due to a lower crystallinity or the coexistence of several phases, for example. Therefore, in our work, the analysis method used is the Scherrer one that has already been employed for VO_2(B) [POP13].

The Scherrer method considers the peak shape and broadening as a Pseudo-Voigt (PV) function built from a simple linear combination of a Gaussian function and a Lorentzian function with a mixing factor η [CHA03][GRA12].

$$\mathrm{PV} = \eta \mathrm{L} + (1-\eta)\mathrm{G} \tag{4.3}$$

For η = 0, we find a Gaussian G and for η = 1, we find a Lorentzian L.

Usually, the instrumental resolution should also be considered, as it can broaden the measured XRD peaks. However, for a cruder evaluation of VO_2(B) platelet size, an easier Scherrer expression can be used by supposing that all contributions are Lorentzian, and that the peak broadening is essentially due to the size of the platelets [GRA12]. The profile adjustment on a given peak makes it possible to measure its integral width β that comprises both size and strain effects simultaneously (eq.(4.4)).

$$\beta = \frac{\lambda}{\mathrm{L} * \cos\theta} + 4\tan\theta * \varepsilon \tag{4.4}$$

Where L is the size of the crystallite, ε the strain, λ the wavelength and θ the angle associated to the chosen diffraction peak.

From the profile fitting function on FullProf Suite® software, it is possible to obtain the values of β and peak position (2θ) and then plot the Williamson-Hall diagram. **Figure 4-5** gives an example of fit for sample elaborated at 1.0 ratio for 48h at 160°C, and **Table 4-2** summarizes the results of the fitting.

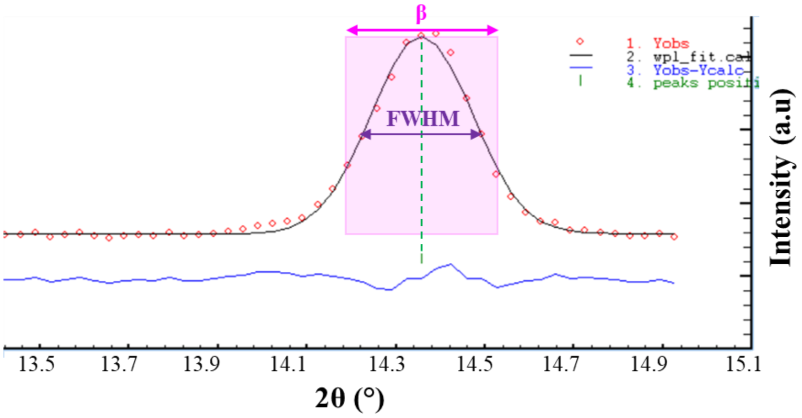

Figure 4-5: FullProf fitting for synthesis at V^{+5}/OA 1.0 during 48h at 160°C. Experimental data is shown in red, the fit in black, the difference between the two in blue, and the peak position in green. Integral width β and FWHM are also indicated.

Table 4-2: Calculation of the βcosθ and sinθ parameters for each (00l) plane indexed for the sample synthesized at V^{+5}/OA 1.0 during 48h at 160°C.

h	k	l	2θ (°)	θ (°)	θ (rad)	β*10^{-3}(rad)	(βcosθ)*10^{-3}	sinθ
0	0	1	14.371	7.186	0.125	5.39	5.35	0.125
0	0	2	29.026	14.513	0.253	5.87	5.68	0.250
0	0	3	44.202	22.100	0.385	5.87	5.44	0.376

Then, we can trace $\beta \cos\theta = f(\sin\theta)$ for $(001)_{VO2(B)}$, $(002)_{VO2(B)}$, and $(003)_{VO2(B)}$ planes and obtain a straight line of the form $y = Ax + B$. From the slope and the intercept, the average platelet size and strain were calculated by eq.(4.5), respectively.

$$\beta \cos\theta = B + A \sin\theta \quad \text{where } B = \frac{\lambda}{L} \text{ and } A = 4\varepsilon \tag{4.5}$$

Figure 4-6(a) shows an example of a Williamson-Hall diagram for sample obtained at 1.0 ratio for 48h. By linear regression, the platelet size is found around 28.5 nm and the strain at 0.01%. Given the (00l) peaks indexed for this calculation, the result corresponds to a rough estimate of the platelet width, as only three points are available for the regression.

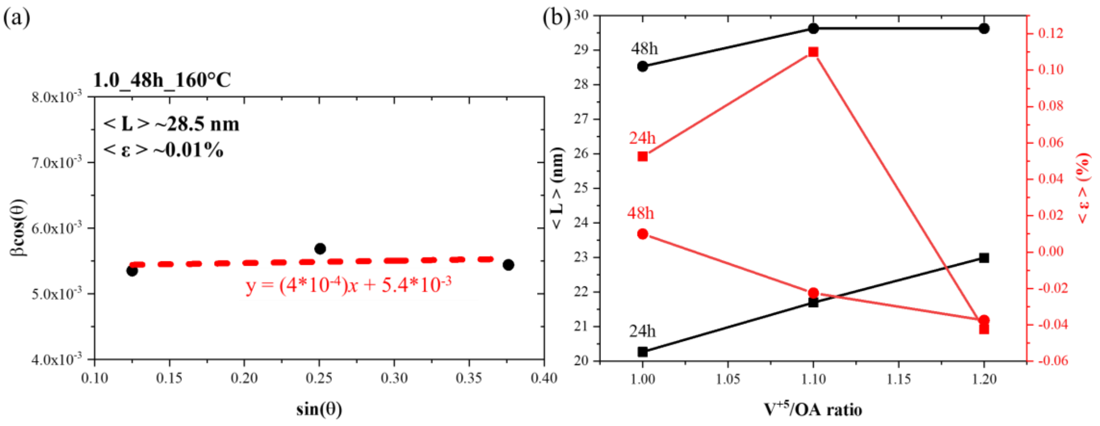

Figure 4-6: (a) Williamson-Hall plot for synthesis at V^{+5}/OA 1.0 during 48h at 160°C. (b) Evolution of VO_2(B) platelet width and strain as a function of synthesis time and V^{+5}/OA ratio.

Similar analyses were performed for other HT synthesis conditions, and the evolution of VO_2(B) platelet width and strain as function of V^{+5}/OA ratio is represented in **Figure 4-6**(b) for different synthesis times. We recall that whatever the synthesis time, as we saw from **Figure 4-3** the increase of the V^{+5}/OA ratio improves the crystalline quality of the nanostructures. Moreover, from the Williamson-Hall diagram, we can observe that all samples present low strain ($\varepsilon < 0.15\%$), and that the platelet width increases with the synthesis time and maybe slightly with the V^{+5}/OA molar ratio. It also seems that the strain evolves towards (low) tensile strain upon increasing this ratio. According to the lattice parameters, as shown in **Table 4-1**, the presence of tensile strain in the platelets go together with the improvement of the material crystallinity.

The XRD and SEM analyses of VO_2(B) nanopowders obtained by HT synthesis have shown that VO_2(B) has a platelet-like morphology. The OA concentration has a minor effect on the morphology, but its increase induces a tensile strain, that helps to improve the material crystallinity. We note that further analysis of $(00l)$ peak characteristics could provide information about intercalation channels along the $\vec{c}_{VO2(B)}$-axis in the VO_2(B) [THE76]. These channels have been presented as a key element of the Wadsley phases [KAT03][LER98], and we believe that they can help us to understand the formation and growth of the VO_2 metastable phases. Moreover, these channels also present an interest for energy storage applications. Therefore, electrochemical characterizations of Li-ion intercalation were performed with the goal to have an indirect proof of the existence of these channels.

4.1.2. From electrochemical characterizations to structure understanding

We have seen in Chapter 1 that VO_2(B) presents empty spaces along the $\vec{c}_{VO2(B)}$-axis due to the VO_6 octahedra connections with neighboring layers. This space induces a mismatch between layers and contributes to the transformation of VO_2(B) into a less stable structure than VO_2(R). In order to probe these channels, the VO_2(B) nanopowder synthesized by HT (molar ratio 1.2, 48h duration) was electrochemically characterized by galvanostatic cycling. The experiment consists in an intercalation of lithium (Li) ions to determine the reaction capacity of VO_2(B) with Li. To do this, a Li-ion battery was fabricated from a mixture of 80wt% of active material (VO_2(B) nanopowder), 10wt% of carbon, and 10wt% of polyvinylidene fluoride (PVDF) dissolved in N-methylpyrrolidone (NMP) solution [LI11]. All elements were deposited on aluminum foil and cut into disc electrodes with a diameter of 12 mm. After assembly under glove box, the electrochemical performances were studied in the voltage region between 1.5 V and 3.5 V with multichannel batteries (**Figure 4-7**).

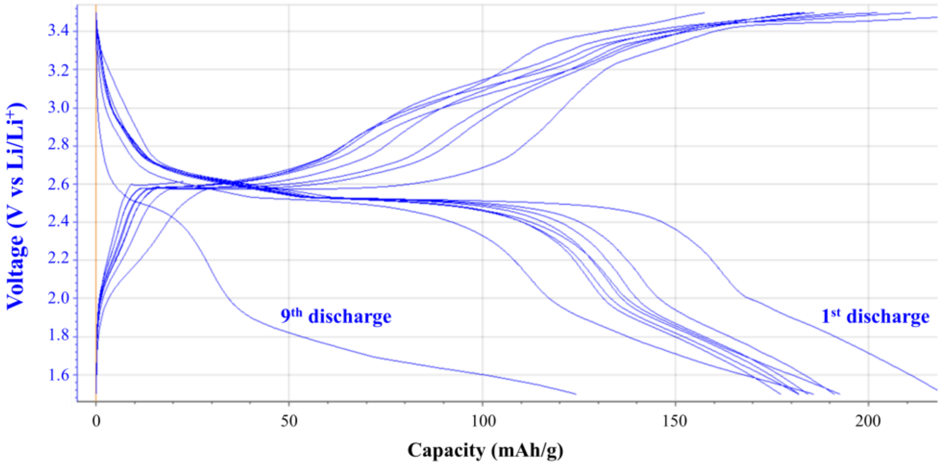

Figure 4-7: Discharge and charge cycles of the electrode made of VO_2(B) synthesized by HT.

The initial discharge capacity for the first cycle was measured at 298 mAh/g at 1.5 V, which is not too far from the theoretical storage capacity established at 323 mAh/g at a redox voltage of 2.6 V [LEE17]. The reaction between vanadium (V) and Li in the electrolyte seems to occur completely. This can be considered as an indirect proof of the intercalation channel existence in the VO_2(B) structure, and highlights its potential for energy storage.

During the cycling, the VO_2(B) electrode showed firstly a slow decrease of the current density around 185 mAh/g, a signature of the reduction of the Li-ion intercalation efficiency. To test the resiliency of our material, the Li-ion insertion cycles were pursued until a very significant degradation of the material or its agglomeration [LIU18][XIA15]. Despite a promising capacity, the electrochemical properties are found strongly deteriorated already after the ninth cycle. This makes impossible further industrial exploitation of this material for batteries without improving its performance. The storage capacity has to remain stable for at least 1000 cycles for an industrially reliable material.

The material degradation could be explained according to three hypotheses. The first is that the intercalation channels could become obstructed during the cycling. The monoclinic structure of VO_2(B) has weaker bonds in these channels (OH-type). Thus, some Li atoms can be trapped during insertion (**Figure 4-8**). Lee *et al*. performed DFT calculations that indicate the potential trapping of Li-atoms in the middle of vacant V-O cages of the VO_2(B) structure, that was further confirmed by scanning transmission electron microscopy (STEM) images [LEE17].

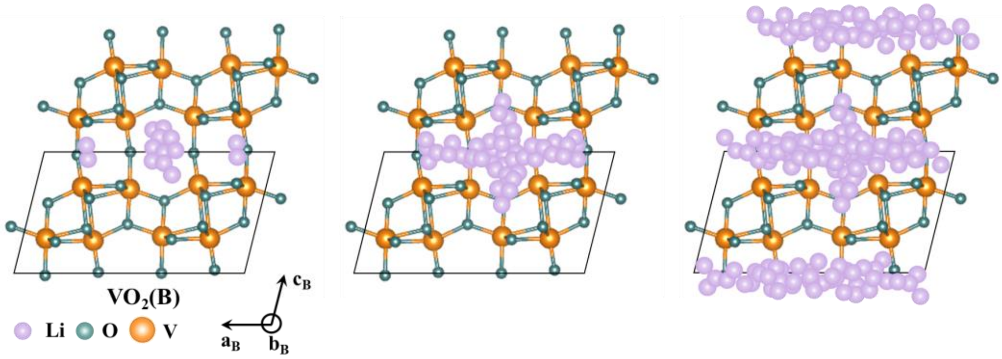

Figure 4-8: Schematic view of Li-ion intercalation in VO_2(B) during charge/discharge cycles. The more intercalation and deintercalation of Li are realized (from left to right), and the more the Li concentration increases in the channels of VO_2(B).

The second hypothesis is that the electrochemical environment may oxidize the VO_2(B), thus forming oxides no longer active in the cycling. Finally, our third hypothesis is that the large specific surface of the nanoplatelets could be drastically reduced by their agglomeration under the electrochemical measurement conditions. The material reactivity may also increase in contact with the liquid solution and be accelerated due to the injected voltage. Indeed, the synthesized VO_2 powders have a very limited stability in ambient conditions. The dark-gray powder after the synthesis transforms into a greenish one after storage in ambient conditions for a few weeks. The XRD measurement of a powder stored in a desiccator (with residual humidity at ~30%.) for three years, shows that the VO_2(B) peaks have disappeared in favor of V_2O_5 or V_6O_{13} , the nanopowder was thus more oxidized (**Figure 4-9**).

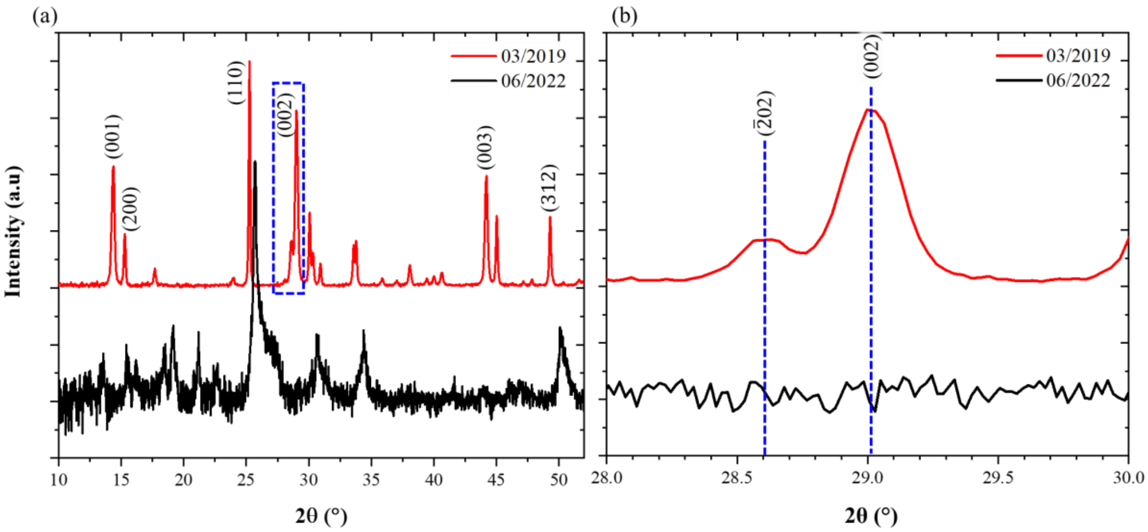

Figure 4-9: Evolution of θ-2θ diffractogram of a VO_2(B) nanopowder stored in desiccator at RT for three years, from 2019 (in red) to 2022 (in black); (b) Enlargement between 28° to 30°.

Such a weak ambient stability of VO_2(B) nanopowders was already reported in the literature [LEE17]. Therefore, the poor energy storage ability of our sample may simultaneously result from several factors, such as enhanced material oxidation under electrochemical conditions and the aggregation of nanostructures that reduces the active surface area. To overcome this bottleneck, the development of VO_2(B) as thin film was proposed by Lee *et al.* [LEE17] and Su *et al.* [SU16] with two main ideas: (i) to limit the decrease of the specific surface caused by nanostructure aggregation and (ii) to stabilize the VO_2(B) structure by the substrate-induced strain.

4.2. VO_2(B) thin film growth on $SrTiO_3$

In Chapter 3, we demonstrated how the underlying substrate structure impacts the VO_2(M1) growth. That inspired us to implement a similar approach in order to stabilize the metastable VO_2(B) phase in thin film form by selecting an appropriate substrate among the ones reported in literature, such as $SrTiO_3$ (STO) [DIN17][LEE16], TiO_2 [DIN17][DIN16], $LaAlO_3$ (LAO) [DIN17][LEE16][EMO18], or MgO [SU16]. We selected (001)-oriented STO for further VO_2(B) development based on previous expertise at C2N for oxide films on STO, and on its availability. Our optimization of sputtering growth revealed that a pure VO_2(B) phase can be stabilized on STO under 2.4% O_2/Ar ratio between 480°C and 525°C. The deposited films were investigated by XRD (**Figure 4-10**(a)), showing three intense peaks at 2θ values of 14.37°, 28.94°, and 44.05° that correspond to $(00l)$ planes of the VO_2(B) phase. The peaks observed at 22.77°, 46.47° and 72.55° are attributed to the $(00l)$ planes of STO substrate. We deduce that VO_2(B) film grows on STO with its ($a_{VO2(B)}$,$b_{VO2(B)}$) base plane perpendicular to $\vec{c}_{STO}$-axis: $(00l)VO_2(B)//(00l)STO$. Additionally, the rocking curve of $(002)_{VO2(B)}$ peak presents a FWHM of 0.2°, indicating the high quality of the film (**Figure 4-10**(b)). As a comparison, the c-cut sapphire sample, which was deposited at the same time, side by side with STO substrate, shows two peaks at 39.79° and 85.81° corresponding to the reflections from the (020) and (040) planes of VO_2(M1) (**Figure 4-10**(a)). Thus, for exactly the same growth conditions, different substrates promote the stabilization of different polymorphs.

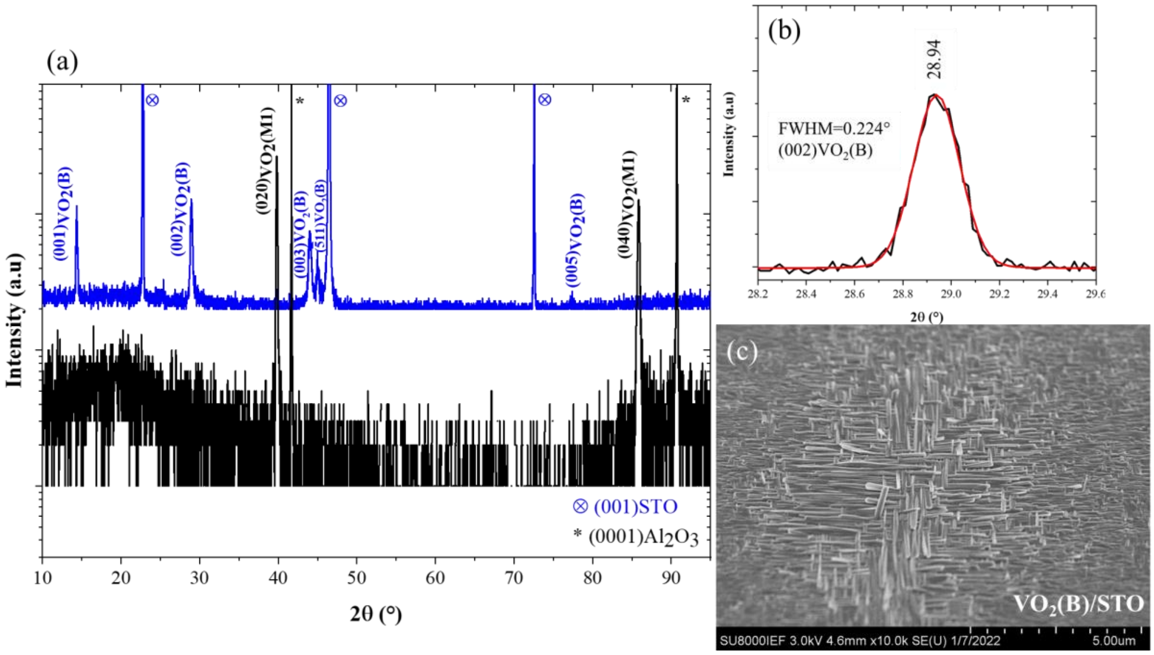

Figure 4-10: (a) θ-2θ diffractograms at RT of a VO_2(B) film directly grown on a (001)STO substrate (blue curve) compared to a VO_2(M1) film on c-sapphire (black curve). (b) Rocking curve of a $(002)_{VO2(B)}$ peak. (c) SEM images of VO_2(B) thin film.

Since the epitaxial relationships between the VO_2(M1) phase and c-cut sapphire were already reported in Chapter 3, the following analyses will focus only on the relationship between the B phase and STO. The in-plane orientation of the VO_2 layer with respect to the substrate was determined by XRD. The φ-scans on tilted planes were performed under symmetrical condition, identically to $VO_2(M1)/Al_2O_3$ (Chapter 2). The results shown in **Figure 4-11** allow the determination of the epitaxial relationships.

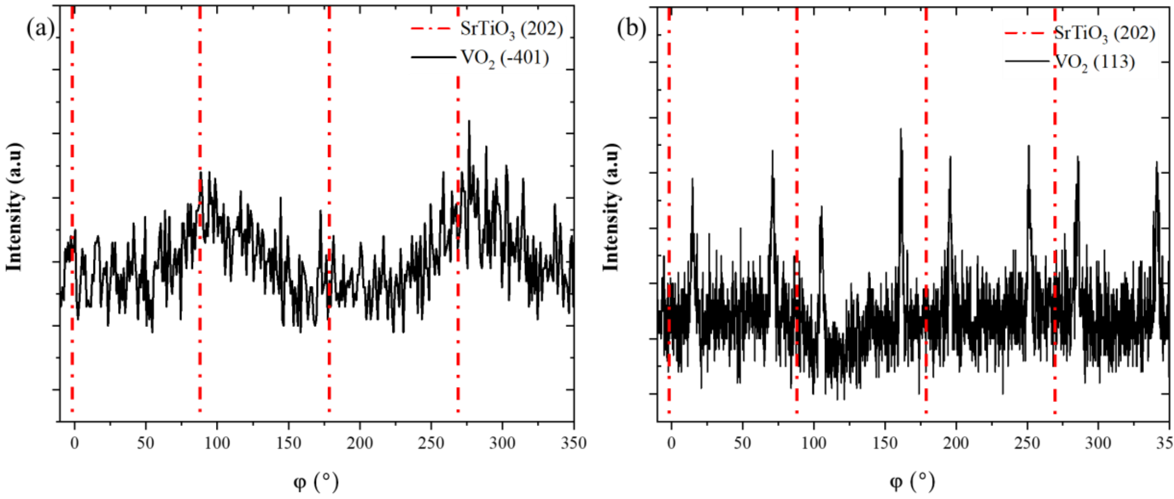

Figure 4-11: φ-scans of a VO_2 layer deposited on (001)STO substrate: (a) $(\bar{4}01)_{VO2(B)}$ and (b) $(113)_{VO2(B)}$ planes are shown in black, and the red dashed lines indicate the positions of the $(202)_{STO}$ planes.

According to the $\theta - 2\theta$ scans, the preferential orientation of the $(001)_{VO2(B)}$ planes is parallel to the $(001)_{STO}$ planes. The azimuths of the $(202)_{STO}$ planes coincide with the azimuths of the $(\bar{4}01)_{VO2(B)}$ planes. The $\vec{b}_{VO2(B)}$-axis is thus aligned with $\vec{b}_{STO}$-axis, i.e. $[010]\mathrm{VO_2(B)}//[010]\mathrm{STO}$. Moreover, the $\vec{b}_{VO2(B)}$ unit vector being at 90° from $\vec{a}_{VO2(B)}$, the $\vec{a}_{VO2(B)}$-axis is aligned with the $\vec{a}_{STO}$-axis of STO: $[001]\mathrm{VO_2(B)}//[001]\mathrm{STO}$. We also did φ-scans of $(113)_{VO2(B)}$ plane (**Figure 4-11**(b)), revealing peaks at 17° on each side of $(202)_{STO}$, in agreement with the $\vec{a}_{VO2(B)}$ and $\vec{b}_{VO2(B)}$-axes aligned with $\vec{a}_{STO}$-axes ($tan^{-1}(b_{VO2(B)}/a_{VO2(B)}) = 17°$). Moreover, as these $(113)_{VO2(B)}$ doublets show the four-fold symmetry of the substrate, they prove the existence of 4 variants as depicted in **Figure 4-11**. We note that the in-plane orientation of the VO_2(B) planes is not well defined, with very weak features in φ-scans. A pole figure was drawn (**Figure 4-12**(a)) to help visualize the VO_2(B) orientations. The VO_2(B) planes and STO substrate planes are depicted in black and red, respectively, and positioned according to the φ-scan results. The alignment of $\vec{a}_{VO2(B)}$- and $\vec{b}_{VO2(B)}$-axes of VO_2(B) unit cell along the $\vec{a}_{STO}$- and $\vec{b}_{STO}$-axes of the substrate appears clearly. Additionally, given the four-fold in-plane symmetry of the STO substrate, in total 4 variants are allowed for VO_2(B) growth on STO, as depicted in **Figure 4-12**(b): X and X' as described above, then Y and Y' at 90° from them with $\vec{a}_{VO2(B)}$-axis aligned with $\vec{b}_{STO}$-axis and $\vec{b}_{VO2(B)}$-axis aligned with $\vec{a}_{STO}$-axis. Given this picture with 4 variants, the φ-scans of **Figure 4-11** should both show 4 peaks, while only two (weak and broad) peaks are observed for the $(\bar{4}01)_{VO2(B)}$ plane. We thus cannot rule out that a variant duo (e.g. X and X' or Y and Y') is more abundant than the other one. We note that 4 variants were indeed reported by Chen *et al.* [CHE14].

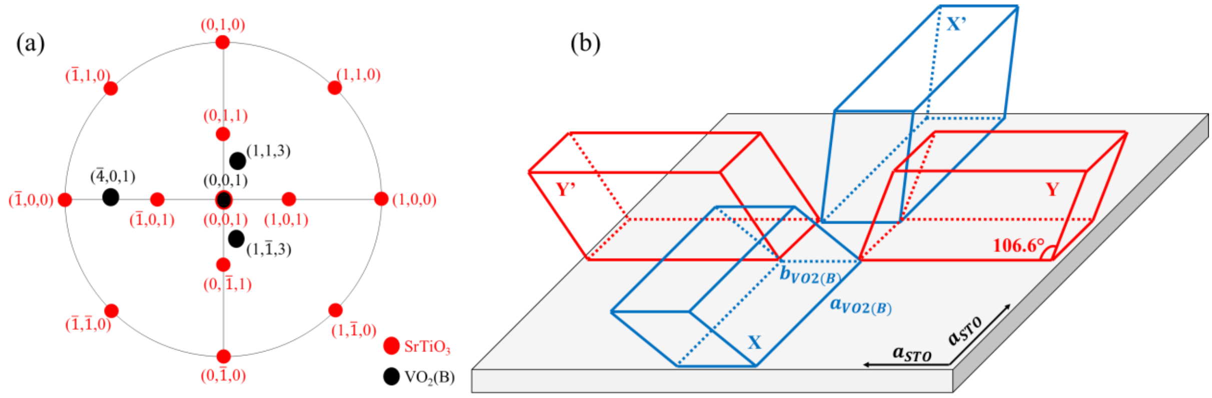

Figure 4-12: (a) Pole figure representing the VO_2(B) planes probed by XRD φ-scan (in black) with respect to STO substrate (in red) and (b) sketch of the 4 VO_2(B) variants grown on a (001)STO substrate [CHE14].

The epitaxial strain was determined according to the same approach as reported in Chapter 3. To do that, one VO_2(B) variant was aligned in-plane with (001)STO substrate with lattice parameter $a_{STO} =$ 3.905 Å (JCPDS-00-035-0734). By superimposing the two structures (**Figure 4-13**), we observe differences in size, and the misfit strain can be determined considering $a_{VO2(B)}$ and $b_{VO2(B)}$ in-plane with STO. It results in a -3.1% compressive strain along $\vec{a}_{VO2(B)}$-axis and a 5.4% tensile strain along the $\vec{b}_{VO2(B)}$-axis. Considering such large deformations, pseudomorphic epitaxy is unlikely.

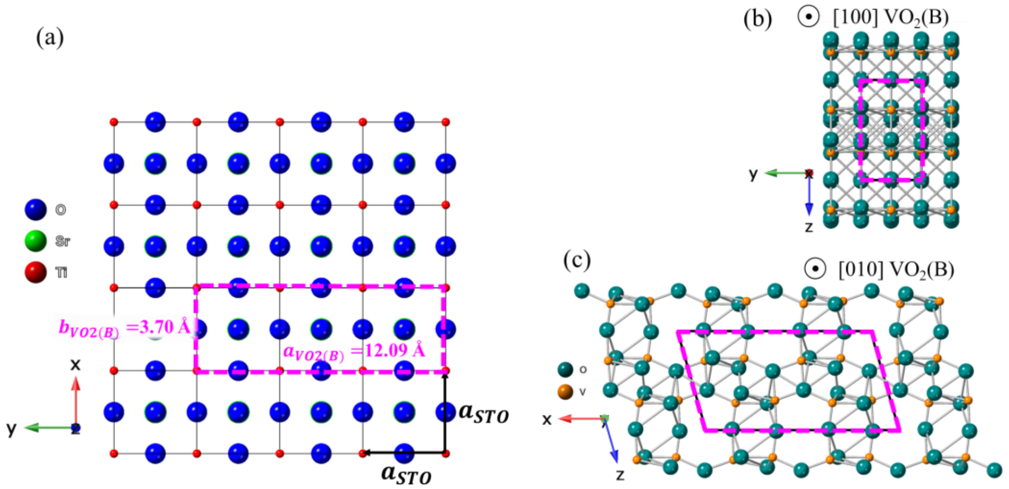

Figure 4-13: Schematic atomic arrangements for (00l)VO_2(B) epitaxy on (00l)STO: (a) (001)STO surface, with VO_2(B) unit cell in pink, and "side views" of VO_2(B) phase according to (b) $\vec{a}_{VO2(B)}$- and (c) $\vec{b}_{VO2(B)}$.

Similar to the growth of VO_2(M1) on c-cut sapphire, the strong lattice mismatch between VO_2(B) and STO leads the layer to grow by heterostructural epitaxy with formation of grains and/or dislocations in order to relax the stress. The dislocations remain confined to the interface, and this type of growth generally leads to strong surface texturing such as we have observed by SEM (**Figure 4-10**(b)). From the film lattice parameters summarized in **Table 4-3**, a residual compressive strain along both in-plane axes is evidenced in the VO_2(B) film.

Table 4-3: Lattice parameters calculated from XRD data for VO_2(B) film deposited on (001)STO substrate and compared to the JCPDS 01-81-2392.

Phase	**a (Å)**	**b (Å)**	**c (Å)**	**β (°)**	**V (10^6 pm3)**
VO_2(B) film	12.05	3.68	6.43	106.7	273.1
VO_2(B) JCPDS 01-81-2392	**12.0930**	**3.7021**	**6.4330**	**106.97**	**274.46**
ε (%)	-0.36	-0.59	-0.04	-0.25	-0.49

*a, b, c and β are calculated from d_{hkl} values of (002), (022), ($\bar{4}$01), and ($\bar{3}$10) planes, V is calculated by $V = abc * sin\beta$, ε is calculated by $\varepsilon = \frac{x_{RT}^{film} - x_{RT}^{bulk}}{x_{RT}^{bulk}}$

In epitaxial growth, the substrate crystallographic structure (symmetry and lattice parameters) and its chemical termination have an impact on the crystal structure, orientation, and phase stabilization of the film [DIN16]. For example, TiO_2 grows epitaxially on sapphire with a rutile structure, while it exhibits an anatase structure on STO and LAO substrates [LOT07][SIL10]. In the same way, we have seen in this chapter that two different VO_2 phases can be obtained on Al_2O_3 and STO for the same deposition conditions. It indicates that epitaxial growth could promote stabilization of different VO_2 polymorphs by selecting an appropriate substrate, also compatible with our applications. Taking into consideration the crystallographic parameters of VO_2 polymorphs and the characterizations performed on RFMS-deposited films, we here propose one hypothesis for the substrate influence on VO_2 growth. From a simultaneous deposition on two different substrates, if two different VO_2 polymorphs are formed, we can suppose that the substrates themselves are responsible for their stabilization, instead of the sputtering deposition parameters, plasma or target effects. Neutral atoms arriving on the surface form precursors, that can be oxidized into different oxidation states between V^{+0} to V^{+5}, probably in some proportion related to their ionization energy. We suggest that this oxidation state is also substrate-dependent: For example, on the STO substrate surface, the reactions between neutral atoms and the surface could oxidize the precursors into V^{+5} and V^{+4}. If the percentage of V^{+5} is slightly higher than V^{+4}, the islands nucleated from the precursors on the surface could form preferentially the VO_2(B), as the B phase is slightly more oxidized than the M1 phase (cf. Chapter 1). We note that the Al_2O_3 structure is different from the STO one, but roughly the same residual strain is measured in the growth plane (**Table 4-4**) and still, the VO_2(M1) phase is stabilized on c-cut sapphire.

Table 4-4: Experimental epitaxial strain values for films deposited by RFMS with VO_2(M1 or B) bulk as reference. The in-plane axes of the substrate are highlighted in color.

VO_2 films	ε_a (%)	ε_b (%)	ε_c (%)	ε_β (%)
M1/c-Al_2O_3	-0.39	+0.08	-0.60	-0.32
M1/r-Al_2O_3	-0.74	+0.52	-0.23	-0.57
B/STO	-0.36	-0.59	-0.04	-0.25

*ε is calculated by $\varepsilon = \frac{x_{RT}^{film} - x_{RT}^{bulk}}{x_{RT}^{bulk}}$

To resume, numerous parameters influence the stabilization of the polymorphic phases of VO_2: the deposition conditions, the sputtering target state, and the substrate. To check our hypothesis on the latter influence on precursor oxidation state, it is first necessary to know the chemical composition of our VO_2 polymorphs and second, to know the elemental composition of the plasma during the deposition. Such investigation could not be performed during this thesis due to the limited time, but will be developed in the perspectives of this work.

4.3. Chemical and structural investigations of polymorphs

4.3.1. XPS characterizations of B and M1 phases

The understanding of VO_2 polymorph growth relies not only on physical characterizations, but the chemical aspects are also mandatory to consider. The VO_2 being at the boundary between the Magnéli and Wadsley phases in the V-O system, the slightest variation of the vanadium oxidation may induce formation of different polymorphs. Therefore, to get insights about the vanadium oxidation states, X-ray photoelectron spectroscopy (XPS) was carried out at room temperature (RT). The experiments were made using an aluminum anode Al K_α at hν=1486.6 eV for excitation of the samples. To minimize surface charging, samples were fixed onto a carbon tape, and the intensity of the probing X-ray radiation was set at a value lower than the usual one. The energy scale for all measurements was calibrated by placing the O 1s line at 530 eV. The energy resolution is 0.3 eV for a detector pass energy of PE=10 eV (used for the spectra of **Figure 4-15**). First acquisitions were made on a wide range of energy (0 to 600 eV) and presented on **Figure 4-14**.

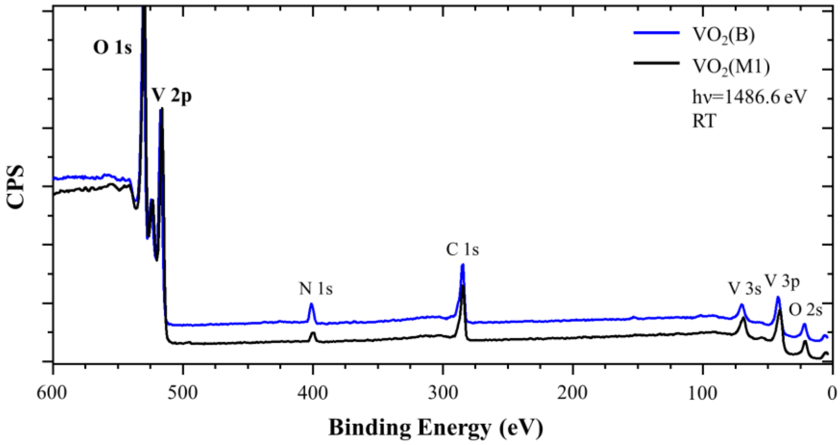

Figure 4-14: Wide scan XPS spectra for the VO_2(M1 and B) polymorphs in thin films recorded at RT.

Two main contributions were observed: an oxygen component (O 1s at 530 eV) and a vanadium component (V $2p_{3/2}$ at 516 eV). Carbon and nitrogen are also detected, due to the contamination of the samples during storage in air and possibly by the nitrogen flow after deposition. Further, high-resolution acquisitions centered on the O 1s and V 2p bands have been recorded and compared to references found in the literature (**Figure 4-15**) [DEM00].

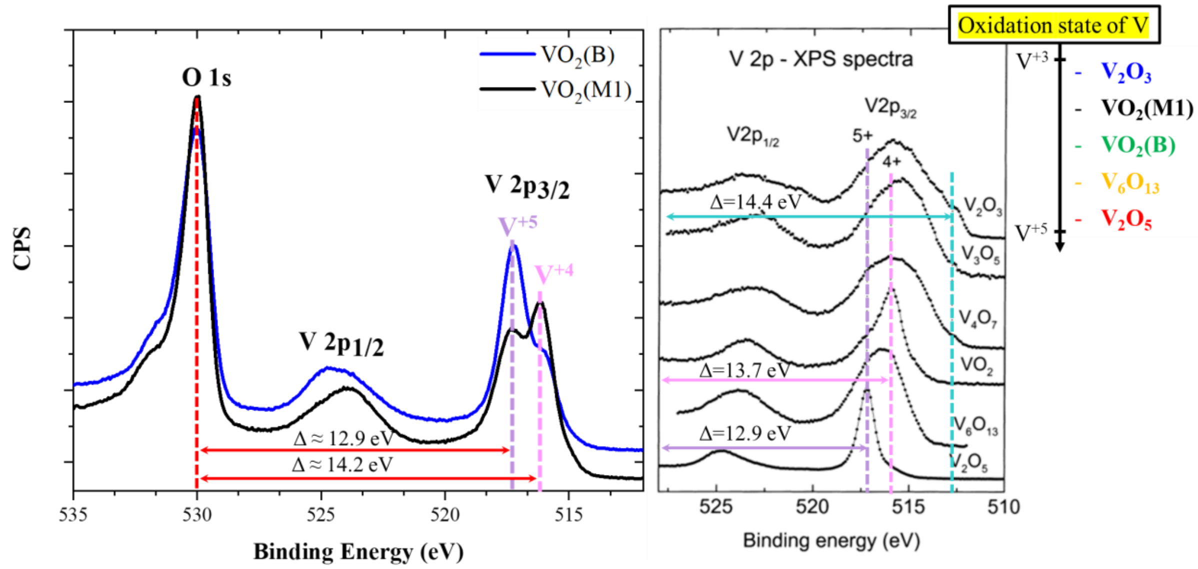

Figure 4-15: XPS O 1s and V $2p_{1/2,\,3/2}$ spectra of VO_2(B) (blue curve) and VO_2(M1) (dark curve) compared to XPS spectra of vanadium oxides [DEM00]. All spectra were recorded at RT.

For both characterized VO_2(M1) and VO_2(B) samples, their V $2p_{3/2}$ peak present several contributions, which were determined at 516 eV for V^{+4} and at 517.3 eV for V^{+5}. Despite the same stoichiometry confirmed by the average binding energy (BE) difference (Δ) between O 1s and V $2p_{3/2}$, we notice that V^{+4} contribution is dominant for VO_2(M1), while for VO_2(B) the main contribution in V $2p_{3/2}$ peak is V^{+5}. Consequently, the average percentage Lorentzian-Gaussian (L-G) was determined by the peak deconvolution for both polymorphs and is summarized in **Table 4-5**. The average contribution of the V^{+4} is estimated from the eq.(4.6).

$$\%V^{+4} = \frac{\text{Area } V^{+4}}{\text{Area } V^{+4} + \text{Area } V^{+5}} \tag{4.6}$$

Table 4-5: XPS fit parameters based on experimental measurements of the VO_2 polymorphic phases. The symbol Δ represents the BE difference between the O 1s and the V $2p_{3/2}$ levels.

VO_2 polymorphs	V $2p_{3/2}$	O 1s	Δ	%L-G	$\%V^{+4}$	$\%V^{+5}$
VO_2(B)	515.9 517.2	530.1 (FWHM 0.95)	14.18 12.86	7.74 17.53	30.6	69.3
VO_2(M1)	516.1 517.4	530.3 (FWHM 0.91)	14.15 12.87	16.97 8.5	66.6	33.3

Thus, VO_2(B) and VO_2(M1) have different proportions of V^{+4} and V^{+5}. The VO_2(B) is more oxidized, in line with his affiliation to the Wadsley phases in which the V presents a mixed oxidation state of V^{+4} and V^{+5} (cf. Chapter 1). However, we cannot exclude that the increase of V^{+5} contribution on the surface of VO$_2$(B) is related to the oxidation of the sample in air, which likely occurs during the storage time.

4.3.2. Temperature-induced phase transitions

Further investigation was focused on VO$_2$(B) structural transition as a function of temperature. Similar to VO$_2$(M1), the B phase exhibits semi-metal-insulator transition but has not been extensively studied during the last decades. In this part, we propose to focus onto the B structure in temperature and compare it to the M1 phase, seen in Chapter 3. Firstly, XRD analysis was performed for temperatures between -163°C and 87°C (**Figure 4-16**).

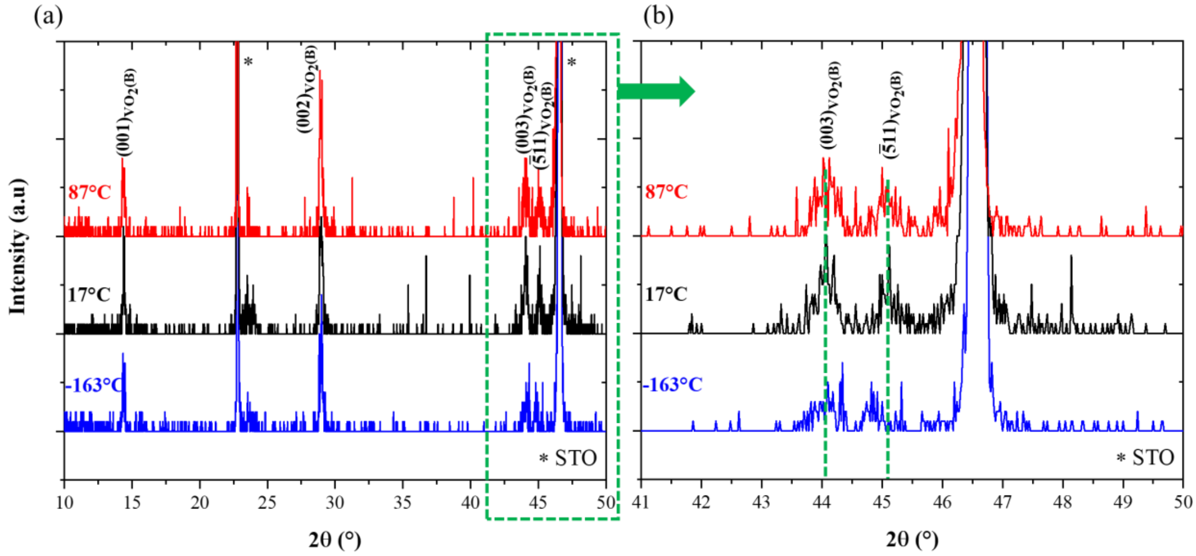

Figure 4-16: XRD θ-2θ diffractogram of VO$_2$(B) layer deposited on (001)STO substrate. (a) Experimental measurements performed at -163°C (blue), 17°C (black) and 87°C (red). (b) Zoom of 41°-50° region.

Unlike the M1 phase, which has a notable structural transition towards the R phase, the VO$_2$(B) phase shows no significant change of diffraction pattern in the 10 to 55° 2θ range. During the cooling, from 17°C to -163°C, only a slight shift of the $(\bar{5}11)_{VO2(B)}$ plane from 45.08° to 44.84° was observed. This could be explained by the fact that during VO$_2$(B) transition towards its insulating state, V(2)-V(2) (cf. **Figure 1-7**) distance shrinks from 2.87 Å at RT to 2.67 Å at -163°C. Therefore, we suggest that the monoclinic phase does not change except for this slight reduction of V-V distance, that could be enough to induce a change in the electronic behavior.

<u>VO$_2$(B) electronic structure</u> was characterized by XPS down to low temperature (TEMPO beamline of SOLEIL synchrotron). Each spectrum was calibrated with gold reference through measurement of its Fermi level position at the same photon energy (hν=120 eV) and pass energy (PE) of the detector. A beam-induced reduction of the VO$_2$ films was observed, then the photon spot was moved to acquired data on pristine VO$_2$.

The VO$_2$(B) valence band (VB) was analyzed at RT and at -223°C (≈ 50K). The first measurement was done at PE=50 eV. Unfortunately, the insulating behavior at low temperature (≤ -123°C) induced a very strong charging effect, making the measurement at PE=50 eV impossible. This charging effect indicates that VO$_2$(B) at low temperature is more insulating than at RT. Thus, a second measurement was realized at PE=20 eV and the **Figure 4-17** shows the experimental results. The valence band maximum (VBM) shift with temperature gives an idea of the behavior of the VO_2(B) phase, with a more insulating state at low temperature.

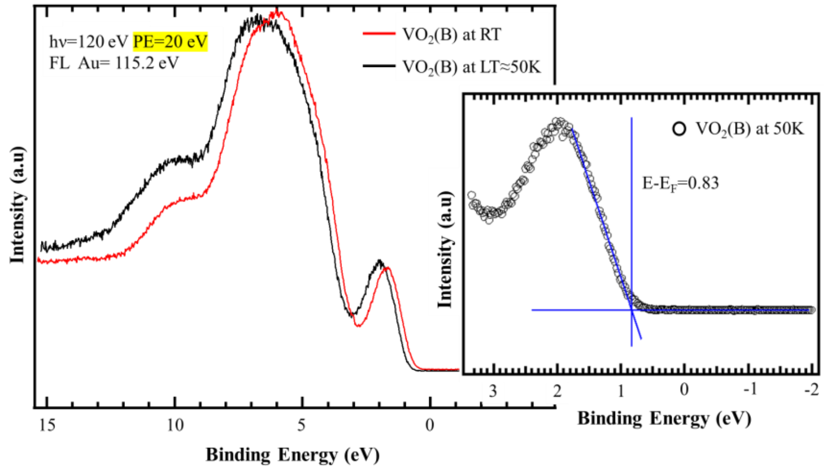

Figure 4-17: XPS valence band spectra of the VO_2(B) layer at a temperature of -223°C (black) and RT (red). On the right is a zoom on the VB edge, to extract its position with respect to Fermi level (E_F).

Contrary to the VO_2(M1/R) transition which is already well-investigated in the literature, there is a lack of information for the VO_2(B) phase. The work of Lee *et al*. [LEE15] on the polymorphic phases of VO_2 illustrated in **Figure 4-18**(a) gives a good description of the insulating gap for the VO_2(M1) phase when the effects of the correlated electrons are taken into account. For VO_2(B), considering the correlations, the gap becomes almost negligible at RT, and VO_2(B) behaves as a semi-metal. When the temperature decreases, the V(2)-V(2) distance in the *ac* plane shortens due to a contraction of the $\vec{c}_{VO2(B)}$-axis (cf. Chapter 1). This contraction entails an expansion of the $\vec{a}_{VO2(B)}$- and $\vec{b}_{VO2(B)}$-axes, increasing the β-angle [OKA93], and conducts to a more insulating character. **Figure 4-18**(b and c) depicts the transition of the VO_2(B) phase band diagram depending on temperature.

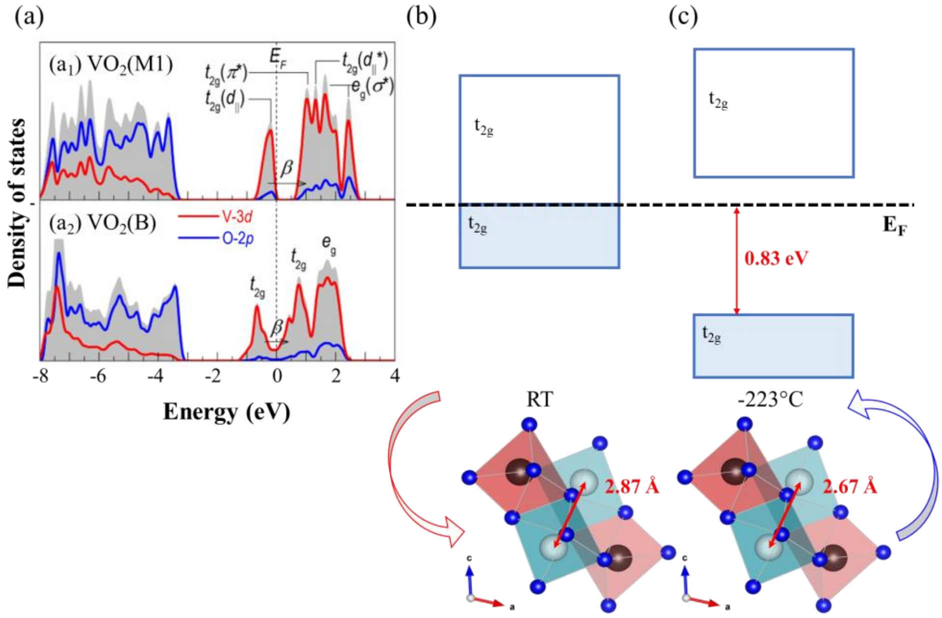

Figure 4-18: (a) Density of states as calculated with the Vienna ab initio package (VASP) of (a_1) M1 and (a_2) B phases [LEE15]. The Fermi level is set as 0 eV, M1 phase has bandgap of 0.6 eV, and B phase appears as semi-metallic. (b) Band diagram representation of VO_2(B) for the monoclinic semi-metal phase at RT, and (c) for the monoclinic insulator phase at -223°C. Unit cells with V-V distances are given below.

VO_2(M1) electronic structure was also characterized in the same way, and **Figure 4-19** shows the spectra below and above the metal-insulator transition temperature.

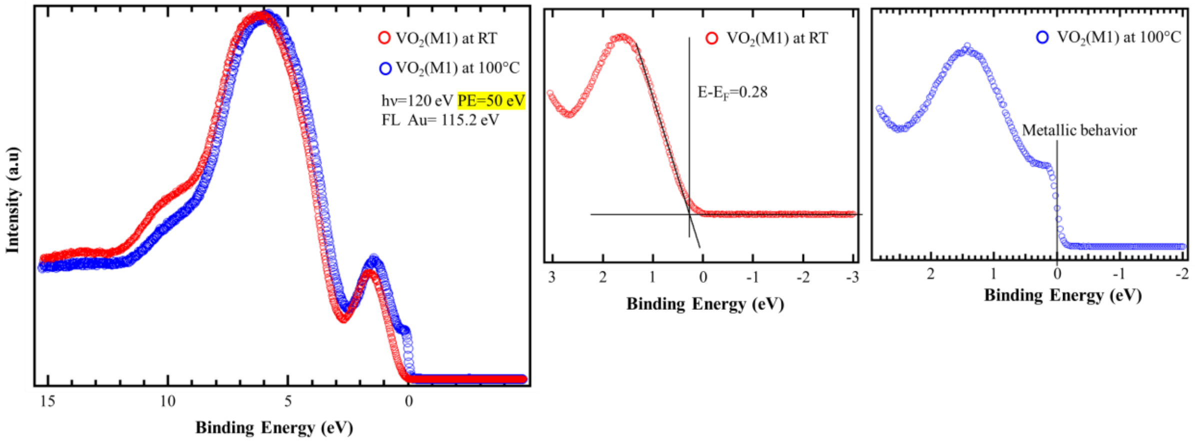

Figure 4-19: XPS valence band spectra of the VO_2(M1) phase below (T=RT < T_{MIT}, in red) and above (T=100°C > T_{MIT}, in blue) the metal-insulator transition temperature. On the right are zoom on the V 3d state at VB edge, to extract its position with respect to Fermi level (E_F) for both spectra.

Experimentally, a difference in the V 3d state as a function of temperature is observed. At RT, this state is located close to the Fermi level ($E - E_F = 0.28\ eV$), while at 100°C, the curve has a steeper slope and cuts the zero energy (Fermi level), indicating a metallic behavior. For the rest of the discussion, we consider a bandgap between VB and conduction band (CB) equal to 0.7 eV from *ab initio* calculations [SAK09][GE20]. For VO_2, these calculations seem to be able to determine the bandgap with a relatively good accuracy (**Figure 4-20**(a)). From this bandgap value and our XPS data, it is possible to represent the band structure of our VO_2(M1) layer. **Figure 4-20**(b) shows a schematic band diagram for the monoclinic insulator phase. The Fermi level is at 0.28 eV from the valence band and then $E_{CB} - E_F = 0.42$ eV. At 100°C, VO_2 becomes metallic and a conductive behavior is observed (**Figure 4-20**(c)).

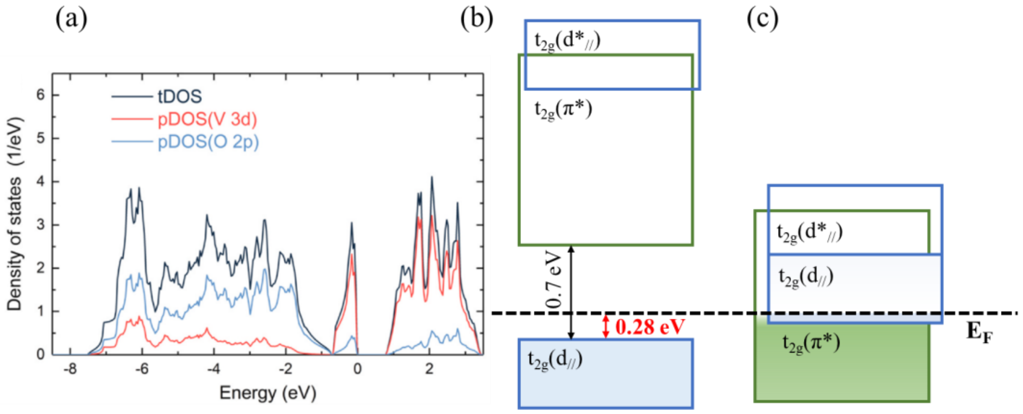

Figure 4-20: (a) Calculated total and partial density of states of the monoclinic structure. The bandgap of 0.75 eV is opened above the Fermi level set as 0 eV, which indicates the insulating nature of VO_2(M1) [GE20]. (b) Schematic band diagram of VO_2 based on XPS experimental data for the monoclinic insulator phase at RT, and (c) for the rutile metal phase at 100 °C.

During our study of the growth mechanisms of polymorphic phases, we highlighted the key role of the substrate. For VO_2(B) growth on STO, as shown on **Figure 4-21** with XRD θ-2θ scans taken over two years of sample storage in desiccator with RH% at ~30%, the substrate stabilizes the metastable phase and slows down its reoxidation. Thanks to this remarkable stability of VO_2(B) thin films, additional structural investigations could be performed and confirm that B and M1 phases are affiliated to the Wadsley and Magnéli families, respectively.

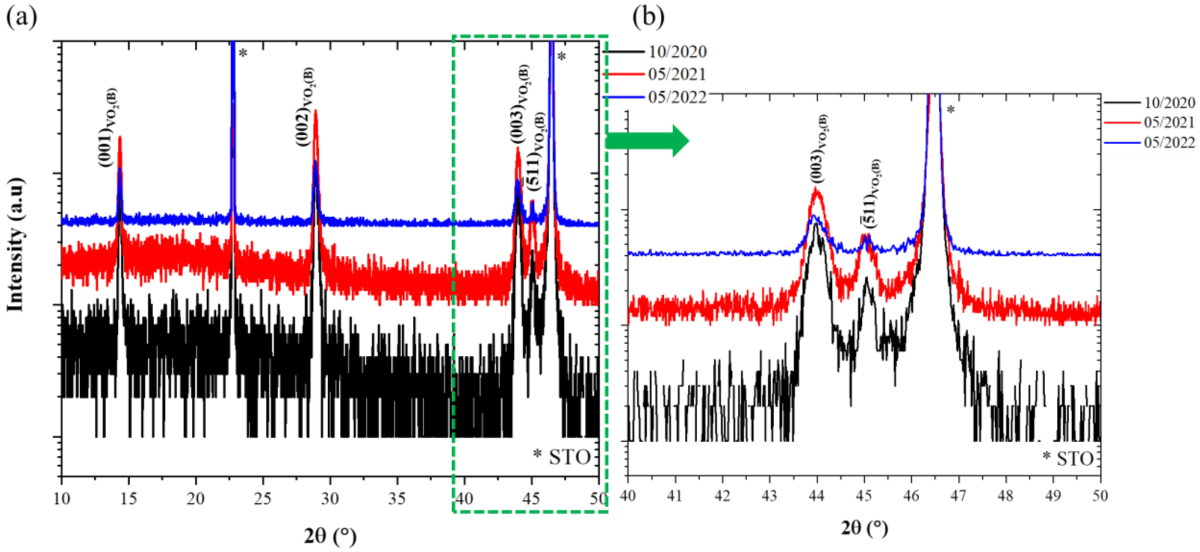

Figure 4-21: (a) θ-2θ diffractograms showing the evolution at RT of a VO_2(B) film on (001)STO between 2020 (black), 2021 (red) and 2022 (blue). (b) Zoom of 40°- 50° region.

4.4. Thickness influence on VO_2(B) growth

During our investigation of VO_2(B) phase growth on (001)STO, we were interested in the effect of the thickness of the thin films. Indeed, previously published works have shown the existence of a critical thickness above which the film is no more comprised of a pure VO_2(B) phase but of a mixture of VO_2(B) and VO_2(M1) phases [EMO18][CHE14]. We have seen that many factors are involved during the growth of thin films (lattice matching, surface energy, interfacial chemistry, etc.) which define the growth mode and the residual stresses. In the case of VO_2(B) on (001)STO, we have presented previously (section 4.2) that the thin films are partially relaxed, with dislocations and grain boundaries to reduce the epitaxial stress. As this relaxation is thickness-dependent, one expects thicker films to be less sensitive to the stress from the substrate. This reduced epitaxial stress could then lead to the growth of a different, more stable phase such as VO_2(M1).

Two VO_2(B) films of different thicknesses (160 nm and 230 nm) have been deposited on (001)STO by RFMS and were measured by XRD. The analysis of the diffractograms (**Figure 4-22**) reveals the exclusive presence of the $(00l)$ family of VO_2(B) planes, as all the other peaks correspond to the reflections of the substrate. The thicker layer (230 nm) shows the highest peak intensity of this $(00l)$ family, with two more peaks appearing at higher diffraction order. If another phase has formed, none of its crystalline planes are parallel to $(001)_{STO}$ surface plane. We will see that it is indeed the case.

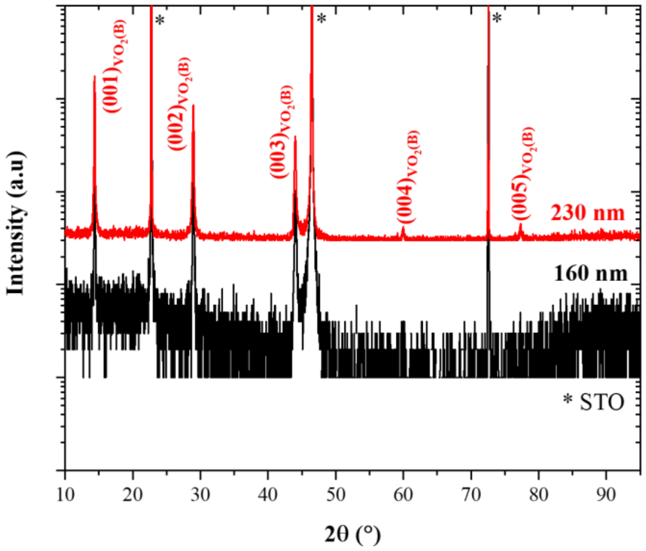

Figure 4-22: θ-2θ diffractograms of VO_2(B) films on (001)STO with 160 nm (black) and 230 nm (red) thickness.

The surface morphology of the films was studied by scanning electron microscopy (SEM) and by atomic force microscopy (AFM). The SEM images displayed in **Figure 4-23** for both thicknesses reveal a rather peculiar morphology, with circular "patches" for which we distinguish four different areas. The central zone (Pt.1) has a nanostructured morphology, reminiscent of the platelets of HT synthesis but aligned along the STO substrate crystalline directions. The second zone (Pt. 2) surrounds the first and extends up to the boundary of the circular areas, comprised of a mixture of small grains and elongated nanostructures. The boundary zone (Pt. 3) has a relatively smooth granular morphology. Finally, the last region (Pt.4) in between the circular domains has a very smooth and uniform surface.

AFM topography measurements in non-contact mode (**Figure 4-24**) confirmed the presence of these distinctive areas with very different roughness values (R_{rms}): In a circular domain, the roughness decreases from 15 nm in the center (Pt.1) to 4 nm at the boundary (Pt.3), while the smooth zone (Pt.4) has a very low roughness of only 2nm (compared to typical values for VO_2 films, see Chapter 2).

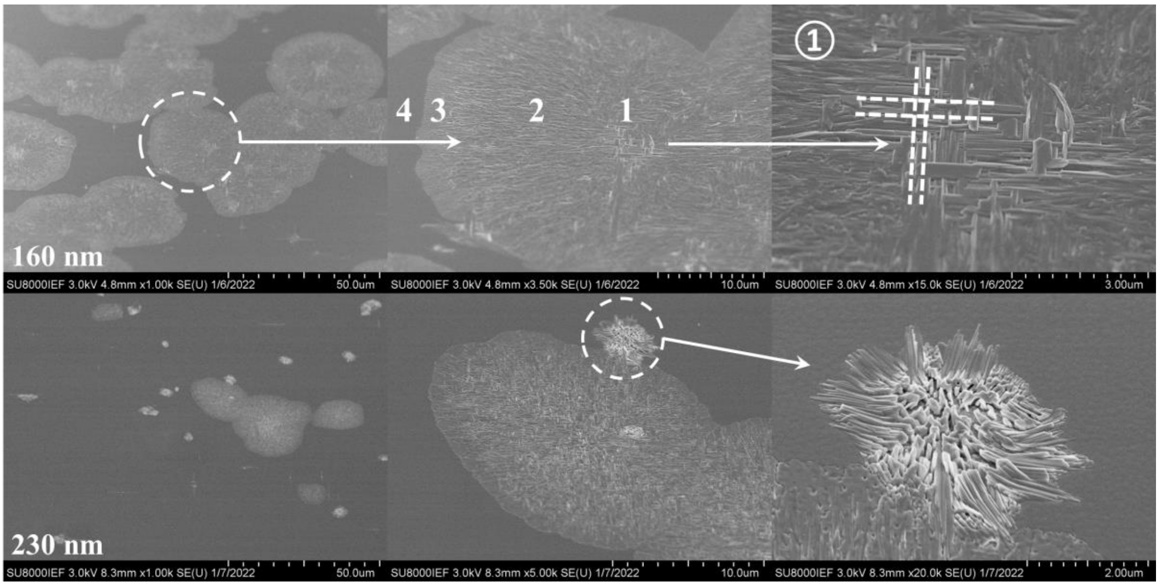

Figure 4-23: SEM images showing the thickness-dependent morphology of VO_2 films for 160 nm and 230 nm-thick VO_2 layers grown on (001)STO substrate. The numbers identify the different zones as defined in the text.

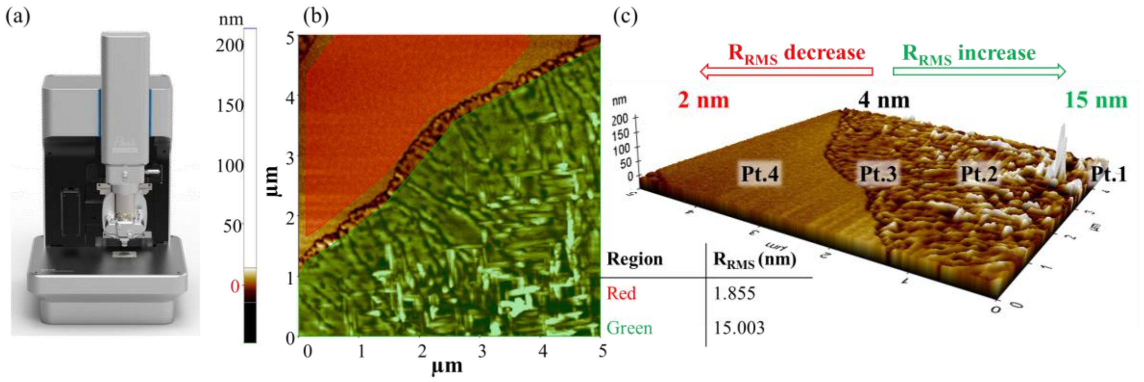

Figure 4-24: (a) Picture of AFM NX10 from Park Systems®. (b) and (c) Topography measurements at room temperature of VO_2 films. The point labels 1 to 4 indicate the different zones as for SEM images.

Strikingly, according to our SEM observations (**Figure 4-23**), the number of highly nanostructured domains reduces with the thickness of the layer. To try and identify locally the crystalline phases in and around these domains, Raman spectroscopy was used. Firstly, we analyzed the central zone (Pt.1), the zone juxtaposed to the first one (Pt.2) and the zone 3 with the rather smooth granular morphology (Pt.3). The results reveal the simultaneous presence of VO_2(M1) and VO_2(B) phases (**Figure 4-25**).

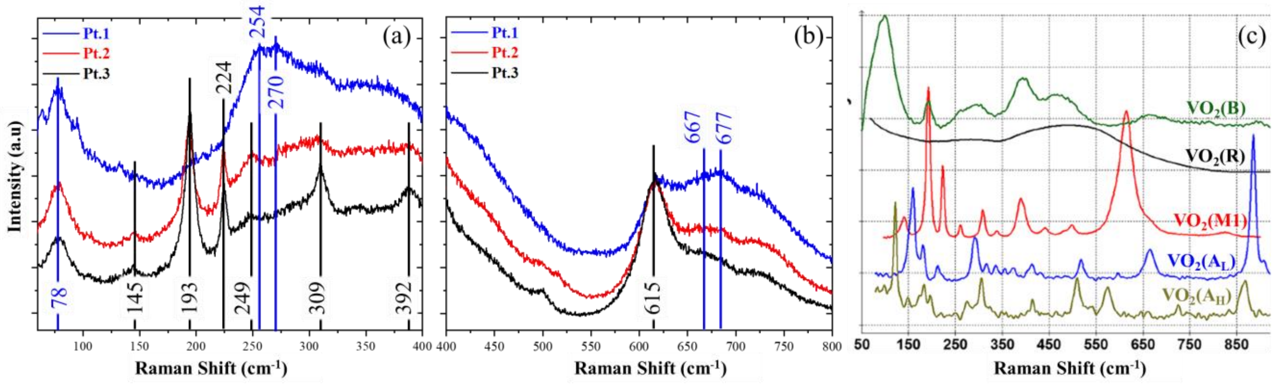

Figure 4-25: (a) and (b) Raman spectra of zones 1, 2 and 3 observed by SEM measurements. The central zone is identified by Pt.1 (blue curve), the intermediate by Pt.2 (red curve), and the region adjacent to the flat zone by Pt.3 (dark curve). (c) Raman scattering in VOw_2 polymorphs from literature: VO_2(M1), VO_2(R), VO_2(B), and VO_2(A) measured at 30°C (A_L) and 220°C (A_H) [SHV19]. Vertical lines in (a) and (b) reproduce the peak positions of (c).

Our detailed interpretation of these Raman spectra is as follows:

i. For Pt.2 and Pt.3, the Raman modes at 193 cm^{-1} and 224 cm^{-1} are a characteristic signature of the VO_2(M1) phase, associated with V-V bond vibrations, together with the band at 615 cm^{-1} related to the V-O stretching mode. [SHI17][SHV19][GON13]. The intensity variations between Pt.2 and Pt.3 for 145, 224, 309 and 392 cm^{-1} hint at an increase of VO_2(M1) phase presence upon approaching the boundary.

ii. Raman bands of VO_2(B) are compared to nanopowders produced by hydrothermal reactions [SHV19]. The bands at 254 cm^{-1} and 270 cm^{-1} can be assigned to the V-O-V bending/wagging and V-O-V stretching modes, respectively. Finally, the broadband range around 667-677 cm^{-1} is associated with the vibrations of V_3-O units. VO_2(B) phase seems thus alone at Pt.1, and then VO_2(M1) gradually appears upon approaching the boundary (Pt. 3).

To summarize, from the Raman measurements, the circular rough domains are mainly composed of VO_2(B). However, its presence reduces from center to periphery, where VO_2(M1) phase becomes predominant. The composition of the smooth area (Pt.4) could not be clearly identified from the Raman spectra due to a low peak definition (**Figure 4-26**). We note the presence of shoulders at 192, 260 and 614 cm^{-1} which coincide with the VO_2(M1) signature [URE17], however the peak intensity is too low to be conclusive. Thinking this zone could be amorphous, "laser annealing" of these areas was performed at different values of 5, 25, and 50% of the laser maximum power. However, as shown in the Raman spectra of **Figure 4-26**, no modification was observed after such annealing. We definitely need more investigation of this smooth area.

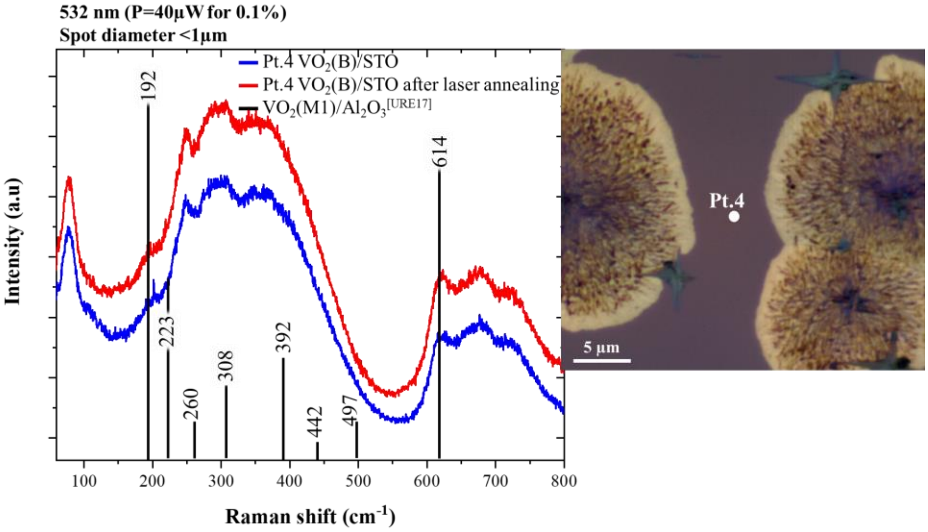

Figure 4-26: Raman spectra of the smooth and uniform zone (Pt.4) shown on the right (optical image) before (blue) and after laser annealing (red) compared to a VO_2(M1) thin film obtained by electron beam evaporation (black vertical lines) [URE17].

4.4.1. Exploration by transmission electron microscopy

To get better insights on the circular domain structure and composition, further characterizations were carried out by transmission electron microscopy (TEM). A TEM lamella running across the rough to smooth zones was prepared by focused ion beam SEM (FIB-SEM) (**Figure 4-27**).

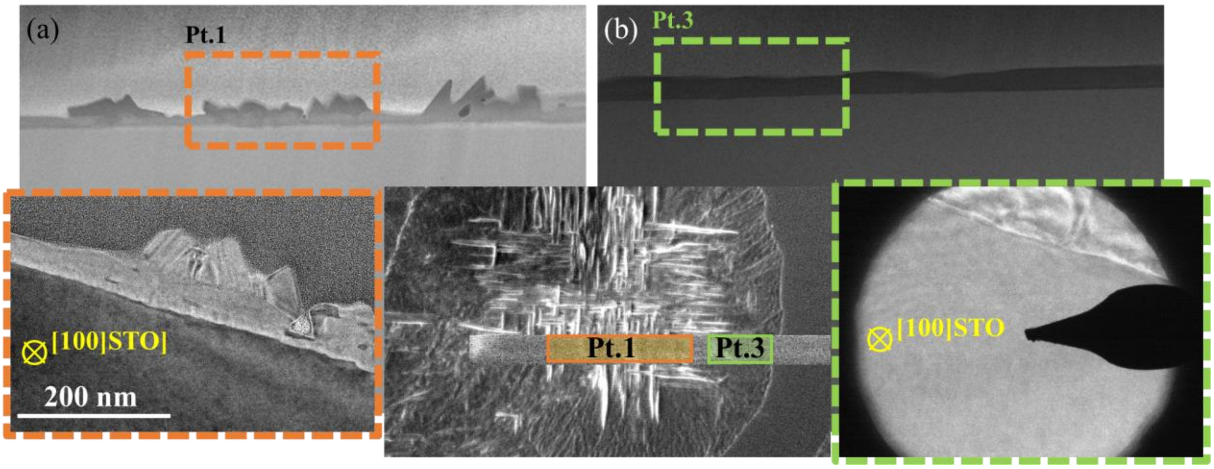

Figure 4-27: SEM image during the preparation of the TEM lamella with the zones 1 and 3 shown from the top (middle) and in TEM cross-sections at (a) Pt.1 and (b) Pt.3.

Each zone was analyzed by electron diffraction, and in both zones at Pt.1 and Pt.3, the VO_2(M1) was identified as tilted by 26° from the $(001)_{STO}$ surface plane (**Figure 4-28**). The inter-reticular distance d_{hkl} determined from the VO_2(M1) diffraction spots can be attributed to the $(\bar{1}11)_{VO2(M1)}$ (d_{hkl} (JCPDS-01-081-0661) = 3.31523 Å) or $(011)_{VO2(M1)}$ (d_{hkl} (JCPDS-01-081-0661) = 3.20344 Å) plane family.

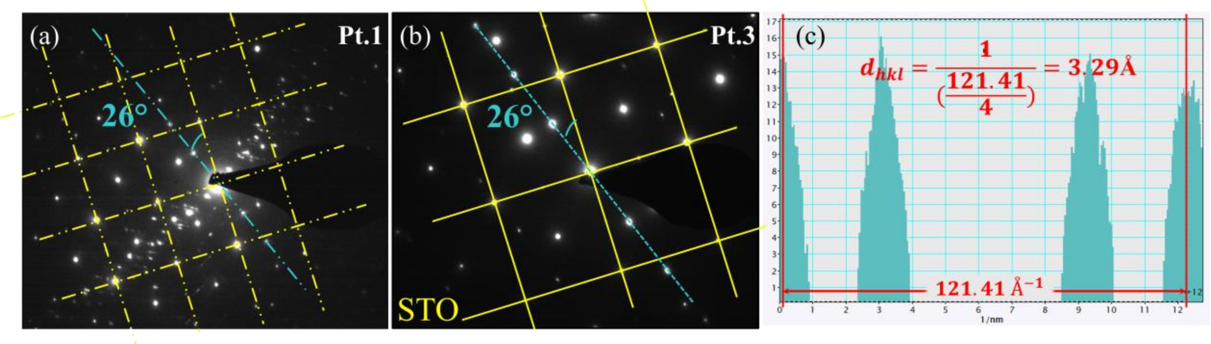

Figure 4-28: Electronic diffraction patterns at RT from (a) smooth and (b) rough zones, STO reciprocal lattice is in yellow. (c) Line profile taken at 26° from [100]STO direction, i.e. along blue line in (b), with real space interreticular distance calculated from the measured spot distance.

Unexpectedly, the recorded HRSTEM (High-Resolution Scanning TEM) images reveal the presence of VO_2(M1) near the substrate interface (**Figure 4-29**), while the (001)-oriented VO_2(B) phase was detected in the upper layer in fin-like structures (**Figure 4-30**). Such observation is at variance with the scenario of stress relaxation favoring the transition towards VO_2(R) growth over VO_2(B), VO_2(R) transforming to VO_2(M1) upon cooling down from growth temperature

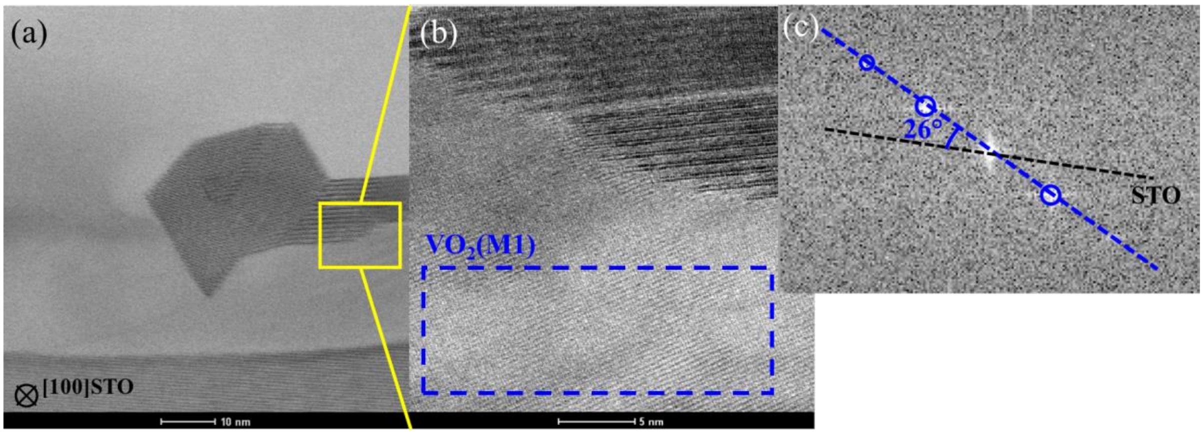

Figure 4-29: HRSTEM cross-section images of a VO_2 layer on STO with $[100]_{STO}$ zone axis (a), showing the interface between B and M1 phases (b) and the Fourier transform (c) of the (blue) M1 boxed area. The $[001]_{STO}$ direction is recalled (in black) to reveal the angle with the imaged VO_2(M1) planes.

Considering the epitaxial stress, the VO_2(B) structure should first appear in contact with the substrate according to $[010]\mathrm{VO_2(B)}//[010]\mathrm{STO}$ or $[100]\mathrm{VO_2(B)}//[100]\mathrm{STO}$ to respect the $(00l)VO_2(B)//(00l)STO$ preferential growth. These orientations were confirmed by HRSTEM, showing $(001)_{VO2(B)}$ planes parallel to the $(001)_{STO}$ substrate planes, as revealed by the characteristic intercalation channels of the VO_2(B) structure (**Figure 4-30**(d)). Moreover, we note that several of the VO_2(B) grains are perfectly aligned perpendicular to $[100]_{STO}$ direction, respecting the in-plane epitaxial relationships. Interestingly, we did not observe any VO_2(B) grain in contact with the STO substrate for this film (160 nm thickness). As for the VO_2(M1) phase, there are two possible scenarios: (i) Both phases grew side by side from the start, with some defects and/or the 26° inclination stabilizing the VO_2(M1) on

STO; (ii) B phase does transform into R phase during growth, due to stress relaxation at grain boundaries or other mechanism, but then the resulting M1 phase obtained at RT is on the side or below the B phase. We could find one previous work by Emond *et al.* [EMO18] reporting a VO_2(M1/B) phase coexistence (on $LaAlO_3$ substrate), but without giving their relative positions.

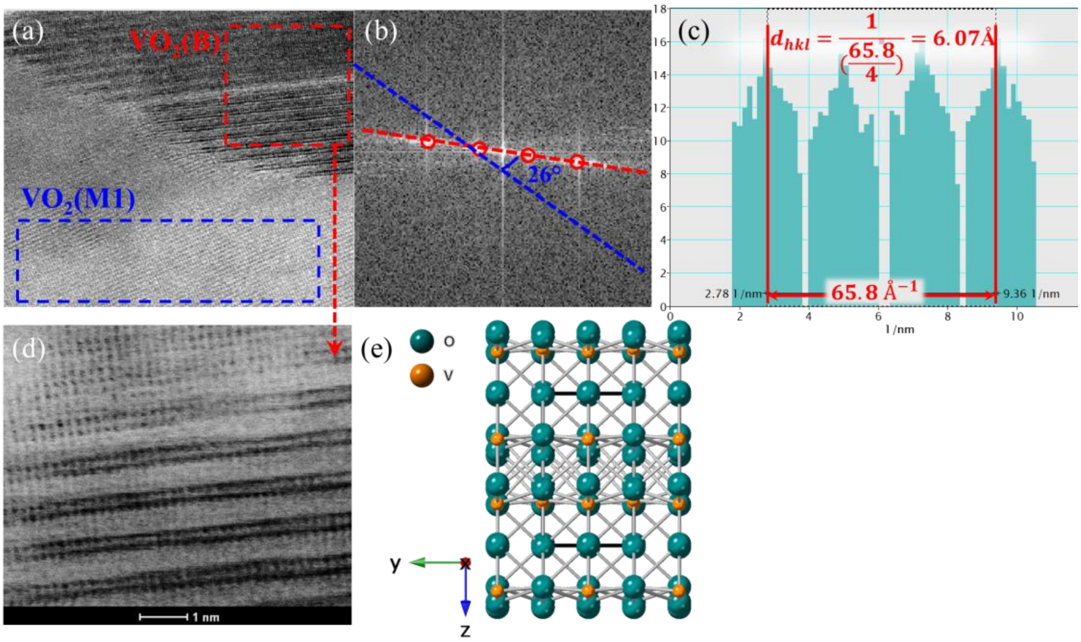

Figure 4-30: HRSTEM cross-section images along $[100]_{STO}$ zone axis of the coexisting M1 and B phases. (a) M1/B interface, with Fourier transforms (b) taken from boxed areas of both phased. A higher magnification image of B phase is shown in (d), evidencing the intercalation channels of the VO_2(B) structure displayed in (d) with the same $[100]_{VO2B}$ zone axis as the experimental image.

About possible defects on the STO substrate, we indeed could observe by HRSTEM the presence of step-like facets tilted by 45° from the $(001)_{STO}$ surface plane (**Figure 4-31**(a) and (b)). These facets then have other orientations than the $(001)_{STO}$ plane of the substrate, for example along $(011)_{STO}$ plane as depicted in **Figure 4-31**(d). Then, a different surface energy may lead to the stabilization of another phase than VO_2(B). Moreover, since the growth rate can also be orientation-dependent, it is possible that the two types of phases coincide at the start, for the one with the higher growth rate to take over. The surface properties of the substrate represent a key parameter in the growth of polymorphic phases and should be seriously considered.

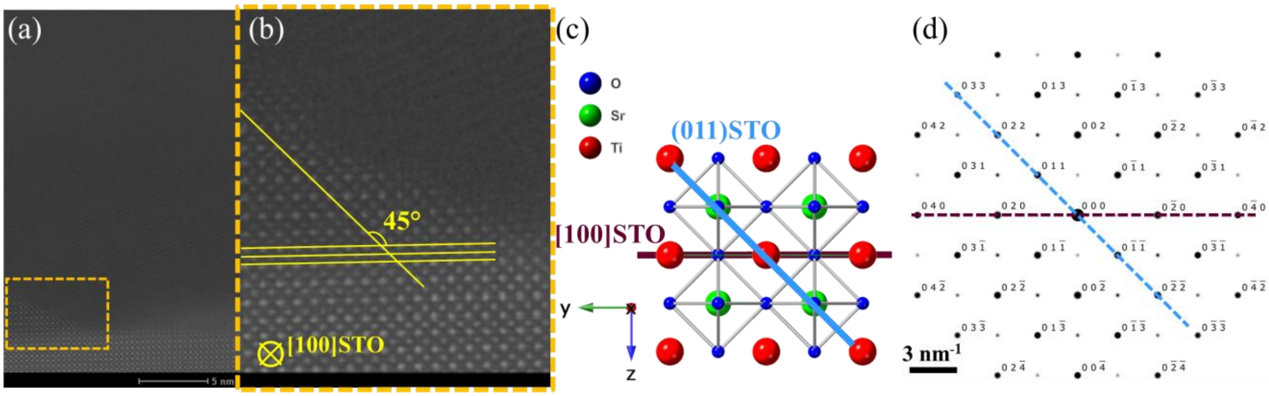

Figure 4-31: (a) and (b) HRSTEM cross-section images along $[100]_{STO}$ zone axis of the interface with STO substrate; (c) Atomic structure of STO projected along $[100]_{STO}$ direction and (d) diffraction pattern calculated for the STO structure, the blue dashed line is at 45° from the surface plane in brown.

To summarize, the VO_2(B) and VO_2(M1) phases coexist in the layer, with the B phase having its $(001)_{VO2(B)}$ planes oriented preferentially parallel to the substrate. The TEM reveals the intercalation channels of the VO_2(B) phase (**Figure 4-30**(d and e)) correlated with structure representation that we determined in section 4.2, and also that the VO_2(M1) phase is localized at the substrate interface, tilted by 26° with respect to the STO substrate. Unfortunately, the smooth area (Pt.4) was not characterized by TEM and could not be clearly identified.

4.4.2. Conductive AFM measurements

We saw that the morphology of the VO_2 films on STO is thickness dependent. The proportion of the circular rough domains decreases with film thickness, and the smooth domain becomes predominant. The thickest investigated VO_2 layer (~230 nm) demonstrated the smoothest morphology, while for an intermediate sample thickness of 160 nm, the smooth domain appears much smaller (**Figure 4-23**). Corroborating with the XRD measurements, we suggest that in globality, these samples are composed of VO_2(B) phase with VO_2(M1) inclusions that are not detected by XRD. The TEM and Raman measurements, reported previously, confirmed that the circular areas are composed of both B and M1 phases, while the composition of the smooth zone is still unknown. Therefore, temperature-assisted conductive AFM (c-AFM) measurements were intended to get simultaneous information about the topography and local conductivity of the film. The latter should be changed for VO_2(M1) near the MIT temperature, thus allowing us to localize the VO_2(M1) in the sample. The c-AFM measurements were performed at room (LT), intermediate ~70°C (MT) and high temperature ~100°C (HT). One should note that these temperature values are indicative due to the lack of accuracy in the temperature control.

The c-AFM measurements were performed by applying 1V bias between the sample and the tip of the AFM (**Figure 4-32**).

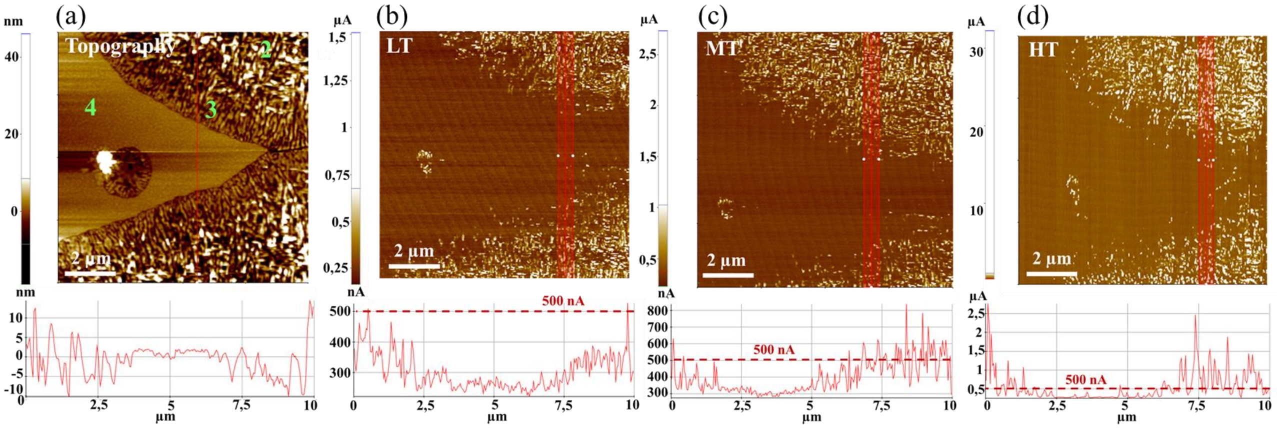

Figure 4-32: (a) Topography and c-AFM measurements at (b) LT, (c) MT and (d) HT for 1V applied bias. A line profile taken along the red line is displayed below each image, averaged on several lines for c-AFM.

We observed that the smooth area (Pt.4) preserves its insulating character up to HT regime (~100°C), while the boundary area (Pt.3) seems to be insulating at LT and MT, with maybe a slight increase of its conductivity at HT, especially on the edge between Pt.4 and Pt.3. The rough zone (Pt.2) shows an increase of conductivity with temperature as a typical semi-conductor behavior. The current map reproduces the topography of rough areas, probably due to increased contact area(s) between tip and surface. In the section 4.3.2, we saw that the valence and conduction bands of VO_2(B) are relatively close, with a small gap, which gives it a semiconducting character: the VO_2(B) conducts but less than metallic VO_2(R).

In order to investigate the effect of higher applied bias, the samples were maintained at MT and the voltage bias was progressively increased from 0 to 3V (**Figure 4-33**). We observed a classical I-V characteristic for the rough area (Pt.2) (**Figure 4-33**(f)), a small but clear change for the boundary (Pt.3), and still no current (or very low) detected on the smooth area (Pt.4).

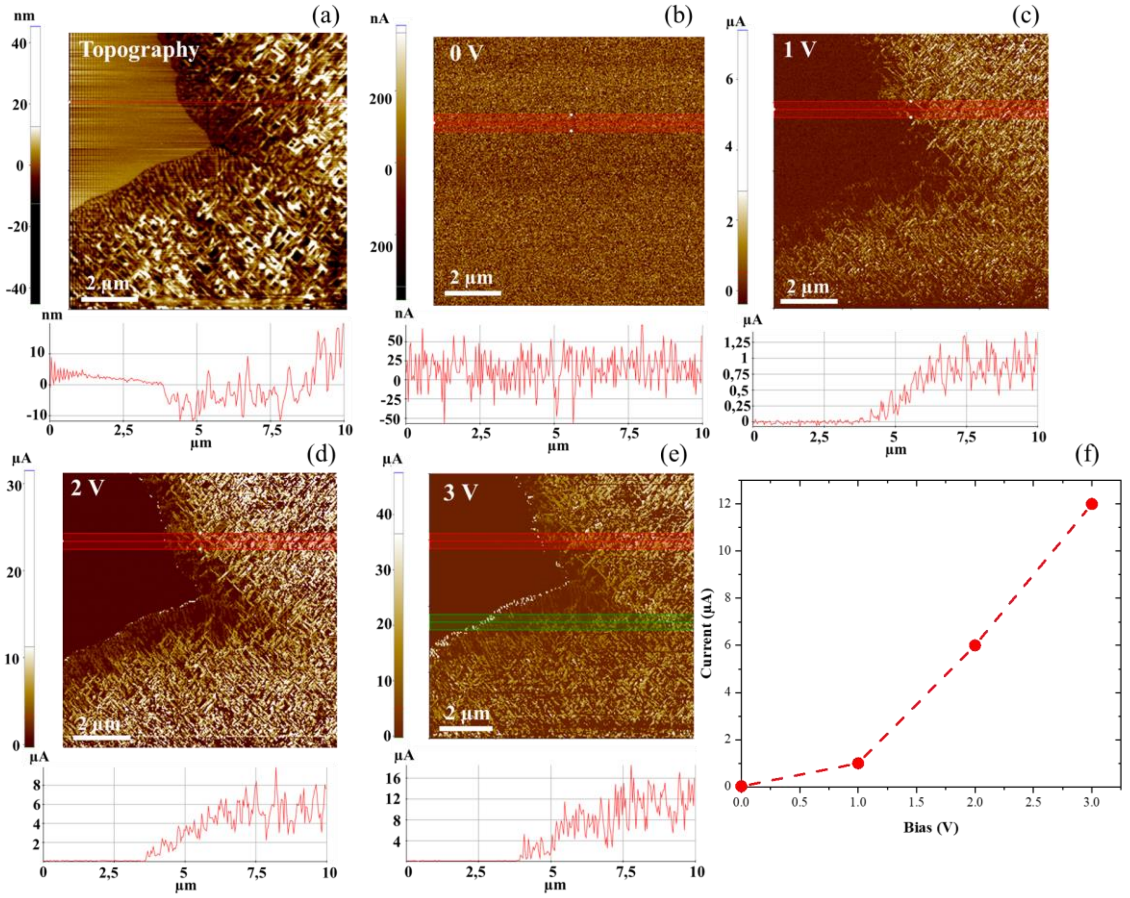

Figure 4-33: (a) Topography and c-AFM measurements at MT for (b) 0V, (c) 1V, (d) 2V, and (e) 3V applied bias. A line profile taken along the red line is displayed below each image, averaged on several lines for c-AFM. (f) I-V characteristic taken on rough area.

Finally, the bias influence was also investigated for the HT range (~100°C) (**Figure 4-34**). Below 4V, no difference in the conductivity on the smooth area was observed, as for the previous measurement in MT range. When the applied bias was 4V, both the smooth area (Pt.4) and the boundary area (Pt.3) become more conductive than the rough area (Pt.2). After cooling down to 40°C, the same area was scanned again under 1V applied bias. We note that the conductivity of the smooth area (Pt.4) was preserved, while the conductivity of the rough areas (Pt.2) was slightly decreased. This irreversible change of the conductivity after simultaneous application of temperature and voltage evidences a material modification. The high current density at the AFM tip may locally modify the material during scanning. However, we cannot definitely conclude on the modification mechanism under applied high voltage and temperature. Co-localized c-AFM and Raman measurements would be a good way to explore such behavior, but were not possible in the frame of this work due to time constraint. Still, these first c-AFM measurements gave important spatially-resolved information on the conductivity of our heterogeneous VO$_2$ layers, paving the way for future investigations.

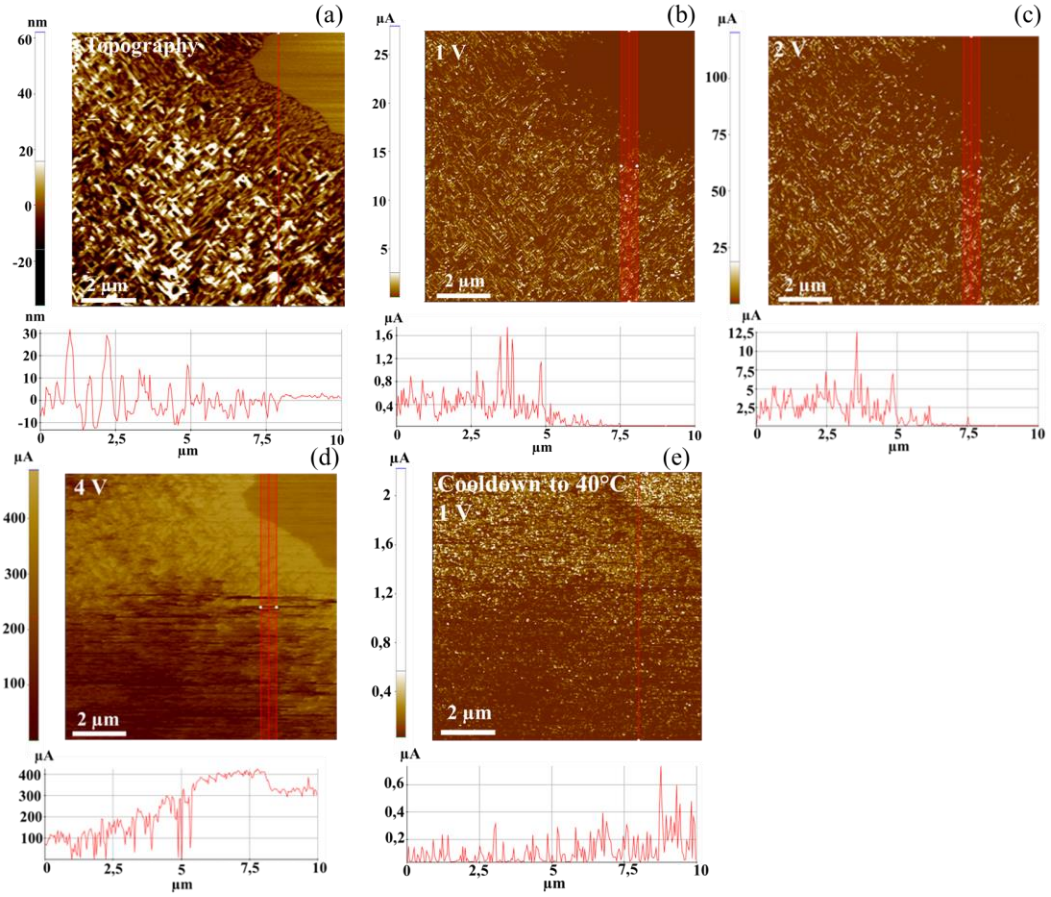

Figure 4-34: (a) Topography and c-AFM measurements at HT for (b) 1V, (c) 2V, (d) 4V, and (e) 1V applied bias. Current map in (e) was after cooling down to 40°C. A line profile taken along the red line is displayed below each image, averaged on several lines for c-AFM.

To summarize, the growth study of VO$_2$(B) thin films deposited on (001)STO substrate at different thicknesses evidenced a spatially heterogeneous growth of VO$_{2,}$ with both B and M1 phases detected along various morphologies. The presence of the M1 phase leads to a decrease in roughness and change in electrical performance. From an appropriate modification of the substrate surface, the fabrication of VO$_2$(B)/VO$_2$(M1) heterostructures seems possible, although the control of their morphology might be a real challenge. This would open the door for various applications in microelectronics and energy storage, where materials with scalable properties are needed.

4.5. Conclusions

In this chapter, we presented our investigation of VO$_2$(B) polymorph in both nanostructure and epitaxial thin film forms. We started our study with nanostructures obtained by the hydrothermal synthesis, and we highlighted the impact of the oxalic acid concentration on the structural properties of VO$_2$(B), especially in terms of the intercalation channels. According to the width of the $(00l)$ peaks corresponding to planes parallel to the (a$_{VO2(B)}$,b$_{VO2(B)}$) base plane, we got an idea of the crystalline quality of the material. We could propose hypothesis concerning the presence of defects or impurities around the $\vec{c}_{VO2(B)}$-axis, to explain the poor electrochemical performance. The VO$_2$(B) nanostructures presented also a poor ambient stability, which is incompatible with industrial applications. Embedding the nanostructures in a chemically stable envelope could be a future approach to solve this problem. Following our objective to obtain thin layers and nanostructures, and in order to achieve a better stabilization of the polymorph phase, the RFMS growth approach was investigated. A detailed study was performed to understand the epitaxial growth of VO_2(B) on (001)STO and to get detailed insights on the structural, chemical, and electrical properties of the material. With XRD, only the VO_2(B) phase was detected, while Raman spectroscopy and TEM measurements evidenced the presence of both VO_2(M1) and VO_2(B) phases. This study opened new questions on the growth mechanism, in particular on the previously suggested VO_2(B)-to-(M1) transition due to epitaxial stress relaxation, and opened new research perspectives. It is worth noting that this work shows for the first time, to our knowledge, the influence of the substrate (Al_2O_3 vs STO) to stabilize the VO_2(M1) and VO_2(B) polymorphs during the same deposition run.

Chapter 5: VO_2 RF devices-Towards optical activation

Contents

We have seen throughout this work that vanadium dioxide (VO_2) is a promising candidate for many emerging applications due to its ability to form numerous polymorphs which are crystallographically interconnected [LIU18]. In previous chapters, we highlighted that the substrate influences the VO_2 phase stabilization in terms of preferential growth orientation, morphology, and epitaxial strain that impact the metal-insulator transition (MIT) performance. In order to assess it for RF applications, c-cut and r-cut sapphire (Al_2O_3) were chosen as substrates due to their low dielectric losses in the RF range. The first generation of RF switches were developed by TE-OX, in partnership with the C2N [ISH19]. Currently they are designed for a thermal trigger, while from the literature it is known that this transition can be also activated optically. Therefore, the purpose of this chapter is the study of both MIT activation ways: thermal and optical. In addition, the investigation of the activation of VO_2 MIT by ultrafast laser light will help TE-OX in the development of next generation RF switches. A test device has been developed during this thesis to study the MIT of VO_2, first thermally and then optically.

5.1. RF switching technology

In the microwave field, a RF switch is a component that has two binary states: an ON state and an OFF state. Ideally, the RF signal has to be transmitted without losses and without distortion when the switch is in its ON state, while in its OFF state, the signal should be completely blocked. Since switches are not perfect, their performance is characterized by different parameters such as the switching time, the insertion losses, the insulation in the OFF state, the power consumption, and its cutoff frequency (f_c) given by the following eq.(5.1):

$$\mathrm{f_c} = \frac{1}{2\pi \mathrm{R} * \mathrm{C}} \tag{5.1}$$

Where R is resistance and C is capacitance. RF switch is considered efficient when its electrical response is close to a perfect switch. Therefore, the higher the cutoff frequency value, the closer the electrical characteristics are to a perfect switch. Additionally, the S-parameters (S_{ij} , i,j=1,2) expressed as a function of frequency allow to characterize the RF switch electrical performance. The coefficient S_{11} expresses the quantity of the reflected signal, while the coefficient S_{21} expresses the amount of transmitted signal. These characteristics can be measured from incident and reflected waves in the RF domain. They are expressed in decibel (dB) and are determined from eq.(5.2).

$$\begin{aligned} \mathrm{b_1} &= \mathrm{S_{11}} * \mathrm{a_1} + \mathrm{S_{12}} * \mathrm{a_2} \\ \mathrm{b_2} &= \mathrm{S_{21}} * \mathrm{a_1} + \mathrm{S_{22}} * \mathrm{a_2} \end{aligned} \tag{5.2}$$

Where a_i represents the incident wave and b_i the reflected wave at the input "i". In the ideal case, the signal is fully reflected when the switch is in its OFF state. Thus, the S_{11} tends toward 0 dB, and the S_{21} parameter toward -∞ dB, and the reverse in the ON state. In practice, the values of the transmission coefficient in the OFF state and reflection in the ON state must be lower than -25 dB, which ensures the good electrical performance of the switch [GRA02]. RF switches exist in two configurations: a first one called series and a second one called shunt. They are based on the same principle, with an element connecting or not two transmission lines and thus modifying the S_{11} and S_{21} parameters (**Figure 5-1**).

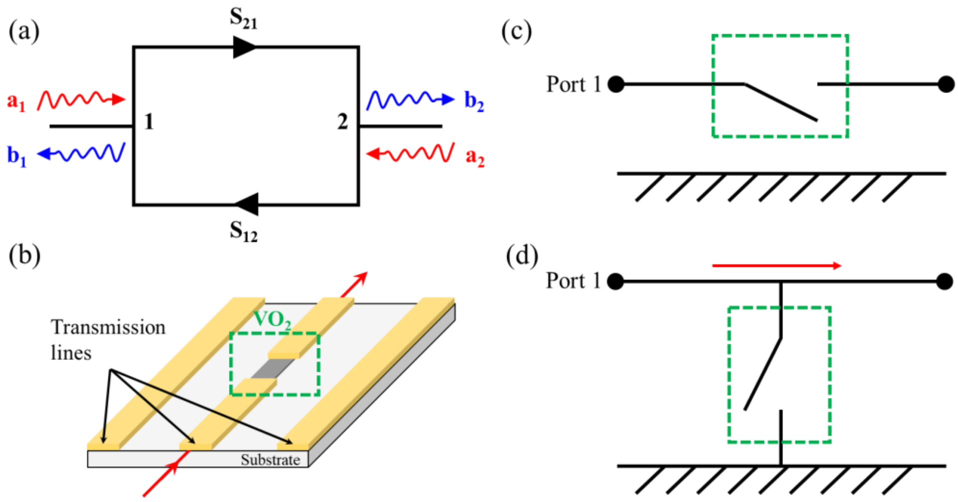

Figure 5-1: (a) Scheme of two-port network with incident wave quantities a_x and reflected wave quantities b_x, where x is the port. Scheme of RF switches in (c) series and (d) shunt configurations. (b) Representation of a switch (series configuration) integrating the VO_2 pattern into a coplanar waveguide.

Nowadays, most commercially available switches are divided into semiconductor-based technologies (usually field-effect transistors and PIN diodes) and micromechanical systems (MEMS). With the development of VO_2, a new generation of VO_2-based RF switches arrived on the market. A VO_2 RF switch integrates the VO_2 pattern into the coplanar waveguide (CPW). When VO_2 is an insulator in, e.g., series configuration, the pattern behaves like a high resistance in parallel with a low capacitance; the switch is in the OFF state. Conversely, when the VO_2 is metallic, it is considered a low resistance in parallel with a low capacitance; the switch is in the ON state, the signal is transmitted.

To fabricate this type of device, the VO_2 must be integrated in thin film form. The substrate could impact the properties of the RF devices; it is essential to be compatible with high frequencies. Indeed, the electromagnetic wave propagates along the coplanar lines of gold partly through air and partly in the substrate (the dielectric part of the RF switch). The wave must remain confined in the vicinity of the gold lines, otherwise its propagation in the substrate would lead to an increase in signal loss. From the permittivity (ε), the losses through the substrate can be calculated. To have good RF performances of the switches, minimizing the losses through the substrate is necessary. Therefore, delta angle (δ) given by eq.(5.3) should be as low as possible. With ε' the real part of the complex dielectric function and ε'' its imaginary part.

$$\tan \delta = \frac{\varepsilon''}{\varepsilon'} \qquad (5.3)$$

For this reason, sapphire (Al_2O_3) substrates with tan(δ)~10^{-4} [SICT] were used during this work.

5.2. VO_2 for reconfigurable RF electronics

We have previously seen the impact of growth parameters on the phase transition of the VO_2(M1) films deposited by RFMS. The results highlight that the crystalline quality and the resistivity change of the films are closely correlated. However, we observed that the optical transition of the samples deposited on c-cut sapphire substrate is less sharp than on r-cut. Our goal here is the improvement of the transition dynamics of the layers by optical means, with the objective to determine the best way for the activation of the transition of thin VO_2(M1) layers. Therefore this study will be also devoted to the investigation of devices based on VO_2(M1) deposited on r-cut sapphire ((012)Al_2O_3). The devices were developed and fabricated in the frame of the DRUIDE project as a collaboration between TE-OX and the C2N. The device fabrication and their optical and electrical measurements will be detailed in this chapter. The main objective of these characterizations is to verify that the technological steps did not damage the transition properties of the material.

5.2.1. Fabrication of VO_2 switches

The RF switches were fabricated using classical fabrication approach, consisting in active material patterning by etching and then the deposition of gold CPW. **Figure 5-2** shows the main fabrication steps for VO_2-switches.

Firstly, the VO_2 film was deposited on r-cut sapphire substrate by RFMS (as described in Chapter 2) with a thickness of 250 nm. Subsequently the photolithography and an etching step were proceeded to fabricate the VO_2 isolated patterns (**Figure 5-2**(c)). Then a second photolithography level was performed for the deposition of the gold coplanar waveguide (CPW) by electron beam evaporation of a Cr/Au (chromium/gold) bilayer of 300 nm, followed by a lift-off process (**Figure 5-2**(e)). The VO_2 microwave switches were fabricated in series and shunt configurations, as shown in **Figure 5-2**(f).

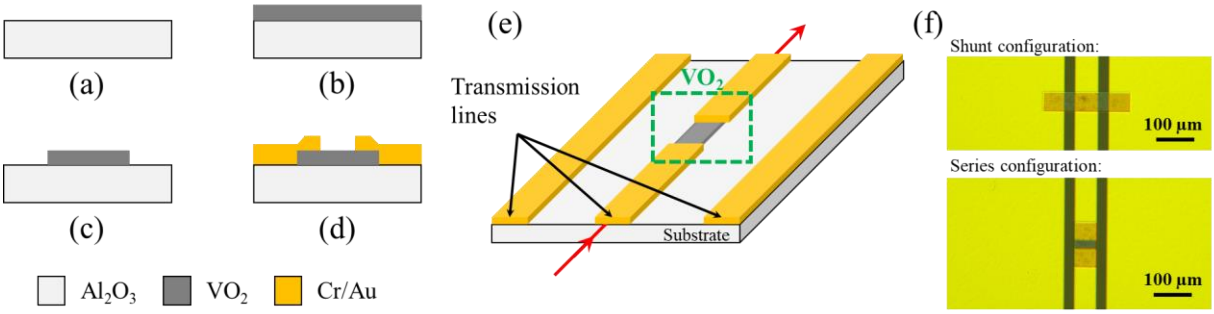

Figure 5-2: Steps of the fabrication process for VO_2 switches. (a) Bare Al_2O_3 substrate; (b) Sputtering deposition of 250 nm VO_2; (c) Patterning of VO_2 by photolithography and etching; (d) Evaporation deposition of 300 nm Cr/Au and patterning of transmission lines by lift-off. (e) Schematic representation of a series switch integrating the VO_2 pattern into the coplanar waveguide. (f) Optical micrograph of fabricated devices in shunt and series configurations.

Scanning Electron Microscopy (SEM) has been used to control transmission lines after the fabrication process. The morphology of the VO_2 pattern was compared to the SEM images of VO_2 film before fabrication. The uniform, close-packed grains do not seem to be affected by the process (**Figure 5-3**). Raman spectroscopy spectra taken along the pattern confirm that these technological steps do not damage the crystalline quality of the VO_2. Such measurements were carried out with a fixed spot at different positions (using a 532 nm laser excitation) on VO_2/(012)Al_2O_3 film and on the VO_2 pad after all fabrication steps. In both cases, the Raman spectra were the same and showed the high quality of the thin layer (**Figure 5-4**).

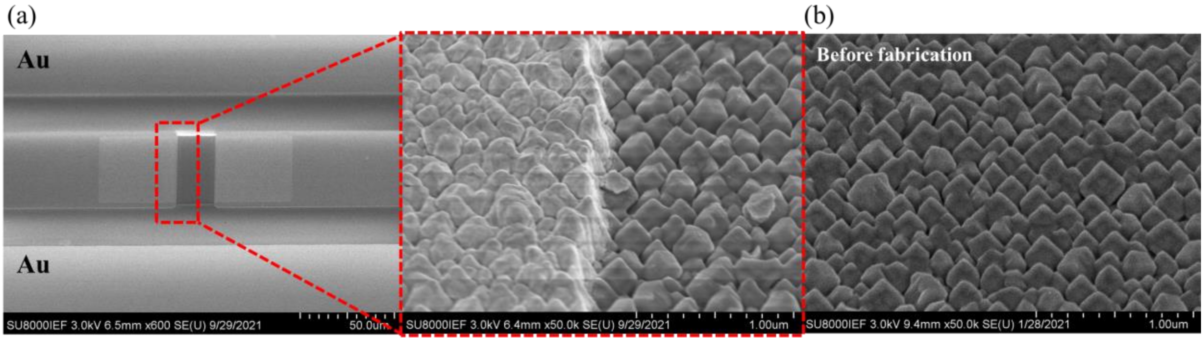

Figure 5-3: SEM images tilted at 45° of (a) a VO_2 switch and (b) a VO_2 film before fabrication process.

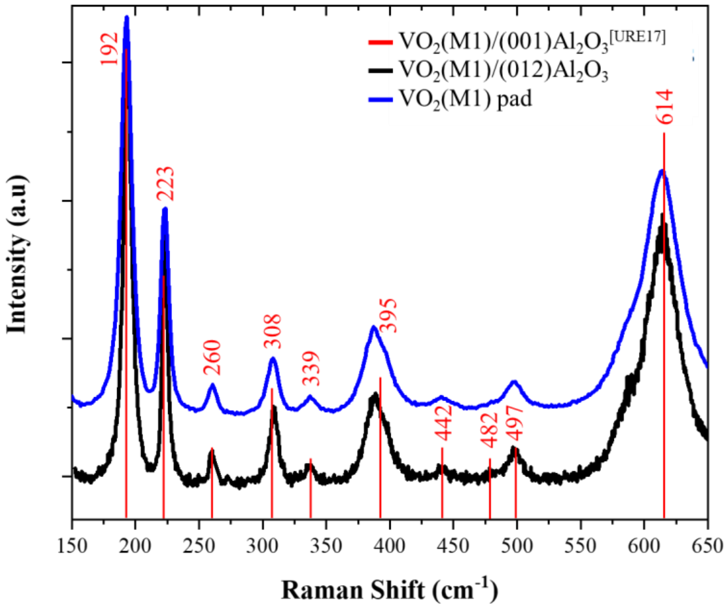

Figure 5-4: Raman spectra of deposited VO_2/(012)Al_2O_3 film before fabrication (black curve) and on the VO_2 pad (blue curve). The measurement was performed using 532 nm laser light with 1% of the power.

5.2.2. Thermally activated switch

In order to assess the performance of the MIT in the fabricated switches, a "home-made" device was developed for thermal actuation of the VO_2 pad. **Figure 5-5** shows the device setup using a VO_2 switch in shunt configuration to simplify the wire bonding of the electrical contacts. The switch was placed on a Peltier module (1MD04-012-08 from TEC microsystems GmbH®). The temperature readings are done by means of a PT100 probe welded next to the switch. Temperature was thus not accurate due to the non-optimal sensor position, but the goal was to follow the transition dynamics to compare them with unprocessed thin films.

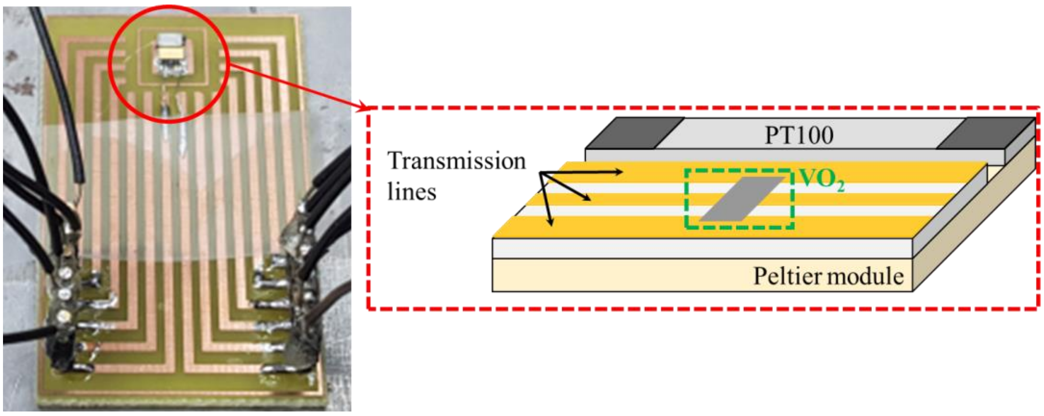

Figure 5-5: Picture of the device for VO_2 resistance (2 points) measurement under thermal activation. The insert shows a switch in shunt configuration placed on a Peltier module for heating. The temperature is monitored using a PT100 probe.

Figure 5-5 shows the resistance measurement of the VO_2 active part of a switch in shunt configuration as compared to VO_2 layers. The processed VO_2 of the switch undergoes the same resistance variation as observed on unprocessed thin layers. The resistance values obtained in both states, insulating and metallic, are close to the values on thin layers with a resistance of 10^5 Ω ($2*10^5$ Ω for the thin layer) in the insulating state at RT and 30 Ω (against about 10 Ω) at 80°C. Both samples were not measured with the same experimental setup, so the temperature scale in particular is not the same.

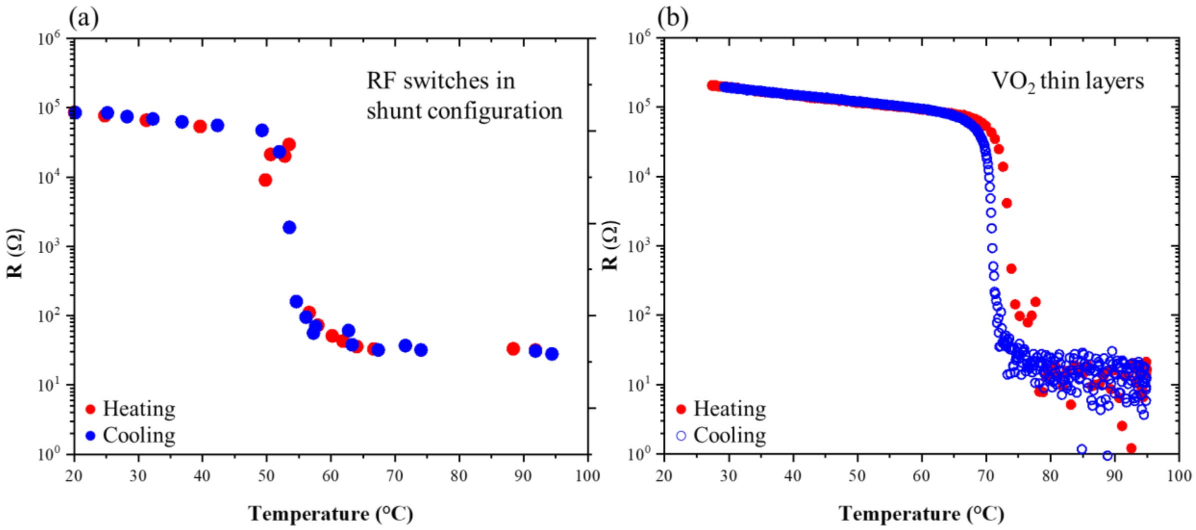

Figure 5-6: Resistance measurements under thermal activation (red = heating, blue = cooling) of (a) a RF switch in shunt configuration (measured in air with 2 probes) and (b) a full VO_2 thin film deposited on r-cut sapphire substrate (measured under vacuum with 4 probes). Note that the temperature scale is not calibrated to VO_2 temperature.

Both samples undergo an abrupt resistance change of around 3-4 orders of magnitude at the transition temperature. The slight difference between these two samples could be explained by the fact that the thin film is not the same as the one used for the fabrication of the device. They might thus not have the same crystalline quality or thickness (slight gradient between the center and the edge of sample). However, the results clearly show that the fabrication steps do not affect the performance and crystal quality of the VO_2.

5.2.3. RF characterization

The device geometry was optimized to get a 50 Ohm impedance matching considering the technology constraints such as the VO_2 and the gold transmission line thicknesses, as well as the gap between the CPW lines, the width of the central signal line, and the permittivity of the substrate. The simulation was carried out using CST (Computer Simulation Technology) software by TE-OX. The results indicate that switches in series configuration have better insertion losses (S_{21}< 1 dB over 60 GHz bandwidth in ON state) compared to the performances of the devices in shunt configuration [ISH19].

RF characterizations were performed using a Keysight (Agilent®) E5071C ENA vector network analyzer, at room temperature (RT) and 80°C, for both series and shunt switches. The measured S_{21} parameters are shown in **Figure 5-7** for one series and one shunt switch, respectively. Appendix 3 summarizes the results for all measured switches, both on c- and r-cut sapphire.

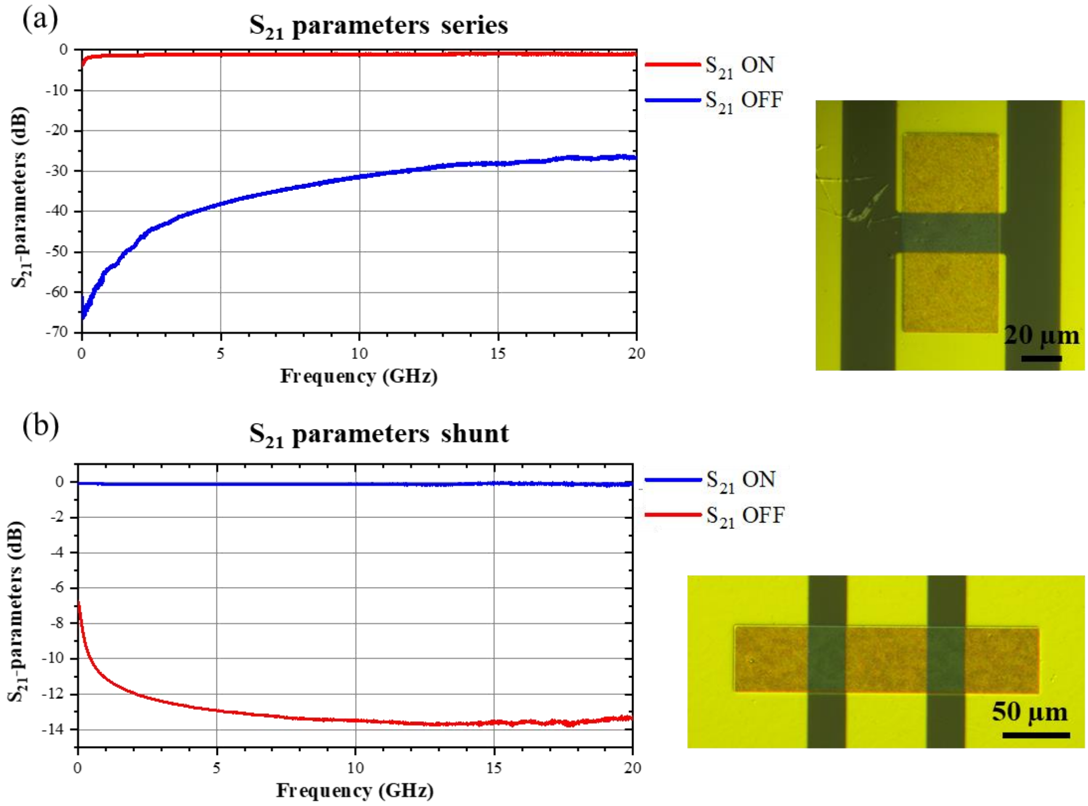

Figure 5-7: S_{21}-parameter measured at RT (in blue) and 80°C (in red) for RF switches in (a) series configuration and (b) shunt configuration. The VO_2 thin film was deposited on r-cut sapphire substrate.

The signal is reflected for the series switch configuration when the VO_2 is insulating (S_{11}~0 dB), and S_{21} parameter exhibits a variation from -60 dB at 1 GHz up to -27 dB at 20 GHz. When the VO_2 is metallic (S_{11}< -10 dB), the S_{21} parameter has a value of -1 dB (**Figure 5-7**(a)). These first results offer promising performance and seem to follow the simulations and the literature. Indeed, the literature on switches in series configuration reports insertion losses of ~ -1 dB and isolation of - 35 dB at 10 GHz [ISH19], whereas the present switch in this work shows insertion losses of ~ -1 dB and isolation of - 31 dB at the same frequency. Interestingly, the shunt switch configuration has much less isolation than the series one. At RT, the VO_2 is insulating, the signal is transmitted in this configuration with insertion losses of -0.1 dB at 10 GHz. When the VO_2 is metallic, the signal is deviated out of the central line, for an isolation S_{21} of around -14 dB at 10 GHz (**Figure 5-7**(b)).

When comparing the insertion losses of the series and shunt configurations, the shunt configuration shows better performances, as S_{21} is around -0.1 dB. However, when comparing the isolation of both switches at 10 GHz, the series configuration shows higher isolation around -31 dB. A comparison with the switches developed on c-cut sapphire is given in Appendix 3 to see if the same behavior was observed, and to assess whether the growth mode of the VO_2 films impacts the RF performance of the switches.

We note that our experimental results for VO_2 switches in both shunt and series configurations follow the characteristics reported in literature (**Table 5-1**). The series switch achieves very high performance in insertion losses and isolation, competitive with other technologies. In this section we demonstrated the feasibility of the VO_2 based RF switches with high performance functional parameters. However, the thermal-heater controlled switching of these structures has too high a response time, in the range of milliseconds with our Peltier module. The next step consists on improving the switching time of the devices by realizing rapid transformation of the VO_2 state. This can be achieved by developing new techniques for optical activation of the RF switches.

Table 5-1: Comparison of VO_2 switches in shunt and series configurations to commercial RF switches in the 0-20 GHz range [REB02][GAT07][KEL05].

	VO_2-series	VO_2-shunt	PIN Diode	FET Transistors	RF MEMS
Insertion loss (dB)	<1	0.05-0.2	<2	0.4-2.5	0.05-0.2
Isolation (dB)	25-65	7-14	30	30	30-40

5.3. Towards ultrafast switches: optical activation of VO_2

Different techniques allow the monitoring and control of the reversible metal-insulator transition of VO_2. As we have seen, thermal control is the most studied and used because of its simplicity of implementation. But it has the disadvantage of a slow VO_2 transition speed, limited by heat transport from the heater to the material: from a few microseconds to a few milliseconds, depending on heater design and proximity to the VO_2 film. In order to develop ultrafast components, with response times at the nanosecond or better, we are looking at how to improve the transition speed. Different methods can be used, such as electrothermal, mechanical, or optical activation (cf. Chapter 1). In this part, we focused on optical control, which is the fastest reported method for VO_2 activation. During optical activation, the laser or LED (light-emitting diode) can induce a local heating of illuminated material. Thus, it is necessary to know the behavior of VO_2 under illumination, and the first part of this section is devoted to this study in the infrared (IR) and ultraviolet (UV) domains. These results will allow us to better understand measurements on RF switches for which the "home-made" device used for the thermal activation of VO_2 was modified to incorporate a LED.

5.3.1. Light absorption by VO_2

The optical activation by laser or LED may induce local heating of the materials (film, substrate, surrounding circuit board). This is especially true in the IR range, as such thermal effects should be reduced if the photons have energy in the UV range. In both cases a main question remains: At what photon flux emitted by the source does the VO_2 transition activate due to light illumination? In the objective to answer this question, optical *n* and *k* indices were first extracted from ellipsometry data (seen Chapter 2) of the VO_2 layer and the sapphire substrate. From **Figure 5-8**, the absorption index

α can be calculated following eq.(5.4), and the power absorbed by the VO_2 ($P_{a(VO2)}$) is then determined according to the Beer-Lambert law given by eq.(5.5).

$$\alpha = \frac{4\pi k}{\lambda} \tag{5.4}$$

$$P_{a(VO2)} = P_i * (1 - R) * [1 - e^{(-\alpha_{VO2(\lambda)} * t)}] \tag{5.5}$$

In eq.(5.4) and eq.(5.5), λ is the wavelength, P_i the incident power, and t the film thickness. R is the reflection index, for an illumination normal to the n_1/n_2 interface $R = \left|\frac{n_1 - n_2}{n_1 + n_2}\right|^2$.

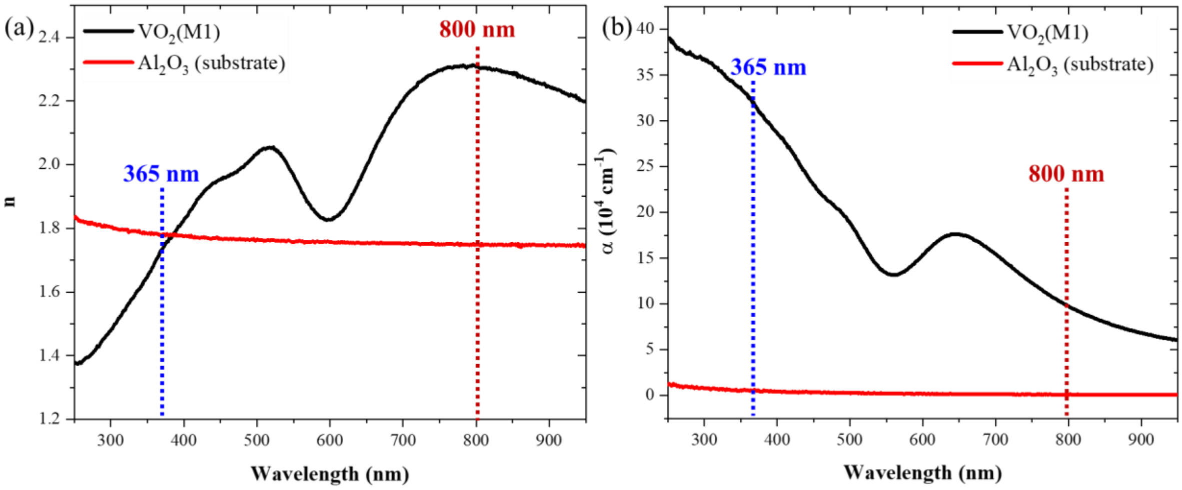

Figure 5-8: Optical properties of VO_2(M1) (in black) and sapphire (in red) as function of the wavelength: (a) n index and (b) absorption factor α.

Two wavelengths have been the subject of specific studies, as we will see below, namely λ=365 nm and λ=800 nm. The optical factors n and α are detailed in **Table 5-2** for the VO_2(M1) phase and the sapphire substrate at these two specific wavelengths.

Table 5-2: Optical properties (n, α) of VO_2 and sapphire substrate using from our work.

Materials	n at 365 nm	n at 800 nm	α (10^4 cm^{-1}) at 365 nm	$\frac{1}{\alpha}$ (nm) at 365 nm	α (10^4 cm^{-1}) at 800 nm	$\frac{1}{\alpha}$ (nm) at 800 nm
VO_2(M1)	1.71	2.30	32.06	31	9.72	100
Al_2O_3	1.78	1.74	0.51	$1.96*10^3$	0.10	10^4

Knowing the optical properties of the VO_2 makes it possible to plot the absorbed power normalized to the incident power. **Figure 5-9** shows the absorption profile for 365 nm and 800 nm according to the penetration depth. Interestingly, at 365 nm all power that is not reflected at the surface (93% of total incident power, with 7% reflected) is absorbed by the VO_2, thus no light reaches the substrate. Unlike at 800 nm, where only about 80% of the power is absorbed by the active layer, while the substrate is transparent to IR light. Consequently, at this wavelength, reflections at the film/substrate interface and heating of other elements of the structure will play a part in VO_2 heating.

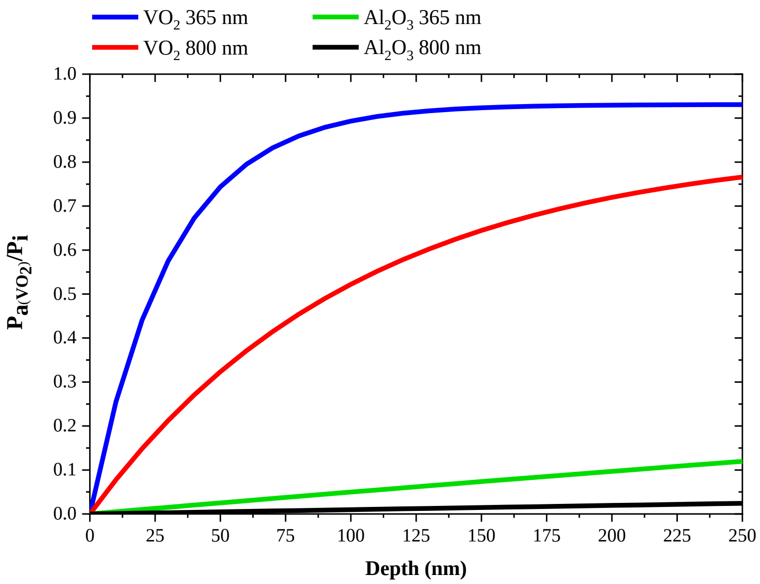

Figure 5-9: Absorbed power ratio with respect to incident one, at 365 nm and 800 nm for the VO_2 and Al_2O_3 as function of the thickness. The reflections at air/VO_2 and VO_2/Al_2O_3 are taken into account.

The temperature increase has been calculated by E. Abraham *et al.* [ABR87] through solving the heat equation for a semi-infinite film, taking into account the incident energy flux (light power) and the dissipation through the substrate. Given a semi-infinite film (infinite in *xy* plane) with a much lower thickness (*t*, in *z* direction) than the spot size (*w*, with $t << w$), the absorbed power by the film can either be dissipated laterally (out of the light spot) or towards the substrate. However, if we suppose that the substrate has a thermal conductivity (K_s) sufficient to dissipate the heat flux, for a thin film the lateral flux becomes negligible ($K_f * t << K_s * w$, with K_f the film thermal conductivity). Then, only the heat flux through the substrate is considered to dissipate the energy absorbed by VO_2. With these approximations, the solution to the heat equation can be written in a simple form, and the maximum temperature rise (ΔT) of the film at the center of the light spot can be calculated following eq.(5.6).

$$\Delta \mathrm{T} = \frac{\mathrm{P_{a(VO2)}}}{2\sqrt{\pi} * \mathrm{K_s} * \mathrm{w}} \tag{5.6}$$

Where K_s is the thermal conductivity of the sapphire substrate at 25°C (42 W/m.K) and *w* is the radius of the LED or laser spot.

From eq.(5.6), we expect that for a given absorbed power, the smaller is the spot size, the higher is the temperature rise. Considering the spot sizes and wavelengths that we experimentally tested for the activation of VO_2 as detailed in the next part, the temperature rise can be estimated for each case from eq.(5.6). The calculated values as summarized in **Table 5-3** show that to get a temperature rise up to 75°C, the spot size must be focused at 50 µm. Above this, the energy provided by the light source is theoretically insufficient to activate the transition of the VO_2 thermally. Moreover, in our optical tests, the VO_2 is not in film form but patterned into a pad for RF switch. Consequently, the same calculations were realized for a VO_2 pad, and the same conclusions were made.

Table 5-3: Temperature rise in VO_2 thin film and VO_2 pad of a RF switch, calculated for a UV source and 300mW incident power. The 50x60 µm^2 footprint of the pad is taken into account with respect to the light spot.

S_{VO2} (cm^2)	λ (nm)	Light spot diameter (2*w*)	ΔT (°C)
Semi-infinite VO_2 film	365	1 cm	0.4
		100 µm	38
		50 µm	75
VO_2 pad	365	1 cm	0
		100 µm	14
		50 µm	75

5.3.2. VO_2 switches by UV diode illumination

The “home-made” device developed previously to control thermal activation of the switch has evolved to test optical activation. To do that, a Thorlabs® M365L2 diode with nominal wavelength of 365 nm was placed as close as possible to the VO_2 switch, without any focusing system (**Figure 5-10**(a and b)). At d=1 cm, the spot diameter of the diode was estimated at 2*w*=1.4 cm. The incident power P_i as function of the current delivered to the diode is presented on **Figure 5-10**(c).

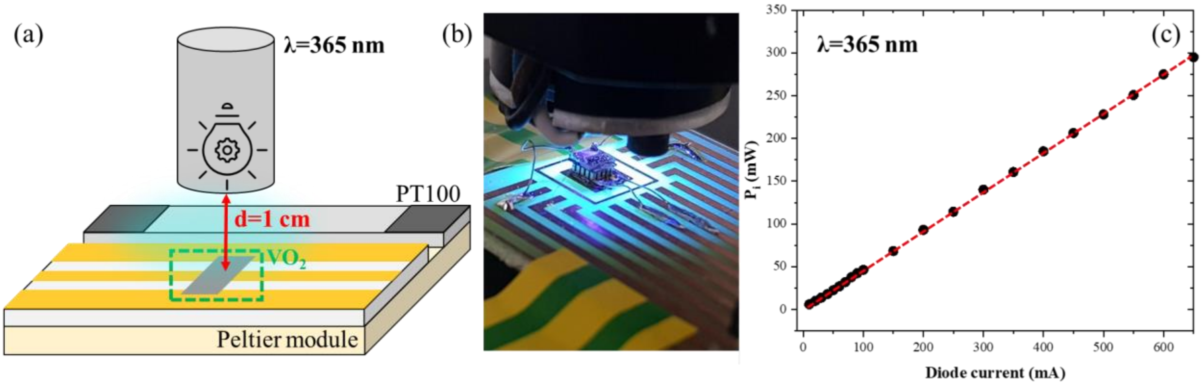

Figure 5-10: (a) Scheme and (b) picture of the device allowing resistance (2 points) measurement under optical activation. (c) Incident power measured in function of the current delivered to the UV diode.

The first measurement to characterize the VO_2 switch is a simple resistance (R) measurement under illumination. The device temperature was monitored by a PT100 probe positioned next to the switch. The illumination was done continuously, and the resistance and temperature values were taken after 2 min 30 sec illumination (resistance stabilization). Between each measurement, the diode was turned off in order for the device to cool down back to RT, thus avoiding a possible accumulation effect on the temperature rise. At variance with the theoretical calculations, from which we expected zero effect on device temperature for unfocused light, the results presented in **Figure 5-11** clearly show that the increase of the diode power heats the device and lowers its resistance. The change in resistance is found proportional to the increase in temperature, and no phase transition was observed during these measurements.

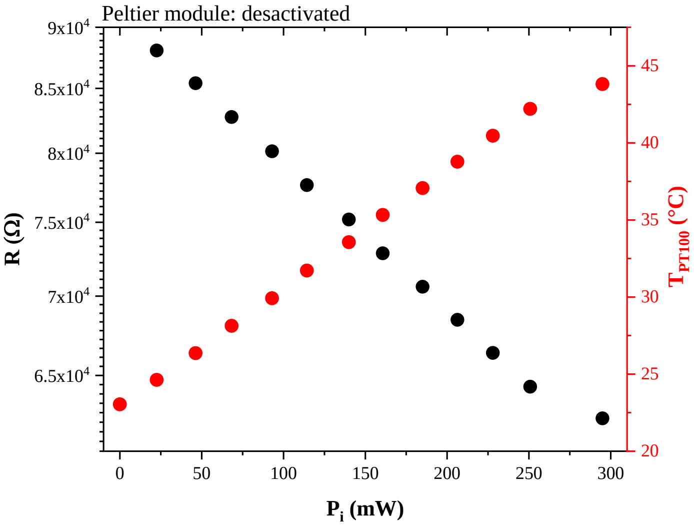

Figure 5-11: Evolution of resistance (*R*) and temperature (T_{PT100}) measured for a VO_2 switch as function of the incident power at λ=365 nm.

The objective is now to determine if it is possible to actuate the VO_2 under optical illumination with our unfocused UV diode. To do this, the diode power was maintained at P_i~300 mW, and the switch resistance was monitored during 15 min (≡900 sec) (**Figure 5-12**). Without the Peltier module, we observed a slow resistance change with a temperature increase from 25°C to 45°C. After 150s, the temperature and the resistance remain stable with no sign of phase transition, even after 900s of illumination. Given these slow dynamics, we assume that heat dissipated by the diode device itself is responsible for the heating of the VO_2, and not illumination-induced heating as calculated previously. To facilitate the transition, the Peltier module was set at around 45°C, and the diode power was also maintained at P_i~300 mW as shown on **Figure 5-12**(b). An abrupt change in resistance was observed about 20s after switching on the diode, while the measured temperature slowly increased up to 65°C.

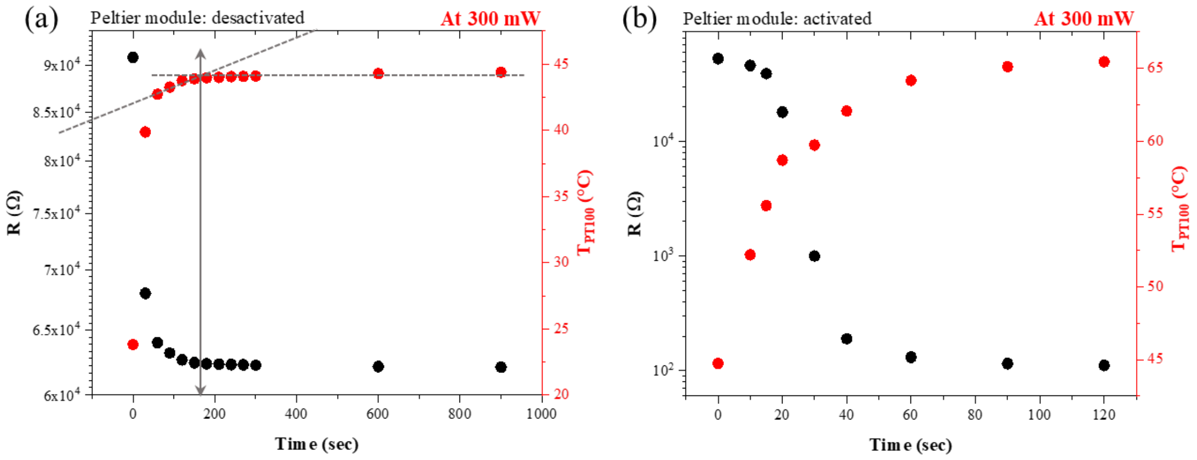

Figure 5-12: Evolution with time of resistance and temperature for VO_2 switch illuminated by 300 mW of unfocused UV light (a) without Peltier module and (b) with Peltier module activated. The diode is switched on at t=0.

We have previously estimated that direct heating induced by the diode illumination was negligible (around 0°C for a light spot diameter ~1 cm). According to our calculation (eq.(5.6)), at this diode power, a spot size 2*w* of 50 µm would be necessary to elevate the VO_2 pad temperature by 75°C.

Consequently, considering the experimental spot size of 2*w*=1.4 cm, the 20°C increase measured by the PT100 probe is probably not from the UV illumination-induced heating but by some form of indirect heating, due for example to the diode itself, in close proximity to the sample. The pulsed mode of the diode was also tested, unfortunately, the conclusions are the same. The diode already has a radiator to evacuate the generated heat, so improvement on this part is not trivial, apart from the displacement of the source away from the switch. By increasing the distance *d*, the spot size will also increase. Therefore, a focusing system is necessary to reduce the spot size and, consequently, to increase the power density on the VO_2 pad. The power density can also be increased by working with ultrashort laser pulses, and detecting the VO_2 transition with a pump-probe measurement, as presented in the following part.

5.3.3. Transition dynamics of VO_2 during an ultrafast photoexcitation

The photoexcitation using ultrafast laser pulses has demonstrated that it provides another route to initiate the transition between the insulating and the metallic phases of VO_2. This MIT can occur very rapidly following femtosecond laser excitation if a sufficient fluence (deposited energy per unit area) is used [OTT19]. In details, it was reported [WEG15] that when VO_2 is in its low-temperature phase (monoclinic and insulating), the photoexcitation above a critical fluence changes the electronic state population. The Coulomb interactions are altered, resulting in the collapsing of the insulating band gap: The energy gap is reduced until the bottom of the π^* band and the top of the $d_{//}$ sub-band touch the Fermi level and make VO_2 metallic, for a first non-thermal transition at the femtosecond scale (**Figure 5-13**).

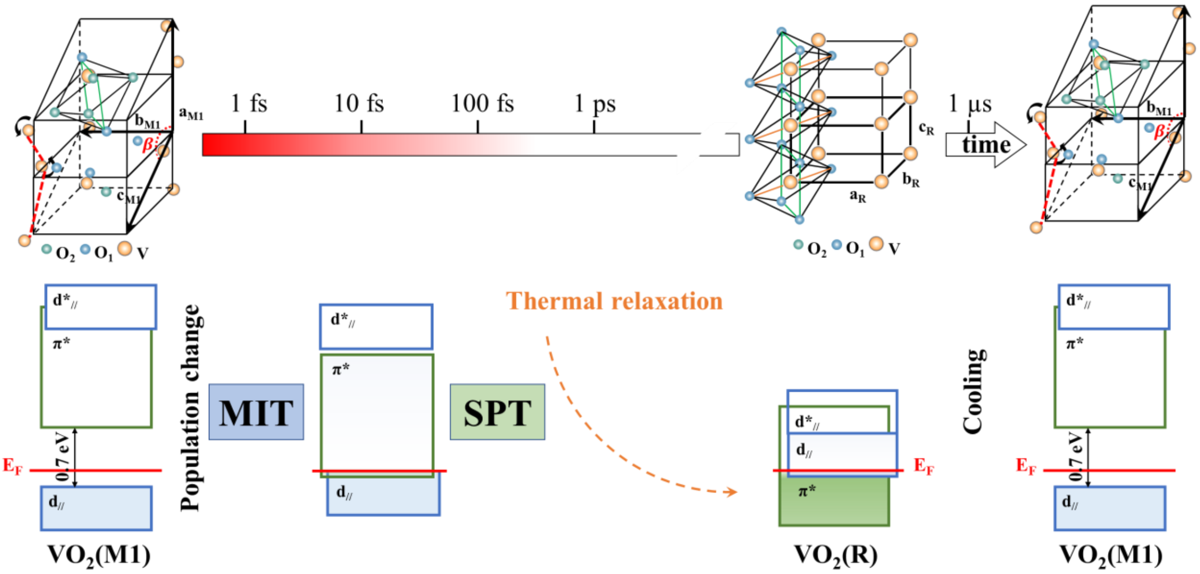

Figure 5-13: Representation of the photoinduced phase transitions of the monoclinic insulating VO_2. From left to right, with indicative timescale at the top: The light-induced electronic population change modifies the Coulomb interaction, leading to the collapse of the electronic band gap. An insulator-to-metal transition (MIT) appears and the VO_2 is in a monoclinic metallic phase (mM). Simultaneously, the depopulation of the VB modifies the charge distribution and the resulting ionic motions lead to a structural phase transition (SPT). The system evolves towards the $VO_2(R)$ rutile phase, before it relaxes back to the $VO_2(M1)$ upon cooling. Inspired from Wegkamp work [WEG15].

At the same time, the depopulation of the top valence-band states leads to charge distribution changes that modify the forces acting on the ions. Consequently, multiple ionic motions occur and trigger a structural phase transition (SPT). The pairing of V-dimers [MOR14] occurs concurrently with the relaxation of excited electrons and holes in the metallic band structure [WEG14], which is accompanied by energy transfer to the lattice. Thus, the system evolves thermally to its high-temperature phase (rutile and metallic), then relaxes back to the VO_2(M1) upon cooling after the laser pulse. **Figure 5-13** summarizes the transition steps occurring during the photoexcitation of the sample.

This section aims to determine the critical fluence required for an ultrafast VO_2 transition. To do that, pump-probe experiments were realized thanks to a 800 nm-wavelength femtosecond laser for the pump, frequency-doubled to 400 nm for the probe. The change in reflectivity ΔR of photoexcited VO_2, normalized to the reflectivity R in the unexcited state was measured. For these experiments, the laser was focused to a spot size of a few dozen micrometers in diameter to maximize the energy deposited (fluence) on the sample. **Figure 5-14**(a) shows the reflectivity change of VO_2 measured for three incident power (P_i) ranges: low (LP < 1.5 mW), medium (1.5 < MP < 3.5 mW), and high (3.5 < HP < 6 mW).

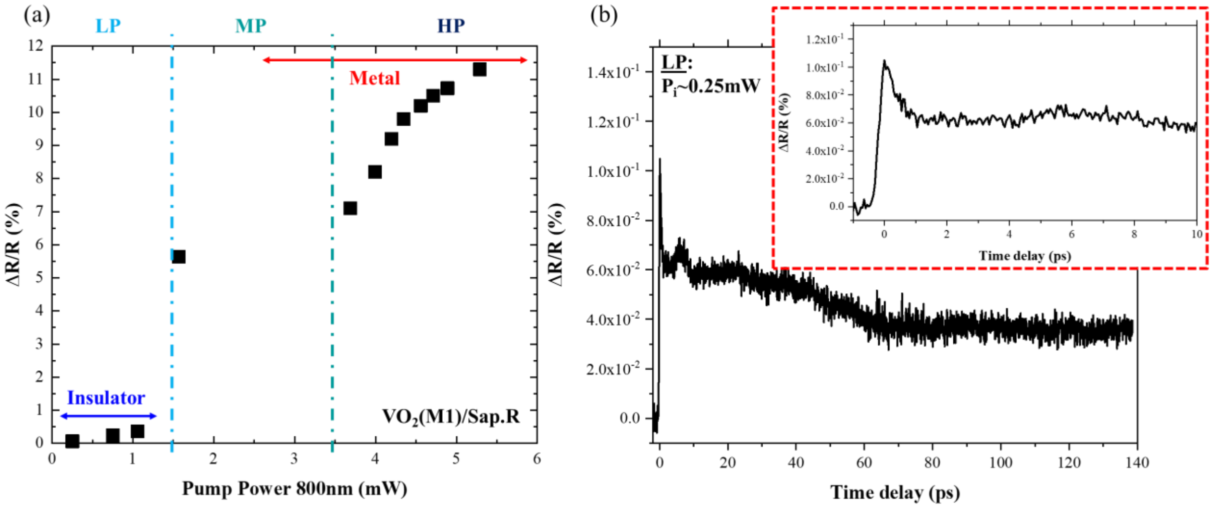

Figure 5-14: (a) Evolution of reflectivity ratio of VO_2 thin film deposited on r-cut sapphire as a function of pump power (P_i) at 800 nm. (b) Time evolution of reflectivity change at low power (P_i~0.25 mW), at 100 ps (bottom) and 10 ps (top) timescales.

i. At low power (e.g., P_i ~0.25 mW), no phase transition was observed as shown on **Figure 5-14(**b). The reflectivity drops after 1 ps indicating a recombination of the photoexcited charge carriers [BRA18]. The persistent reflectivity change (~$4*10^{-2}$ %) could be attributed to photo-induced effects that vanish with time. Since the experiments use a femtosecond pulse which is more energetic than the VO_2 band gap ($1.55\text{ eV} > E_g(VO_2) \approx 0.7\text{ eV}$), the major effect is related to photoexcited carriers that increase the layer reflectivity.

ii. When the power increases (P_i >1.5 mW), the phase transition into the metallic state appears, and this is faster as the power is higher (Figure 5-15).

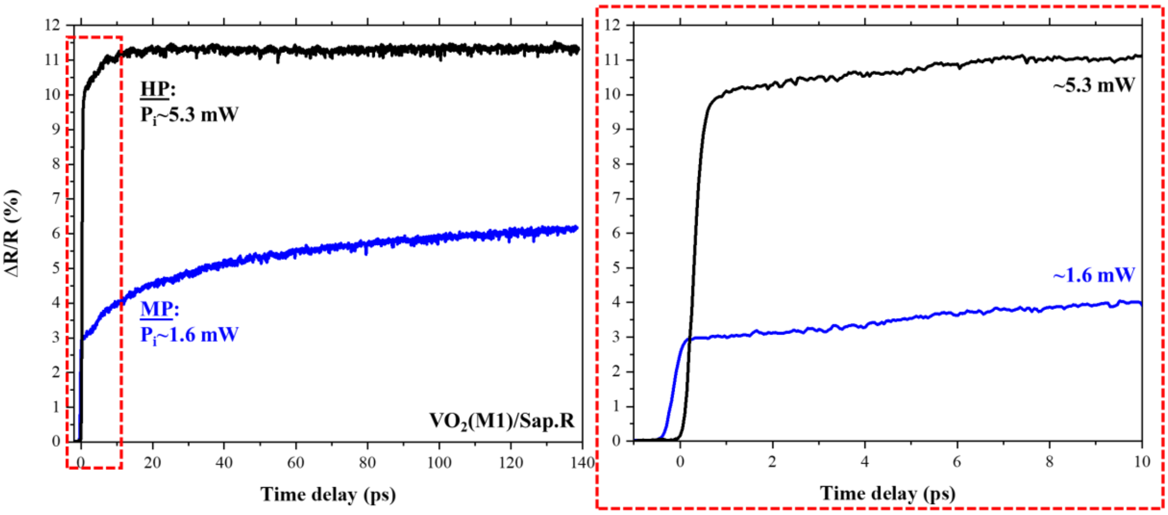

Figure 5-15: Time evolution of reflectivity change at medium (blue curve) and high (black curve) powers, at 100 ps (left) and 10 ps (right) timescales.

iii. At high power, e.g. P_i~5.3 mW (**Figure 5-15**) the photoexcited VO_2 exhibits a metallic-type optical response already in less than 1 ps, and its reflectivity ratio saturates after about 10 ps. Since no further reflectivity ratio change was observed, contrary to the P_i~1.6 mW case for which ΔR/R does not reach saturation even after 140 ps, we can suppose that the VO_2 phase transition is completed in 10 ps at this high power [ROA71].

We first consider direct heating by laser light, through energy transfer from photogenerated electron-hole pairs to lattice vibrations (phonons), to interpret the observed phase change. The excess energy of the photogenerated carriers can be estimated from incident photon energy E_λ and bandgap $E_{g(VO2)}$, and supposing that all this energy is converted to heat, an upper limit for the resulting temperature rise (ΔT) is given by eq.(5.7).

$$\Delta T = \frac{F_{a(VO2)}(E_\lambda - E_{g(VO2)})}{C_p * \rho * t * E_\lambda} \tag{5.7}$$

Where $F_{a(VO2)}$ is the absorbed fluence by VO_2 ($F_{a(VO2)} = E_{pulse}/w^2$ with E_{pulse} pulse energy), C_p its specific heat capacity ($C_p(VO_2)$= 0.8 J/g/K [CHA73]), ρ its density ($\rho(VO_2)$= 4.66 g/cm^3), and t the film thickness. Based on this model, the temperature rise of the VO_2 is estimated for one IR pulse. **Table 5-4** summarizes the results for the three studied laser powers.

Table 5-4: Temperature rise in VO_2 thin film with IR photoexcitation source.

Laser spot size (µm²)	λ (nm)	P_i (mW)	ΔT (°C)
$\pi * 50^2$	800	0.25	14
		1.6	92
		5.3	305

Referring to **Table 5-4** and our experimental results, we can conclude that the pump IR laser is indeed able to trigger the ultrafast transition of our VO_2 sample, and that laser-induced thermal heating can account for the necessary temperature rise. We note that we did not consider the progressive heating of the VO_2 subjected to laser pulses at 1 kHz, which probably gives a stationary increase of sample temperature. Regarding the other photoinduced effects in VO_2 (**Figure 5-13**), we can assume that the higher is the photogenerated electron density, which for 100% quantum efficiency is equal to the photon density n_{ph} given by eq.(5.8), the higher are the ionic motions, and the faster is the transition.

$$n_{ph} = \frac{F_{a(VO2)}}{E_{\lambda}} \tag{5.8}$$

At P_i~1.6 mW ($F_{a(VO2)}$ ~3.9 mJ/cm²), the absorbed photon density is n_{ph}~ $1.6*10^{16}$ photon/cm², whereas at P_i~5.3 mW ($F_{a(VO2)}$ ~13.0 mJ/cm²), n_{ph}~ $5.2*10^{16}$ photon/cm². The VO_2 layer absorption of a lower photon density might lead to smaller ionic motions and, therefore, to a slower transition. This hypothesis could explain the gradual enhancement of reflectivity observed at 1.6 mW during 140 ps.

5.4. Conclusion and discussion

In this chapter, we presented our investigation of VO_2 RF devices with thermal and optical activation. We started our study by demonstrating that technological steps of VO_2-based RF switch fabrication did not damage the structural and electrical properties of the material, including phase change under thermal stimulus. Subsequently, RF performances of the switches have been measured and the results obtained are close to commercially available devices such as MEMS or PIN diodes. However, the VO_2-based thermally controlled switches presented a low switching speed from milliseconds to a few seconds. In order to improve the transition speed, we started exploring the optical activation, whose results observed in the literature (cf. Chapter 1) seem promising. Our first tests of optical activation with a UV diode were rather unsuccessful. The heat convection produced by the diode device itself induced a temperature rise of the sample, allowing for a partial VO_2 transition to occur. To limit the heat emitted by the diode and succeed in ultrafast transition, it will be necessary to move the source away from the switch and to focus the light on the VO_2 pattern. Therefore, we turned to pump-probe measurements in order to assess the ultrafast transition performance of our films. Due to thesis time constraint, only measurements at 800 nm were performed. However, the first results are promising and show that it is possible to make our VO_2 films transit in less than 10 ps.

Although this study highlighted the capacity of VO_2 to transit at ultrafast speed, many questions concerning the transition mechanism remain. We know from the state-of-the-art (cf. Chapter 1) that the phase transition may occur in several steps where the Mott and Peierls mechanisms operate simultaneously. Depending on the activation mode, we think that the mechanism initiating the transition can change (Mott driving Peierls or Peierls driving Mott). A strong pressure, e.g., can lead to dimerization of the V-V bonds (structural transition = Peierls). The dimers, which were initially in zig-zag are realigned, leading to a modification of the electronic structure (band structure modification = Mott) [MAR10]. In the case of optical activation, it is the opposite. The charge distribution is disturbed by the valence band depopulation, causing the activation of ionic motions in the structure and then leads to the alignment of the dimers. In the case of thermal activation by laser heating, the ionic movement activates slowler (~10 ps) than in optical activation through direct electronic excitation (<1 ps) [WEG15]. In order to discriminate between these transition mechanisms, combined structural and laser pump-probe measurements are needed with time resolution in the sub-picosecond range.

Conclusion and perspectives

The continuously growing demand on the communication systems is pushing the radiofrequency (RF) industry to find new solutions to improve device performance, especially through the Internet of Things (IoT) development. TE-OX® company has focused its RF activity on the development of RF devices based on vanadium dioxide (VO_2), which has demonstrated promising behavior for the manufacture of ultrafast and reliable components. The development of such systems is challenging, because the device performances rely not only on its architecture but also on the material quality, which should be as close as possible to the single crystal. An additional obstacle on the way to this development is the complexity of VO_2 phase diagram that presents multiple oxides with various vanadium oxidation states, making this material highly sensitive to the growth conditions. Moreover, in the case of stoichiometric VO_2, the numerous polymorphic phases impede the achievement of high-quality, single-crystalline VO_2(M1) thin films. The expertise acquired previously at TE-OX on the VO_2 polymorphs revealed promising potential applications based not only on the most common VO_2(M1) phase but also on metastable VO_2(B) phase. For this reason, the understanding and control of the VO_2 polymorphs stand as very challenging objectives of this work.

Radiofrequency magnetron sputtering (RFMS) was selected as an industrially scalable deposition technique, allowing the growth of thin films on large surfaces without the use of toxic gas or source compound. A precise control on the vanadium oxidation state was revealed to be a very important factor which relies on multiple growth parameters such as the oxygen flow, the RF power, and the substrate temperature during the deposition but also on the substrate-induced epitaxial stress. Thus, the goal of this work was to correlate the effects of all these factors to get better understanding of the mechanisms leading to the stabilization of the VO_2(M1) and VO_2(B) polymorphs.

During this work, first, the growth parameters of high-quality VO_2(M1) thin films on c-cut and r-cut sapphire (Al_2O_3) substrates were optimized. The resistivity measurements under thermal activation showed a sharp metal to insulator transition (MIT), with a resistivity ratio greater than four orders of magnitude and a narrow hysteresis cycle of less than 1°C width, highlighting excellent VO_2(M1) quality. The detailed structural analyses carried out by X-ray diffraction (XRD) revealed that the growth mode can be altered by the substrate crystalline orientation, due to different epitaxial stresses and symmetries. Twelve different in-plane crystallographic orientation variants of VO_2(M1) were evidenced for c-cut sapphire, against only two for r-cut sapphire. The morphology with 12 growth variants has crystalline grains of multiple in-plane orientations and a higher film roughness, which are found to hinder the structural and optical transition performances. Indeed, when a thermal stimulus is applied, the phase transition might be more inhomogeneous due to the orientation mismatches between grains, the grain boundaries, and the existence of other defects that affect the transition dynamics. Additionally, the growth study revealed that the films exhibit substrate-induced strains, leading to a reduction of the transition temperature. The films developed by RFMS on c-cut and r-cut sapphire present a compressive strain along the $\vec{c}_{VO2(R)}$-axis (or $\vec{a}_{VO2(M1)}$-axis). According to literature, this deformation impacts the band structure of VO_2 and leads to a narrowing of the energy gap between the conduction and valence bands. Thus, the MIT becomes easier and the transition temperature is lowered, as we experimentally observed in the present study.

In the continuity of the investigation of the formation and stabilization mechanisms of VO_2 polymorphic phases, the growth was also performed on the $SrTiO_3$ (STO) perovskite substrate. We evidenced that for strictly identical deposition conditions, STO and sapphire substrates stabilize different polymorphic phases of VO_2: An epitaxial VO_2(B) phase grows on (001)-oriented STO, whereas the M1 phase is obtained on c-cut sapphire. Furthermore, structural analyses showed that the lattice mismatch between VO_2(B) and STO leads to epitaxially strained layers. This strain is certainly involved in the stabilization of the VO_2(B) metastable phase and its slower reoxidation rate in thin films compared to nanopowders. With the support of X-ray photoelectron spectroscopy (XPS) measurements, we confirmed that in VO_2(B) the vanadium has a higher oxidation state than in VO_2(M1). There might thus be an interplay between epitaxial strain, oxidation state of precursors on the substrate, and plasma composition, but further investigations are needed to separate these different contributions to drive the stabilization and morphology of the VO_2(B) phase.

We were also interested in the thickness-dependence of VO_2(B) phase stability, as previous reports mentioned the formation of the VO_2(M1) phase beyond some critical thickness. Therefore, detailed structural characterizations were carried out on films with thicknesses of 160 nm and 230 nm. The XRD data only showed the (001)-oriented VO_2(B) phase aligned with the (001)STO surface plane, while Raman spectroscopy revealed the simultaneous presence of B and M1 phases in both samples. Scanning transverse electron microscopy (STEM) cross-section images of the 160 nm-thick sample confirmed the coexistence of both phases within the film, with a M1 phase tilted by 26° with respect to the (001) substrate plane, and (001)VO_2(B) planes parallel to the latter in agreement with XRD data. Surprisingly, the STEM cross sections also revealed that the M1 phase is in contact with the STO substrate and grows laterally with respect to the B phase, so that in some (restricted) areas of the film only VO_2(M1) phase remains. To get deeper insights on this growth mode, further structural characterizations should be performed on films with different thicknesses. Nevertheless, this thesis evidenced the importance of the substrate-induced strain as a key mechanism in the formation and stabilization of VO_2 polymorphic phases in thin films.

Following the first goal of this work, the high-quality VO_2(M1) thin films, with sharp resistivity change at the transition temperature and hysteresis width smaller than 1°C, were used for the fabrication of RF-switch demonstrators. The excellent RF performances of our VO_2 switches were confirmed by the characterization of their insertion losses (< -1 dB at 10 GHz) and isolation (> -30 dB at 10 GHz) in the 1-20 GHz frequency range which are competitive with existing technologies on the market. The major bottleneck that currently limits expansion of this technology is the low attained switching speed (from milliseconds to a few seconds) due to the thermal activation. To improve this parameter, we have started to explore the optical activation. Our first tests showed that an unfocused diode is insufficient to activate the VO_2 transition from its insulating to the metallic state. Then, exploratory pump-probe measurements were carried out at a wavelength of 800 nm, showing that the transition of VO_2 can be completed within 10 ps. The technological optimization of the optical activation is still ongoing to integrate a focused light source in RF switches and pave the way to a new generation of ultrafast electronic or RF devices.

References

[ABR12] E. Abreu, M. Liu, J. Lu, K.G. West, S. Kittiwatanakul, W. Yin, S.A. Wolf and R.D. Averitt, "VO_2 nanosheets: controlling the THz properties through strain engineering", *New Journal of Physics*, vol. 14, 2012.

[ABR87] E. Abraham and J.M. Halley, "Some calculations of temperature profiles in thin films with laser heating", *App. Phys. A Solids and Surfaces*, vol. 42, 279–285, 1987.

[AET13] N.B. Aetukuri, A.X. Gray, M. Drouard, M. Cossale, L. Gao, A.H. Reid, R. Kukreja, H. Ohldag, C.A. Jenkins, E. Arenholz, K.P. Roche, H.A. Dürr, M.G. Samant and S.S.P. Parkin, " Control of the metal-insulator transition in vanadium dioxide by modifying orbital occupancy", *Nature Physics*, vol. 9, 661–666, 2013.

[ALI06] R.A. Aliev, V.N. Andreev, V.M. Kapralova, V.A. Klimov, A.I. Sobolev and E.B. Shadrin, "Effect of grain sizes on the metal-semiconductor phase transition in vanadium dioxide polycrystalline thin films", *Physics of the Solid State*, vol. 48, 929–934, 2006.

[ARY98] F. Aryasetiawan and O. Gunnarsson, "The GW method", *Rep. Prog. Phys.*, vol. 61, 237–312, 1998.

[ASP14] D. Aspnes, "Drude Dispersion Model", *Horiba Jobin Yvon-Technical Note*, 3–4, 2014.

[BEA16] E. Beaucé, "Transition de phases et phénomènes critiques dans une grille de booléens: Théorie de la percolation", 2016.

[BER03] F. Bernoux, J.-P. Piel, B. Castellon, C. Defranoux, J.-H. Lecat, P. Boher and J.-L. Stehlé, "Ellipsométrie - Théorie", *Techniques de l'ingénieur*, vol. 33, 2003.

[BER16] J.F. Bérar, G. Calvarin and D. Weigel, "Un goniomètre original très précis pour la diffraction des rayons X sur poudre à température controlée", *J. Appl. Cryst.*, vol. 13, 201–206, 1980.

[BER98] Ö. Bergström, T. Gustafsson and J.O. Thomas, "Lithium insertion into V_6O_{13} studied by deformation electron density refinement of single-crystal X-ray data", *Solid State Ionics*, vol. 110, 179–186, 1998.

[BOU10] D. Bouyge, A. Crunteanu, O. Massagué, J.C. Orlianges, C. Champeaux, A. Catherinot, A. Velez, J. Bonache, F. Martin and P. Blondy, "Applications of vanadium dioxide (VO_2)-loaded electrically small resonators in the design of tunable filters", *Proceedings of the 40th European Microwave Conference*, 822–825, 2010.

[BRA17] M. Brahlek, L. Zhang, J. Lapano, H.T. Zhang, R. Engel-Herbert, N. Shukla, S. Datta, H. Paik and D.G. Schlom, "Opportunities in vanadium-based strongly correlated electron systems", *MRS Communications*, vol. 7, 27–52, 2017.

[BRA18] J.M. Braun, H. Schneider, M. Helm, R. Mirek, L.A. Boatner, R.E. Marvel, R.F. Haglund and A. Pashkin, "Ultrafast response of photoexcited carriers in VO_2 at high-pressure", *New Journal of Physics*, vol. 20, 2018.

[BRI18] B. Brière, "Propriétés optiques de matériaux à fortes corrélations électroniques en conditions extrêmes", Université de Tours, 2018.

[BRU01] V.I.E. Bruyère, L.A. Garcia Rodenas, P.J. Morando and M.A. Blesa, "Reduction of vanadium(V) by oxalic acid in aqueous acid solutions", *J. Chem. Soc., Dalton Trans.*, 3593–3597, 2001

[BUR69] L.A. Bursill and B.G. Hyde, "*Crystallographic shear in the higher titanium oxides: structure, texture, mechanisms and thermodynamics*", 1969.

[BUT18] N.A. Butakov, I. Valmianski, T. Lewi, C. Urban, Z. Ren, A.A. Mikhailovsky, S.D. Wilson, I.K. Schuller and J.A. Schuller, "Switchable Plasmonic-Dielectric Resonators with Metal-Insulator Transitions", *ACS Photonics*, vol. 5, 371–377, 2018.

[CAV01] A. Cavalleri, C. Tóth, C.W. Siders, J.A. Squier, F. Ráksi, P. Forget and J.C. Kieffer, "Femtosecond structural dynamics in VO_2 during an ultrafast solid-solid phase transition", *Physical Review Letters*, vol. 87, 237401-1-237401–4, 2001.

[CEL95] C. Celzard, "Contribution à l'étude du phénomène de percolation dans des matériaux composites à propriétés anisotropes", Université de Nancy I, 1995.

[CHA03] D. Chateigner, "Diffraction des rayons X sur échantillons polycristallins", *J. Appl. Crystallography*, vol. 36, 369, 2003

[CHA73] C.V. Chandrashekhar, H.L.C. Barros and J.M. Honig, "*Heat capacity of VO_2 single crystals*", Mat. Res. Bull., vol. 8, 369-374, 1973.

[CHE14] A. Chen, Z. Bi, W. Zhang, J. Jian, Q. Jia and H. Wang, "Textured metastable VO_2(B) thin films on $SrTiO_3$ substrates with significantly enhanced conductivity", *Appl. Phys. Lett.*, vol. 104, 071909-1-071909-4, 2014.

[CHE17] Y. Chen, S. Zhang, F. Ke, C. Ko, S. Lee, K. Liu, B. Chen, J.W. Ager, R. Jeanloz, V. Eyert and J. Wu, "Pressure-Temperature Phase Diagram of Vanadium Dioxide", *Nano Letters*, vol. 17, 2512-2516, 2017.

[CHE96] Y. Chen and J. Washburn, "Structural transition in large-lattice-mismatch heteroepitaxy", *Phys. Rev. Lett.*, vol. 77, 4046–4049, 1996.

[CHR02] K. Christensen, "Percolation theory", 2002.

[COM07] Complete Ease, Software Manual Version 3.18, JA Woollam Co, 2007.

[COS03] S. Coste, "Evolutions structurale et microstructurale de précurseurs d'oxyde de tellure élaborés par voie sol-gel", Université de Limoges, 2003.

[CRU10] A. Crunteanu, J. Givernaud, J. Leroy, D. Mardivirin, C. Champeaux, J.C. Orlianges, A. Catherinot and P. Blondy, "Voltage- and current-activated metal-insulator transition in VO_2-based electrical switches: a lifetime operation analysis", *Science and Technology of Advanced Materials*, vol. 11, 2010.

[CUI18] Y. Cui, Y. Ke, C. Liu, Z. Chen, N. Wang, L. Zhang and Y. Zhou, "Thermochromic VO_2 for Energy-Efficient Smart Windows", *CePress Reviews*, 1707–1746, 2018.

[DEL21] A. D'Elia, C. Grazioli, A. Cossaro, B.W. Li, C.W. Zou, S.J. Rezvani, N. Pinto, A. Marcelli and M. Coreno, "Strain mediated Filling Control nature of the Metal-Insulator Transition of VO_2 and electron correlation effects in nanostructured films", *Applied Surface Science*, vol. 540, 32–35, 2021.

[DEM00] M. Demeter, M. Neumann and W. Reichelt, "Mixed-valence vanadium oxides studied by XPS", *Surface Science*, 454-456, 2000.

[DIN16] H. Ding, S.S. Dwaraknath, L. Garten, P. Ndione, D. Ginley and K.A. Persson, "Computational Approach for Epitaxial Polymorph Stabilization through Substrate Selection", *ACS Applied Materials and Interfaces*, vol. 8, 13086–13093, 2016.

[DIN17] Z. Ding, Y. Cui, D. Wan, H. Luo and Y. Gao, "High-performance thermal sensitive VO_2(B) thin films prepared by sputtering with TiO_2(A) buffer layer and first-principles calculations study", *RSC Advances*, vol. 7, 29496–29504, 2017.

[DUC72] J. Duchene, M. Terraillon and M. Pailly, "R.F. and D.C. reactive sputtering for crystalline and amorphous VO_2 thin film deposition", *Thin Solid Films*, vol. 12, 231–234, 1972.

[DUM07] F. Dumas-Bouchiat, C. Champeaux, A. Catherinot, A. Crunteanu and P. Blondy, "RF-microwave switches based on reversible semiconductor-metal transition of VO_2 thin films synthesized by pulsed-laser deposition", *Appl. Phys. Lett.*, vol. 91, 2–5, 2007.

[EMO18] N. Émond, B. Torriss and M. Chaker, "Natural and induced growth of VO_2(M) on VO_2(B) ultrathin films", *Scientific Reports*, vol. 8, 1–8, 2018.

[ENJ86] R. Enjalbert and J. Galy, "A refinement of the structure of V_2O_5", *Acta Crystallographica Section C - Crystal Structure Communications*, vol. 42, 1467–1469, 1986.

[EYE02] V. Eyert, "The metal-insulator transitions of VO_2: A band theoretical approach", *Ann. Phys.* (Leipzig), vol. 11, 650–704, 2002.

[FAN13] L.L. Fan, Y.F. Wu, C. Si, G.Q. Pan, C.W. Zou and Z.Y. Wu, "Synchrotron radiation study of VO_2 crystal film epitaxial growth on sapphire substrate with intrinsic multi-domains", *Applied Physics Letters*, vol. 102, 2013.

[FAN18] L. Fan, X. Wang, F. Wang, Q. Zhang, L. Zhu, Q. Meng, B. Wang, Z. Zhang and C. Zou, "Revealing the role of oxygen vacancies on the phase transition of VO_2 film from the optical-constant measurements", *RSC Advances*, vol. 8, 19151–19156, 2018.

[GAL99] J. Galy and G. Miehe, “Ab initio structures of (M2) and (M3) VO_2 high pressure phases”, *Solid State Sciences*, 1, 433-448, 1999.

[GAN12] N. Ganganagappa and A. Siddaramanna, "One step synthesis of monoclinic VO_2(B) bundles of nanorods: Cathode for Li ion battery", *Materials Characterization*, vol. 68, 58–62, 2012.

[GAT07] E. Gatard, R. Sommet, P. Bouysse, R.Quéré, M. Stanislawiak, and J.-M.Bureau, "High Power S Band Limiter Simulation with a Physics-Based Accurate Nonlinear PIN Diode Model", *IEEE, Proceedings of the 2nd European Microwave Integrated Circuits Conference*, 2007.

[GE20] Y. Ge, F. Zhao, L. Wang and X. Wang, "A novel perspective on the design of thermochromic VO_2 films: Combining ab initio calculations with FDTD simulations", *Surface and Coatings Technology*, vol. 402, 2020.

[GEO56] A. Georg, "Etudes des oxydes de vanadium", *Acta Chemica Scandinavica*, vol. 10, 623–628, 1956.

[GIV08] J. Givernaud, C. Champeaux, A. Catherinot, A. Pothier, P. Blondy and A. Crunteanu, "Tunable band stop niters based on metal-insulator transition in vanadium dioxide thin films", *IEEE MTT-S Int. Microw. Symp. Dig.*, 2008.

[GOL95] C. Goldsmith, T.-H. Lin, B. Powers, W.-R. Wu and B. Norvell, "Micromechanical membrane switches for microwave applications", *IEEE MTT-S International Microwave Symposium*, 1995.

[GON13] I.N. Goncharuk, A.V. Ilinskiy, O.E. Kvashenkina and E.B. Shadrin, "Electron-electron correlations in Raman spectra of VO_2", *Physics of the Solid State*, vol. 55, 164–174, 2013.

[GOO71] J.B. Goodenough, "The two components of the crystallographic transition in VO_2", *Journal of Solid State Chemistry*, vol. 3, 490–500, 1971.

[GRA02] P.D. Grant, R.R. Mansour and M.W. Denhoff, "A comparison between RF MEMS switches and semiconductor switches", *Canadian Journal of Electrical and Computer Engineering*, vol. 27, 33–39, 2002.

[GRA12] P. Gravereau, "Introduction à la pratique de la diffraction des rayons X par les poudres", 2012.

[GRO84] C.R.M. Grovenor, H.T.G. Hentzell and D.A. Smith, "The development of grain structure during growth of metallic films", *Acta Metallurgica*, vol. 32, 773–781, 1984.

[GUO11] H. Guo, K. Chen, Y. Oh, K. Wang, C. Dejoie, S.A. Syed Asif, O.L. Warren, Z.W. Shan, J. Wu and A.M. Minor, "Mechanics and dynamics of the strain-induced M1-M2 structural phase transition in individual VO_2 nanowires", *Nano Letters*, vol. 11, 3207–3213, 2011.

[HAV05] M.W. Haverkort, Z. Hu, A. Tanaka, W. Reichelt, S.V. Streltsov, M.A. Korotin, V.I. Anisimov, H.H. Hsieh, H.J. Lin, C.T. Chen, D.I. Khomskii and L.H. Tjeng, "Orbital-assisted metal-insulator transition in VO2", Physical Review Letters, vol. 95, 4–7, 2005.

[HE15] X. He, Y. Zeng, X. Xu, C. Gu, F. Chen, B. Wu, C. Wang, H. Xing, X. Chen and J. Chu, "Orbital change manipulation metal-insulator transition temperature in W-doped VO_2", *Royal Society of Chemistry*, vol. 17, 11638–11646, 2015.

[HIR78] Y. Hirotsu, S.P. Faile and H. Sato, "Microsyntactic intergrowth in V_nO_{2n-1}", *Materials Research Bulletin*, vol. 13, 895–900, 1978.

[HON17] B. Hong, K. Hu, Z. Tao, J. Zhao, N. Pan, X. Wang, M. Lu, Y. Yang, Z. Luo and C. Gao, "Polymorph separation induced by angle distortion and electron delocalization effect via orbital modification in VO_2 epitaxial thin films", *Physical Review B*, vol. 95, 1–8, 2017.

[HOR07] I. Horcas, R. Fernández, J.M. Gómez-Rodríguez, J. Colchero, J. Gómez-Herrero and A.M. Baro, "WSXM: A software for scanning probe microscopy and a tool for nanotechnology", *Review of Scientific Instruments*, vol. 78, 2007.

[HOR76] H. Horiuchi, N. Morimoto and M. Tokonami, "Crystal structures of V_nO_{2n-1} ($2 \leq n \leq 7$)", *Journal of Solid State Chemistry*, vol. 17, 407–424, 1976.

[HUA18] Y. Huang, D. Zhang, Y. Liu, J. Jin, Y. Yang, T. Chen, H. Guan, P. Fan and W. Lv, "Phase transition analysis of thermochromic VO_2 thin films by temperature-dependent Raman scattering and ellipsometry", *Applied Surface Science*, vol. 456, 545–551, 2018.

[HUM05] C. Humphreys, A.M. Russell and K.L. Lee, "Defects and their effects on Materials Properties", *Introduction to Analytical Electron Microscopy*, 18–27, 2005.

[ILI12] A.V. Ilinskiy, O.E. Kvashenkina and E.B. Shadrin, "Phase transition and correlation effects in vanadium dioxide", *Semiconductors*, vol. 46, 422–429, 2012.

[IMA98] M. Imada, A. Fujimori and Y. Tokura, "Metal-insulator transitions", *Reviews of Modern Physics*, vol. 70, 1039–1263,1998.

[ISH19] O.M. Ishchenko, F. Hamouda, P. Aubert, O. Tandia, M. Modreanu, D.I. Sharovarov, F.Y. Akbar, A.R. Kaul and G. Garry, "Strongly Electronic-Correlated Material for Ultrafast Electronics Application", *Proceedings of the IEEE Conference on Nanotechnology*, 420-425, 2019.

[KAT03] H. Katzke, P. Tolédano and W. Depmeier, "Theory of morphotropic transformations in vanadium oxides", *Phys. Rev. B - Condens. Matter Mater. Phys.*, vol. 68, 1–7, 2003.

[KAT03b] H. Katzke and R. Schlögl, "General structural relationships between rutile-type VO_2 and the Magnéli-phases V_nO_{2n-1}", *Zeitschrift fur Kristallographie*, vol. 218, 432–439, 2003.

[KAT03c] H. Katzke and R. Schlögl, "Mechanism of the morphotropic transformation between the rutile and corundum structural types", *Acta Crystallographica Section B: Structural Science*, vol. 59, 456–462, 2003.

[KEL05] D. Kelly, C. Brindle, C. Kemerling, and M. Stuber, "The State-of-the-Art of Silicon-on-Sapphire CMOS RF Switches", *IEEE, Compound Semiconductor Integrated Circuit Symposium,* 2005.

[KOT04] G. Kotliar and D. Vollhardt, "Strongly Correlated Materials: Insights From Dynamical Mean-Field Theory", *Physics Today*, vol. 57, 53–59, 2004.

[KRA17] A. Krammer, A. Magrez, W.A. Vitale, P. Mocny, P. Jeanneret, E. Guibert, H.J. Whitlow, A.M. Ionescu and A. Schüler, "Elevated transition temperature in Ge doped VO_2 thin films", *Journal of Applied Physics,* vol. 122, 2017.

[KUB07] C. Kübler, H. Ehrke, R. Huber, R. Lopez, A. Halabica, R.F. Haglund and A. Leitenstorfer, "Coherent structural dynamics and electronic correlations during an ultrafast insulator-to-metal phase transition in VO_2", *Physical Review Letters*, vol. 99, 1–4 2007.

[LEE11] S.H. Lee, M.K. Kim, J.W. Lee, Z. Yang, S. Ramanathan and S. Tiwari, "Vanadium dioxide (VO_2) is also a ferroelectric: Properties from memory structures", *Proceedings of the IEEE Conference on Nanotechnology*, 735–739, 2011.

[LEE15] S. Lee, T.L. Meyer, C. Sohn, D. Lee, J. Nichols, D. Lee, S.S.A. Seo, J.W. Freeland, T.W. Noh and H.N Lee, "Electronic structure and insulating gap in epitaxial VO_2 polymorphs", *APL Materials,* vol. 3, 2015

[LEE16] S. Lee, I.N. Ivanov, J.K. Keum and H.N. Lee, "Epitaxial stabilization and phase instability of VO_2 polymorphs", *Scientific Reports,* vol. 6, 1–7, 2015.

[LEE17] S. Lee, X.G. Sun, A.A. Lubimtsev, X. Gao, P. Ganesh, T.Z. Ward, G. Eres, M.F. Chisholm, S. Dai and H.N. Lee, "Persistent Electrochemical Performance in Epitaxial VO_2(B)", *Nano Letters,* vol. 17, 2229–2233, 2017.

[LER98] C. Leroux, G. Nihoul and G. Van Tendeloo, "From to Theoretical structures of polymorphs and in situ electron microscopy", *Physical Review B - Condensed Matter and Materials Physics*, vol. 57, 5111–5121, 1998.

[LI11] H. Li, P. He, Y. Wang, E. Hosono and H. Zhou, "High-surface vanadium oxides with large capacities for lithium-ion batteries: from hydrated aerogel to nanocrystalline VO_2(B), V_6O_{13} and V_2O_5", *Journal of Materials Chemistry*, vol. 21, 10999–11009, 2011.

[LI94] W. Li, J.R. Dahn and D.S. Wainwright, "Rechargeable Lithium Batteries with Aqueous Electrolytes", *Science*, vol. 264, 1115–1118, 1994.

[LIU12] L. Liu, F. Cao, T. Yao, Y. Xu, M. Zhou, B. Qu, B. Pan, C. Wu, S. Wei and Y. Xie, "New-phase VO_2 micro/nanostructures: investigation of phase transformation and magnetic property", *New Journal of Chemistry*, vol. 36, 619–625, 2012.

[LIU15] M. Liu, A.J. Sternbach, M. Wagner, T.V. Slusar, T. Kong, S.L. Bud'ko, S. Kittiwatanakul, M.M. Qazilbash, A. McLeod, Z. Fei, E. Abreu, J. Zhang, M. Goldflam, S. Dai, G.X. Ni, J. Lu, H.A. Bechtel, M.C. Martin, M.B. Raschke, R.D. Averitt, S.A. Wolf, H.T. Kim, P.C. Canfield and D.N. Basov, "Phase transition in bulk single crystals and thin films of VO_2 by nanoscale infrared spectroscopy and imaging", *Physical Review B - Condensed Matter and Materials Physics*, vol. 91, 2015.

[LIU17] P. Liu, K. Bian, K. Zhu, Y. Xu, Y. Gao, H. Luo, L. Lu, J. Wang, J. Liu and G. Tai, "Ultrathin Nanoribbons of in Situ Carbon-Coated $V_3O_7{\cdot}H_2O$ for High-Energy and Long-

Life Li-Ion Batteries: Synthesis, Electrochemical Performance, and Charge-Discharge Behavior", *ACS Applied Materials and Interfaces*, vol. 9, 17002–17012, 2017.

[LIU18] B.T. Liu, X.M. Shi, X.Y Lang, L. Gu, Z. Wen, M. Zhao and Q. Jiang, "Extraordinary pseudocapacitive energy storage triggered by phase transformation in hierarchical vanadium oxides", *Nature Communications*, vol. 9, 1–9, 2018

[LIU22] Y. Liu, C. Wang, W. Huang, S. Wang, H. Qiu, W. Ge, M. Chen, H. Zhang, Y. Gu, X. Zhang, X. Li, X. Gao and Y. Yang, "Unraveling Structural Phase Transformation by Simultaneously Determining the Lattice Constants and Mismatch Angle in VO_2/Al_2O_3 Epitaxial Thin Films", *Frontiers in Materials*, vol. 9, 1–9, 2022.

[LIV10] J. Livage, "Hydrothermal synthesis of nanostructured vanadium oxides", *Materials*, vol. 3, 4175–4195, 2010.

[LON10] V.M. Longo, M. das Graça Sampaio Costa, A. Zirpole Simões, I.L.V. Rosa, C.O.P. Santos, J. Andrés, E. Longo and J.A. Varela, "On the photoluminescence behavior of samarium-doped strontium titanate nanostructures under UV light. A structural and electronic understanding", *Physical Chemistry Chemical Physics*, vol. 12, 7566–7579, 2010.

[LOT07] A. Lotnyk, S. Senz and D. Hesse, "Epitaxial growth of TiO_2 thin films on $SrTiO_3$, $LaAlO_3$ and yttria-stabilized zirconia substrates by electron beam evaporation", *Thin Solid Films*, vol. 515, 3439–3447, 2007.

[LU20] Q. Lu, C. Sohn, G. Hu, X. Gao, M.F. Chisholm, I. Kylänpää, J.T. Krogel, P.R.C. Kent, O. Heinonen, P. Ganesh and H.N. Lee, "Metal–insulator transition tuned by oxygen vacancy migration across TiO_2/VO_2 interface", *Scientific Reports*, vol. 10, 1–7, 2020.

[LUT10] H. Lüth, "Solid Surfaces, Interfaces and Thin Films", *Springer Fifth Edition*, 2010.

[MAR08] C. Marini, E. Arcangeletti, D. di Castro, L. Baldassare, A. Perucchi, S. Lupi, L. Malavasi, L. Boeri, E. Pomjakushina, K. Conder and P. Postorino, "Optical properties of $V_{1-x}Cr_xO_2$ compounds under high pressure", *Physical Review B - Condensed Matter and Materials Physics*, vol. 77, 1–9, 2008.

[MAR10] C. Marini, L. Baldassarre, M. Baldini, A. Perucchi, D. di Castro, L. Malavasi, S. Lupi and P. Postorino, "Evidence for a monoclinic metallic phase in high-pressure VO_2", *High Pressure Research*, vol. 30, 55–59, 2010.

[MAR72] M. Marezio, D.B. McWhan, J.P. Remeika and P.D. Dernier, "Structural Aspects of MIT in Cr-Doped VO_2", *Physical Review B*, vol. 5, 2538–2541, 1972.

[MAR94] A. Marty and S. Andrieu, "Croissance et structure des couches minces", *Journal De Physique. IV*, vol.6, 1996.

[MOA17] A. Moatti, R. Sachan, J. Prater and J. Narayan, "Control of Structural and Electrical Transitions of VO_2 Thin Films", *ACS Applied Materials and Interfaces*, vol. 9, 24298–24307, 2017.

[MOL14] R. Molaei, R. Bayati, F. Wu and J. Narayan, "A microstructural approach toward the effect of thickness on semiconductor-to-metal transition characteristics of VO_2 epilayers", *Journal of Applied Physics*, vol. 115, 2014.

[MOR14] V.R. Morrison, R.P. Chatelain, K.L. Tiwari, A. Hendaoui, A. Bruhács, M. Chaker and B.J. Siwick, "A photoinduced metal-like phase of monoclinic VO_2 revealed by ultrafast electron diffraction", *Science AAAS*, vol. 346, 445–448, 2014.

[MOR59] F.J. Morin, "Oxides which show a metal-to-insulator transition at the neel temperature", *Physical Review Letters*, vol. 3, 34-36, 1959.

[MOT49] N.F. Mott, "The basis of the electron theory of metals, with special reference to the transition metals", *Proceedings of the Physical Society*, Section A, vol. 62, 416–422, 1949.

[MOT68] N.F. Mott, "Metal-Insulator Transitions", *Review of Modern Physics*, vol. 40, 677–683, 1968.

[MUL20] A. Muller, R.A. Khadar, T. Abel, N. Negm, T. Rosca, A. Krammer, M. Cavalieri, A. Schueler, F. Qaderi, J. Bolten, M. Lemme, I. Stolichnov and A.M. Ionescu, "Radio-Frequency Characteristics of Ge-Doped Vanadium Dioxide Thin Films with Increased Transition Temperature", *ACS Applied Electronic Materials*, vol. 2, 1263–1272, 2020.

[NAR03] J. Narayan and B.C. Larson, "Domain epitaxy: A unified paradigm for thin film growth", *Journal of Applied Physics*, vol. 93, 278–285, 2003.

[NI11] S. Ni, H. Zeng and X. Yang, "Fabrication of VO_2(B) nanobelts and their application in lithium ion batteries", *Journal of Nanomaterials*, 1–5, 2011.

[OKA93] Y. Oka, T. Yao, N. Yamamoto, Y. Ueda and A. Hayashi, "Phase Transition and V^{4+}-V^{4+} Pairing in VO_2(B)", *Journal of Solid State Chemistry*, vol. 105, 271–278, 1993.

[OKA98] Y. Oka, S. Sato, T. Yao and N. Yamamoto, "Crystal Structures and Transition Mechanism of VO_2(A)", *Journal of Solid State Chemistry*, vol. 141, 594–598, 1998.

[OTT19] M.R. Otto, L.P. René de Cotret, D.A. Valverde-Chavez, K.L. Tiwari, N. Émond, M. Chaker, D.G. Cooke and B.J. Siwick, "How optical excitation controls the structure and properties of vanadium dioxide", *Proceedings of the National Acaemy of Sciences of the United States of America*, vol. 116, 450–455, 2019.

[PAE20] G.J. Paez, C.N. Singh, M.J. Wahila, K.E. Tirpak, N.F. Quackenbush, S. Sallis, H. Paik, Y. Liang, D.G. Schlom, T.L. Lee, C. Schlueter, W.C. Lee and L.F.J. Piper, "Simultaneous Structural and Electronic Transitions in Epitaxial $VO_2/TiO_2(001)$", *Physical Review Letters*, vol. 124, 2020.

[PAE20b] G.J. Paez, C.N. Singh, M.J. Wahila, K.E. Tirpak, N.F. Quackenbush, S. Sallis, H. Paik, Y. Liang, D.G. Schlom, T.L. Lee, C. Schlueter, W.C. Lee and L.F.J. Piper, "Supplementary Information - Simultaneous Structural and Electronic Transitions in Epitaxial VO2/TiO2(001)", Physical Review Letters, vol. 124, 2020

[PAN15] K. Pan, K. Freeman, D. Brown, E. Shin, W. Wang and G. Subramanyam, "Vanadium dioxide thin film series single-pole single throw switch", *National Aerospace and Electronics Conference, Proceedings of the IEEE*, 2015

[PAO15] A. Paone, R. Sanjines, P. Jeanneret, H.J. Whitlow, E. Guibert, G. Guibert, F. Bussy, J.L. Scartezzini and A. Schüler, "Influence of doping in thermochromic $V_{1-x}W_xO_2$ and $V_{1-x}Al_xO_2$ thin films: Twice improved doping efficiency in $V_{1-x}W_xO_2$", *Journal of Alloys and Compounds*, vol. 621, 206–211, 2015.

[PAS11] A. Pashkin, C. Kübler, H. Ehrke, R. Lopez, A. Halabica, R.F. Haglund, R. Huber and A. Leitenstorfer, "Ultrafast insulator-metal phase transition in VO_2 studied by multiterahertz spectroscopy", *Physical Review B - Condensed Matter and Materials Physics*, vol. 83, 1–9, 2011.

[PAU90] P. Paufler, B. G. Hyde, S. Andersson, "Inorganic crystal structures", *Crystal Research and Technology*, vol. 25, 676, 1990.

[PEI55] R. Peierls, "Quantum Theory of Solids", Oxford University, 1955.

[PET16] T. Peterseim, M. Dressel, M. Dietrich and A. Polity, "Optical properties of VO_2 films at the phase transition: Influence of substrate and electronic correlations", *Journal of Applied Physics*, vol. 120, 2016.

[PIS09] V. Pishchik, L.A. Lytvynov and E.R. Dobrovinskaya, "Sapphire", *Springer*, 2009.

[PON18] A. Ponchet, G. Patriarche, J.B. Rodriguez, L. Cerutti and E. Tournié, "Interface energy analysis of III-V islands on Si(001) in the Volmer-Weber growth mode", *Applied Physics Letters*, vol. 113, 0–5, 2018.

[POP13] S.R. Popuri, M. Miclau, A. Artemenko, C. Labrugere, A. Villesuzanne and M. Pollet, "Rapid hydrothermal synthesis of VO_2(B) and its conversion to thermochromic VO_2(M1)", *Inorganic Chemistry*, vol. 52, 4780–4785, 2013.

[POP14] S.R. Popuri, A. Artemenko, C. Labrugere, M. Miclau, A. Villesuzanne and M. Pollet, "VO2(A): Reinvestigation of crystal structure, phase transition and crystal growth mechanisms", *Journal of Solid State Chemistry*, vol. 213, 79-86, 2014.

[POU75] J.P. Pouget, H. Launois, J.P. D'Haenens, P. Merenda and T.M. Rice, "Electron Localization Induced by Uniaxial Stress in Pure VO_2", *Physical Review Letters*, vol. 35, 873–875, 1975.

[QAZ08] M.M. Qazilbash, A.A. Schafgans, K.S. Burch, S.J. Yun, B.G. Chae, B.J. Kim, H.T. Kim and D.N. Basov, "Electrodynamics of the vanadium oxides VO_2 and V_2O_3", *Physical Review B - Condensed Matter and Materials Physics*, vol. 77, 1–10, 2007.

[QU11] B.Y. Qu, L. Liu, Y. Xie and B.C. Pan, "Theoretical study of the new compound VO_2(D)", *Physics Letters, Section A: General, Atomic and Solid State Physics*, vol. 375, 3474–3477, 2011.

[RAM18] J.A. Ramirez-Rincon, C. L. Gomez-Heredia, A. Corvisier, J. Ordonez-Miranda, T. Girardeau, F. Paumier, C. Champeaux, F. Dumas-Bouchiat, Y. Ezzahri, K. Joulain, O. Ares and J.J. Alvarado-Gil, "Thermal hysteresis measurement of the VO_2 dielectric function for its metal-insulator transition by visible-IR ellipsometry", *Journal of Applied Physics*, vol. 124, 2018.

[REB02] G.M. Rebeiz, "RF MEMS: theory, design, and technology", *John Wiley & Sons*; 1st edition, 2002.

[ROA71] W.R. Roach and I. Balberg, "Optical induction and detection of fast phase transition in VO_2", *Solid State Communication*, vol. 9, 551–555, 1971.

[ROD21] L. Rodríguez, F. Sandiumenge, C. Frontera, J.M. Caicedo, J. Padilla, G. Catalán and J. Santiso, "Strong strain gradients and phase coexistence at the metal-insulator transition in VO_2 epitaxial films", *Acta Materialia*, vol. 220, 2021.

[SAC06] A. Sacchetti, M.C. Guidi, E. Arcangeletti, A. Nucara, P. Calvani, M. Piccinini, A. Marcelli and P. Postorino, "Far-infrared absorption of $La_{1-x}Ca_xMnO_{3-y}$ at high pressure", *Physical Review Letters*, vol. 96, 3–6, 2006.

[SAK09] R. Sakuma, T. Miyake and F. Aryasetiawan, "Quasiparticle band structure of vanadium dioxide", *Journal of Physics Condensed Matter*, vol. 21, 2009.

[SAS] "Titanium oxide (TiO_2) property", Springer, vol. 814, 4–5

[SCH04] U. Schwingenschlögl and V. Eyert, "The vanadium Magnéli phases V_nO_{2n-1}", *Ann. Phys. (Leipzig)*, vol. 13, 475–510, 2004

[SHI17] K. Shibuya and A. Sawa, "Polarized Raman scattering of epitaxial vanadium dioxide films with low-temperature monoclinic phase", *Journal of Applied Physics*, vol. 122, 2017.

[SHV19] P. Shvets, O. Dikaya, K. Maksimova and A. Goikhman, "A review of Raman spectroscopy of vanadium oxides", *Journal of Raman Spectroscopy*, vol. 50, 1226–1244, 2019.

[SICT] Le Syndicat des Industriels des Céramiques Techniques, Tableau comparatif des propriétés électriques, https://ceramique-technique.com

[SIL10] V.F. Silva, V. Bouquet, S. Députier, S. Boursicot, S. Ollivier, I.T. Weber, V.L. Silva, I.M.G. Santos, M. Guilloux-Viry and A. Perrin, "Substrate-controlled allotropic phases and growth orientation of TiO_2 epitaxial thin films", *Journal of Applied Crystallography*, vol. 43, 1502–1512, 2010.

[SMI57] F.M Smits, "Measurement of Sheet Resistivities with the Four Point probe", *The Bell System Technical Journal*, 711–718, 1957

[SON16] Z. Song, L. Zhang, F. Xia, N.A.S. Webster, J. Song, B. Liu, H. Luo and Y. Gao, "Controllable synthesis of VO_2(D) and their conversion to VO_2(M) nanostructures with thermochromic phase transition properties", *Inorganic Chemistry Frontiers*, vol. 3, 1035–1042, 2016.

[SRI15] A. Srivastava, H. Rotella, S. Saha, B. Pal, G. Kalon, S. Mathew, M. Motapothula, M. Dykas, P. Yang, E. Okunishi, D.D. Sarma and T. Venkatesan, "Selective growth of single phase VO_2(A, B, and M) polymorph thin films", *APL Materials*, vol. 3, 2015.

[STE00] G. Stefanovich, A. Pergament and D. Stefanovich, "Electrical switching and Mott transition in VO_2", *Journal of Physics Condensed Matter*, vol. 12, 8837–8845, 2000.

[SU16] K. Su, T. Naka, N.H. Azhan, K. Okimura and M. Higuchi, "Oriented growth of VO_2(B) thin films on Mo foils by reactive sputtering for lithium ion batteries", *Thin Solid Films*, vol. 616, 95–100, 2016.

[SUG90] S. Suga, M. Taniguchi, M. Fujisawa, H. Kanzaki, A. Fujimiori, H. Daimon, Y. Ueda, K. Kosuge and S. Kachi, "Vacuum-ultraviolet reflectance and photoemission study of the metal-insulator phase transitions in VO_2, V_6O_{13}, and V_2O_3", *Physical Review B*, vol. 41, 4993–5009, 1990.

[TAN85] C. Tang, P. Georgopoulos, M.E. Fine and J.B. Cohen, "Local atomic and electronic arrangements in $W_xV_{1-x}O_2$", *Physical Review B*, vol. 31, 1000–1111, 1985.

[THE16] V. Théry, A. Boulle, A. Crunteanu, J.C. Orlianges, A. Beaumont, R. Mayet, A. Mennai, F. Cosset, A. Bessaudou and M. Fabert, "Role of thermal strain in the metal-insulator and structural phase transition of epitaxial VO_2 films", *Physical Review B*, vol. 93, 1–9, 2016.

[THE76] F. Théobald, R. Cabala and J. Bernard, "Essai sur la structure de VO_2(B)", *Journal of Solid State Chemistry*, vol. 17, 431–438, 1976.

[THE77] F. Théobald, "Hydrothermal Study of VO_2-$VO_{2.5}$-H_2O", *System Journal of the Less-Common Metals*, vol. 53, 55–71, 1977.

[THO77] J. A. Thornton, "High rate thick film growth", *Annual Review of Materials Science*, vol. 7, 1977.

[TSE07] K. Tse, D. Liu, K. Xiong and J. Robertson, "Oxygen vacancies in high-k oxides", *Microelectronic Engineering*, vol. 84, 2028–2031, 2007.

[URE17] F. Ureña-Begara, A. Crunteanu and J.P. Raskin, "Raman and XPS characterization of vanadium oxide thin films with temperature", *Applied Surface Science*, vol. 403, 717–727, 2017.

[VIC21] J.L. Victor, C. Marcel, L. Sauques, N. Penin and A. Rougier, "High quality thermochromic VO_2 thin films deposited at room temperature by balanced and unbalanced HiPIMS", *Solar Energy Materials and Solar Cells*, vol. 227, 2021.

[WAD63] A.D. Wadsley, "Nonstoichiometric Metal Oxides", *Nonstoichiometric Compounds, Advances in Chemistry*, 1963.

[WAI21] N. Wainstein, G. Adam, E. Yalon and S. Kvatinsky, "Radiofrequency Switches Based on Emerging Resistive Memory Technologies - A Survey", *Proc. IEEE*, vol. 109, 77–95, 2021.

[WAL74] K. Waltersson, B. Forslund, K.A. Wilhelmi, S. Andersson and J. Galy, "The crystal structure of V_3O_7", *Acta Crystallographica Section B Structural Crystallography and Crystal Chemistry*, vol. 30, 2644–2652, 1974.

[WEG14] D. Wegkamp, M. Herzog, L. Xian, M. Gatti, P. Cudazzo, C.L. McGahan, R.E. Marvel, R.F. Haglund, A. Rubio, M. Wolf and J. Stähler, "Instantaneous band gap collapse in photoexcited monoclinic VO_2 due to photocarrier doping", *Physical Review Letters*, vol. 113, 2–6, 2014.

[WEG15] D. Wegkamp and J. Stähler, "Ultrafast dynamics during the photoinduced phase transition in VO_2", *Progress in Surface Science*, vol. 90, 464–502, 2015.

[WHA74] D.B. McWhan, M. Marezio, J.P. Remeika and P.D. Dernier, "X-ray diffraction study of metallic VO_2", *Physical Review B*, vol. 10, 490–495, 1974.

[WON13] F.J. Wong, Y. Zhou and S. Ramanathan, "Epitaxial variants of VO_2 thin films on complex oxide single crystal substrates with 3m surface symmetry", *Journal of Crystal Growth*, vol. 364, 74–80, 2013.

[WUR07] U. Würzburg, "Physics of correlated electron materials", *Summer School on Ab-initio Many-Body Theory*, 2007

[XIA15] X. Xiao, S. Li, H. Wei, D. Sun, Y. Wu, G. Jin, F. Wang and Y. Zou, "Synthesis and characterization of VO_2(B)/graphene nanocomposite for supercapacitors", *Journal of Materials Science: Materials in Electronics*, vol. 26, 4226–4233, 2015.

[YAN10] T.H. Yang, C. Jin, R. Aggarwal, R.J. Narayan and J. Narayan, "On growth of epitaxial vanadium oxide thin film on sapphire (0001)", *Journal of Materials Research*, vol. 25, 422–426, 2010.

[YAN11] Z. Yang, C. Ko and S. Ramanathan, "Oxide Electronics Utilizing Ultrafast Metal-Insulator Transitions", *Annu. Rev. Mater. Res.*, vol. 41, 337–367, 2011.

[YUA13] H. Yuan, W. Zhang and P. Zhang, “Hole-lattice coupling and photoinduced insulator-metal transition in VO_2”, *Physical Rew B*, 88, 035119, 2013.

[ZAG15] M. Zaghrioui, J. Sakai, N.H. Azhan, K. Su and K. Okimura, "Polarized Raman scattering of large crystalline domains in VO_2 films on sapphire", *Vibrational Spectroscy*, vol. 80, 79–85, 2015.

[ZHA12] Y. Zhao, J. Hwan Lee, Y. Zhu, M. Nazari, C. Chen, H. Wang, A. Bernussi, M. Holtz and Z. Fan, "Structural, electrical, and terahertz transmission properties of VO_2 thin films grown on c-, r-, and m-plane sapphire substrates", *Journal of Applied Physics*, vol. 111, 2012.

[ZHA20] H. Zhang, Z. Zou, S. Zhang, J. Liu and S. Zhong, "A review of the Doping Modification of $LiFePO_4$ as a Cathode Material for Lithium Ion Batteries", *International Journal of Electrochemical Science*, vol. 15, 12041–12067, 2020.

[ZHA21] Y. Zhang, W. Xiong, W. Chen and Y. Zheng,"Recent progress on vanadium dioxide nanostructures and devices: Fabrication, properties, applications and perspectives", *Nanomaterials*, vol. 11, 1–48, 2021.

[ZHO11] H. Zhou, M.F. Chisholm, T.H. Yang, S.J. Pennycook and J. Narayan, "Role of interfacial transition layers in VO_2/Al_2O_3 heterostructures", *Journal of Applied Physics*, vol. 110, 2011.

[ZOU17] Z. Zou, Z. Hou, J. Wang, Y. Gao, Z. Wan and S. Han, "Hydrothermal synthesis and electrochemical performance of Al-doped VO_2(B) as cathode materials for lithium-ion battery", *International Journal of Electrochemical Science*, vol. 12, 4979–4989, 2017.

[ZUR84] A. Zur and T.C. McGill, "Lattice match: An application to heteroepitaxy", *Journal of Applied Physics*, vol. 55, 378–386, 1984.

[ZYL75] A. Zylberszteijn and N.F. Mott, "Metal-insulator transition in vanadium dioxide", *Physical Review B*, vol. 11, 4383–4395, 1975.

Appendix 1: Temperature calibration of the RFMS setup

The radiofrequency magnetron sputtering (RFMS) deposition chamber is equipped with a sample holder mounted on a heating rod, and held in contact with the latter by two screws to prevent its moving due to the vibrations from the pumping system. It thus ensures the same thermal contact for all depositions. The temperature is piloted by a power supply and controlled by a thermocouple placed inside the heating rod. A temperature difference between the inside of the heating rod and the sample surface was observed and a necessary calibration was performed. To do that, a K-type thermocouple was glued with high-performance silver paste at the surface of the sample holder. A silicon (Si) substrate was glued next to the center of the sample holder to follow the temperature of the Si substrate optically. The measurement was made with an optical pyrometer at ε=0.68 (ε emissivity, value for Si) as shown in **Figure A1-1**(a).

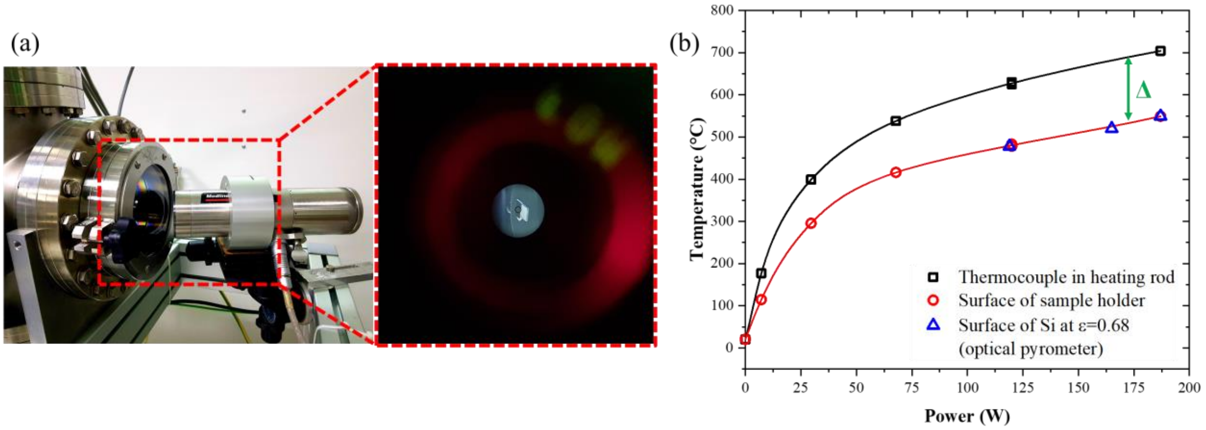

Figure A1-1: (a) Pictures of optical pyrometer installed facing the sample holder. It focuses on measuring the Si substrate surface at emissivity ε=0.68. (b) Evolution of the temperature measured in the heating rod by K-type thermocouple (black square), at the surface of the sample holder by a K-type thermocouple (red circle), and at the surface of the Si substrate. This evolution is measured as function of the power supplied to the heating rod.

Higher set temperature induces a higher difference between the temperatures of the heating rod and of the one measured at the Si sample surface. An offset (Δ) of about 150° was estimated for a temperature measured at the sample surface in the range of 450 to 550°C, the same range as used in our work. Each deposition of VO_2 was carried out with a sample of Si sticked next to the main sample to facilitate the optical control of the temperature. Optical pyrometry systematically monitored the temperature to have the most reproducible deposition conditions.

Appendix 2: Hydrothermal synthesis of VO_2(B) nanopowders

The synthesis of VO_2(B) nanostructures was carried out by the hydrothermal (HT) method using the V_2O_5 and an aqueous solution of oxalic acid ($H_2C_2O_4$) as precursors. The chemical reaction between the precursors can be followed according to the solution color change in time that gives an estimate of the Vanadium oxidation state (**Figure A2-1**):

i. Orange: V_2O_5 is not reduced (V^{+5})
ii. Green: V_2O_5 is partially reduced (V^{+4}, V^{+5})
iii. Dark blue: V_2O_5 is reduced (V^{+4}, V^{+3})

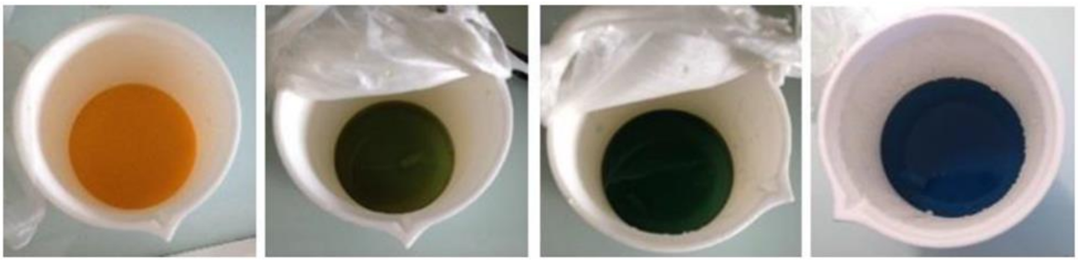

Figure A2-1: Evolution of the solution color during the reduction of V^{+5} (orange) in V^{+4} (dark blue). Pictures taken as part of an internship at TE-OX.

The prepared solution was poured into one Teflon liner of 130 mL volume capacity and placed in an Autoclave Maxitech® France composed of one stainless steel reactor (**Figure A2-2**). An autoclave, is used to carry out chemical reactions under pressure and temperature conditions above 100°C and 1 bar.

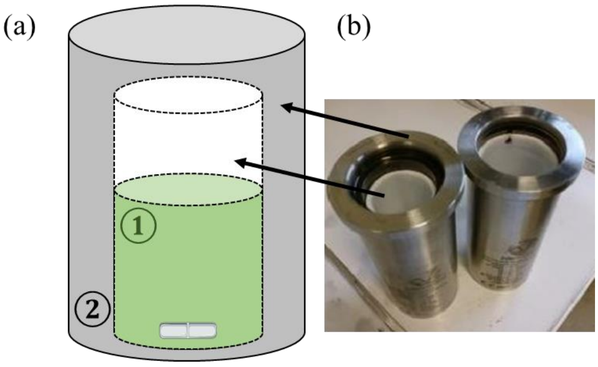

Figure A2-2: (a) Scheme and (b) picture of vanadium solution ① poured into Teflon liner and placed in the stainless steel reactor ② A magnetic stirrer is used to homogenize the solution.

The autoclave was installed on a hotplate with a magnetic stirrer (**Figure A2-3**(a)). The heating of the autoclave was achieved with an external oven around the stainless steel reactor and was connected to a temperature regulator which allows setting up and controlling the external temperature and internal solution. A thermocouple was placed inside the autoclave and connected to a temperature regulator in order to monitor the temperature. For all experiments presented in Chapter 4, the synthesis temperature was 160°C.

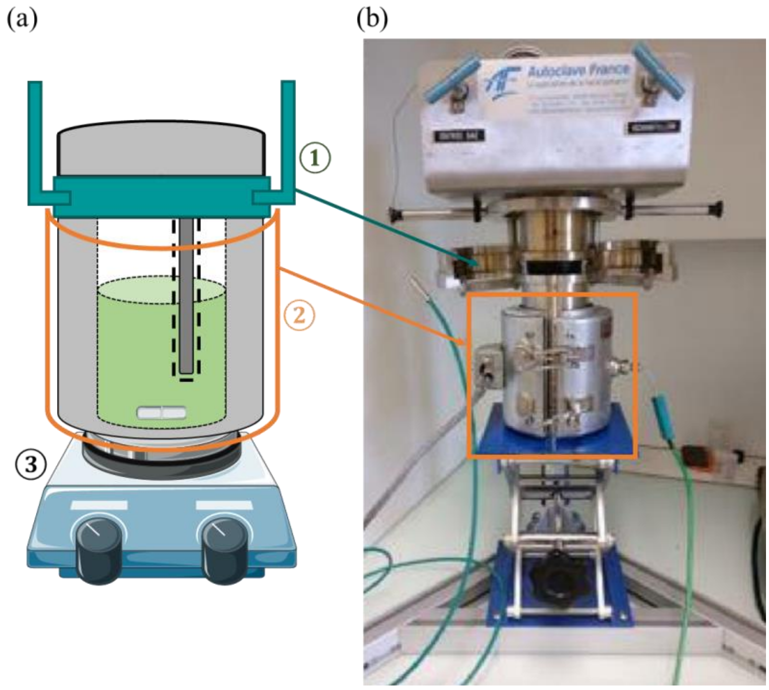

Figure A2-3: (a) Scheme and (b) picture of the HT setup. Reactive solution was placed into a Teflon liner with a thermocouple to control the temperature inside the autoclave. ① a reactor lid was installed to securize the synthesis ② the stainless steel reactor was covered by a heater oven and ③ installed on a hotplate with a magnetic stir.

Appendix 3: RF characterizations of VO_2 switches on c-cut sapphire substrate

In Chapter 3 we observed that the VO_2 layers deposited on the c-cut and r-cut sapphire substrates present similar electrical performances whereas their optical and structural properties were impacted by their different growth morphologies. In particular, the structural transition was noted to be slightly slower for the VO_2(M1) deposited on c-cut sapphire, therefore we were interested to verify how it could affect the RF performance of VO_2 switches. Firstly, resistivity measurements under thermal activation of VO_2 were compared before (full thin film) and after fabrication. The goal is to verify if the fabrication process as presented in Chapter 5, damages the electrical performance of our high quality VO_2 deposited on c-cut sapphire substrate. As shown in **Figure A3-1**, both samples undergo an abrupt resistance change of around 4 orders of magnitude. The slight difference in the resistance between these two samples could come from the measurement setup. We used the four-probe method for the thin film layer, whereas after the fabrication process, a two-probe method was used, which is less accurate but still allows us to verify that our samples retain their good transition performances.

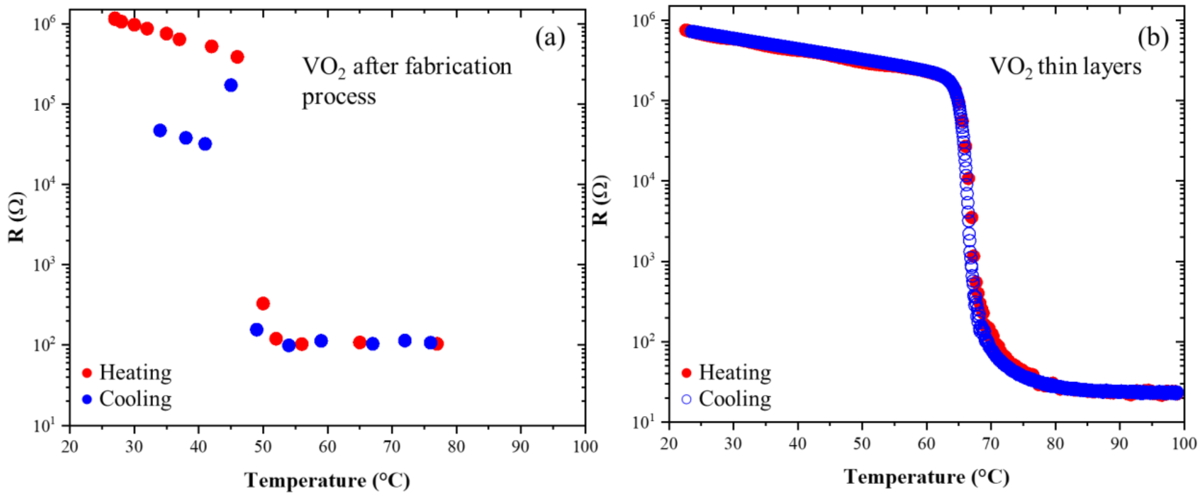

Figure A3-1: Resistance measurements as function of temperature (red = heating, blue = cooling) of (a) a VO_2 component after the fabrication process (measured in air with 2 probes) and (b) a full VO_2 thin film deposited on c-cut sapphire substrate (measured under vacuum with 4 probes).

The same vector network analyzer (VNA) was employed to compare RF performances of VO_2 switches fabricated on c-cut and r-cut sapphire as presented in Chapter 5. The results for both series and shunt switches presented on **Figure A3-2** show high performance of the series switches. When the VO_2 is insulating, the signal is reflected (S_{11}~0 dB) and S_{21} parameter exhibits a variation from -55 dB at 1 GHz up to -25 dB at 20 GHz. When the VO_2 is metallic, the S_{21} parameters turns to a value of -1 dB (**Figure A3-2(b)**).

Our measurements highlight that a VO_2 switch in the shunt configuration presents the same behavior indifferently of the substrate orientation used. The signal is transmitted when the VO_2 is insulating and deviated from the central line in the metallic state. It should be noted that in both cases (c-cut and r-cut sapphire), the isolation parameter is weak. **Table A3-1** synthesizes the experimental results for VO_2

switches in both shunt and series configurations on c-cut sapphire compared to the switches developed on r-cut sapphire substrate. It should be noted that in the case of the switches fabricated on c-cut sapphire, the insertion losses are slightly higher in series configuration and the isolation is lower in the shunt configuration.

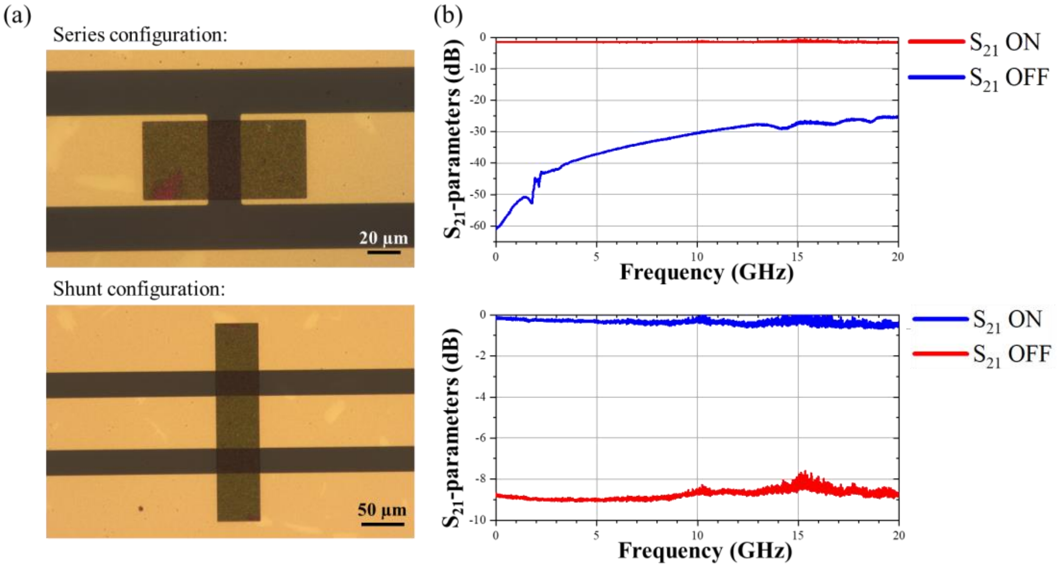

Figure A3-2: VO_2 switch in series and shunt configuration: (a) optical image and (b) experimental results for the S_{21}-parameter measurements. The VO_2 thin film was deposited on c-cut sapphire substrate.

Table A3-1: Comparison of VO_2 switch performances in series and shunt configurations for VO_2 deposited on c-cut and r-cut sapphire substrates. Both mean value and standard deviation (Std dev) are given, in red for metallic state and in blue for the insulating one.

VO_2 switch configuration	Insertion loss (dB) at 10 GHz		Isolation (dB) at 10 GHz	
	Mean value	Std dev	Mean value	Std dev
Series (r-cut sapphire)	1.2	0.3	31.2	0.8
Series (c-cut sapphire)	3.3	0.7	31.3	2.6
Shunt (r-cut sapphire)	0.1	0.2	14.1	0.3
Shunt (c-cut sapphire)	0.2	0.2	8.9	0.1

Considering the results obtained for VO_2 switch performances in series and shunt configurations on c-cut and r-cut sapphire substrates (**Table A3-1**), we can affirm that the growth mode induced by the two types of sapphire substrates impact the device performance. This is especially true for VO_2 in its metallic state, where performances are found lower on c-cut compared to r-cut sapphire. We have seen in Chapter 3 that substrate orientation highly impacts the VO_2 growth mode, and in particular the formation of multiple crystallographic variants, which finally influence the transition dynamics of the layers (higher hysteresis width (ΔH) and/or lower transition temperature T_{MIT}). For example, we have evidenced the coexistence of the insulator and metallic states of VO_2 during the transition for films deposited on c-cut sapphire substrates. Consequently, if the same phase coexistence appears during RF measurements, it could explain the lower performances of switches developed on c-cut sapphire substrates. A more extensive statistical study is needed for definite conclusion, because several other hypotheses could also explain the low isolation of switches in the shunt configuration:

i. In the 3D simulations of the switches, the roughness of the VO_2 layer was not considered. A high roughness would impact the interface and the contact quality between the VO_2 and the deposited gold coplanar waveguide (CPW).
ii. A problem during the fabrication process of the switches.

As perspective, it would be interesting to investigate how the growth of a VO_2 film with controlled defect introduction will impact the RF performance.

List of Figures

Chapter 1

Chapter 2

Chapter 3

Chapter 4

Chapter 5

Appendices

List of Tables

Chapter 1

Chapter 3

Chapter 4

Chapter 5

Appendices

Résumé en français

« Étude du polymorphisme de VO_2 pour des applications en microélectronique et radiofréquences »

Dans l'industrie des communications, des efforts permanents sont déployés afin d'améliorer les performances des dispositifs et d'augmenter la vitesse de transfert de données. Ces systèmes souvent complexes doivent répondre à des exigences technologiques comme la rapidité de commutation, une basse consommation énergétique, une grande fiabilité, de faibles pertes d'insertion, et une bonne isolation en état OFF pour un commutateur radiofréquence (RF) [WAI21]. Au cours des dernières décennies, plusieurs technologies ont été proposées reposant principalement sur l'utilisation de matériaux semi-conducteurs, mais aucune d'entre elle n'a pu répondre à l'ensemble des critères. Les recherches menées sur les matériaux à changement de phase (PCM) explorent une alternative attrayante pour l'obtention de nouveaux composants électroniques offrant un fonctionnement ultra-rapide et fiable [DUM07][GIV08][BOU10].

Pour développer ses activités RF, la société TE-OX® s'est orientée vers l'utilisation du dioxyde de vanadium (VO_2). Ce dernier appartient à une famille d'oxydes [KAT03][YAN11] dont une majeure partie présente une transition métal-isolant (MIT)[SCH04]. Contrairement au V_2O_3 par exemple, dont la température de transition (T_{MIT}) est de -105°C, le VO_2 présente une transition réversible d'un état isolant (M1) vers un état métallique (R), à 68°C et s'accompagne d'une variation de 4 à 5 ordres de grandeur de la résistivité [MOR59]. Bien que le VO_2 semble de prime abord simple à élaborer étant donné que seulement deux éléments le composent (V, O), son appartenance à un riche diagramme de phase où des interconnexions entre oxydes existent, rend difficile la fabrication de ce matériau. Par ailleurs, pour la même stœchiométrie VO_2, il convient de noter que de nombreux polymorphes existent (M1, R, A, B, D, etc.). L'obtention de VO_2 de haute qualité nécessite par conséquent une parfaite maîtrise de sa croissance et une bonne compréhension des mécanismes conduisant à la formation et à la stabilisation de ce matériau.

Ce travail de thèse, financé dans le cadre d'une bourse CIFRE entre l'entreprise TE-OX et le Centre de Nanosciences et de Nanotechnologies (C2N), poursuit deux objectifs distincts et complémentaires : d'une part l'optimisation de la croissance des couches minces de VO_2(M1) de haute qualité pour la fabrication de commutateurs RF, et d'autre part, la stabilisation d'une phase dite métastable (B) pour une meilleure compréhension des mécanismes de croissance. Pour synthétiser ces matériaux, deux voies ont été explorées : la synthèse hydrothermale pour l'analyse des phases métastables sous forme de poudre et le dépôt de couches minces par pulvérisation cathodique radiofréquence à effet magnétron (RadioFrequency Magnetron Sputtering ou RFMS).

1. Des oxydes de vanadium au VO_2

Bien que le VO_2 soit un simple oxyde binaire, les différents degrés d'oxydation du vanadium conduisent à la formation d'oxydes tels que V_2O_3, V_3O_5, V_6O_{13} ou encore V_2O_5. La plupart de ces oxydes présentent une MIT, en revanche, leurs températures de transition très éloignées de la température ambiante n'offrent que peu d'intérêt pour les applications liées à cette étude. Par ailleurs, pour une même stœchiométrie, le VO_2 présente divers polymorphes (M1, R, A, B, D, etc.) avec des propriétés physiques très différentes. Nous soupçonnons fortement l'impact de l'ordonnancement de l'oxygène sur la formation des polymorphes. Une légère modification de la composition en oxygène lors de l'élaboration des oxydes peut par ce fait considérablement modifier la nature et les propriétés du matériau visé. Par conséquent, le moyen d'élaboration doit donc être maîtrisé afin d'obtenir un VO_2 stœchiométrique.

2. Fabrication de films de VO_2 par RFMS

Les couches de VO_2 ont été réalisées par RFMS à partir d'une cible de vanadium métallique (99.9%) et d'un mélange d'argon (Ar) et d'oxygène (O_2) pour une pression totale de 2,5 x 10^{-2} mbar. Les oxydes de vanadium étant particulièrement sensibles à leur environnement, un contrôle précis de la présence d'oxygène et de la température du substrat est nécessaire. Ces paramètres ont été optimisés et contrôlés afin d'obtenir des films purs. En accord avec les travaux de la littérature [DIN16][LEE16] et de l'expertise de TE-OX, des substrats de saphir-c et -r ont été sélectionnés afin d'identifier les conditions expérimentales permettant la stabilisation du VO_2(M1). La **Figure 1** résume les différents types d'oxydes obtenus en fonction des paramètres de dépôt. On peut distinguer que les croissances ont été réalisées dans une gamme de température comprise entre 450 - 550°C, et pour un ratio O_2/Ar (en flux) compris entre 2 et 4%. L'analyse par diffraction des rayons X (DRX) a montré que les films obtenus en dessous de 450°C sont amorphes et/ou sans orientation préférentielle de croissance, et que la cristallinité des films s'améliore avec l'augmentation de la température. Par ailleurs, une quantité inférieure à 2.2% conduit à la stabilisation d'oxydes à faible degré d'oxydation (V_2O_3) et, lorsque celle-ci dépasse les 2.8% les oxydes à fort degré d'oxydation se forment. La croissance de films de VO_2 est obtenue dans la gamme 480 - 525°C pour un ratio O_2/Ar compris entre 2.4 et 2.6%.

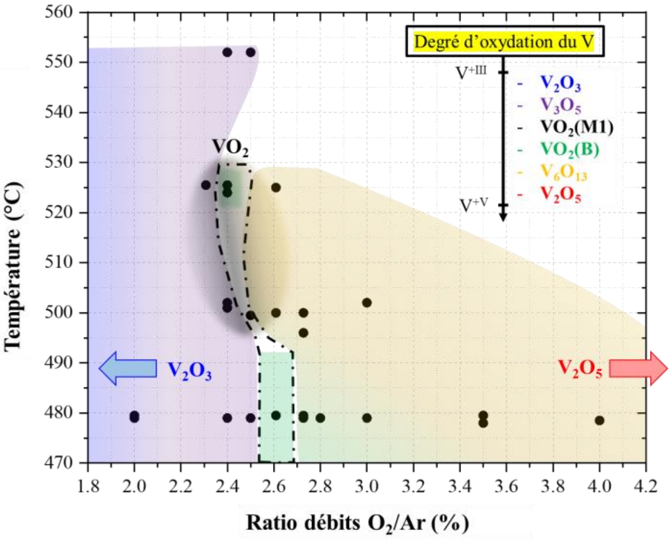

Figure 1: Diagramme de phase expérimental des oxydes de vanadium obtenus par pulvérisation cathodique radiofréquence à effet magnétron, en fonction de la température de croissance et du rapport des flux O_2/Ar introduits dans la chambre de dépôt.

Les films de VO_2 purs déposés sur les substrats de saphir-c et -r présentent la phase monoclinique M1 avec deux orientations cristallographiques préférentielles de croissance : (0k0)VO_2(M1)/saphir-c et (h00)VO_2(M1)/saphir-r (**Figure 2**(a)). Il est aussi important de noter que, pour chaque film, aucun autre oxyde de vanadium ou phase de VO_2 n'a été détecté. Les mesures Raman couplées avec les résultats DRX confirment la phase obtenue ainsi que la qualité cristalline des couches (**Figure 2**(b)) [URE17]. La variation d'intensité entre les spectres est probablement due à une différence d'épaisseur et/ou de morphologie.

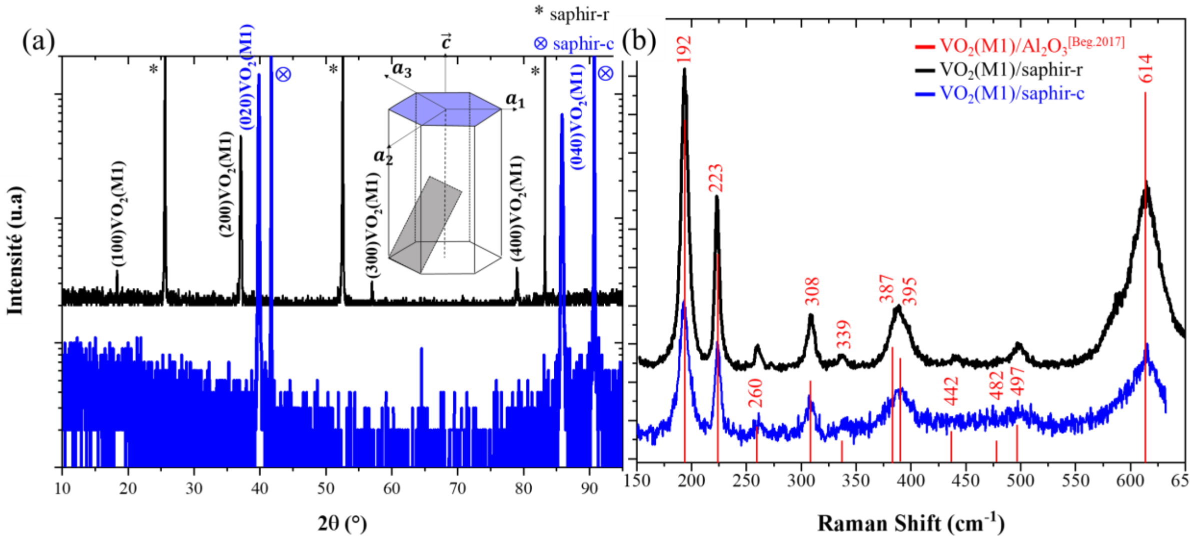

Figure 2: (a) Diffractogrammes DRX et (b) spectres Raman de films de VO_2(M1) déposés sur des substrats de saphir-c et -r. Les mesures ont été réalisées à température ambiante.

2.1. Croissance épitaxiale sur saphir

Le développement des films de VO_2(M1) dans les mêmes conditions expérimentales sur saphir-c (001) et -r (012) nous a permis d'étudier l'influence de l'orientation cristallographique du substrat sur la croissance des films par épitaxie. En dépit des nombreuses études sur la croissance de VO_2(M1), peu d'entre elles analysent en détail cette dépendance [FAN13][ZHA12][WON13]. A partir d'analyses DRX, nous avons proposé dans nos travaux une description complète de l'épitaxie de VO_2 sur saphir-c et -r, permettant une meilleure appréhension des mécanismes de stabilisation de la phase.

a) VO_2(M1)/saphir-c

Pour établir les relations épitaxiales entre le substrat de saphir-c et le film, des φ-scans sont réalisés par DRX. Le plan $(104)_{Al_2O_3}$ visible sur la **Figure 3**(a) avec ses trois pics espacés de 120°, traduit la triple symétrie de la structure hexagonale du saphir le long de l'axe $\vec{c}$. Les six triples pics espacés de 60° visibles pour le plan $(220)_{VO_2(M1)}$ appartiennent à la pseudo-symétrie sextuple apparaissant par la combinaison de la double symétrie du VO_2(M1) autour de l'axe [010] et de la triple symétrie du saphir. En zoomant sur un triple pic (**Figure 3**(b)), le VO_2(M1) montre que chacun des pics principaux est entouré de deux pics satellites plus petits.

Contrairement à certains travaux de la littérature qui affirment que ce triplet est une signature de la structure monoclinique [ZHA12], nous avons attribué le triplet à deux familles de plans du VO_2(M1) très proches qui peuvent ainsi être mesurées simultanément par DRX lors d'un φ-scan. Nous avons démontré expérimentalement que le pic central appartenait au plan $(\bar{2}22)_{VO2(M1)}$, et les satellites au plan $(220)_{VO2(M1)}$. Les mesures complémentaires réalisées pour le plan $(011)_{VO2(M1)}$ ont confirmé cette interprétation. De manière analogue, six doubles pics ont été observés du fait d'une contribution du plan $(\bar{1}11)_{VO2(M1)}$. A partir de ces analyses, nous avons pu déterminer les relations d'épitaxie et le nombre de variants cristallographiques pour la croissance des films de VO_2(M1) sur saphir-c.

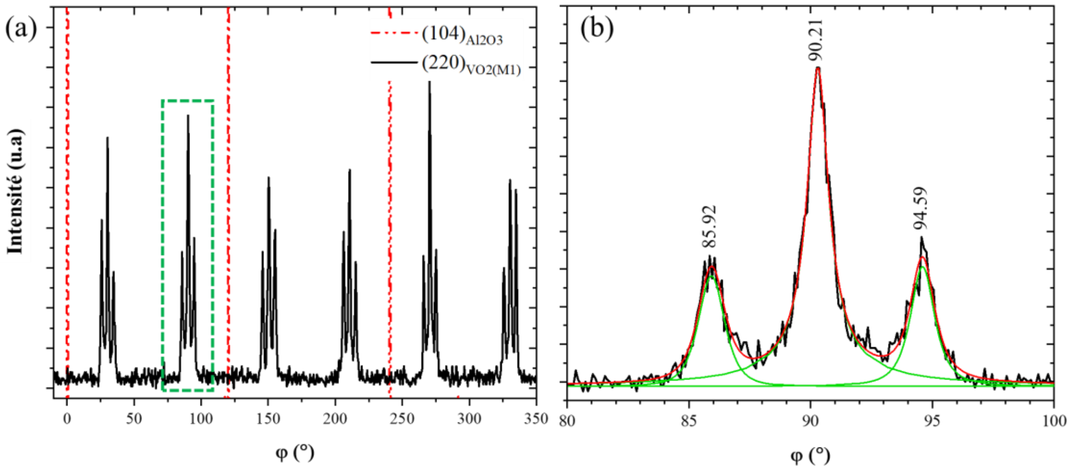

Figure 3: (a) φ-scans réalisés à température ambiante, d'un film de VO_2(M1) déposé sur un saphir-c. Le scan des plans $(220)_{VO2(M1)}$ est visible en noir et celui du saphir en rouge. (b) Le zoom autour de φ=90° permet de mettre en évidence un triple pic.

Au cours de la croissance des films, le VO_2(M1) se développe sur le substrat de saphir-c avec une orientation préférentielle suivant la direction [0h0]. Les axes $\vec{a}_{VO2(M1)}$ et $\vec{c}_{VO2(M1)}$ de la maille monoclinique sont dans le plan (001)Al_2O_3, avec $\vec{a}_{VO2(M1)}$ qui se positionne à ±30° d'un des azimuts du saphir-c (a_1, a_2 et a_3 (**Figure 4**)). En tenant compte des 122.6° de l'angle β entre $a_{VO2(M1)}$ et $c_{VO2(M1)}$, et des trois azimuts du saphir, le VO_2(M1) possède 12 orientations de croissance, toutes identifiées dans les φ-scans. Ces résultats ont été confirmés par des cartographies de l'espace réciproque.

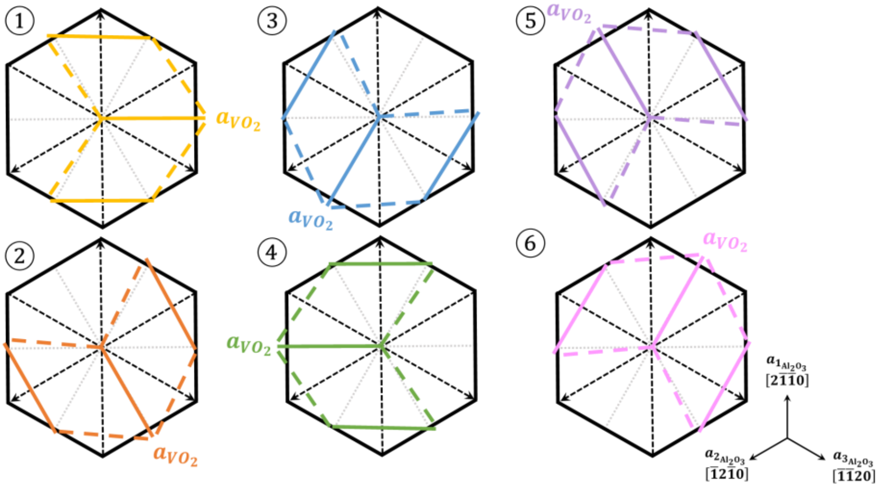

Figure 4: Schéma des 12 variants de VO_2(M1) dans le plan (001) du saphir. ① et ② sont les 4 avec leurs axes $a_{VO2(M1)}$ de chaque côté de l'azimut $a_{3(Al2O3)}$, ③ et ④ de $a_{2(Al2O3)}$, et ⑤ et ⑥ de $a_{1(Al2O3)}$.

b) VO$_2$(M1)/saphir-r

De manière analogue au VO$_2$(M1)/saphir-c, des φ-scans ont été réalisés pour les plans (006)$_{Al2O3}$ et (220)$_{VO2(M1)}$. Les résultats présentés sur la **Figure 5**, indiquent que la trace de (220)$_{VO2(M1)}$ se trouve dans le plan (012)$_{Al2O3}$ à ±90° de la trace du plan (006)$_{Al2O3}$. Nous pouvons en déduire que l'axe $\vec{c}_{VO2(M1)}$ est perpendiculaire à l'axe $\vec{a}_{Al2O3}$ du saphir. Puisque l'axe $\vec{b}_{VO2(M1)}$ est à 90° de $c_{VO2(M1)}$, nous pouvons ajouter que $b_{VO2(M1)}$ se trouve également dans le plan du saphir-r. Grâce à ces mesures et aux résultats des φ-scans réalisés pour le plan (011)$_{VO2(M1)}$, seulement deux variants possibles ont été détectés : le premier suivant $b_{VO2(M1)}$, et le second suivant son opposé à 180° (**Figure 5(b)**).

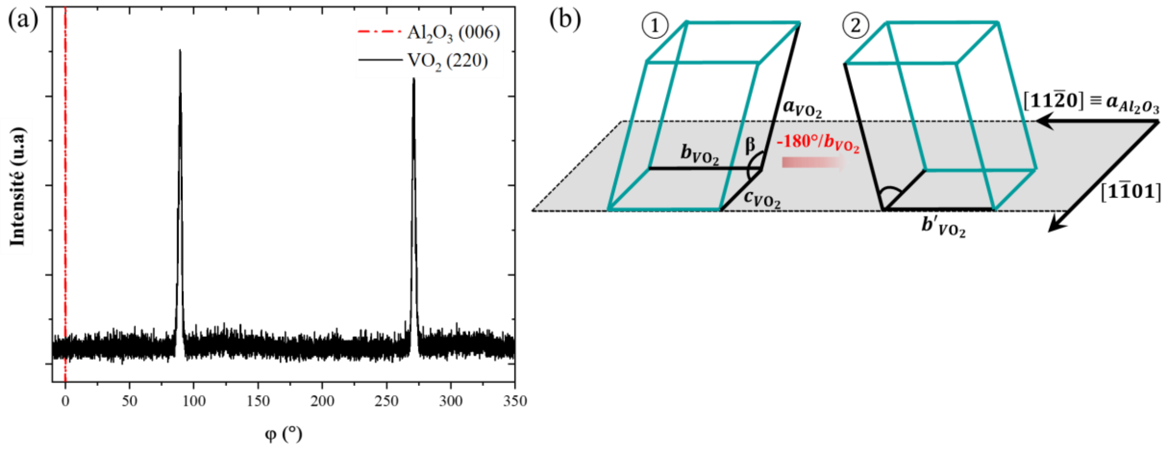

Figure 5: (a) φ-scan d'un film de VO$_2$(M1) déposé sur un saphir-r. Le plan (220)$_{VO2(M1)}$ est visible en noir et celui du saphir en rouge. (c) Schéma représentatif de l'épitaxie du VO$_2$(M1) sur un substrat de saphir-r. ① et ② sont les deux variants identifiés à partir des φ-scans.

2.2. Influence du substrat sur la dynamique de transition de phase

Les caractérisations des films déposés sur les substrats de saphir de type -c et -r montrent que l'orientation crystalline du substrat conduit à une contrainte de compression plus importante suivant la direction [001] pour les films possédant 12 variants de VO$_2$(M1)/saphir-c. Pour les applications ciblées par TE-OX la dynamique de la transition de phase s'avère très importante, pour cela, des mesures de résistivité ont été réalisée pour les films VO$_2$(M1) déposés sur saphir-c et -r en fonction de la température (**Figure 6**(a)).

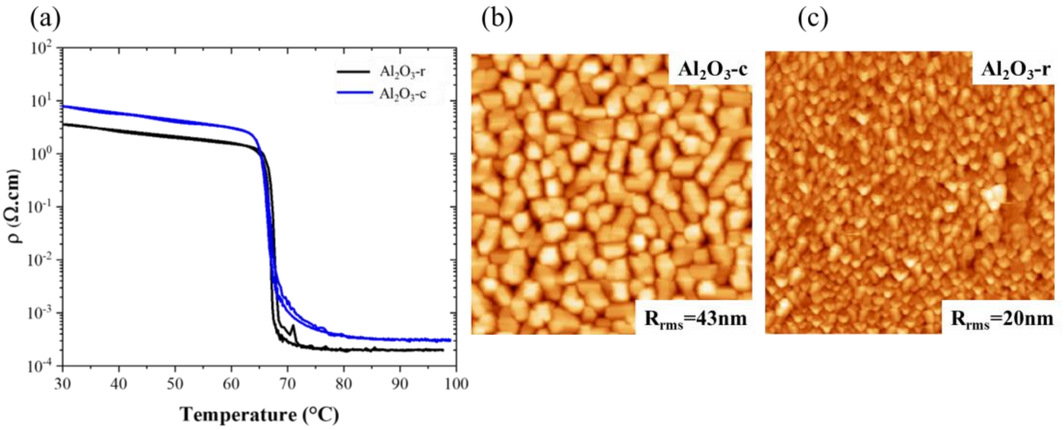

Figure 6: (a) Evolution de la résistivité en fonction de la température et images AFM (5 x 5 µm^2) de la topographie des films de VO$_2$(M1) déposés sur saphir-c (b) et -r (c).

Les deux couches montrent une variation importante de leur résistivité, caractéristique du VO_2, à la transition de phase. Lorsque $T<T_{MIT}$, la résistivité est élevée et propre à l'état isolant M1, tandis qu'à $T> T_{MIT}$, la résistivité chûte brutalement de 4 ordres de grandeur. Les comportements de ces deux types d'échantillons sont très proches, avec une même température de transition en résistivité de 67°C pour le VO_2(M1)/saphir-c et le VO_2(M1)/saphir-r. Cette valeur légèrement inférieure à celle des monocristaux pourrait s'expliquer par l'état de contrainte des films [ABR12]. Les croissances multiples de VO_2(M1)/saphir-c conduisent à une compression de la maille monoclinique suivant la direction [001]. Cette déformation conduit à un déplacement de la bande π^* vers les basses énergies dans la structure électronique de VO_2. Ce déplacement entraîne un rétrécissement entre la bande de valence et la bande de conduction qui favorise une transition plus rapide vers la phase métallique lorsque la température augmente : la température de transition est par conséquent inférieure à la température du monocristal massif de VO_2 (T_{MIT} = 68°C).

De plus, l'étude des films par AFM (**Figure 6**) montre que les couches déposées sur saphir-r sont composées de grains orientés préférentiellement dans une seule direction formant ainsi un film continu avec une rugosité (R_{rms}) d'environ 20 nm. L'échantillon déposé sur saphir-c possède des grains avec plus d'orientations différentes. La MIT dépendant généralement de la qualité cristalline du matériau, une taille de cristallite et une densité de défauts plus importantes peuvent également conduire à une modification de la température de transition.

3. Synthèse de VO_2(B) par voie chimique et physique

L'étude des phases polymorphiques de VO_2 repose essentiellement sur la stabilisation des phases métastables, notamment de la phase B, qui présente un intérêt pour les applications de stockage d'énergie. Notre stratégie pour ce travail consiste dans un premier temps à explorer des nanofils de VO_2(B) synthétisés par la méthode hydrothermale (HT), en s'appuyant sur une expertise déjà bien établie au sein de la société TE-OX, puis d'aller de l'avant en développant des couches minces par la pulvérisation cathodique radiofréquence à effet magnétron (RFMS). Dans le premier cas, les nanofils obtenus dans une solution sont libres de contraintes externes tandis que dans le deuxième cas, la croissance épitaxiale des films minces sur un substrat induit des contraintes comme nous l'avons vu précédemment. Ces deux approches différentes vont permettre d'approfondir notre compréhension du VO_2 et de l'impact de la morphologie sur la stabilité de la phase B.

3.1. Fabrication des nanofils de VO_2(B) par voie HT

Les nanofils de VO_2(B) ont été obtenus par synthèse HT à partir de précurseurs de V_2O_5 et d'une solution aqueuse d'acide oxalique (OA). La synthèse HT étant connue comme une technique sensible aux conditions expérimentales du fait de l'interaction entre tous les paramètres, le taux de remplissage ainsi que la température ont été maintenus constants. Dans ce travail, nous nous sommes concentrés sur l'étude de l'influence de la concentration des précurseurs et du temps de synthèse. Trois rapports molaires de V_2O_5/OA ont été fixés à 1.0, 1.1 et 1.2 et le temps de réaction a été fixé à 24 ou 48h. L'analyse DRX des poudres obtenues montre que tous les pics correspondent à des réflections de la phase B du VO_2 sans présence d'autres oxydes ou phases polymorphiques (**Figure 7**).

L'ajustement réalisé pour chaque pic $(002)_{VO2(B)}$ montre qu'avec l'augmentation du temps de synthèse, la largeur à mi-hauteur (FWHM) diminue. Le pic devient plus étroit ce qui indique que la cristallinité des poudres augmente avec le temps de synthèse, et également avec la concentration de OA.

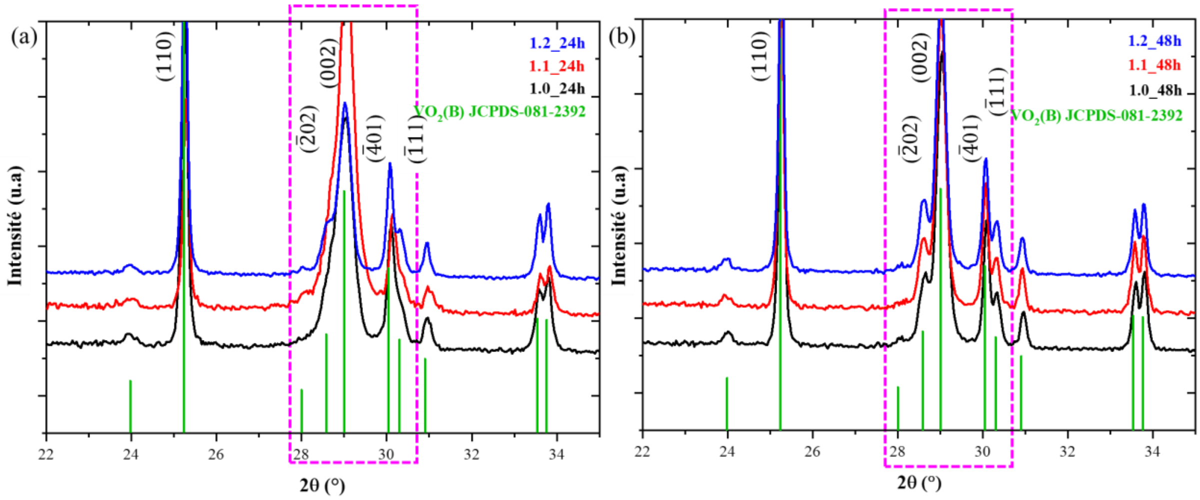

Figure 7: Diffractogrammes DRX de nanopoudres de VO_2 synthétisées à 160°C durant (a) 24h et (b) 48h.

Durant l'analyse physico-chimique du VO_2(B), nous nous sommes heurtés à la mauvaise stabilité de cette phase. Bien que celle-ci soit conservée dans des conditions de pression, température et humidité contrôlées (température ambiante et RH%=30%), l'oxydation des poudres obtenues commence après quelques semaines et continue jusqu'à obtention de V_2O_5 qui est l'oxyde de vanadium le plus stable dans les conditions ambiantes.

La réoxydation accelérée des nanofils rend toute analyse structurale de la phase difficile et empêche son industrialisation. En conséquence, par la suite les travaux ont été focalisés sur le développement des couches minces de VO_2(B). Cette deuxième approche est avantageuse car elle permettrait de stabiliser la structure par les contraintes épitaxiales, induites par le substrat.

3.2. Influence du substrat sur la stabilisation du VO_2(B)

Au cours du développement des films de VO_2, des substrats de $SrTiO_3$ (STO) (001) et de saphir-c ont été introduits en même temps dans le bâti de RFMS. Les films obtenus ont été étudiés par DRX et par microscopie électronique à balayage (MEB, **Figure 8**) et présentent des morphologies très différentes. Les films développés sur saphir-c comme décrit précédemment, confirment la croissance de la phase M1. Avec exactement les mêmes conditions expérimentales, les couches obtenues sur STO montrent la stabilisation du VO_2(B). Le VO_2(B) a alors une orientation préférentielle de croissance suivant l'axe $\vec{c}$ du STO : (00l)VO_2(B)//(00l)STO.

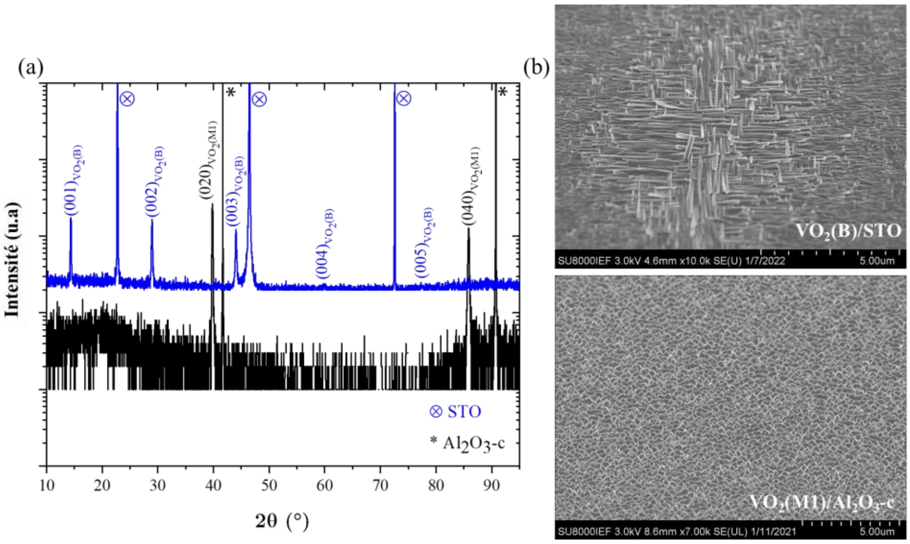

Figure 8: (a) Diffractogrammes DRX et (b) images MEB de films de VO_2(M1) et VO_2(B) déposés sur des substrats de saphir-c et STO(001), respectivement.

La nature et l'orientation cristalline du substrat ayant un impact important sur la stabilisation des polymorphes de VO_2, une étude approfondie de la croissance épitaxiale du VO_2(B)/STO(001) a été réalisée. Les φ-scans réalisés pour le VO_2(B) et le STO, mettent en évidence les 4 orientations de croissance possibles de la maille monoclinique de VO_2(B) sur le STO (**Figure 9**).

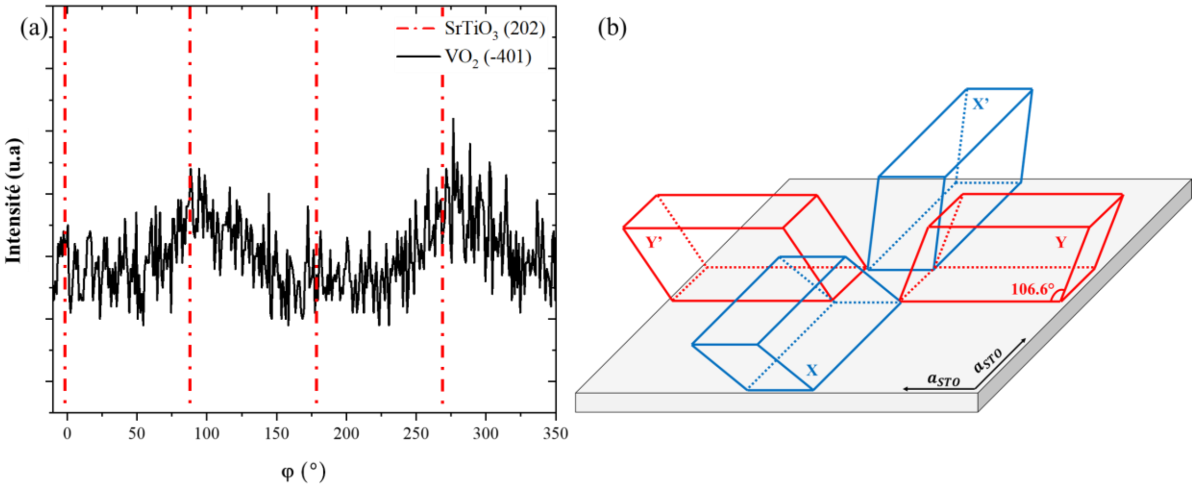

Figure 9: (a) φ-scans réalisés à température ambiante, d'un film de VO_2(B) déposé sur un substrat de STO(001). Le plan $(\bar{4}01)_{VO2(B)}$ est visible en noir et celui du STO en rouge. (b) Schéma représentatif de l'épitaxie du VO_2(B) sur STO avec ses 4 variants cristallographiques.

Au cours des recherches sur la croissance de VO_2 en film mince, nous avons mis en évidence le rôle clé du substrat sur la stabilisation des phases polymorphiques de VO_2. Les caractérisations démontrent que pour des conditions de dépôt strictement identiques, deux phases différentes de VO_2 peuvent être stabilisées. Il est également mis en évidence que le substrat permet une compression de la maille dans le plan de croissance, ce qui ralentit la réoxydation des phases métastables comme le VO_2(B).

4. Commutateurs radiofréquences à base de VO_2

Dans le cadre du développement technologique de l'entreprise TE-OX, l'expertise sur les couches minces acquise lors de cette thèse a permis le développement de commutateurs RF à base de VO_2 activés thermiquement et optiquement.

Une première étude réalisée à λ=365 nm a permis de mettre en évidence l'importance de la focalisation du spot lumineux. Sous éclairement continu, nous observons que la résistance d'un commutateur à base de VO_2 chute proportionnellement à mesure que la température augmente (**Figure 10**). Aucune transition de phase n'a été observée lors de ces mesures. Pour diminuer la chaleur émise par la diode, il est nécessaire d'éloigner la source du commutateur et de focaliser la taille du spot afin d'assurer une densité d'énergie absorbée (fluence) suffisante pour activer la transition.

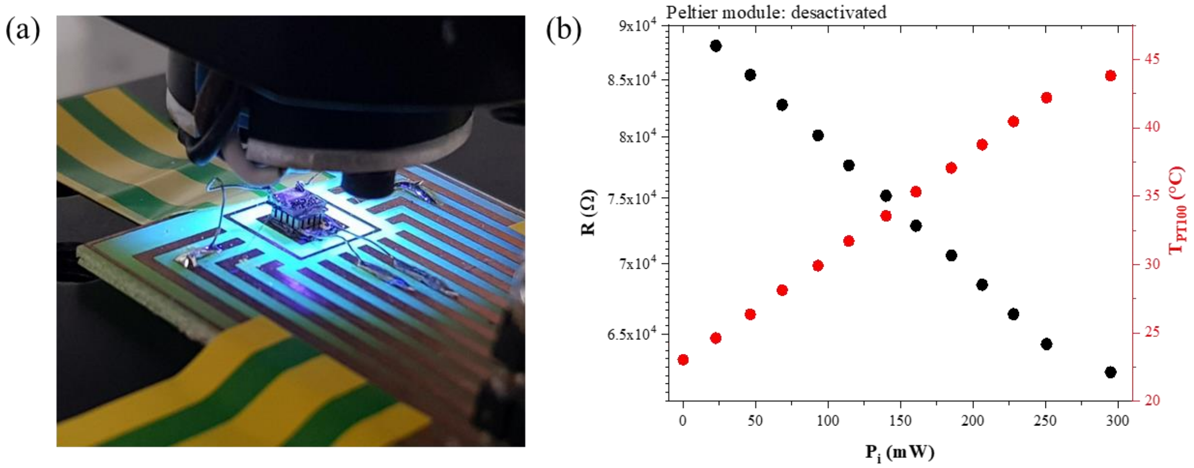

Figure 10: (a) Photo du dispositif permettant la mesure de résistance sous activation optique et (b) évolution de la résistance et de la température mesurée par la sont (PT100) en fonction de la puissance incidente délivrée par la diode à λ=365 nm.

C'est dans ce but que nous nous sommes tournés vers les mesures pompe-sonde. Les premiers résultats obtenus à λ=800 nm sont prometteurs et démontrent que notre VO_2 peut transiter en moins de 10 ps. Faute de temps, nous n'avons pas encore pu comparer ces résultats avec une source UV qui nous permettrait d'avoir une meilleure compréhension des mécanismes liés à la transition de phase du VO_2.

5. Conclusion

Les résultats présentés dans ce travail de recherche sur les polymorphes de VO_2 fournissent une approche générale pour comprendre et utiliser la transition de phase métal-isolant. Le développement des films par RFMS sur les substrats d'Al_2O_3 et de $SrTiO_3$ a permis de mettre en évidence que le fort désaccord de maille entraîne la croissance de VO_2 par coïncidence de domaines, avec formation de multiples variants : 12 pour le VO_2(M1)/saphir-c, 2 pour VO_2(M1)/saphir-r et 4 pour VO_2(B)/$SrTiO_3$. Par ailleurs, les différentes études menées sur les couches de VO_2(M1) ont montré que la déformation de l'axe $\vec{c}_{VO2(R)}$ ($\equiv \vec{a}_{VO2(M1)}$) suite à une compression, conduit à une diminution de la température de transition. Les couches minces d'une excellente qualité cristalline développées au cours de cette thèse, ont été utilisées pour la fabrication de commutateurs RF. Les étapes technologiques de la fabrication n'ont pas impacté la qualité du matériau. Les dispositifs commandés thermiquement montrent des performances compétitives avec les technologies existantes, avec une très bonne fiabilité attendue du fait de la simplicité de leur architecture. Afin d'améliorer la vitesse de la commutation, les premiers essais d'activation optique ont été entrepris et seront continués au sein de l'entreprise.